

**Imperial College**  
**London**

**Choline Kinase Inhibition as a Treatment  
Strategy of Cancers with Deregulated Lipid  
Metabolism**

**Sebastian Trousil**

**Imperial College London**  
**Department of Surgery and Cancer**

A dissertation submitted for the degree of Doctor of Philosophy

## **Declaration**

I declare that this dissertation is my own and original work, except where explicitly acknowledged.

The copyright of this thesis rests with the author and is made available under a Creative Commons Attribution Non-Commercial No Derivatives licence. Researchers are free to copy, distribute or transmit the thesis on the condition that they attribute it, that they do not use it for commercial purposes and that they do not alter, transform or build upon it. For any reuse or redistribution, researchers must make clear to others the licence terms of this work.

# Abstract

Aberrant choline metabolism is a characteristic shared by many human cancers. It is predominantly caused by elevated expression of choline kinase alpha, which catalyses the phosphorylation of choline to phosphocholine, an essential precursor of membrane lipids. In this thesis, a novel choline kinase inhibitor has been developed and its therapeutic potential evaluated. Furthermore the probe was used to elaborate choline kinase biology.

A lead compound, ICL-CCIC-0019 ( $IC_{50}$  of  $0.27 \pm 0.06 \mu\text{M}$ ), was identified through a focused library screen. ICL-CCIC-0019 was competitive with choline and non-competitive with ATP. In a selectivity screen of 131 human kinases, ICL-CCIC-0019 inhibited only 5 kinases more than 20% at a concentration of  $10 \mu\text{M}$  (< 35% in all 131 kinases). ICL-CCIC-0019 potently inhibited cell growth in a panel of 60 cancer cell lines (NCI-60 screen) with a median  $GI_{50}$  of  $1.12 \mu\text{M}$  (range:  $0.00389\text{--}16.2 \mu\text{M}$ ). Importantly, proliferation of normal cells was only minimally affected (MCF-10A, ST-T1b and CCD-18Co;  $GI_{50}$   $30\text{--}120 \mu\text{M}$ ). In HCT116 cells, ICL-CCIC-0019 potently inhibited the formation of phosphocholine ( $EC_{50}$   $0.67 \pm 0.28 \mu\text{M}$ ), which consequently decreased the formation of phosphatidylcholine. The compound arrested cells in the G1 phase of the cell cycle, and induced endoplasmic reticulum stress and apoptosis. A single injection of ICL-CCIC-0019 at  $10 \text{ mg/kg}$  decreased tumour uptake of the choline kinase specific PET tracer [ $^{18}\text{F}$ ]fluoromethyl-[1,2- $^2\text{H}_4$ ]-choline at 24 hours ( $AUC_{0\text{--}60}$   $-23\%$ ). Treatment of HCT116 colon cancer cell xenograft bearing mice with  $5 \text{ mg/kg}$  ICL-CCIC-0019 i.p. resulted in strong tumour growth inhibition.

Human breast cancer cell lines oncogenically transformed by HER2 exhibit increased levels of phosphocholine and are therefore more likely respond to CHKA inhibition. To identify such patients more readily, a novel, non-invasive, PET-imaging-based HER2-targeting diagnostic tool, [ $^{18}\text{F}$ ]GE-226, was developed. [ $^{18}\text{F}$ ]GE-226 ( $K_D = 76 \text{ pM}$ ) uptake was 11 to 67-fold higher in 10 HER2 positive versus negative cell lines *in vitro*. Tumour uptake correlated with HER2 expression in 5 different tumour models ( $r^2 = 0.78$ ), and a

fluorophore-labelled tracer analogue co-localised with HER2 expression. Tracer uptake was not influenced by short-term or continuous treatment with trastuzumab, but reflected HER2 degradation by short-term HSP90 inhibition.

Taken together, these data further validate CHKA as a drug target and warrant the further development of ICL-CCIC-0019, potentially in the setting of HER2 positive cancers.

# Acknowledgement

I would like to express my deepest appreciation to Professor Eric Aboagye for providing me the opportunity to conduct this work in a stimulating environment. His enthusiastic guidance and inspiration shaped my scientific thinking and allowed me to develop a wide array of research skills. I would like to thank my secondary supervisor Dr. Rohini Sharma for many insightful discussions and for involving me in multiple projects, which greatly broadened my scientific horizon.

I would like to express my special thanks to Dr. Maciej Kaliszczak for constantly supporting my project and professional development. He taught me many aspects of pharmacology and the most challenging *in vivo* experiments. Dr. Quang-Dé Nguyen generously shared his vast expertise in molecular imaging and was a permanent source of help throughout all imaging experiments. I would like to thank Dr. Duncan Hiscock, Dr. Susan Hoppmann and Peter Iveson from GE Healthcare for the exciting collaboration on the HER2 project.

I would like to extend my thanks to Dr. Laurence Carroll and Dr. Andrew Kalusa for synthesis of choline kinase inhibitors, Dr. Ola Åberg for conducting the molecular modelling experiments, Peter Iveson for synthesis of [ $^{18}\text{F}$ ]GE-226, Dr. Diana Brickute, Dr. Robin Fortt, Dr. Graham Smith and Frazer Twyman for synthesis of [ $^{18}\text{F}$ ]D4-FCH, Dr. Giampaolo Tomasi for kinetic modelling of PET data and Dr. Susan Hoppmann for conducting the experiment with fluorescein labelled GE-226.

Outside academia, I want to thank to Dr. David Pinato for innumerable engaging conversations and for sharing the journey of this PhD.

Most importantly, I want to express my heartfelt gratefulness to my parents, my sister Stefanie, my aunt Edda and my other half Jeehyea. Their constant support, trust and love allowed me to perform at my best and will always be appreciated.



# Publications

The following publications are associated with this dissertation:

[1] **Trousil S**, Carroll L, Kalusa A, Aberg O, Kaliszczak M, Aboagye EO. Design of symmetrical and nonsymmetrical *N,N*-dimethylaminopyridine derivatives as highly potent choline kinase alpha inhibitors. *MedChemComm*. 2013;4:693–6.

[2] **Trousil S**, Hoppmann S, Nguyen Q-D, Kaliszczak M, Tomasi G, Iveson P, Hiscock, Duncan, Aboagye, EO. Positron emission tomography imaging with  $^{18}\text{F}$ -labeled  $Z_{\text{HER2}:2891}$  Affibody for detection of HER2 expression and pharmacodynamic response to HER2-modulating therapies. *Clin Cancer Res*. 2014;20:1632-43.

The following publications have been contributed to during the course of this degree, but are not included in this work:

[3] Kaliszczak M, **Trousil S**, Aberg O, Perumal M, Nguyen Q-D, Aboagye EO. A novel small molecule hydroxamate preferentially inhibits HDAC6 activity and tumour growth. *Br J Cancer*. 2013;108:342–50.

[4] Witney TH, Pisaneschi F, Alam IS, **Trousil S**, Kaliszczak M, Twyman F, Brickute D, Nguyen Q-D, Schug Z, Gottlieb E, Aboagye EO. Preclinical evaluation of  $^{18}\text{F}$ -fluoro-pivalic acid as a novel imaging agent for tumor detection. *J Nucl Med*. Forthcoming 2014.





# Table of Contents

<b>1</b>	<b>Introduction</b>	<b>29</b>
1.1	Deregulated choline metabolism in cancer . . . . .	30
1.2	Choline biochemistry . . . . .	31
1.3	Kennedy (CDP-choline) pathway for PtdCho synthesis . . . . .	33
1.3.1	Choline transport . . . . .	33
1.3.2	Choline kinase alpha and beta . . . . .	35
1.3.3	Cytidyltransferase and phosphocholine transferase . . . . .	36
1.3.4	Alternative ways to generate PtdCho . . . . .	37
1.3.5	PtdCho catabolic pathways . . . . .	38
1.4	Molecular imaging of choline metabolism . . . . .	39
1.4.1	MRS . . . . .	40
1.4.2	PET imaging . . . . .	41
1.5	Regulation of choline biochemistry in cancer . . . . .	44
1.6	Inhibition of CHKA as a treatment strategy in cancer . . . . .	46
1.6.1	CHKA RNAi impedes proliferation . . . . .	46
1.6.2	Pharmacological inhibitors of CHK . . . . .	47
1.7	Aims of thesis . . . . .	50
<b>2</b>	<b>Materials and Methods</b>	<b>51</b>
2.1	Synthetic procedures . . . . .	51
2.1.1	Synthesis of choline kinase inhibitors . . . . .	51
2.1.2	Radiochemistry of [ <sup>18</sup> F]D4-FCH . . . . .	52
2.1.3	Radiochemistry of [ <sup>18</sup> F]GE-226 . . . . .	53
2.2	Cell Culture . . . . .	54
2.3	[ <sup>18</sup> F]D4-FCH-based CHK activity assay . . . . .	55

2.3.1	Whole cell assay . . . . .	55
2.3.2	Cell lysate-based assay using [ <sup>18</sup> F]D4-FCH . . . . .	56
2.4	Enzyme-based CHKA activity assays . . . . .	56
2.4.1	Kinase Glo assay . . . . .	56
2.4.2	ADP Glo assay . . . . .	57
2.4.3	PEP / LDH coupled CHKA activity assay (IC <sub>50</sub> ) . . . . .	57
2.5	Molecular modelling . . . . .	59
2.6	Growth inhibition assay (GI <sub>50</sub> ) . . . . .	60
2.7	[ <sup>3</sup> H]choline whole cell CHK inhibition assay (EC <sub>50</sub> ) . . . . .	60
2.8	siRNA transfections . . . . .	61
2.9	Caspase 3/7 Glo assay . . . . .	61
2.10	Western blotting . . . . .	61
2.11	RNA extraction and qRT-PCR . . . . .	62
2.12	DNA cell cycle analysis using flow cytometry . . . . .	63
2.13	Transfection of U2OS cells with CHKA and CHKB . . . . .	63
2.14	Native gel western blots to detect protein dimerisation . . . . .	64
2.15	[ <sup>3</sup> H]choline uptake . . . . .	64
2.16	Lactate dehydrogenase assay . . . . .	64
2.17	[ <sup>3</sup> H]choline pulse-chase experiment . . . . .	65
2.18	Immunofluorescence . . . . .	65
2.19	High-performance liquid chromatography (HPLC) . . . . .	66
2.20	<i>In vitro</i> metabolism . . . . .	66
2.21	Cell permeability in Caco-2 cells . . . . .	67
2.22	Plasma protein binding . . . . .	68
2.23	Tumour model for the evaluation of ICL-CCIC-0019 . . . . .	68
2.24	Pharmacokinetic and plasma metabolite studies . . . . .	68
2.25	PET-CT imaging studies related to ICL-CCIC-0019 . . . . .	69
2.26	Kinetic modelling of [ <sup>18</sup> F]D4-FCH data . . . . .	70
2.27	Antitumour Activity . . . . .	70
2.28	shRNA targeting CHKA . . . . .	70
2.29	Drug combination experiments . . . . .	71
2.30	Surface Plasmon Resonance . . . . .	71
2.31	Cells and treatments for evaluation of [ <sup>18</sup> F]GE-226 . . . . .	72

	11
2.32 <i>In vitro</i> [ <sup>18</sup> F]GE-226 uptake assay . . . . .	72
2.33 Small animal experimental models and treatments for [ <sup>18</sup> F]GE-226 PET studies . . . . .	72
2.34 [ <sup>18</sup> F]GE-226 PET-CT imaging . . . . .	73
2.35 ELISA . . . . .	73
2.36 Metabolic stability of [ <sup>18</sup> F]GE-226 . . . . .	73
2.37 Biodistribution . . . . .	74
2.38 Kinetic modelling of [ <sup>18</sup> F]GE-226 . . . . .	74
2.39 Synthesis of fluorescein labelled GE-226 . . . . .	75
2.40 Small animal model for fluorescent GE-226 experiment . . . . .	75
2.41 Immunohistochemistry . . . . .	76
2.42 Sequencing . . . . .	76
2.43 Statistical analysis . . . . .	76
<b>3 Design and Evaluation of Choline Kinase Inhibitors</b>	<b>77</b>
3.1 Analysis of CHKA crystal structure . . . . .	77
3.2 Development and validation of CHKA inhibition assay . . . . .	79
3.2.1 Radioactive assays using [ <sup>18</sup> F]D4-FCH . . . . .	80
3.2.2 Assays using purified CHKA2 . . . . .	82
3.3 Evaluation of choline kinase inhibitors . . . . .	89
3.3.1 CHKA enzymatic inhibition . . . . .	89
3.3.2 Molecular Modelling . . . . .	91
3.3.3 Fragment-based screen of ATP mimics . . . . .	94
3.3.4 Antiproliferative activity . . . . .	95
3.3.5 Inhibition of CHK in HCT116 cells . . . . .	96
3.4 Discussion . . . . .	98
<b>4 Use of ICL-CCIC-0019 to elucidate CHKA biology in cancer</b>	<b>101</b>
4.1 Selection of cancer cell lines . . . . .	101
4.1.1 The Cancer Cell Line Encyclopaedia (CCLE) . . . . .	102
4.1.2 Validation of HCT116 model by siRNA . . . . .	102
4.1.3 Establishment and evaluation of isogenic CHKA and CHKB overexpressing U2OS cells . . . . .	104
4.2 ICL-CCIC-0019 has low off-target effects . . . . .	105

4.3	ICL-CCIC-0019 has potent antiproliferative activity . . . . .	106
4.4	Effect of ICL-CCIC-0019 on CHKA dimerisation . . . . .	111
4.5	ICL-CCIC-0019 reduces membrane lipid formation . . . . .	111
4.6	ICL-CCIC-0019 induces cell death via endoplasmic reticulum stress mechanism . . . . .	112
4.7	ICL-CCIC-0019 arrests cells in G1 phase of cell cycle . . . . .	112
4.8	ICL-CCIC-0019 prompts caspase 3/7 activation . . . . .	113
4.9	<i>In vitro</i> pharmacology . . . . .	113
4.9.1	Microsomal stability . . . . .	114
4.9.2	Cell permeability and ABC transporter substrate specificity . . . . .	115
4.9.3	Plasma protein binding . . . . .	117
4.10	Pharmacokinetics of ICL-CCIC-0019 . . . . .	117
4.10.1	Tolerability . . . . .	117
4.10.2	Pharmacokinetics . . . . .	119
4.10.3	<i>In vivo</i> metabolism . . . . .	120
4.11	ICL-CCIC-0019 inhibits CHK activity <i>in vivo</i> . . . . .	121
4.12	Antitumour activity . . . . .	125
4.13	[ <sup>18</sup> F]FLT PET . . . . .	125
4.14	Inducible CHKA shRNA model . . . . .	125
4.14.1	Identification of shRNA sequence that sufficiently silences CHKA . . . . .	126
4.14.2	Characterisation of HCT116-shCHKA3 cell line . . . . .	126
4.14.3	[ <sup>18</sup> F]D4-FCH PET imaging of CHKA shRNA model . . . . .	127
4.15	Effects of combined CHK and HDAC inhibition . . . . .	128
4.16	Discussion . . . . .	132
<b>5</b>	<b>Affibody PET Imaging of HER2 Expression</b>	<b>143</b>
5.1	Introduction . . . . .	143
5.2	Affibody-HER2 binding properties . . . . .	146
5.3	[ <sup>18</sup> F]GE-226 exhibits specific and lineage-independent HER2 binding . . . . .	147
5.4	[ <sup>18</sup> F]GE-226 exhibits a different binding site than trastuzumab and predicts detection of HER2 degradation by NVP-AUY922 . . . . .	148
5.5	[ <sup>18</sup> F]GE-226 discriminates differential HER2 expression <i>in vivo</i> . . . . .	148

5.6	Localisation and intensity of fluorescein-labelled GE-226 correlates with DAKO HercepTest . . . . .	153
5.7	[ <sup>18</sup> F]GE-226 can correctly assess HER2 status independently of prior trastuzumab treatment and predicts for response to NVP-AUY922 <i>in vivo</i> . . . . .	154
5.8	Discussion . . . . .	159
<b>6</b>	<b>Summary and concluding remarks</b>	<b>165</b>
6.1	Summary of work . . . . .	165
6.2	Advances to previous studies and future directions . . . . .	167
<b>A</b>	<b>Spectra of relevant compounds</b>	<b>171</b>
<b>B</b>	<b>Kinase screen</b>	<b>179</b>
	<b>References</b>	<b>183</b>



# List of Figures

1.1	Fate of choline . . . . .	32
1.2	Kennedy pathway . . . . .	34
1.3	Enzymes involved in phospholipid metabolism . . . . .	38
1.4	Metabolite analysis by $^1\text{H}$ and $^{31}\text{P}$ MRS . . . . .	40
1.5	Principle of PET imaging . . . . .	42
1.6	Scheme of the two-compartment, single input 3k model used to interpret choline PET data . . . . .	43
3.1	Crystal structure of CHKA . . . . .	78
3.2	Overview of designed choline kinase inhibitor scaffolds . . . . .	79
3.3	Cell-based inhibition assay using $^{18}\text{F}$ ]D4-FCH . . . . .	81
3.4	Radio-HCPL chromatogram of cell lysate-based assay . . . . .	82
3.5	Kinase Glo assay . . . . .	83
3.6	ADP Glo assay . . . . .	85
3.7	Assay principle of PK/LDH coupled kinase activity assay . . . . .	86
3.8	Identification of suitable microplates for PK/LDH coupled choline kinase assay . . . . .	87
3.9	Stability of NADH in 100 mM Tris buffer . . . . .	87
3.10	Reaction progress curves and linearity of NADH signal . . . . .	88
3.11	Determination of $\text{IC}_{50}$ . . . . .	89
3.12	Structures of all tested compounds . . . . .	90
3.13	Inhibition of $\Delta 49\text{N}$ CHKA2 and growth of human HCT116 cancer cell lines . . . . .	92
3.14	Lineweaver-Burk plots of compounds <b>8</b> and <b>12</b> . . . . .	92
3.15	Validation of molecular model . . . . .	93
3.16	Proposed binding modes of <i>bis</i> -DMAP compounds . . . . .	93

3.17	Proposed binding modes of nonsymmetrical inhibitors . . . . .	94
3.18	ATP mimicking fragments included in screen against CHKA2 . . . . .	95
3.19	Assay principle of Bligh and Dyer extraction . . . . .	97
4.1	CHKA mRNA expression in cancer cell lines . . . . .	103
4.2	Effects of CHKA knockdown in HCT116 cells . . . . .	104
4.3	Selection of individual clones by FACS . . . . .	105
4.4	Characterisation of isogenic U2OS CHKA and CHKB model . . . . .	106
4.5	Selectivity of ICL-CCIC-0019 . . . . .	107
4.6	ICL-CCIC-0019 preferentially inhibits growth of cancer cells . . . . .	108
4.7	NCI-60 screen . . . . .	109
4.8	ICL-CCIC-0019 does not destabilise CHKA dimers . . . . .	111
4.9	ICL-CCIC-0019 treatment decreases formation of choline-containing lipids . . . . .	112
4.10	CHKA inhibition induces ER stress . . . . .	113
4.11	ICL-CCIC-0019 induces G1 arrest and subsequently increases sub-G1 population . . . . .	114
4.12	ICL-CCIC-0019 activates caspases 3 and 7 and reduces cell survival . . . . .	115
4.13	Microsomal stability, cell permeability and plasma protein binding of ICL-CCIC-0019 . . . . .	116
4.14	Body weight changes in response to ICL-CCIC-0019 . . . . .	118
4.15	Plasma and tissue pharmacokinetics of ICL-CCIC-0019 . . . . .	119
4.16	ICL-CCIC-0019 inhibits choline kinase activity <i>in vivo</i> . . . . .	122
4.17	[ <sup>18</sup> F]D4-FCH imaging derived tumour TACs of HCT116 xenograft-bearing mice . . . . .	123
4.18	Pharmacokinetic modelling of competitive inhibition of CHKA by ICL-CCIC-0019 using [ <sup>18</sup> F]D4-FCH . . . . .	124
4.19	Antitumour activity of ICL-CCIC-0019 . . . . .	125
4.20	ICL-CCIC-0019 treatment increased [ <sup>18</sup> F]FLT uptake <i>in vivo</i> . . . . .	126
4.21	pTRIPZ vector map . . . . .	127
4.22	Selection of HCT116 cells transduced with CHKA targeting shRNA . . . . .	128
4.23	Characterisation of HCT116-shCHKA3 cell line . . . . .	129
4.24	<i>In vivo</i> characterisation of HCT116-shCHKA model . . . . .	130
4.25	[ <sup>3</sup> H]choline uptake in vorinostat and C1A treated HCT116 cells . . . . .	132



5.1	Functional interaction between HER2 and CHKA . . . . .	144
5.2	Interaction of GE-226 with HER2 as determined by surface plasmon resonance	147
5.3	[ <sup>18</sup> F]GE-226 binds with high selectivity and sensitivity to HER2 . . . . .	149
5.4	[ <sup>18</sup> F]GE-226 possesses a different binding site than trastuzumab and detects HER2 degradation upon HSP90 inhibition . . . . .	150
5.5	Tumour profiles of [ <sup>18</sup> F]GE-226 in differentially HER2 expressing xenograft models . . . . .	151
5.6	Plasma metabolite profile and tissue pharmacokinetics of [ <sup>18</sup> F]GE-226 . . .	152
5.7	Biodistribution of [ <sup>18</sup> F]GE-226 in tumour-bearing BALB/c nude mice . . .	153
5.8	Tissue pharmacokinetic analysis of [ <sup>18</sup> F]GE-226 using a single input 2-tissue 3k model . . . . .	154
5.9	Specificity of [ <sup>18</sup> F]GE-226 receptor interaction as determined by blocking studies . . . . .	155
5.10	GE-226 co-localises with HER2 protein expression in tumours with spatial heterogeneity . . . . .	155
5.11	[ <sup>18</sup> F]GE-226 binding does not interfere with trastuzumab treatment . . . .	156
5.12	HER2 expression analysis and genomic DNA sequencing in relation to up- take rate constants in trastuzumab-treated or control xenografts . . . . .	157
5.13	[ <sup>18</sup> F]GE-226 can predict response to HSP90 inhibition . . . . .	158
6.1	Consequences of choline kinase inhibition. . . . .	167



# List of Tables

1.1	Tissue distribution of choline transporters . . . . .	35
1.2	Structures of choline kinase inhibitors and their pharmacological characteristics . . . . .	48
3.1	CHKA2 enzyme kinetics assay components . . . . .	88
3.2	IC <sub>50</sub> and GI <sub>50</sub> of inhibitors . . . . .	91
3.3	Inhibitory activity of ATP mimicking fragments against CHKA2 . . . . .	95
3.4	Growth inhibition of all compounds in various cancer cell lines . . . . .	96
3.5	Inhibition of [ <sup>3</sup> H]PCho formation in HCT116 cells . . . . .	97
4.1	Growth inhibitory properties of ICL-CCIC-0019 and mutation analysis of NCI-60 panel . . . . .	110
4.2	Plasma metabolites of ICL-CCIC-0019 . . . . .	120
4.3	List of expected metabolites . . . . .	121
4.4	Combination index of ICL-CCIC-0019 and HDAC inhibitors C1A or vorinostat . . . . .	131
5.1	Summary of GE-226 binding kinetics to human and rhesus HER2. . . . .	146



# List of Schemes

2.1	Synthesis of symmetrical compounds <b>1</b> , <b>3</b> , <b>5–8</b> and <b>13</b> . . . . .	52
2.2	Synthesis of nonsymmetrical compounds <b>2</b> , <b>4</b> , and <b>9–12</b> . . . . .	53
2.3	Radiolabelling of [ <sup>18</sup> F]D4-FCH . . . . .	54
2.4	FASTlab-compatible automated synthesis of [ <sup>18</sup> F]GE-226 . . . . .	54



# Abbreviations

[ <sup>18</sup> F]D4-FCH	[ <sup>18</sup> F]fluoromethyl-[1,2- <sup>2</sup> H <sub>4</sub> ]-choline
[ <sup>18</sup> F]FDG	[ <sup>18</sup> F]fluorodeoxyglucose
[ <sup>18</sup> F]FLT	[ <sup>18</sup> F]3'-fluoro-3'-deoxy-L-thymidine
%ID/mL	per centage injected dose per mL tissue
<sup>1</sup> H MRS	proton magnetic resonance spectroscopy
5-FU	5-fluorouracil
ABC	ATP-binding cassette
AMPK	AMP-activated protein kinase
AP-1	activator protein 1
ATF	activating transcription factor
BCA	bicinchoninic acid
BN-PAGE	blue native polyacrylamide gel electrophoresis
CCLC	Cancer Cell Line Encyclopaedia
CCT	CTP:phosphocholine cytidyltransferase
CDP	cytidine diphosphate
CHK	choline kinase
CHKA	choline kinase alpha
CHKB	choline kinase beta
CHOP	C/EBP homology protein
CHPT1	gene name for CPT (CDP-choline:1,2-diacylglycerol cholinephosphotransferase)
CHT	choline transporter
CI	combination index
CKI1	yeast choline kinase

CPT	CDP-choline:1,2-diacylglycerol cholinephosphotransferase
CTL	choline transporter-like protein
CTP	cytidine triphosphate
DAG	diacylglycerol
DMAP	<i>N,N</i> -dimethylaminopyridine
DOX	doxycycline
EC <sub>50</sub>	half-maximal inhibitory concentration in biological assay
EGF	epidermal growth factor
EGFR	epidermal growth factor receptor
eIF2 $\alpha$	initiation factor-2 alpha
ER	endoplasmic reticulum
ErbB	v-Erb-B2 avian erythroblastic leukemia viral oncogene homolog
ERK8	extracellular signal regulated kinase 8
Ets-1	v-ets avian erythroblastosis virus E26 oncogene homolog 1
FASN	fatty acid synthase
FBA	fluorobenzaldehyde
FFPE	formalin-fixed paraffin embedded
FISH	fluorescence in situ hybridisation
GI <sub>50</sub>	half-maximal growth inhibitory concentration
GMP	good manufacturing practice
GPC	glycerophosphocholine
GPCPD-1	glycerophosphocholine phosphodiesterase 1
GRP78	glucose-regulated protein 78
HAT	histone acetyltransferases
HBBS	Hank's buffered salt solution
HC-3	hemicholinium-3
HDAC	histone deacetylase
hENT1	human equilibrative nucleoside transporter type 1
HER2	human epidermal growth factor receptor 2
HIF1A	hypoxia inducible factor 1 alpha
HMEC	human mammary epithelial cells
HPLC	high-performance lipid chromatography
HRAS	Harvey-RAS



i.p.	intraperitoneal
i.v.	intravenous
IC <sub>50</sub>	half-maximal inhibitory concentration in enzyme-based assay
IGF-1R	insulin-like growth factor 1
IHC	immunohistochemistry
IRE1 $\alpha$	inositol-requiring protein 1 alpha
KRAS	Kirsten-RAS
LC-MS	liquid chromatography-mass spectrometry
LDH	lactate dehydrogenase
LXR	liver X receptor
MAPK	mitogen-activated protein kinase
MAPKAP-K3	mitogen-activated protein kinase-activated protein kinase 3
MDR1	multidrug resistance protein 1, also known as P-glycoprotein
MgCl <sub>2</sub>	magnesium chloride
MM-GBSA	molecular mechanics generalised Born surface area
MMP9	matrix metalloproteinase 9
NRAS	neuroblastoma-RAS
NUV	normalised uptake value
OCT	organic cation transporters
p.o.	peroral
PAF	platelet-activating factor
P <sub>app</sub>	permeability coefficient
PBS	phosphate buffered saline
PBST	phosphate-buffered saline plus 0.1% Tris
PC-PLD	phosphatidylcholine specific phospholipase D
PCho	phosphocholine
PCYT1A	gene name for CCT (CTP:phosphocholine cytidyltransferase)
PDGF	platelet-derived growth factor
PE	phosphatidylethanolamine
PEMT	phosphatidylethanolamine N-methyltransferase
PEP	phosphoenolpyruvate
PERK	protein kinase RNA (PKR)-like ER kinase
PET	positron emission tomography

PI3K	phosphatidylinositol-4,5-bisphosphate 3-kinase
pIF	parent input function
PK/LDH	phosphoenolpyruvate kinase / lactate dehydrogenase
PKA	protein kinase A
PKC	protein kinase C
PLA2	phospholipase A2
PLD	phospholipase D
PPAR	peroxisome proliferator-activated receptors
PPB	plasma protein binding
ppm	parts per million
pRb	retinoblastoma protein
PtdCho	phosphatidylcholine
qRT-PCR	quantitative real-time PCR
Ral-GDS	Ral guanine nucleotide dissociation stimulator
RCP	radiochemical purity
RIPA	radioimmunoprecipitation assay
RNAi	RNA interference
ROI	region of interest
RSK1	ribosomal S6 kinase 1
s.c.	subcutaneous
SAM	S-adenosyl methionine
SCR	scramble non-targeting control
SD	standard deviation
SEM	standard error of the mean
SLC22	solute carrier 22 family of proteins
SP	standard precision mode
Sp1	specific protein 1
SRB	sulforhodamine B
SREBP	sterol regulatory element-binding protein
TAC	time versus radioactivity curves
TBST	Tris-buffered saline plus 0.1% Tris
TCA	tricarboxylic acid
TEER	trans epithelial electric resistance

TEF4	transcriptional enhancer factor 4
TPB	tetraphenylborate
UPR	unfolded protein response
Vb	blood volume
XP	extra precision mode



# Chapter 1

## Introduction

Although cancer is a conglomerate of immensely complex and heterogeneous diseases, the majority of neoplasms share the characteristic of a deregulated cellular metabolism [5]. Otto Warburg first observed almost a century ago, that cancer cells very distinctly utilise glucose [6–8]. Most normal cells metabolise glucose in the presence of oxygen to pyruvate by glycolysis and subsequently to carbon dioxide through oxidative phosphorylation in the mitochondria. Under anaerobic conditions, pyruvate emerging from glycolysis is redirected away from the mitochondria to be reduced to lactate. Cancer cells, however, tend to metabolise the majority of glucose to lactate, even under aerobic conditions [6–8]. This seemingly paradox phenomenon called Warburg effect evokes tumours to take up more glucose than normal tissues, which can be clinically exploited by positron emission tomography (PET) imaging and radiolabelled glucose ( $[^{18}\text{F}]$ fluorodeoxyglucose,  $[^{18}\text{F}]$ FDG) as a marker [9]. While oxidative phosphorylation is highly efficient to generate energy equivalents in form of ATP — 36 mol ATP can be gained from 1 mol of glucose — anaerobic glycolysis to lactate only yields in 2–4 mol of ATP from 1 mol of glucose. Importantly, however, resting and proliferating cells, have diverging demands to satisfy metabolic needs. Normal cells mainly require ATP to maintain cellular functions. In contrast, proliferating cells additionally need to accumulate large amounts of biomass for DNA, protein and lipid synthesis while maintaining their redox environment under cellular stress. It was recently proposed that anaerobic glycolysis better satisfies the sum of these needs [10].

With increasing understanding of tumour heterogeneity, it has become apparent that glycolysis is not the only deregulated metabolic trait and that other nutrients than glucose are essential for proliferation. Many cancer cells rely, for example, on sufficient supply of

glutamine. While normal cells only use this amino acid as a nitrogen source, highly proliferating cells shunt it into energy metabolism, where it is converted to  $\alpha$ -ketoglutarate to replenish the tricarboxylic acid (TCA) cycle [11]. In addition, lipid metabolism typically also undergoes rearrangements under malignant transformation [12]. This is not unexpected, as lipids are required for the synthesis of cell membranes and therefore in demand in highly proliferating tissues. Membrane lipids usually comprise of two hydrophobic fatty acid chains and a polar, hydrophilic head group, connected by glycerol. This amphiphilic character is required for the typical bilayer structure of membranes. The most abundant membrane lipid is phosphatidylcholine (PtdCho), which contains choline as the polar head group. Both fatty acid and choline metabolic pathways are deregulated in cancer, but choline biochemistry and its implications on energy homeostasis and proliferation are less well understood. This thesis focuses on the investigation of choline metabolism with the aim to identify therapeutic strategies.

## 1.1 Deregulated choline metabolism in cancer

Aberrant choline metabolic profiles have been described by proton magnetic resonance spectroscopy ( $^1\text{H}$  MRS) in most of human cancers, including brain, breast, bone colon, colorectal, endometrial, lung, oesophageal, ovarian, and prostate carcinomas [13–26]. Hyperactivated choline metabolism is characterised by elevated intracellular concentrations of phosphocholine (PCho) and total choline-containing metabolites [27]. The overexpression of choline kinase alpha (CHKA), has been identified to be mainly responsible for this phenotype [28]. Importantly, CHKA expression is of prognostic significance in clinical breast and lung cancer, where overexpression correlates with disease progression, poor prognosis and reduced survival [29, 30]. Additionally, CHKA has been linked drug resistance by activating multidrug resistance transporters and to invasiveness through an unknown mechanism, but potentially involving interleukin 6 and 8 [31, 32].

While it can be anticipated that precursors of membrane lipid synthesis, such as PCho, need to be elevated in cancer to satisfy the demand for lipid building blocks in highly proliferating tissues, choline handling has additional implications in oncogenic development and disease progression. A tight relationship between PCho and malignant transformation has been described in breast cancer [33]. Cell lines at different stages of malignancy — ranging from normal human mammary epithelial cells (HMEC) to spontaneously immor-

talised, chemically immortalised, oncogene-transformed HMECs and breast cancer-derived cells with low and high metastaticity — show with increasing malignant progression correlative elevated PCho accumulation [33].

The notion that these metabolic rearrangements are specifically related to cancer is further substantiated by the observation that the tumour microenvironment profoundly influences the cholinic phenotype. Acetic extracellular pH significantly reduces PCho accumulation [34], while hypoxia induces CHKA expression and PCho accumulation by direct interaction of hypoxia inducible factor 1 alpha (HIF1A) with CHKA's putative promoter region [35]. These results, however, are conflicting with other reports, which described opposite effects in hypoxic conditions and microarray data indicating an inverse regulation of HIF on CHKA expression [36–38].

Consequently, the active involvement of CHKA in cancer progression, its interaction with the tumour microenvironment and — as later described — the regulation by oncogenic signalling pathways make it a putative drug target.

## 1.2 Choline biochemistry

Apart from its involvement in oncogenic transformation, choline is an essential nutrient that is required for normal cellular physiology of all cells [39]. The adequate dietary intake of around 500 mg/day is usually met or exceeded by healthy adults [40]. Short term dietary choline deprivation, as for example during pregnancy, embryonic development, lactation and in liver cirrhosis patients, can be overcome through a salvage mechanism in the liver, where choline is synthesised through the second most abundant phospholipid phosphatidylethanolamine (PE) [41, 42]. Prolonged deficiency, however, leads to apoptosis, liver and muscle damage [43], as well as increases homocysteine levels [44], which contribute to the risk for cardiovascular conditions and Alzheimer's disease [45, 46]. The physiological choline concentration in the plasma ranges between 10–50  $\mu\text{M}$  [47]. Choline is an essential component of four types of biomolecules: it (i) forms the polar head of the membrane lipids PtdCho and sphingomyelin, (ii) is required for the biosynthesis of the neurotransmitter acetylcholine, (iii) is a component of the potent lipid mediators platelet-activating factor (PAF) and sphingosylphosphorylcholine, and (iv) can be oxidised to betaine, which serves as an osmolyte and methyl group donor in various reactions (Figure 1.1).

The predominant metabolite of choline is the membrane lipid PtdCho, which consti-

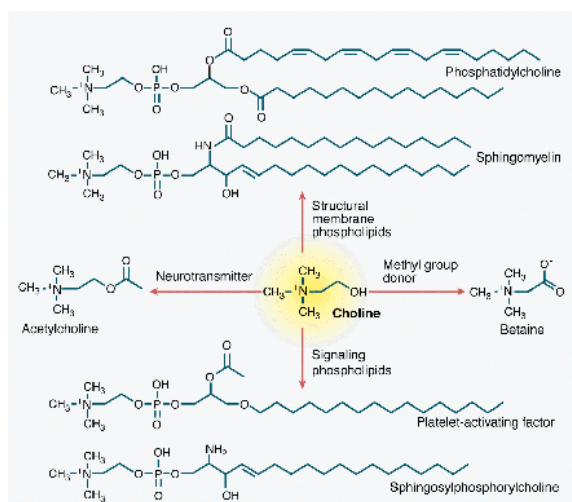


Figure 1.1: Fate of choline. Choline can be used for 4 classes of biomolecules: the membrane lipids phosphatidylcholine and sphingomyelin, the neurotransmitter acetylcholine, the osmolyte and methyl group donor betaine or for the lipid mediators platelet-activating factor and sphingosylphosphorylcholine. Figure from: Blusztajn, J. K. *Science*. 1998;281,794–795; REF. [39].

tutes half of the total membrane lipid content [48]. Besides acting as a natural barrier to the surrounding environment, the cell membrane functions as an important energy storage and serves as precursor of lipid second messengers [42]. PtdCho biosynthesis occurs through the Kennedy (or CDP-choline) or phosphatidylethanolamine *N*-methyltransferase (PEMT) pathways.

Perhaps the best-characterised choline metabolite is the neurotransmitter acetylcholine. Among other functions, acetylcholine transmits signals in the central and peripheral nervous system, where it is required at all pre- and postganglionic parasympathetic and all preganglionic sympathetic neurons. Acetylcholine is also required at the neuromuscular junction, where it translates neuronal impulses into muscle movement. Furthermore, acetylcholine is important for synaptic plasticity, learning and memory and loss of cholinergic neurons is one of the hallmarks of Alzheimer's disease [49, 50].

Choline is also a component of the lipid mediators PAF and sphingosylphosphorylcholine. PAF is a very potent proinflammatory phospholipid contributing to immune response, inflammation and the cancer microenvironment. PAF is usually produced from membrane glycerophosphocholines and signals through its G-protein coupled PAF receptor [51]. This results in platelet aggregation, adhesion of neutrophils to endothelial cells, proliferation of fibroblasts and endothelial cells, migration of granulocytes to sites of inflammation and production of angiogenic factors [52]. PAF-mediated signals activate mitogen-activated protein kinase (MAPK), phosphatidylinositol-4,5-bisphosphate 3-kinase (PI3K),



phospholipase A2 (PLA2) and protein kinase C (PKC) pathways [52] and inhibition of PAF reduces cell proliferation *in vitro* and metastasis in mouse xenografts [53]. Similar to PAF, sphingosylphosphorylcholine exerts a wide spectrum of biological actions, including promotion of cell growth, migration, adhesion and cytoskeleton rearrangement [54–56]. Finally, choline’s oxidation product betaine, is an important osmolyte and a vital carbon source for methylation processes [57]. Betaine replenishes methionine levels through the transfer of a methyl group to homocysteine. Subsequently synthesised S-adenosyl methionine (SAM) serves as a major dietary source for methyl groups [57]. Epigenetic regulation through methylation signatures, which are commonly found to be deregulated in cancers, rely on sufficient one-carbon sources, which potentially could explain elevated choline oxidase (the enzyme that governs the conversion from choline to betaine) expression in some cancers. The reaction to betaine cannot be reversed and therefore also poses a way for tissues to excrete choline [41].

### 1.3 Kennedy (CDP-choline) pathway for PtdCho synthesis

Upon choline uptake into cells, the synthesis of PtdCho from choline is catalysed by three enzymes, which together form the Kennedy or CDP-choline pathway (Figure 1.2). In the first step, choline kinase alpha (CHKA) or beta (CHKB) phosphorylate choline in the presence of ATP and  $Mg^{2+}$  to PCho. The activating nucleotide cytidine triphosphate (CTP) is then added through CTP:phosphocholine cytidyltransferase (CCT) to form CDP-choline. In the final step, CDP-choline:1,2-diacylglycerol cholinephosphotransferase (CPT) catalyses the formation of PtdCho from CDP-choline and diacylglycerol (DAG) [42]. These biochemical processes and their implications on carcinogenesis are discussed below in greater detail.

#### 1.3.1 Choline transport

Choline is a quaternary amine and due to its charge requires transport proteins to cross the lipophilic cell membrane. Three distinct systems are responsible for choline uptake (Table 1.1): organic cation transporters (OCT), choline transporter family (CHT) and choline transporter-like protein family (CTL).

OCTs or solute carrier 22 family of proteins (SLC22) are polyspecific for various organic cationic compounds. The sodium-independent transport is based on passive diffusion, is

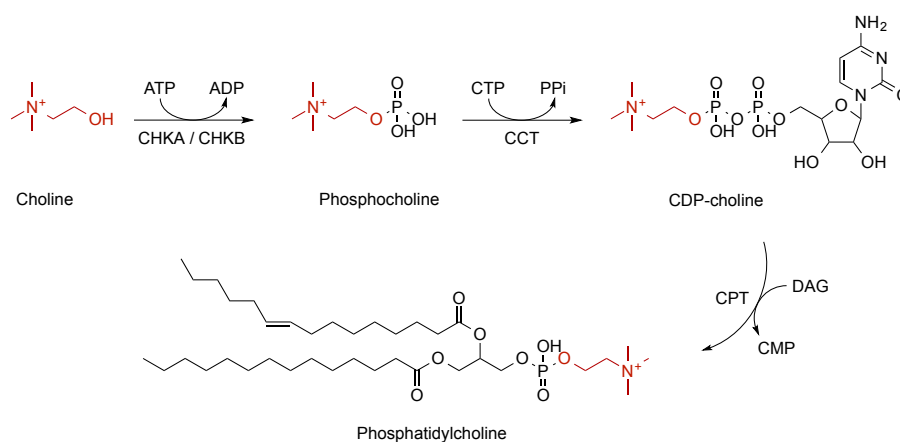


Figure 1.2: Kennedy pathway describing PtdCho synthesis. Choline kinase alpha or beta (CHKA, CHKB) catalyses the reaction from choline to phosphocholine. The activating nucleotide cytidine triphosphate (CTP) is added by CTP : phosphocholine cytidylyltransferase (CCT). The final reaction between diacylglycerol (DAG) and CDP-choline is catalysed by CDP-choline:1,2-diacylglycerol cholinephosphotransferase (CPT) and leads to the formation of the membrane lipid PtdCho. CTP, cytidine triphosphate; PPi, diphosphate, CMP, cytidine monophosphate.

therefore reversible, and the affinity for its substrates is usually low (OCT1–3  $K_M^1$  for choline ca. 300  $\mu\text{M}$  to 16 mM) [58]. They are mainly located in the liver and kidneys to provide organic cationic compounds, such as choline, carnitine, creatinine and guanidine for metabolic pathways in these organs [59].

CHTs are predominately located in brain regions rich in cholinergic neurons. They are responsible for the provision of choline for acetylcholine synthesis [59] and characterised by very high affinity for choline ( $K_M$  for choline 0.5–3  $\mu\text{M}$ ) [59].

In the context of tumour choline metabolism, the intermediate-affinity, choline-specific CTL family of transporters forms the mainstay of cross-membrane choline trafficking [25, 60]. CTLs are expressed in a variety of tissues, including brain, heart, small intestine, kidney, liver, lung, skeletal muscle, pancreas, spleen, ovary, and testis [59, 61]. They are characterised by a  $K_M$  of 20–70  $\mu\text{M}$  for choline and their main purpose is choline transport for PtdCho synthesis. The different classes of choline transporters are linked to their specific biochemical function and many organs rely on a combination of choline transporters to secure sufficient supply. For example, neurons derive choline through high-affinity transporters for acetylcholine synthesis and CTL-mediated transport for PtdCho production [59, 62, 63]. Additionally, the  $K_M$  for transfer of choline to acetylcholine and PCho are different in brain cells [64].

<sup>1</sup>Michaelis-Menten constant  $K_M$  is the substrate concentration at which the reaction velocity is at half-maximum.

Table 1.1: Tissue distribution of choline transporters. Data from: Michel *et al.* Exp Biol Med. 2006;231:490–504. REF. [59].

	Name	Chromosome	Organism	Tissue distribution
Choline-specific				
I. CHT1s	hCHT1b	2q12	Human	Brain, spinal cord
	mCHT1	17D	Mouse	Brain, spinal cord
	rCHT1b	9q11	Rat	Brain, spinal cord
	CHO-1	IV	C. elegans	Brain, synaptic vesicles
II. CTL1s	hCTL1b	9q31.2	Human	Multiple tissues
	mCTL1	4B2	Mouse	Muscle
	rCTL1	5q24	Rat	Brain, spinal cord, colon
	tCTL1		Torpedo	Central nervous system, myelin
Choline-nonspecific				
OCTs	hOCT1	6q26	Human	Liver
	hOCT2	6q26	Human	Kidney, brain
	mOCT1	17A1	Mouse	Intestine, liver, kidney
	mOCT2	17A1	Mouse	Kidney
	rOCT1b	1q11–q12	Rat	Liver, kidney, intestine
	rOCT2b	1q11	Rat	Kidney

### 1.3.2 Choline kinase alpha and beta

CHK<sup>2</sup> exists in at least three isoforms, CHKA1, CHKA2 and CHKB, of which the A, but not the B isoforms, have been implicated in cancer [65]. CHKA1 (50 kDa) and 2 (52 kDa) originate from the *CHKA* gene on chromosome 11, while the *CHKB* gene on chromosome 22 encodes for CHKB (43 kDa) [66–68]. The two genes have a sequence homology of ca. 60% [69]. CHK is a cytoplasmic protein, although presence in the nucleus has been reported in some studies [65, 70]. The significance nuclear localisation awaits to be understood, but potentially it translocates with other enzymes to contribute to endonuclear PtdCho synthesis and lipid signalling [65]. All isoforms are inactive in their monomeric form and homo- or heterodimerisation is required for full activity. Differences in dimer composition augment enzyme activity. In normal mouse tissues, 60% of the kinase activity can be attributed to CHKA/B dimers, while alpha and beta homodimers contribute in equal parts to the remaining enzymatic activity. Importantly, in a model of carcinogen-induced liver cancer in mice, the A/A homodimer becomes with ca. 75% the prevailing contributor to total CHK activity, with the A/B heterodimer (15%) and B/B homodimer (10%) only having subordinate roles [69]. CHKA1 and 2 are different splice variants, whereby the CHKA2 isoform has an insertion of 18 amino acids. X-ray crystallography revealed that that this sequence segment is adjacent to an  $\alpha$ -helix, which

<sup>2</sup>CHKA and CHKB refer to the respective isoforms, while CHK is used when both isoforms are implied or isoform selectivity is unknown.

is responsible for enzyme dimerisation. When inserted, the  $K_M$  for choline is reduced to 0.098 mM compared to 1.69 mM for CHKA1 [71]. These data suggest that this sequence facilitates dimerisation and thereby enhances enzymatic activity.

CHKA and CHKB have differential roles in embryonic development and tissue physiology. Heterozygote CHKA knockout mice are viable, fertile and without any obvious phenotype. Homozygote deletion of CHKA causes embryonic death within the first 7.5 days [72]. In heterozygote CHKA knockout mice CHK activity is significantly reduced in liver and testes, but remains unaffected in muscle. PtdCho membrane content remains stable and the ethanolamine pathway, a salvage pathway under choline deprivation (discussed below), does not seem to compensate for the loss of CHKA activity [72]. CHKB is implicated in muscle development, as mice with a truncated, dysfunctional CHKB protein exhibit hindlimb muscular dystrophy, forelimb bone deformity and megamitochondria [73, 74]. This can be partly reversed when these mice are supplemented with CDP-choline to circumvent impaired CHK activity [75]. As knockout of CHKA but not CHKB is lethal, it can be anticipated that CHKB cannot compensate for loss of CHKA.

In normal cells, the rate-limiting step of the Kennedy pathway is considered to be CCT [42, 76, 77], while in malignant cells with altered choline biochemistry, the regulatory role appears to be taken over by CHKA. Only a minor increase in PtdCho content is found in breast cancer cells compared to healthy controls and the increase of total choline-containing metabolites is predominantly due to elevated PCho synthesis [78]. In epithelial ovarian cancer cells, 3.5-fold increased CHKA mRNA expression is accompanied by a 50% reduction of CCT1 expression while the CCT2 expression is almost completely abolished compared to healthy control cells [25]. Furthermore, glioblastoma cells that are resistant to radiotherapy have ca. 7-fold higher PCho concentrations compared to corresponding radiosensitive cell lines, however, their CDP-choline levels are only 1.6-fold higher in radioresistant cells [28].

### 1.3.3 Cytidyltransferase and phosphocholine transferase

CTP:phosphocholine cytidyltransferase catalyses the reaction from PCho to CDP-choline. The two isoforms, CCT $\alpha$  and CCT $\beta$ , are encoded by *PCYT1A* and *PCYT1B*, respectively [42]. CCT exists in homodimers and their subcellular localisation regulates their activity. Decrease in PtdCho, increase in DAG or changes in CCT phosphorylation prompts it to become membrane-bound and active. Conversely, in its soluble, cytosolic form, it is inac-

tive [79]. On transcriptional level, CCT expression is regulated by the transcription factors specific protein 1 (Sp1), retinoblastoma protein (pRb), transcriptional enhancer factor 4 (TEF4), v-ets avian erythroblastosis virus E26 oncogene homolog 1 (Ets-1) and E2F, but not by transcription factors involved in *de novo* fatty acid or cholesterol biosynthesis, such as sterol regulatory element-binding protein (SREBP), liver X receptor (LXR) or peroxisome proliferator-activated receptors (PPAR), suggesting that its regulation is linked to cell cycle, growth and differentiation, but not lipid or energy metabolism [80]. CCT $\alpha$ <sup>-/-</sup> deletion in mice is embryonically lethal, whereas CCT $\beta$ <sup>-/-</sup> knockout mice are viable but with reduced fertility [81, 82]. CCT $\alpha$ , but not CCT $\beta$ , has a nuclear localisation signal, which is cleaved during caspase-mediated apoptosis, to impede lipid synthesis during cell death [83].

In the final step of the Kennedy pathway, CPT condenses CDP-choline with DAG to form PtdCho. This enzyme is sparsely characterised, at least in part because attempts to purify it failed due to its membrane-bound nature [84]. It is sufficiently expressed in most tissues, and therefore does not limit PtdCho synthesis. Its activity is mainly regulated by the supply of CDP-choline and DAG [85, 86].

### 1.3.4 Alternative ways to generate PtdCho

In parallel to the Kennedy pathway, PtdCho can be synthesised through the ethanolamine kinase pathway. With similarities to its choline counterpart, three enzymes, namely ethanolamine kinase 1 and 2, CTP:phosphoethanolamine cytidyltransferase and CDP-ethanolamine:1,2-diacylglycerol ethanolamine phosphotransferase, catalyse the generation of PE. PEMT is then responsible for the sequential methylation of the nitrogen to obtain PtdCho [84]. The methylation requires three molecules of S-adenosyl methionine, which in turn is converted to homocysteine [87]. PEMT is only expressed in liver and localises in the endoplasmic reticulum and mitochondria-associated membranes [88]. In normal physiology, the Kennedy pathway is predominantly responsible for PtdCho synthesis, while the ethanolamine kinase pathway contributes only at high demand or starvation [89, 90]. While choline can be synthesised through this pathway and subsequent cleavage by lipases, the capacity for *de novo* synthesis is limited and comes at the cost of generating homocysteine, a risk factor for heart disease, and therefore only occurs under conditions of extreme demand [42].

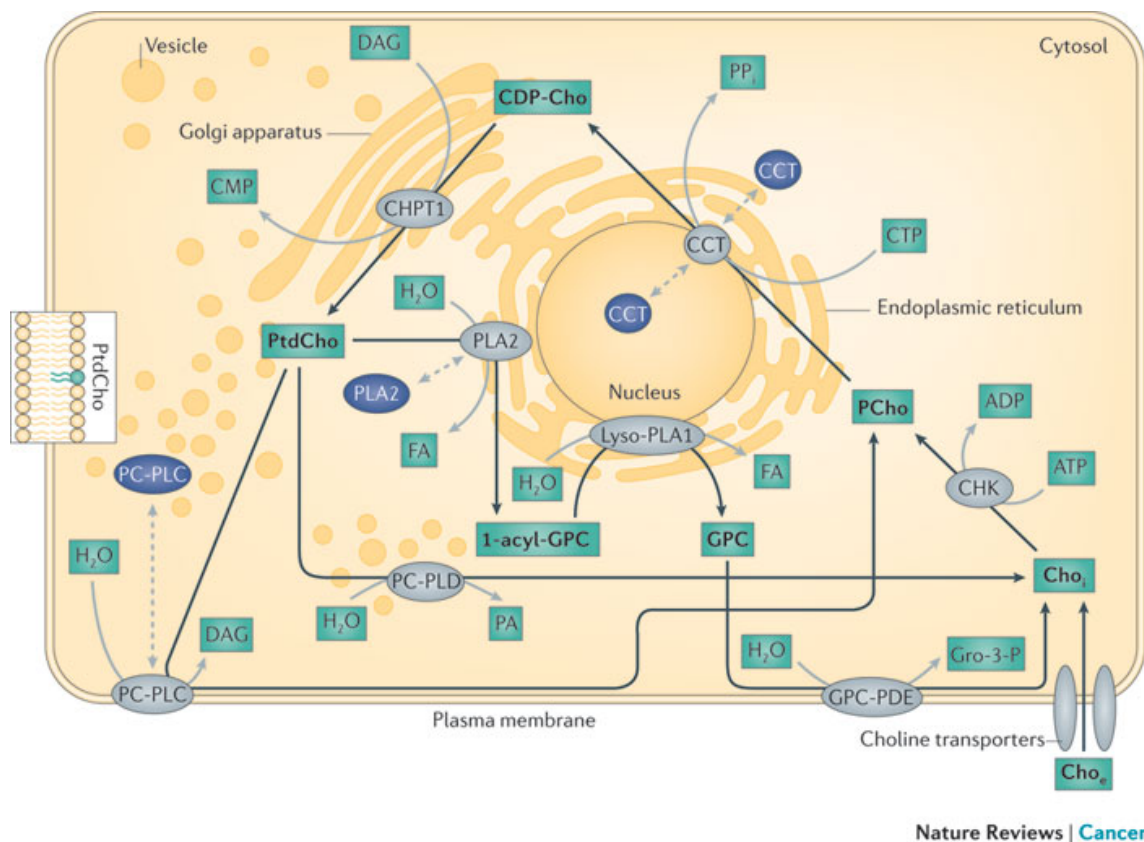


Figure 1.3: The major enzymes involved in choline phospholipid metabolism in the cell. Enzymes shown in grey indicate active choline cycle enzymes, which are shown in the organelle in which they are active. Enzymes shown in dark blue indicate the location of choline cycle enzymes that are deactivated by translocation to a different organelle. Black arrows represent the choline metabolism pathway, proteins in grey catalyse the reaction that is depicted by the corresponding black arrow and choline cycle metabolites are shown in bold. Dashed grey arrows show translocation to different subcellular locations, which can deactivate (dark blue) or activate (grey) the enzyme. CCT, CTP: phosphocholine cytidyltransferase; CDP-Cho, cytidine diphosphate-choline; CHK, choline kinase; Cho<sub>e</sub>, extracellular free choline; Cho<sub>i</sub>, intracellular free choline; CHPT1, diacylglycerol cholinephosphotransferase 1; CMP, cytidine monophosphate; CTP, cytidine triphosphate; FA, fatty acid; GPC, glycerophosphocholine; GPC-PDE, glycerophosphocholine phosphodiesterase; Gro-3-P, glycerol-3-phosphate; Lyso-PLA1, lyso-phospholipase A1; PCho, phosphocholine; PC-PLC, phosphatidylcholine-specific phospholipase C; PC-PLD, phosphatidylcholine-specific phospholipase D; PLA2, cytoplasmic phosphatidylcholine-specific phospholipase A2; PP<sub>i</sub>, diphosphate. Figure and legend from: Glunde *et al.* Nat Rev Cancer. 2011;11,835–848. REF. [28].

### 1.3.5 PtdCho catabolic pathways

#### 1.3.5.1 Phospholipase D

PtdCho-specific phospholipase D (PC-PLD) exists in two isoforms, PC-PLD1 and 2 [91]. It has been reported to localise at Golgi membranes, the cell membrane or in the cytosol and its subcellular distribution may depend on the cell type or physiological context [28]. PC-PLD catalyses the reaction that breaks down PtdCho into phosphatidic acid and free

choline (Figure 1.3) [91]. It represents the only mechanism that can directly generate free choline. Apart from having structural importance to the membrane, phosphatidic acid acts as a precursor for many lipids and signalling molecules that can recruit proteins to the cell membrane to activate them [27].

PC-PLD activity or protein expression is upregulated in melanoma, gastric, ovarian, breast, renal and colorectal cancers or cell lines [19, 28]. High PC-PLD activity correlates with invasiveness of breast cancer cell lines, which could be linked to upregulation of matrix metalloproteinase 9 (MMP9) [92].

### **1.3.5.2 Phospholipase C**

PtdCho-specific phospholipase C catalyses the breakdown from PtdCho to DAG and PCho (Figure 1.3) [93]. Little is known about PC-PLC, as it exists in no less than 13 isoforms, which have not been cloned to date [28]. DAG is not only a precursor for many lipids, but together with phosphatidic acid one of the most important lipid second messenger signalling molecules, that can be derived from PtdCho. Its activates PKC, which regulates signalling pathways related to proliferation, apoptosis, cell survival and migration [94].

### **1.3.5.3 Catabolic pathways leading to glycerophosphocholine**

Additionally, PtdCho can be cleaved to form glycerophosphocholine (GPC) and free choline via specific phospholipase A2, lysophospholipase and GPC phosphodiesterase EDI3 (Figure 1.3) [42, 95]. GPC alterations have been well documented in cancer due to its resonance on  $^1\text{H}$  MRS and typically inversely correlate with PCho content. This lead to the description of a glycerophosphocholine to phosphocholine switch that is associated with a malignant phenotype [33]. The exact role of GPC or the enzymes in these pathways are poorly understood, in part because of the plethora of isoforms for each enzyme [28].

## **1.4 Molecular imaging of choline metabolism**

Hyperactivated CHKA and intracellular enrichment of PCho in cancer can consequently be exploited for diagnosis, patient stratification and treatment surveillance. Due to their non-invasive character, MRS and PET imaging are predominantly used in preclinical and clinical settings to investigate choline metabolism.

### 1.4.1 MRS

MRS is based on the principle that when nuclear magnetic resonance active atomic nuclei, such as  $^1\text{H}$  or  $^{31}\text{P}$ , are placed in an electromagnetic field, they absorb energy and a resonating radiofrequency signal can be detected [27]. This signal depends on the chemical environment of nuclei and therefore the number of chemical bonds, neighbouring nuclei, and overall chemical structure. These steric effects can alter the frequency, which is referred to as chemical shift [27]. Choline-containing metabolites resonate at a chemical shift of 3.2 and 3.3 parts per million (ppm) and the peak arises from the nine  $^1\text{H}$  of the quaternary ammonium moiety (Figure 1.4) [27]. In cell extracts, free choline, PCho and GPC can be distinguished, as the different chemical structures slightly alter the chemical shifts. *In vivo* imaging of lesions does not permit separation of the individual choline peaks and gives rise to a single peak representing total choline-containing metabolites [27].

In  $^{31}\text{P}$  MRS the signal arises from the phosphate groups of extracted metabolites, and therefore — with respect to choline-containing metabolites — PCho and GPC can be detected. Due to its low sensitivity,  $^{31}\text{P}$  MRS has limited application *in vivo* [28].

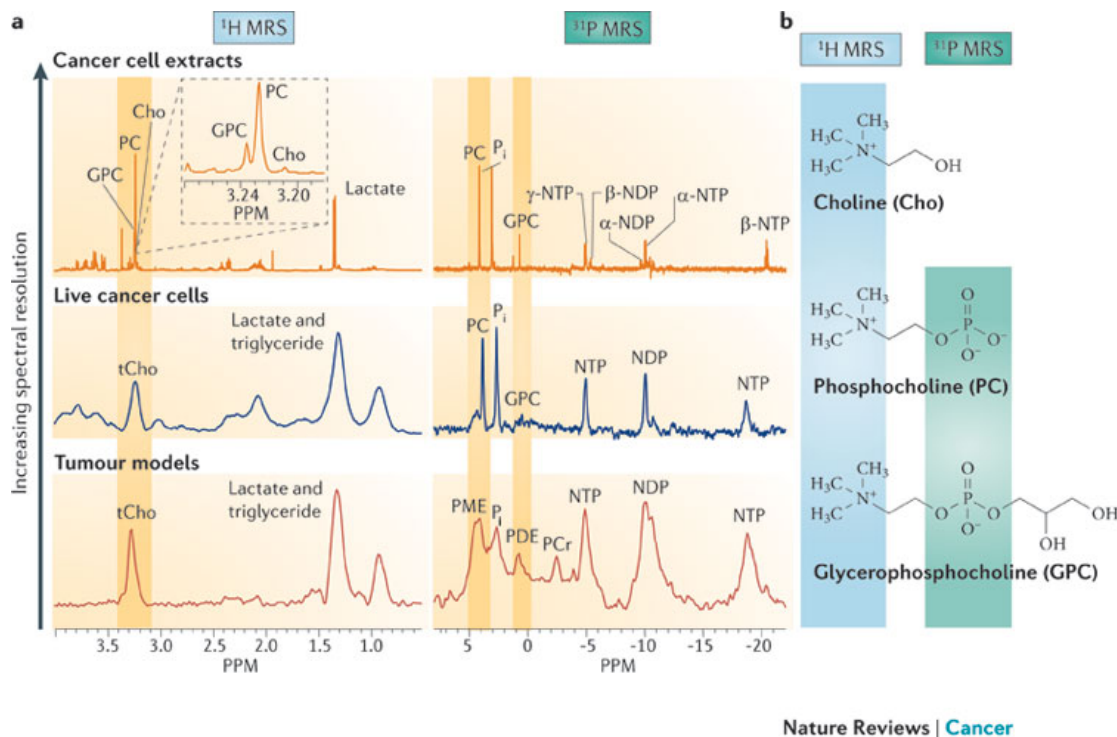


Figure 1.4: Metabolite analysis by  $^1\text{H}$  and  $^{31}\text{P}$  MRS. A, Typical MRS spectra obtained from cancer cell extracts, live cells or *in vivo* tumour models. B, Structures of the different choline containing metabolites. Highlighted in blue are the nine equivalent protons resonating in  $^1\text{H}$  MRS and in green the  $^{31}\text{P}$  containing phosphate giving rise to the  $^{31}\text{P}$  MRS signal. Figure from: Glunde *et al.* Nat Rev Cancer. 2011;11,835–848. REF. [28].



As indicated above, deregulated choline biochemistry denoted by a marked increase in PCho or total choline-containing metabolites has been detected by  $^1\text{H}$  MRS in a vast array of human cancers. In addition, this technique can be — at least in a preclinical setting — used to monitor drug response. PCho content decreases upon inhibition of PI3K by PI-103, HER2 by trastuzumab, protein kinase A (PKA) by H-89, fatty acid synthetase (FASN) by orlistat, and CHKA by MN58B and hemicholinium-3 (HC-3) [96–99]. Interestingly, pan HDAC inhibition by LAQ824 and vorinostat increases CHKA expression and PCho peaks through an unknown mechanism [100, 101].

### 1.4.2 PET imaging

PET imaging traces the behaviour of radiolabelled metabolites or ligands in the body. A typical PET experiment comprises of synthesis and radiolabelling of the tracer, intravenous administration, monitoring of tissue distribution by a PET scanner and interpretation of the reconstructed images.

Commonly used tracers in oncology visualise glucose ( $^{18}\text{F}$ FDG), thymidine ( $^{18}\text{F}$ -3'-fluoro-3'-deoxy-L-thymidine;  $^{18}\text{F}$ FLT) and choline metabolism. The isotopes have very short half-lives and the most commonly used include  $^{11}\text{C}$  (20.4 minutes),  $^{18}\text{F}$  (109.8 minutes),  $^{64}\text{Cu}$  (12.7 hours),  $^{68}\text{Ga}$  (67.7 minutes) and  $^{89}\text{Zr}$  (78.4 hours). Because of the rapid decay, the radioactivity usually needs to be synthesised by a cyclotron and therefore only has a limited radius where it can be delivered to. The nuclei are positrons, which are positively charged electrons. The signal arises through annihilation of the positron with an electron in the tissues. This process emits two gamma rays in form of 511 keV photons travelling in  $180^\circ$  direction to each other. A detector ring measures the exact time and location of the impact, allowing reconstruction of a three dimensional image (Figure 1.5).

PET imaging of choline metabolism has been successfully used for patient stratification and treatment surveillance in breast, prostate, brain, oesophageal and lung cancer [70, 102–109].

Several choline metabolic PET tracers are clinically used or currently investigated. All of them mimic choline and are taken up into cells by choline transporters. Phosphorylation by CHKA traps the tracer in the cell and accumulation in regions with hyperactivated CHKA are characterised by high tissue tracer uptake.

$^{11}\text{C}$ choline is associated with the shortest half-life of choline tracers and is rapidly metabolised to PCho and betaine [110]. It is particularly useful in prostate cancer, as

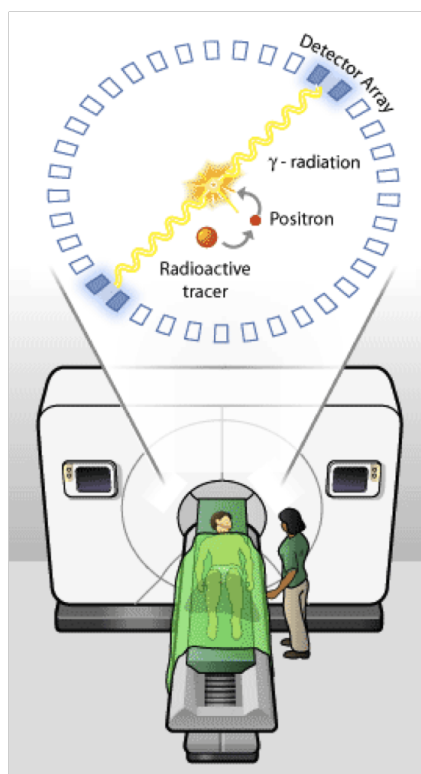


Figure 1.5: Principle of PET imaging. A positron originating from a radioactive tracer annihilates with an electron, resulting in two gamma-rays that can be detected. Signals are then converted into a three-dimensional picture.

its renal excretion is almost negligible. It gives therefore superior images in comparison with  $[^{18}\text{F}]\text{FDG}$ , for which the accumulation of radioactivity in the bladder obstructs vision of the pelvic region. The conversion to betaine over time (75% parent tracer is converted to betaine in liver and kidney within the first 15 minutes [110]) bears the disadvantage that the measured radioactivity is not entirely related to the Kennedy pathway (specific signal), but its oxidation product (non-specific signal). Furthermore, betaine could be excreted from cells into the blood stream, which would skew results. Several attempts were taken to increase the half-life of choline tracers by use of fluorinated labels.  $[^{18}\text{F}]\text{fluoromethylcholine}$  and  $[^{18}\text{F}]\text{fluoroethylcholine}$  are specific for CHKA, but are metabolically unstable, which makes longer scans difficult to interpret [111]. This led to the development of a deuterated tracer,  $[^{18}\text{F}]\text{fluoromethyl-}[1,2\text{-}^2\text{H}_4]\text{-choline}$  ( $[^{18}\text{F}]\text{D4-FCH}$ ) [112].  $[^{18}\text{F}]\text{D4-FCH}$  is characterised by superior metabolic stability (only 10% of parent tracer are converted to betaine in liver and 30% in kidneys within the first 15 minutes [110]), which increases the specific signal related to PCho, while retaining equal affinity to CHKA [110].  $[^{18}\text{F}]\text{D4-FCH}$  is currently under clinical evaluation [113].

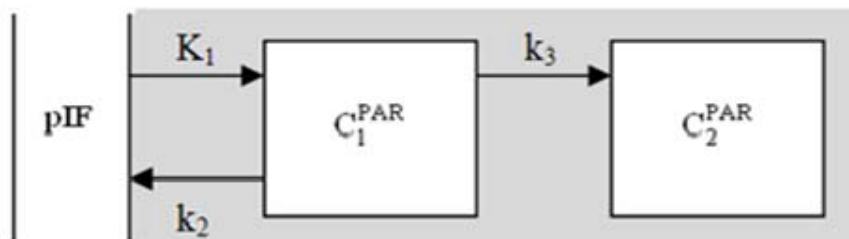


Figure 1.6: Scheme of the two-compartment, single input 3k model used to model choline PET data. The parent input function (pIF) represents the tracer concentration in plasma. The constants  $K_1$  and  $k_2$  describe the rate at which tracer is transferred from plasma to tissue and back. The irreversible intracellular trapping is described by  $k_3$ . Figure from: Witney *et al.* Clin Cancer Res. 2012;18,1063–1072. REF. [110]

Choline PET imaging provides distinctly different information to MRS. While the latter represents a “snap shot” of intracellular metabolite concentrations, the use of PET tracers monitors the enzymatic activity over time. Therefore it derives kinetic information, which can be modelled to further understand biological processes.

Kinetic modelling relates the signals in a tissue, e.g. tumour, to plasma radioactivity. Therefore it considers the haemodynamic parameters in addition to tissue distribution. The obtained signal in a region of interest from a choline PET scan is the sum of membrane transport and phosphorylation by CHKA. For an accurate model, the tracer metabolism over the time of imaging needs to be taken into consideration to distinguish the specific signal from metabolic by-products.

Choline PET has typically been described by two-tissue, single input irreversible compartment (3k) pharmacokinetic model [110] (Figure 1.6). The parent input function (pIF; parent relates to the administered, non-metabolised tracer) represents the radioactivity measured in plasma. In clinical scans, this parameter is derived by obtaining blood samples over a time course and measurement of the containing radioactivity. As such an approach is not feasible in small-animal studies due to the limited blood volume, pIF is estimated by drawing three dimensional regions of interest (ROI) over the heart and measuring its radioactivity over time [114].  $K_1$  (mL/cm<sup>3</sup>/min) and  $k_2$  (1/min) describe the rate of tracer transfer from plasma to tissue and back. The choline kinase reaction is represented by  $k_3$ , which denotes the irreversible trapping of the tracer. Although the CHKA reaction is in principle reversible, it can be assumed that at least in tumour no significant amounts of PCho are dephosphorylated.

## 1.5 Regulation of choline biochemistry in cancer

CHK activity is stimulated by hormones such as oestrogens and insulin, growth factors like epidermal growth factor (EGF) and platelet-derived growth factor (PDGF), as well as oncogenes including Ras, Raf and Mos [69, 115–121]. Although many mitogenic and growth promoting factors result in CHK activation, the exact mechanisms remain unclear. In particular, interaction with other proteins or kinases and possible phosphorylation sites on human CHK isoforms remain to be further characterised.

Incubation of serum-starved HeLa cells with either EGF or insulin enhances uptake of radiolabelled choline and its incorporation in phospholipids. Cells need to be stimulated for at least 24 hours to obtain increased PCho production, whereas no changes occur in the first 4 hours of incubation [119]. This delay in response suggests that no direct interaction between the corresponding growth factor receptors and CHK exist and that serum starved cells require synthesis of downstream proteins to activate CHK. CCT activity was not altered in these experiments, which further supports notion that CHK is the predominant rate-limiting step of the Kennedy pathway in cancer.

More recently, a mechanistic link between EGFR and CHK through c-Src was proposed [122]. EGFR forms a complex with the cytosolic kinase c-Src, which recruits CHKA to the cell membrane. This interaction is dependent on c-Src activity, which was shown to phosphorylate and activate CHKA at Tyr197 and Tyr333. Loss of the c-Src kinase domain or mutations at the CHKA phosphorylation sites decreases CHKA recruitment and activity. While c-Src is required for CHKA phosphorylation, EGFR co-expression is not necessary, but potentiates the effect [122]. It is likely that similar receptor tyrosine kinases — especially of the v-Erb-B2 Avian Erythroblastic Leukemia Viral Oncogene Homolog (ErbB) family, such as HER2 — could also interact with CHKA through c-Src. These results reveal for the first time an activating phosphorylation in human CHKA and demonstrate a link to growth factor signalling. However, confirmation of these results *in vivo* and the effects on cell proliferation when disrupting this EGFR-c-Src-CHKA complex need to be further studied.

Activating phosphorylation sites of choline kinase were more intensively characterised in yeast (CKI1; only one isoform exists in this organism). CKI1 is phosphorylated by PKA and PKC. PKA activates CKI1 in a dose- and time-dependent manner through phosphorylation at Ser30 and Ser85 [123–125]. PKC predominantly activates CKI1 through

phosphorylation at Ser25, although several other putative target sites have been identified [126]. CKI1 stimulation is greater through PKA than PKC [123, 126]. The role of PKA and PKC-mediated CHKA regulation in humans is less well investigated. While pharmacological inhibition of PKA with H-89 effectively inhibits CHK activity, possible phosphorylation sites remain to be discovered [127].

At transcriptional level, CHK is regulated by the transcription factor activator protein 1 (AP-1) and potentially HIF1A and c-Myc. Exposure of cells to UV irradiation or carcinogens induces AP-1 mediated transcription through increased binding of c-Jun, which results in increased PCho concentrations and CHK expression [128, 129]. As indicated above, ambiguous results on CHK regulation were reported under hypoxic conditions. Myc also has a potential role in CHK regulation, as c-Myc expressing fibroblasts have 3-fold higher PCho levels than the corresponding knockout cell line [130].

High PCho levels reflecting augmented CHK activity are also associated with expression of the family of Ras oncogenes [131]. These small GTPases are encoded by three *RAS* genes, Harvey-*RAS* (*HRAS*), Kirsten-*RAS* (*KRAS*), and neuroblastoma-*RAS* (*NRAS*), which are frequently mutated in human cancers. Transformation of NIH3T3 cells with either of the *RAS* genes results in increased CHK activity makes cells 2–3 times more sensitive to CHK inhibitors than untransformed cells [131]. The exact mechanism of Ras-induced CHKA activation remains unclear. Ras does not directly interact with CHKA and the regulation is independent of PLD activation [120]. Ramirez de Molina *et al.* proposed that Ral guanine nucleotide dissociation stimulator (Ral-GDS) in conjunction with PI3K plays a pivotal role in CHKA activation in the setting of Ras mutations. Cells overexpressing wild-type Ras show vast CHK activation, which is reduced when transfected with mutant Ras isoforms that only interact with either Ral-GDS or PI3K. When a mutant Ras isoform, engineered to simultaneously and selectively interact with these two downstream targets only, is introduced, CHK activity is again comparable to Ras overexpressing cells [120]. Although a Ras/Ral-GDS/PI3K interaction seems apparent, these data do not rule out other Ras downstream targets, which could equally be responsible for CHK activation. Furthermore, a mechanistic link is missing, in particular as it was shown in a different context that PI3K and CHK do not physically interact [132]. CHK regulation has also been associated with Rho kinase signalling by activation of RhoA and ROCK, but similar constraints in the study design apply [133].

Several downstream modulators of CHK have been proposed, which are known to pro-

mote cell survival. These include DAG, phosphatidic acid, Akt, MAPK, cell cycle regulating proteins and PCho. Several reports suggest that choline-related effects are mediated through the pool of membrane lipids like PtdCho, which are cleaved by phospholipase C and D to form the mitogenic metabolites DAG or PA [134–136]. As previously mentioned, PtdCho content in cancer cells is often not vastly altered and CHK as opposed to CCT seems to regulate the Kennedy pathway in cancer. This suggests, that lipid signalling might only in part explain the growth promoting signalling of CHK. Recently, an RNAi screen against the human kinome in triple negative breast cancer cell lines MDA-MD-468 identified CHKA as a key regulator for Akt phosphorylation [132]. CHKA was among the strongest hits in the screen and its knockdown resulted in more than 50% reduction of Akt phosphorylation [132]. Reduced Akt phosphorylation occurs downstream of PI3K and silencing CHKA also results decreased Erk1/2 phosphorylation [132, 136]. Overexpression of human CHKA leads to differential expression of proteins important for cell cycle progression, in particular for the G1-S phase transition, while inhibiting apoptosis. This effect can be reversed with CHK inhibitors [137].

More defined studies of CHK up- and downstream targets will be vital to thoroughly understand its regulation in cancer. Most of the publications cited above describe the functional effects upon CHK overexpression or inhibition, and — apart from c-Src — could not identify interaction partners of CHK, which could explain how CHK deregulation feeds into oncogenic signalling pathways.

## **1.6 Inhibition of CHKA as a treatment strategy in cancer**

Due to its involvement in oncogenic transformation, upregulation in a variety of cancers and interaction with key signal transduction pathways, CHKA has emerged as a potential target for cancer therapeutics. Several RNA interference (RNAi) studies have supported this and led to the discovery of small molecule inhibitors.

### **1.6.1 CHKA RNAi impedes proliferation**

Transcriptional silencing of CHKA depletes the intracellular PCho pool [136, 138], which translates into reduced proliferation of MDA-MB-231, MDA-MB-468 and HeLa cells [136, 139] and induction of apoptosis [140]. Furthermore, it promotes differentiation, prevents anchorage-independent growth in HeLa cells and abolishes their ability to form xenografts

in athymic mice [136, 139]. This is associated with a reduction of Akt and Erk phosphorylation and differential expression of genes involved in proliferation, cell cycle regulation and DNA repair [136, 141]. These effects are more pronounced in cancer cells than normal cells [141], giving hope that CHK inhibitors would potentially be selectively cytotoxic to tumours, while sparing other tissues. CHKA inhibition sensitises cells to chemotherapy, as treatment with 5-fluorouracil (5-FU) potentiates the effect of siRNA against CHKA in MDA-MB-231 cells [141].

Krishnamachary and colleagues have established a gene therapy mouse model targeting CHK [142]. Athymic mice bearing MDA-MB-231 xenografts were intravenously (i.v.) injected short-hairpin RNA delivered through a lentiviral vector. CHK mRNA levels were reduced by 35%, which diminished CHK activity and tumour volume. A gene therapy approach targeting solid tumours would be challenging to translate into humans, because of ethical and technical considerations, but this experiment substantiates the evidence for CHK to be a potential drug target.

### 1.6.2 Pharmacological inhibitors of CHK

Several small molecule CHK inhibitors have been developed and typically comprise of two cationic moieties in form of quaternary pyridinium salts connected by a lipophilic linker. Table 1.2 summarises CHK inhibitors published to date.

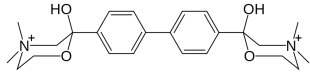
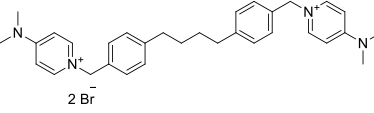
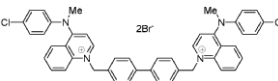
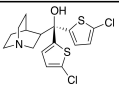
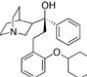
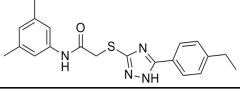
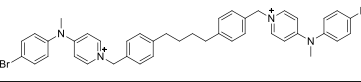
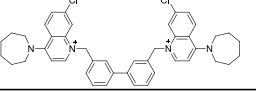
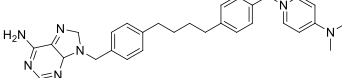
HC-3 is amongst the first discovered small-molecule inhibitors of CHK and targets both CHT transporters and CHKA [143, 151]. Different reports exist regarding its potency. It has been shown to have an  $IC_{50}^3$  against purified human CHKA of 0.95  $\mu\text{M}$  [143], an  $EC_{50}^3 > 500 \mu\text{M}$  in extracts containing yeast CKI [144], and a  $GI_{50}^3$  of  $> 500 \mu\text{M}$  against SKBR-3 and NIH3T3 cells [143, 145]. The large discrepancy between the published data is unclear, but could be due to incomplete description of the methodology and the caveat of different assays used. More importantly, interference with high-affinity choline transporters prevents uptake of choline for acetylcholine synthesis and causes neurotoxicity and apnoea [63]. This led to the development of novel CHK inhibitors with increased antiproliferative activity, but that do not interact with CHTs and therefore possess reduced neurological toxicity.

Through systematic screening, MN58B was identified (Table 2; REF. [144]). MN58B

---

<sup>3</sup> $IC_{50}$  refers to the half-maximal inhibitory concentration in an enzyme-based assay,  $EC_{50}$  to the half-maximal inhibitory concentration in biological assays, whereas  $GI_{50}$  describes the half-maximal growth inhibitory concentration in cells.

Table 1.2: Structures of choline kinase inhibitors and their pharmacological characteristics as published in the literature. Data from REFS [132, 143–150].

Compound	Inventor	Structure	Binding site	IC <sub>50</sub> (μM)	GI <sub>50</sub> (μM) 72h	
Hemicholinium-3			Choline, additionally inhibits CHT transporters	0.95	SKBR-3: > 500 NIH3T3: 600	
MN58B	Juan Carlos Lacal, University of Madrid		Expected to be choline competitive	22	MCF7: 0.6 HT29: 1.4 HeLa: 1.2 A431: 2.1 U937: 0.5 K562: 0.7	
TCD-828	TCD Pharma	No properties disclosed, but CHK inhibition demonstrated in Mol Cancer 2009;8:131				
TCD-717	TCD Pharma		Expected to be choline competitive	Not disclosed	Not disclosed	
V-11-023907	Vertex		ATP	0.47	Not disclosed	
V-11-0711	Vertex		ATP	0.02	HeLa: 26.5 HT29: 15 H23: 50 HCT116: 20	
CK37 (distributed by Merck)	Jason Chesney, University of Louisville		Choline		5-10 μM in various cell lines after 48h treatment	
Compound 10 ChemMedChem. 2002;7(4):663-9	University of Granada		Mixed; predominately choline	0.09	Only 2 conc. tested: 1 μM: 80% survival 10 μM: 15% survival in SKBR-3	
Compound 14 ChemMedChem. 2002;7(4):663-9	University of Granada		Mixed; predominately choline	0.08	Only 2 conc. tested: 1 μM: 80% survival 10 μM: 20% survival in SKBR-3	
Compound 14 MedChem 2012;50:154-62	University of Granada		Mixed; predominately choline	Only 2 conc. tested: 10 μM: 67% 50 μM: 90% CHKA inhibition	Only 2 conc. tested: 10 μM: 90% survival 50 μM: 55% survival in HepG2	

has an IC<sub>50</sub> of 4.2 μM and a GI<sub>50</sub> of 0.5–2.1 μM after 72-hour treatment in different cell lines [146]. The lower GI<sub>50</sub> than IC<sub>50</sub> is indicative of off-target effects. MN58B inhibits tumour growth by 70% in HT-29 and A431 mouse xenografts [146]. PCho conversion is only inhibited by 60% at 20 μM MN58b in MDA-MB-468 and 6 μM in MDA-MB-231 cells [96, 132]. Therefore, it is not able to completely inhibit the CHK reaction at pharmacologically relevant doses. Pharmacokinetic or target selectivity data have not been reported for this compound. TCD-717, a further development of MN58B, is currently under Phase I clinical investigation (clinical trials number NCT01215864) in solid tumours, but preclinical data are undisclosed [152].

MN58B effects cell death by induction of cytotoxic ceramides and endoplasmic reticulum (ER) stress. Ceramides are a class of bioactive lipids, that stimulate growth inhibition, apoptosis, differentiation and senescence [153]. Jurkat cells are upon drug treatment in-



sensitive to changes in pRb phosphorylation. pRb is governed by an inhibiting phosphorylation, and therefore is inactive when phosphorylated, but acts as a tumour suppressor in its hypophosphorylated state. Lack of phospho-pRb dephosphorylation causes a metabolic crisis and the release of cermides and subsequent induction of apoptosis [154]. Conversely, in normal primary lymphocytes phospho-pRb is dephosphorylated by MN58B treatment, which transiently induced G0/1 arrest. Once the drug is removed, these cells proliferate again.

Additionally, MN58B enhances ER stress response. The ER is an organelle that ensures correctness of protein folding and maturation as well as vesicular transport. Imbalance in protein synthesis and degradation, calcium overload or PtdCho depletion cause ER stress, a mechanism to resolve these perturbations [155, 156]. Transcription factors are released, which activate gene expression of diverse sets of genes that counteract this stress. If unsuccessful, cells enter the apoptotic pathway [156]. Several approved drugs use ER stress-induced apoptosis as their main mechanism of action, including vorinostat, sorafenib and bortezomib [157]. MN58B and TCD-717 induce ER stress response by increasing the expression of inositol-requiring protein 1 (IRE1 $\alpha$ ) and glucose-regulated protein 78 (GRP78), a chaperone to counteract missfolded proteins. Additionally, the transcription factors CHOP and C/EBP $\beta$  are activated, which cause a pronounced apoptotic response [157]. Importantly, these effects were exclusive to cancer cells and not observed in normal counterparts [157].

Structurally distinct from the pyridinium analogues is CK37 [149]. It was identified by an *in silico* screen of more than 2.6 million compounds. Despite being uncharged, it is competitive with choline, but only weakly inhibits recombinant CHKA: 25  $\mu$ M decrease PCho formation by 60%, which translates into a modest GI<sub>50</sub> of 5-10  $\mu$ M in different cell lines. At high concentrations, it is capable of decreasing Akt and Erk phosphorylation [149].

The only ATP competitive CHKA inhibitors developed to date are V-11-023907 and V-11-0711, of which only the latter has been tested in cell systems [147]. It has the highest reported inhibitory activity against CHKA — with the caveat that different and not comparable assays were used across various studies. Interestingly and in contrast to CHKA siRNA, it failed to induce apoptosis and cell death. Cell proliferation, as measured by percentage confluency over time, was delayed but reversible when the compound was withdrawn from the medium [148]. It cannot be excluded that cross-reactivity with other

targets prevents antiproliferative activity, but this divergence from data of choline competitive inhibitors and CHKA siRNA suggests that either inhibition of the choline pocket is required or that CHKA possesses scaffolding properties, which are independent of its catalytic activity [148].

## 1.7 Aims of thesis

Given the extensively characterised deregulated choline biochemistry in cancer and favourable preliminary results from genetic and pharmacologic interventions, the main aim of this project is to develop novel choline kinase inhibitors to elucidate choline biochemistry in cancer. The following milestones were set:

1. Development of novel, synthetically accessible scaffolds and detailed characterisation of their mode of inhibition.
2. Comprehensive *in vitro* and *in vivo* pharmacological evaluation, including data on selectivity, antiproliferative activity, antitumour activity, pharmacokinetics, and pharmacodynamics.
3. Elucidation of the mechanisms leading to cell death subsequent to CHKA inhibition.
4. Application of [ $^{18}\text{F}$ ]D4-FCH PET imaging to assess target inhibition *in vivo*.
5. Development of imaging tools that could facilitate the selection of patients that might benefit from CHKA inhibitors.

## Chapter 2

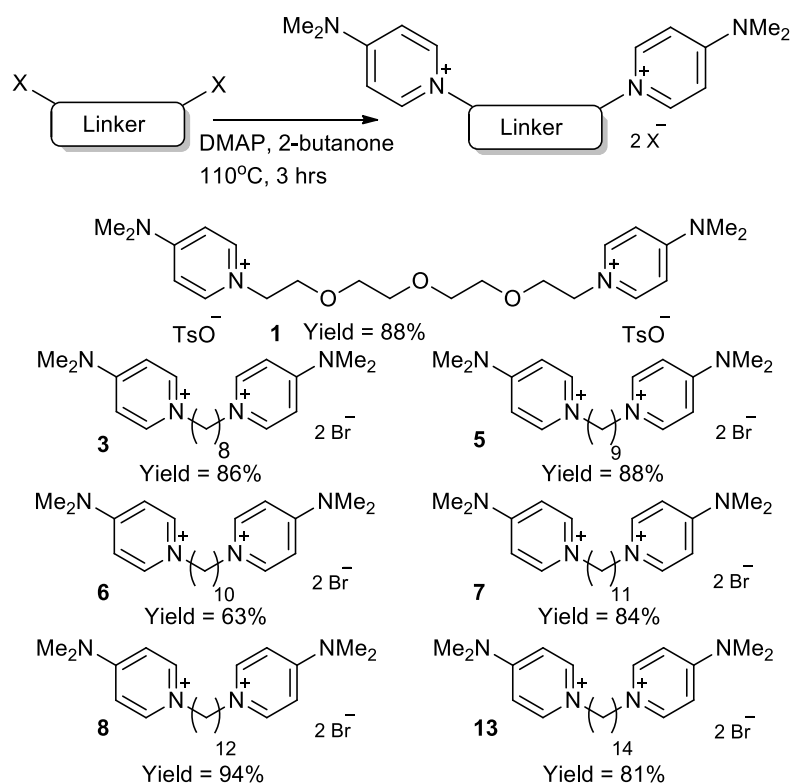
# Materials and Methods

### 2.1 Synthetic procedures

#### 2.1.1 Synthesis of choline kinase inhibitors

Choline kinase inhibitors were synthesised by Dr. Laurence Carroll and Dr. Andrew Kalusa, Imperial College London, according to procedures described in [1]. In brief, for synthesis of the symmetrical compounds (Scheme 2.1), each linker was dissolved in 2-butanone with DMAP and subsequently heated to 110°C for three hours. Precipitation began to occur within 10 minutes of the reaction starting, due to the insolubility of the desired doubly-charged *bis*-DMAP products in 2-butanone, allowing for a straight forward purification by filtration. Yields were good in each example (ca. 80% in all but one case) and the reactions could be easily carried out routinely on a large scale.

For synthesis of the ATP-mimicking compounds (Scheme 2.2), initially, nonsymmetric half-linker compounds **14–16** (where **14** = C12 linker, **15** = C8 linker, **16** = PEG4 linker) were synthesised using a modified procedure based upon our route for the symmetrical compounds. When a 1:1 ratio of DMAP to linker was used, in 2-butanone at 110°C for three hours, yields of the desired compound containing only one DMAP end group were ca. 70%. However, under these reaction conditions, up to 15% of the analogous symmetrical compound was also formed, and due to the similar nature of these compounds, separation proved difficult. A revised chemical procedure was developed, using only half an equivalent of DMAP (four times less than the initial procedure for the symmetrical synthesis), which gave lower yields of the desired compounds (ca. 50%), but importantly, afforded none of the unwanted symmetrical analogue. With compounds **14–16** in hand, subsequent

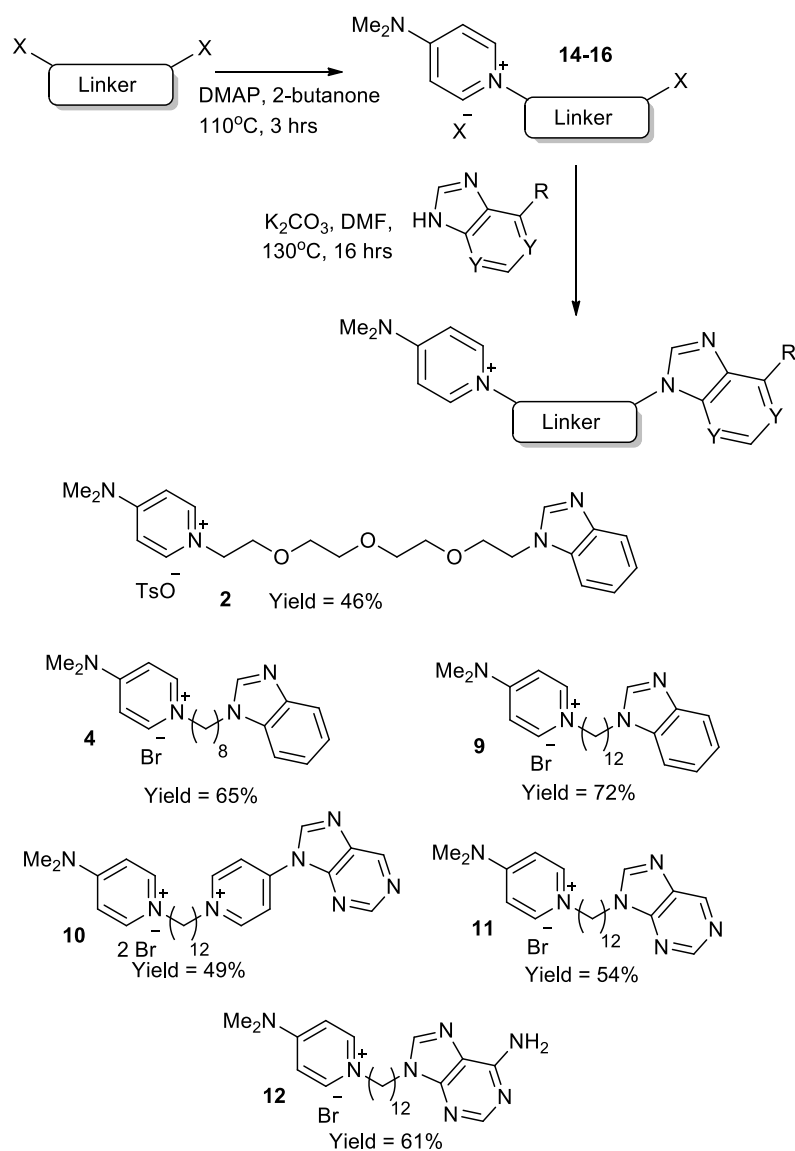
Scheme 2.1: Synthesis of symmetrical compounds **1**, **3**, **5–8** and **13**

coupling of a number of ATP-mimicking groups was attempted. Benzimidazole was used as an initial test compound, due to its symmetry preventing any possibly regioisomers, to ascertain conditions required for coupling. After optimisation, it was found that by using DMF as a solvent instead of 2-butanone, and adding 1.2 equivalents of  $\text{K}_2\text{CO}_3$ , coupling occurred in moderate to good isolated yields (46–72%) to give compounds **2**, **4**, and **9–12**. One drawback, which became apparent upon using adenine or purine, was the formation of an N-9 substituted product, as well as the N-3 substituted product, in approximately a 2:1 ratio of N-3 to N-9, which has been noted in previous work. Separation of these compounds could be carried out efficiently by column chromatography, giving the pure nonsymmetrical N-3 substituted compounds for biological testing.

NMR spectra of relevant compounds can be found in Appendix A. Compounds were dissolved in sterile  $\text{H}_2\text{O}$  and aliquots stored at a concentration of 40 mM at  $-80^\circ\text{C}$ .

### 2.1.2 Radiochemistry of [ $^{18}\text{F}$ ]D4-FCH

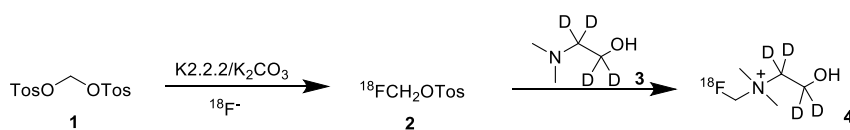
Radiosynthesis of [ $^{18}\text{F}$ ]D4-FCH was carried out by Dr. Diana Brickute, Dr. Robin Fortt, Dr. Graham Smith and Frazer Twyman, Imperial College London. [ $^{18}\text{F}$ ]D4-FCH was ra-

Scheme 2.2: Synthesis of nonsymmetrical compounds **2**, **4**, and **9-12**

diolabelled using a FASTlab-compatible procedure via [ $^{18}\text{F}$ ]-fluoromethyl tosylate, shown in Scheme 2.3 and described elsewhere [110, 158]. Typical non-decay corrected end of synthesis yields were 5-15% with a radiochemical purity of 100% and a pseudo-specific activity of 5–14 GBq/ $\mu\text{mol}$ .

### 2.1.3 Radiochemistry of [ $^{18}\text{F}$ ]GE-226

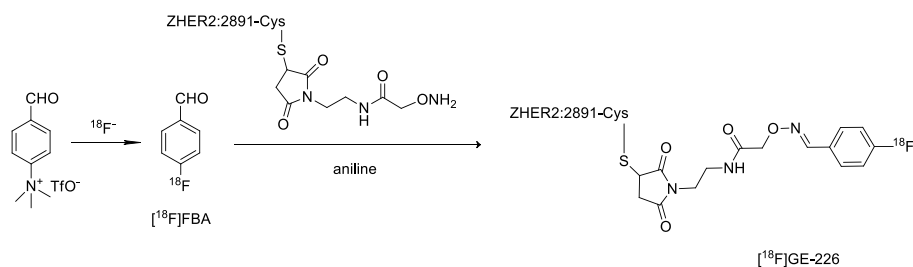
Radiosynthesis was carried out by Peter Iveson, GE Healthcare.  $Z_{\text{HER2:2891}}$  (ABY-025), synthesised as described elsewhere [159], was provided by Affibody AB. [ $^{18}\text{F}$ ]GE-226 was labeled using a fluorobenzaldehyde (FBA) strategy optimised for automated manufacture

Scheme 2.3: Radiolabelling of  $[^{18}\text{F}]\text{D4-FCH}$ .

on FASTlab (Scheme 2.4), as previously described [160]. Typical non-decay corrected end of synthesis yields were 30% and a radiochemical purity of 95%. The specific activity across all preparations was 38–110 GBq/ $\mu\text{mol}$  with a median of 46.2 GBq/ $\mu\text{mol}$ .

## 2.2 Cell Culture

A431 (squamous carcinoma; Sigma-Aldrich), A549 (lung carcinoma; ATCC), Ishikawa (endometrial adenocarcinoma; Sigma-Aldrich), HEK293T (embryonic kidney; ATCC), MCF wild type (breast adenocarcinoma; ATCC), MCF7-vector (piRES), MCF7-p95HER2 and MCF7-HER2 (the latter three cell lines were a kind gift of Professor José Baselga's laboratory, Memorial Sloan-Kettering Cancer Center [161]), MDA-MB-231 (breast adenocarcinoma; ATCC), MDA-MB-361 [breast (brain metastasis), Sigma-Aldrich], MDA-MB-468 (breast adenocarcinoma; ATCC), U2OS (osteosarcoma; Sigma-Aldrich), SKBR-3 (breast adenocarcinoma; ATCC) and SKOV-3 ovarian adenocarcinoma (ovarian carcinoma; Sigma-Aldrich) cells were maintained in DMEM (Sigma-Aldrich). A2780 (ovarian carcinoma; Sigma-Aldrich), AGS (gastric adenocarcinoma; Sigma-Aldrich), HCT116 (colon carcinoma; ATCC), HGC-27 (gastric adenocarcinoma; Sigma-Aldrich), NCI-N87 (gastric adenocarcinoma; ATCC) and OE-33 (esophageal carcinoma; ATCC) cells were maintained in RPMI (Sigma-Aldrich). St-T1b cells (immortalised endometrial stromal cells), a kind gift of Professor Jan Brosen's laboratory, Imperial College London [162], and MCF-10A (mammary gland from human female with fibrocystic disease); ATCC) cells were maintained in DMEM/F12 (Invitrogen). CCD-18Co (normal human colon; ATCC)

Scheme 2.4: FASTlab-compatible automated synthesis of  $[^{18}\text{F}]\text{GE-226}$ .

were cultured in Eagle's Minimum Essential Medium (Sigma-Aldrich). Growth media were supplemented with 10% FCS (Lonza), glutamine and antibiotics (both Invitrogen). MCF-10A were additionally supplemented with 5% horse serum (used instead of FCS), 20 ng/ml EGF (both Invitrogen), 10 µg/ml insulin, 0.5 µg/ml hydrocortisone and 100 ng/ml cholera toxin (all Sigma-Aldrich). Caco-2 cells (ATCC) were maintained in DMEM containing 4.5 g/L glucose (Invitrogen), 20% FCS and antibiotics. Cells were cultured at 37°C in humidified atmosphere containing 5% CO<sub>2</sub>.

## 2.3 [<sup>18</sup>F]D4-FCH-based CHK activity assay

### 2.3.1 Whole cell assay

CHK activity was evaluated by a cell-based assay using [<sup>18</sup>F]D4-FCH and a method previously described [112]. In brief, HCT116 cells were grown in 15 cm culture dishes (Corning) and allowed to recover overnight. Cells were treated with 1 mM HC-3 (Sigma-Aldrich) or 1 µM MEK inhibitor PD0325901 (obtained from the Division of Signal Transduction Therapy, University of Dundee) for 24 hours. Cells were pulsed with 5.55 MBq [<sup>18</sup>F]D4-FCH for 1 hour, washed 3 times in PBS, scraped into 2 mL microcentrifuge tubes and homogenised in 2 mL methanol (Sigma-Aldrich). After centrifugation at 14 000 × *g* at 4°C for 5 minutes, the supernatant was dried on a rotary evaporator at a bath temperature of 40°C. The residues were resuspended in 1.1 mL mobile phase A (see below), clarified using a 0.2 µm filter and analysed by radio-HPLC on an Agilent 1100 series HPLC system (Agilent Technologies) comprised of a γ-RAM Model 3 gamma detector and Laura 3 software (Lablogic). A Waters µBondapak C18 reverse-phase column (300 × 7.8 mm) was used as stationary phase. Samples were separated at a flow rate of 3 mL/minute using a mobile phase comprised of solvent A (acetonitrile/water/ethanol/acetic acid/1.0 M ammonium acetate/0.1 M sodium phosphate; 800/127/68/2/3/10) and solvent B (acetonitrile/water/ethanol/acetic acid/1.0 M ammonium acetate/0.1 M sodium phosphate; 400/400/68/44/88/10; all Sigma-Aldrich) with a gradient of 0% B for 6 minutes, 0–100% B in 10 minutes, 100% B for 0.5 minutes, 100%–0% B in 1.5 minutes and 0% B for 2 minutes.

### 2.3.2 Cell lysate-based assay using [ $^{18}\text{F}$ ]D4-FCH

Exponentially growing HCT116 cells were trypsinised, washed 3 times with PBS and cytosolic extracts isolated using NE-PER Nuclear and Cytoplasmic Extraction reagent (Thermo Scientific, Cat. Nr.: 78833) according to manufacturer's instructions. In brief,  $10 \times 10^6$  cells were transferred into a 1.5 ml eppendorf tube, spun down at  $500 \times g$  for 5 minutes. The pellet was subjected to 10 times its volume CERI buffer containing protease and phosphatase inhibitors (e.g. for a cell pellet with 30  $\mu\text{L}$  volume, 300  $\mu\text{L}$  CERI buffer was added). Samples were vortexed for 15 seconds and incubated for 10 minutes on ice. For each 300  $\mu\text{L}$  CERI buffer used, 16.5  $\mu\text{L}$  CERII buffer was added. After briefly vortexing, samples were incubated for 1 minute on ice and again quickly vortexed. Samples were centrifuged at  $16\,000 \times g$  for 5 minutes and protein concentration of collected supernatants determined by bicinchoninic acid (BCA) assay (Pierce) and immediately used for experiments. Indicated protein concentrations were incubated with 10 mM ATP, 100 mM  $\text{MgCl}_2$ , 100 mM Tris pH 7.5 (all Sigma-Aldrich) and 740 kBq [ $^{18}\text{F}$ ]D4-FCH at a total volume of 150  $\mu\text{L}$ . Reactions were carried out for 30 minutes at  $37^\circ\text{C}$ , terminated by addition of 600  $\mu\text{L}$  ice-cold methanol (Sigma-Aldrich) and processed and separated by radio-HPLC, as described in section 2.3.1.

## 2.4 Enzyme-based CHKA activity assays

### 2.4.1 Kinase Glo assay

In white-walled 96-well plates (Costar) and a total volume of 50  $\mu\text{L}$ , 80 ng  $\Delta 49\text{N}$  CHKA2 (a kind gift of Professor Arnon Lavie (University of Illinois) and Professor Manfred Konrad (Max Planck Institute for Biophysical Chemistry) [71]) was incubated with reaction buffer containing 600  $\mu\text{M}$  choline chloride, 10  $\mu\text{M}$  ATP, 100 mM Tris pH 7.5, 10 mM  $\text{MgCl}_2$ . For initial optimisation experiments, choline concentrations above  $K_M$  were chosen to ensure sufficient substrate availability. Reactions were carried out at  $37^\circ\text{C}$  or as recommended by the manufacturer at room temperature for uniform temperatures across the plate. The reaction was stopped by addition of 50  $\mu\text{L}$  Kinase Glo reagent (Promega) and luminescence read after 15 minutes on a Tecan Infinite M200 microplate reader. Data were analysed by fitting of sigmoidal curves with variable slope by least squares (ordinary) fitting method in GraphPad Prism version 5.01.



### 2.4.2 ADP Glo assay

In a total volume of 25  $\mu\text{L}$ , 50 ng  $\Delta 49\text{N}$  CHKA2 was incubated with reaction buffer containing 600  $\mu\text{M}$  choline, 1 mM ATP, 100 mM Tris pH 7.5 and 10 mM  $\text{MgCl}_2$ . Choline and ATP concentrations were above their respective  $K_M$  in order to ensure sufficient substrate availability. The reaction was carried out in white-walled 96-well plates (Costar) by incubation at room temperature. The reaction was stopped by addition of 25  $\mu\text{L}$  ADP Glo Reagent (Promega) and incubation for 40 minutes. Then, 50  $\mu\text{L}$  Kinase Detection Reagent (Promega) was added and luminescence read after 30 minutes on a Tecan Infinite M200 microplate reader. Reaction progress was determined by fitting of curves using Michaelis-Menten kinetics in GraphPad Prism version 5.01.

### 2.4.3 PEP / LDH coupled CHKA activity assay ( $\text{IC}_{50}$ )

Choline kinase activity was measured using a modified spectrophotometric pyruvate kinase / lactate dehydrogenase-coupled assay [71]. In a total volume of 50  $\mu\text{L}$ , 20 ng  $\Delta 49\text{N}$  CHKA2 was subjected to reaction buffer containing 72  $\mu\text{M}$  choline ( $K_M$ ), 450  $\mu\text{M}$  ATP ( $K_M$ ), 100 mM Tris pH 7.5, 100 mM KCl, 10 mM  $\text{MgCl}_2$ , 500  $\mu\text{M}$  phosphoenolpyruvate, 4 units pyruvate kinase, 5 units lactate dehydrogenase and 250  $\mu\text{M}$  NADH (all from Sigma-Aldrich) in presence of varying concentrations of inhibitor. The reaction was carried out at 37°C in UV-star half-area 96-well microplates (Greiner Bio-one) and initiated by addition of reaction buffer. ADP formation was indirectly measured by detection of NADH depletion at 340 nm on a Tecan Infinite M200 microplate reader. Half-maximal inhibitory concentrations ( $\text{IC}_{50}$ ) were calculated by fitting of sigmoidal curves with variable slope by least squares (ordinary) fitting method in GraphPad Prim version 5.01.

The mode of inhibition was determined by Lineweaver-Burk plots. To assess competitiveness with choline, ATP was kept constant at 450  $\mu\text{M}$ , while choline concentrations were varied between 40  $\mu\text{M}$  and 20 mM. Competitiveness with ATP was determined by keeping choline constant at 72  $\mu\text{M}$  while varying ATP concentrations between 10  $\mu\text{M}$  and 5 mM. Both experiments were carried out in absence or presence of 0.1, 1, 10  $\mu\text{M}$  inhibitor. Double reciprocal plots of substrate concentrations versus velocity were obtained as described elsewhere [143] and linear regression (best fit by minimised sum of squares) performed in GraphPad Prism version 5.01. Due to the endogenous ATPase activity of CHKA2, which results in higher than anticipated velocity at low substrate concentrations, data are curved

in some cases where the lowest substrate concentration had to be excluded once reciprocal velocity changed in non-linear fashion.

## 2.5 Molecular modelling

All calculations were performed at Imperial College High Performance Computing cluster by Dr. Ola Åberg. Ligands were drawn in ChemDraw, imported into Maestro (version 9.2.112, Schrodinger) and prepared using LigPrep, Epik (pH  $7 \pm 2$ ) and OPLS2005 force fields. The protein was imported from the PDB-database (3G15.pdb). Chain A was used throughout the study and the Protein Preparation Wizard was used to remove water molecules, to add hydrogens, hydrogen bonding network optimisation and finally for a restrained energy minimisation. For some dockings two water molecules close to the binding site of HC-3 that connects Asp306, Asn345 and Glu349 and Arg444 were kept, as well as one water molecule that is involved in bridging hydrogen bonding between the carboxylate of Glu206 and N7 of ADP. Docking grids were constructed from the resulting proteins using the grid generator in GLIDE. The box was placed around HC-3 and ADP (virtually connected via a carbon chain bond into a single ligand for convenient positioning of the box around the site). The size of the grid box was adjusted to dock ligands  $< 36$  Å. Docking of the inhibitors **3–13** (compound 7 in multiple protonation states) was performed with GLIDE in standard precision (SP) or extra precision (XP) mode, sample nitrogen inversions, sample ring conformations (2.5 kcal/mol) and expanded sampling. 15 000 poses per ligand were kept during the initial state and 800 were kept for energy minimisation (dielectric constant 2.0 and maximum minimisation steps 1000). The van der Waals radii of the ligands were scaled with 0.8 and with a partial cut-off of 0.15. No constraints were used. The ligand interaction diagram script (Schrodinger) was used to generate 2D-representations of the binding modes. For subsequent scoring of the docked ligands with the molecular mechanics generalised Born surface area (MM-GBSA) method the Prime module within Schrodinger was used. The flexible residues including the water molecule within 5 Å from the ligand were minimised with a harmonic constraint applied. All non-flexible residues were frozen. The ligand interaction diagram tool was used to construct Figures 3.15–3.17. Docking was evaluated both in the presence and in the absence of ADP and crystal water molecules in close proximity to the binding site. The presence or absence of the water molecules that connects Asp306, Asn345 and Glu349 and Arg444

did not alter the binding poses significantly, however removal of the water molecule in the ATP-site resulted in the loss of a hydrogen bond and lower scores, hence in subsequent dockings the water molecule in the ATP site was kept.

## 2.6 Growth inhibition assay ( $GI_{50}$ )

Half-maximal growth inhibitory concentrations ( $GI_{50}$ ) were determined in clear 96-well plates (Costar) using sulforhodamine B (SRB) assay as described elsewhere [163]. Cell numbers were optimised that the SRB-derived signal was in the linear range of the assay and the following seeding densities were used: 2 000 cells per well, HCT116; 2 500, MCF7 and A2780; 3 000, HEC-1B; 4 000, A431 and A549; 7 000, Ishikawa and Caco-2; 10 000, MDA-MB361; 20 000, St-T1b and CCD-18Co. Cells were seeded in a volume of 150  $\mu$ L and allowed to attach overnight. Cells were treated in sextuplicates with medium or 9 different concentrations of inhibitor in 50  $\mu$ L medium and incubated for 72 hours at 37°C. Cells were fixed by addition of 50  $\mu$ L 10% trichloroacetic acid (Sigma-Aldrich) for 1 hour at 4°C, washed with tap water and dried. Cells were stained with 50  $\mu$ L 0.4% SRB in 1% acetic acid (both Sigma-Aldrich) for 1 hour, rinsed with 1% acetic acid and dried. The stained protein was solubilised by addition of 150  $\mu$ L 10 mM Tris and optical densities measured at 540 nm using a Multiskan EX spectrophotometer (Thermo Scientific). Growth inhibition curves were plotted as percentage of control cells and  $GI_{50}$  determined by fitting of sigmoidal curves with variable slope by least squares (ordinary) fitting method in GraphPad Prism version 5.01.

## 2.7 [ $^3$ H]choline whole cell CHK inhibition assay ( $EC_{50}$ )

Inhibitor-dependent reduction of CHK activity in whole cells was determined in HCT116 cells by monitoring the decrease of PCho formation following a modified Bligh and Dyer extraction [164]. In brief, HCT116 cells were seeded in 6-well plates and treated with 0.16, 0.8, 4, 20 and 100  $\mu$ M inhibitor for 1 hour and pulsed in presence of inhibitor with 18.5 kBq/mL [ $^3$ H]choline chloride (PerkinElmer) at a total volume of 2 mL for an additional hour. Cells were washed 3 times in cold PBS and 750  $\mu$ L of methanol/chloroform (2:1; both from Sigma-Aldrich) added. The solubilised cytosolic content was transferred into microcentrifuge tubes and 200  $\mu$ L H<sub>2</sub>O added. Samples were centrifuged for 10 minutes and 750  $\mu$ L supernatant transferred to fresh microcentrifuge tubes. 250  $\mu$ L chloroform

and 250  $\mu\text{L}$   $\text{H}_2\text{O}$  were added and samples vortexed and centrifuged. 650  $\mu\text{L}$  of the upper aqueous phase was transferred to a fresh microcentrifuge tube and 500  $\mu\text{L}$  12 mM sodium phosphate (pH 7.0) and 750  $\mu\text{L}$  5 mg/mL tetraphenylborate (TPB) in heptan-4-one (all from Sigma-Aldrich) added. Samples were vortexed and the phases separated by centrifugation. The choline-containing upper phase was discarded and any residual choline re-extracted with 500  $\mu\text{L}$  TPB from the lower PCho phase. After vortexing and centrifugation, 200  $\mu\text{L}$  of the lower aqueous phase was added to 2 mL of Ultima Gold scintillation cocktail (PerkinElmer) and radioactivity measured on a Beckman multipurpose LS6500 scintillation counter. [ $^3\text{H}$ ]PCho content was normalised to protein as determined by BCA assay and compared to drug-naïve control cells.

## 2.8 siRNA transfections

HCT116 cells were transfected with siRNAs targeting CHKA (12.5 nM; Dharmacon, Cat. Nr.: L-006704-00-0005), CHKB (12.5 nM, Dharmacon, L-006705-00-0005), or non-targeting scramble control (SCR; 12.5 nM; Dharmacon, D-001810-10-2). For CHKA and CHKB double knockdown 25 nM siRNA each was used. Plated cells were transfected with RNAiMAX (Invitrogen) according to manufacturer's instructions.

## 2.9 Caspase 3/7 Glo assay

Apoptosis was determined using Caspase 3/7 Glo assay (Promega) according to the manufacturer's instructions. Briefly, cells were seeded into white opaque 96-well plates and treated in at least quadruplicate. Caspase Glo reagent was added and luminescence measured after 60 minutes on a Tecan Infinite M200 microplate reader. Values were normalised to protein content of cell treated in parallel as determined by SRB assay.

## 2.10 Western blotting

Cells were lysed in radioimmunoprecipitation assay (RIPA) buffer containing protease and phosphatase inhibitors (all from Sigma-Aldrich). Snap-frozen tumour samples were homogenised in RIPA buffer using CK14 bead-containing tubes with a PreCellys 24 homogeniser (2 cycles of 25 seconds at 6500 revolutions per minute; Bertin Technologies). Equal amounts of protein (20  $\mu\text{g}$ ) were resolved on 4–15% mini-protean TGX gels (Biorad)

and transferred to PVDF membranes (Trans-Blot Turbo Transfer Packs, Biorad). Membranes were blocked for 1 hour in 5% milk in Tris-buffered saline or phosphate buffered saline containing 0.1% v/v tween-20 (TBST or PBST) and incubated with the following antibodies overnight at 4°C: Actin (Abcam, Cat. Nr.: ab6276), pAkt (Cell Signaling, 4060), Akt (Cell Signaling, 2920), ATF4 (Cell Signaling, 11815), Bax (Millipore, 06-499), Bcl2 (Millipore, 05-729), CHKA (Sigma-Aldrich, HPA024153), EGFR (Cell Signaling, 4267), pErk (Cell Signaling, 4370), Erk (Cell Signaling, 4695), GAPDH (Cell Signaling, 5174S), HER2 (Cell Signaling, 2165 for visualisation of p95HER2 and full-length HER2 bands and Cat. Nr: 4290 for blots where only full-length HER2 is shown), HSP90 (Cell Signaling, 4876), HSP90 (Santa Cruz Biotechnology, sc-69703), IRE1 $\alpha$  (Cell Signaling, 3294), and Ubiquitin (Cell Signaling, 3936). Secondary HRP-conjugated mouse and rabbit antibodies (Santa Cruz Biotechnology, sc-2004 and sc-2005, respectively) were applied for 1 hour at room temperature. Signals were visualised using Amersham ECL Western Blotting Detection Reagent (GE Healthcare) and Amersham Hyperfilm (GE Healthcare).

## 2.11 RNA extraction and qRT-PCR

RNA was extracted from cells using RNeasy Mini Kit (Qiagen) and 1  $\mu$ g total RNA reverse transcribed using QuantiTect Reverse Transcription Kit (Qiagen). Gene expression was analysed by quantitative real-time PCR (qRT-PCR) using SYBR green method. Primers and Platinum SYBR Green qPCR SuperMixUDG (Invitrogen) were added according to manufacturer's instructions to 5  $\mu$ L cDNA (1:10 dilution) for a total volume of 20  $\mu$ L. The following custom designed primers were supplied by Invitrogen: CHKA (F: CGGAAGTATCCCACCAAGAA; R: TCCCAGAGGAAATGAGATG), ETNK1 (F: AGCCTCCTGCAACACCTG; R: TGTGATTCCATCTGTGAAGACC); ETNK2 (F: GC-TATGAGTACATGCAGGGTGT; R: TGCCATTTCTAAGGCGATTAAC), PCYT1A (F: GCAACCAGCTCCTTTTTCTG; R: GCAAACCTCCACAATGAGGT), PPIA (F: CT-GCACTGCCAAGACTGA, R: CATTCTGGACCCAAA). Primers were used at a final concentration of 500 nM. The following primer assays from PrimerDesign were used: CHPT1 (F: TCTGCTCTTTTATTGGGATGTTTG; R: CAACACAAAGACAATCAC-TAAAGC), PLD1 (F: CTCTGCTGCTGATTGGTCTG; R: GATATAGATATAGTGC-CTGCTGCTGTTC), PLD2 (F: GCCAGCACTTTCCTCTACATTG, R: CATCGCCCAC-CTTGTTTTCAG), GPCPD1 (F: CCCTGGACTTCCTCTCTGTG; R: GAAGTTTCCA-

CAAGGGCTCAG). Primers were used at a final concentration of 300 nM. Gene expression assays were performed on an ABI 7900HT Fast Real-Time PCR machine (Applied Biosystems) under the following conditions: 50°C for 2 minutes, 95°C for 2 minutes, 40 cycles of 95°C for 3 seconds and 60°C for 30 seconds, followed by a dissociation step. Data were analysed using comparative CT method as described elsewhere with PPIA as internal control [165].

## 2.12 DNA cell cycle analysis using flow cytometry

HCT116 cells were incubated with drugs or siRNA for indicated times. Supernatant and cells were harvested, washed and centrifuged. The cell pellet was resuspended in 1 mL ice-cold PBS and the suspension added to 9 mL 70% ethanol, while mixing gently. Cells were fixed for at least 2 hours at -20°C. Cells were centrifuged and rehydrated in 3 mL cold PBS for 15 minutes. Samples were stained in 500 µL buffer containing 100 mM Tris pH 7.4, 150 mM NaCl, 1 mM CaCl<sub>2</sub>, 0.5 mM MgCl<sub>2</sub>, 0.1% Triton X-100, 0.1 mg/ml RNase A, 50 µg/ml propidium iodide (all items from Sigma-Aldrich) at 37°C for 3 hours protected from light. Data of 10 000 cells per treatment were acquired on a BD FACSCanto flow cytometer (BD Bioscience) and analysed using FlowJo 7.6.4 software (Tree Star).

## 2.13 Transfection of U2OS cells with CHKA and CHKB

U2OS cells were transfected with GFP-tagged ORF clones of CHKA or CHKB (Insight Bio, Cat. Nr: RG207209 and RG210253, respectively) using Lipofectamine 2000 (Invitrogen) according to manufacturer's instructions. In brief, 4 µg DNA was diluted with OptiMEM (Invitrogen) to a volume of 100 µL and combined with a solution of 12.5 µL transfection reagent and 87.5 µL OptiMEM. After incubation for 20 minutes at room temperature, the transfection complexes were added to  $2.5 \times 10^5$  cells in 2 mL OptiMEM seeded in 6-well plates. After 6 hours, the medium was replaced with fresh complete growth medium. The following day, cells were transferred to 15 cm dishes and 48 hours post transfection, cells were exposed to 0.5 mg/mL G418 (Invitrogen) for selection. Individual clones were picked using cloning cylinders (Sigma-Aldrich). GFP expression of individual clones was determined using flow cytometry. Cells were trypsinised, washed 3 times with PBS and diluted to a concentration of  $1 \times 10^6$  cells per mL. Fluorescence was detected on a FACS canto flow cytometer and analysed using FlowJo 7.6.4 software.

## 2.14 Native gel western blots to detect protein dimerisation

Native gels were run using blue native polyacrylamide gel electrophoresis (BN-PAGE) method [166]. Cell homogenates were obtained by addition of passive lysis buffer (Promega) containing protease and phosphatase inhibitors to cell pellets and incubation for 30 minutes on a tube rotor at 4°C. After centrifugation for 20 minutes at  $12\,000 \times g$  at 4°C, the protein concentration of the collected supernatants was determined by BCA assay. Samples were prepared by mixing 30 µg protein with an equal volume of 2 × sample buffer (62.5 mM Tris-HCl, pH 6.8, 25% (v/v) glycerol, 0.01% (w/v) bromophenol blue, 0.02% (w/v) Coomassie Blue G250; all from Sigma-Aldrich). As control,  $\Delta 49N$  CHKA2 was either applied under native conditions (100 ng diluted to 10 µL in 100 mM Tris buffer pH 7.4 added to 10 µL 2 × sample buffer) or denatured using SDS [100 ng diluted in RIPA buffer, 1 × NuPAGE LDS sample buffer and 1 × sample reducing agent (both Invitrogen)] and incubated at 70°C for 10 minutes. Samples were resolved on 4–15% mini-protean TGX gels using 1 × native running buffer (25 mM Tris, 192 mM glycine, pH 8.3). The cathode buffer was additionally supplemented with 750 µL Coomassie Blue G250 [final concentration ca. 0.04% (w/v)]. Membranes were transferred and probed as described in section 2.10.

## 2.15 [<sup>3</sup>H]choline uptake

HCT116 cells were seeded at a density of  $3 \times 10^5$  cells/well into 12-well plates. In some experiments, cells were treated as indicated. Cells were incubated with 18.5 kBq/mL [<sup>3</sup>H]choline chloride in 500 µL for 1 hour, washed 3 times with PBS, trypsinised, neutralised with complete medium and centrifuged. Pellets were washed 3 times with PBS and lysed in 120 µL RIPA buffer. The radioactivity of 100 µL lysate was counted on a Packard Cobra II gamma counter (Perkin Elmer) and normalised to protein content, as determined by BCA assay.

## 2.16 Lactate dehydrogenase assay

Cell membrane integrity was assessed using a fluorescent kit measuring lactate dehydrogenase (LDH) release (CytoTox-ONE™, Promega) according to the manufacturer's instructions. In brief, HCT116 cells (5 000 cells/well) were incubated in 96-well plates for

4 hours with test compounds at a total volume of 100  $\mu\text{L}$ . Plates were allowed to adjust to room temperature and 50  $\mu\text{L}$  CytoTox-ONETM solution was added. The reaction was terminated after 10 minutes by addition of 25  $\mu\text{L}$  stop solution. The fluorescence was measured at an excitation wavelength of 560 nm and an emission wavelength of 590 nm. Background readings were subtracted and results expressed in per cent to maximal LDH release, as measured after incubation with Triton X-100.

### 2.17 [ $^3\text{H}$ ]choline pulse-chase experiment

HCT116 cells were seeded at a density of  $3 \times 10^5$  cell per well into 12-well plates and incubated overnight. Cells were treated with 1 or 10  $\mu\text{M}$  ICL-CCIC-0019 for 1 hour and pulsed in presence of inhibitor with 18.5 kBq/mL [ $^3\text{H}$ ]choline chloride in 500  $\mu\text{L}$  for 1 additional hour. Then, cells were briefly rinsed with RPMI and incubated with fresh, non-radioactive medium for 6 hours. Metabolites were extracted as described in section 2.7, but additionally the radioactivity of the choline-containing and chloroform (lipid-containing) fractions was measured.

### 2.18 Immunofluorescence

HCT116 cells ( $3 \times 10^4$ ) were seeded into 4-well chamber slides (BD Biosciences), cultured overnight and treated with 1 or 10  $\mu\text{M}$  ICL-CCIC-0019 for 24 hours or 2  $\mu\text{g}/\text{mL}$  tunicamycin (Sigma-Aldrich) for 4 hours. Cells were washed  $2 \times 5$  minutes with PBS and fixed with 4% formaldehyde (Sigma-Aldrich) in PBS for 15 minutes at room temperature. Cells were washed  $3 \times 5$  minutes with PBS and permeabilised with 100  $\mu\text{L}$  0.1% Triton-X100 (Sigma-Aldrich) in PBS for 10 minutes at room temperature. Cells were washed  $3 \times 5$  minutes with PBS at room temperature and blocked with 1% BSA / 0.1% Triton in PBS (PBST-BSA) for 1 hour at room temperature. Cells were incubated with CHOP primary antibody (Cell Signaling, Cat. Nr: 2895S) at a dilution of 1:3000 in 100  $\mu\text{L}/\text{well}$  PBST-BSA overnight at  $4^\circ\text{C}$ . The next day, cells were washed  $3 \times 10$  min PBS and incubated with secondary Alexa fluor 594 goat anti-mouse IgG antibody (Invitrogen, Cat. Nr: A-21125) at a dilution of 1:400 in 100  $\mu\text{L}$  PBST-BSA for 1 hour at room temperature in the dark. Cells were washed  $3 \times 10$  minutes with PBS actin fibres stained with Phalloidin Alexa Fluor 488 (Invitrogen, Cat. Nr: A12379) for 15 min at room temperature. Cells were washed  $3 \times 10$  minutes with PBS and coverslips mounted using ProLong Gold Antifade Reagent



containing DAPI (Invitrogen, Cat. Nr: P-36931). Images were acquired on an Olympus BX51 microscope and DP controller software version 2.1.

## 2.19 High-performance liquid chromatography (HPLC)

The HPLC system comprised of a Waters 600E series connected to a Waters 717 autosampler and a Waters 2487 dual UV detector. The stationary phase was a Gemini-NX 5  $\mu\text{m}$  C18, 150  $\times$  4.6 mm column (Phenomenex) protected by a guard column. The mobile phase solvent A was water with 0.1% trifluoroacetic acid and solvent B was methanol with 0.1% trifluoroacetic acid (all Sigma-Aldrich). Compounds were separated at a flow rate of 1 mL/min using a gradient of 95% A for 1 minute, 95–5% A for 4 minutes, 5% A for 10 minutes, 5–95% A for 1 minute and 95% A for 4 minutes. ICL-CCIC-0019, propranolol and verapamil were detected at a wavelength of 290 nm, hydrocortisone at 240 nm and vinblastine at 254 nm. Between each injection the column was rinsed for 2 minutes. The analysis was carried out at room temperature.

## 2.20 *In vitro* metabolism

Human and mouse liver microsomes (BD Bioscience, Cat. Nr.: 452117, 452702, 452116 and 452792) were used to predict phase I metabolism. These subcellular fractions of liver homogenates contain a variety of metabolic enzymes. While mouse microsomes originated from a pure-bred strain of female CD-1 mice, human microsomes represent a pool of 150 donor livers to reduce intra-subject variability. Furthermore, S9 fractions were used, which additionally contain cytosol and therefore different metabolic enzymes. In a total volume of 250  $\mu\text{L}$ , compounds were incubated at a concentration of 10  $\mu\text{M}$  with 1 mg/mL microsomes, 100 mM Tris pH 7.0 and 1 mM freshly prepared NADPH (Sigma-Aldrich). Control samples did not contain microsomes. After incubation for 60 minutes at 37°C, the reaction was stopped by placing samples on ice and addition of 1 mL ice-cold methanol containing 10  $\mu\text{M}$  hydrocortisone (Sigma-Aldrich) as internal standard. Proteins were allowed to precipitate for 30 minutes at  $-20^\circ\text{C}$ . Samples were centrifuged at 14 000  $\times g$  for 10 minutes and supernatants dried on a rotary evaporator. Residues were resuspended in 300  $\mu\text{L}$  water containing 0.1% trifluoroacetic acid (Sigma-Aldrich), filtered and analysed by HPLC, as described in section 2.19. Peak areas were normalised to internal standard and data expressed as per cent parent compound detected compared to control.

## 2.21 Cell permeability in Caco-2 cells

Caco-2 cells ( $8 \times 10^4$ ) were seeded on the permeable support of transwell plates (Millipore, Cat. Nr.: PSRP010R5) and allowed to form a tight monolayer for 21 days with medium changes every other day. Cells were gently washed 3 times with warm Hank's buffered salt solution (HBSS, Thermo Scientific) and monolayer integrity confirmed by measuring trans epithelial electric resistance (TEER), where values of ca.  $400 \Omega \cdot \text{cm}^2$  indicated tightness [167, 168]. Compounds were added at a concentration of  $10 \mu\text{M}$  in HBSS either to the apical side to determine absorption (i.e. permeability from the apical side to the basal side;  $P_{\text{app A-B}}$ ) or to the basolateral side to measure secretion (i.e. permeability from the basal to the apical;  $P_{\text{app B-A}}$ ). After 2 hours on an orbital shaker at  $37^\circ\text{C}$ , drug concentrations were quantified by HPLC as described in section 2.19. After the experiment, monolayer integrity was re-assessed by applying lucifer yellow to the upper compartment and quantifying transport to the lower compartment. The concentration in the receiver well was  $< 1\%$  confirming an intact cell layer throughout the experiment. Permeability was calculated with the following equation:

$$P_{\text{app}} = \frac{V_a \times \text{drug conc. acceptor}}{A \times T \times \text{initial drug conc. donor}} \quad (2.1)$$

where  $V_a$  is the volume of the acceptor in  $\text{cm}^3$ ,  $A$  the area of the cell monolayer in  $\text{cm}^2$  ( $0.7 \text{ cm}^2$ ), and  $T$  time in seconds (7200). The  $P_{\text{app}}$  is expressed in  $\text{cm}/\text{sec}$ .

The mass balance is the percentage of drug left at the end of the experiment. It was determined to ensure that results are not biased by e.g. intracellular metabolism, compounds bound to culture dish or intracellular retention. The mass balance was calculated with the following equation:

$$\text{MB} = \frac{(C_{at} \times V_a) + (C_{bt} \times V_b)}{C_0 \times V_d} \quad (2.2)$$

where  $C_a$  and  $C_b$  are the drug concentrations and  $V_a$  and  $V_b$  the volumes in chambers A and B at the end of experiment (time  $t$ ), respectively,  $C_0$  is the drug concentration in the donor chamber at time 0 and  $V_d$  is the volume of the donor solution added. A mass balance greater than 80% is regarded as acceptable [169] and values  $> 90\%$  were measured.

## 2.22 Plasma protein binding

Plasma protein binding was determined using rapid equilibrium dialysis (RED) plates (Thermo Scientific, Cat Nr.: 90006) according to manufacturer's instructions. In brief, 10  $\mu\text{M}$  compound was diluted in human or mouse plasma (Sera Laboratories, Cat. Nr.: PLH-123-H and PLHCD-808-J) and 300  $\mu\text{L}$  applied to the sample chamber, while 500  $\mu\text{L}$  PBS was pipetted into the receiver chamber. Plates were covered with sealing tape and incubated at 37°C for 4 hours on an orbital shaker at 100 revolutions per minute. Samples from both chambers were transferred to microcentrifuge tubes and 250  $\mu\text{L}$  PBS added to plasma samples and 250  $\mu\text{L}$  plasma added to PBS samples. Proteins were precipitated by addition of 1 mL methanol containing 10  $\mu\text{M}$  hydrocortisone as internal standard and incubation at -20°C for 30 minutes. Samples were centrifuged at 14 000  $\times g$  for 10 minutes, supernatants dried on a rotary evaporator, residues solubilised in 300  $\mu\text{L}$  water containing 0.1% trifluoroacetic acid, filtered and analysed by HPLC, as described in section 2.19.

## 2.23 Tumour model for the evaluation of ICL-CCIC-0019

All animal experiments were conducted in accordance with the United Kingdom Home Office Guidance on the Operation of The Animals (Scientific Procedures) Act 1986 Amendment Regulations 2012 and within the published guidelines for the welfare and use of animals in cancer research [170].

Xenografts were established in female BALB/c nude mice aged 6–8 weeks (Harlan) by subcutaneous (s.c.) injection of 100  $\mu\text{L}$  HCT116 cells ( $5 \times 10^6$  in PBS) on the back of mice. Tumour dimensions were measured frequently using a calliper and volumes calculated by the following equation:  $\text{volume mm}^3 = (\pi/6) \times a \times b \times c$ , where  $a$ ,  $b$ , and  $c$  represent 3 orthogonal axes of the tumour. When tumour volumes reached approximately 50–100  $\text{mm}^3$  (ca. 10 days post injection), mice were used for subsequent studies.

## 2.24 Pharmacokinetic and plasma metabolite studies

Plasma pharmacokinetic parameters of ICL-CCIC-0019 were established in female BALB/c mice aged 6-8 weeks (Harlan). Mice were intraperitoneally (i.p.) or perorally (p.o.) administered a single dose of 10 mg/kg and blood collected by cardiac puncture after 5, 15, 30 minutes and 1, 2, 4, 6 and 24 hours. For tissue pharmacokinetic studies, HCT116 xenograft

bearing mice were administered 10 mg/kg ICL-CCIC-0019 i.p. and blood collected after 5 minutes, 2, 6 and 24 hours. Plasma was obtained by centrifugation at  $1\,000 \times g$  for 10 minutes. Samples were snap-frozen and stored at  $-80^{\circ}\text{C}$  prior to analysis. Analysis was carried out by Cyprotex Inc. using liquid chromatography–mass spectrometry (LC–MS). For analysis of plasma metabolites, 2 hour samples of tissue pharmacokinetic studies were pooled and analysed by Cyprotex using LC–MS.

## 2.25 PET-CT imaging studies related to ICL-CCIC-0019

Mice were anaesthetised through isoflurane inhalation and scanned on a Siemens Multimodality Inveon small animal PET-CT scanner for [ $^{18}\text{F}$ ]D4-FCH PET studies using HCT116 xenografts. Low dose CT scans were first acquired (80 kVp, 0.5 mA, 220 degree rotation, 600 ms per degree exposure time, 80  $\mu\text{m}$  reconstruction pixel size) for PET attenuation correction and anatomical reference. PET images were acquired following a bolus i.v. injection of approximately 3.7 MBq tracer in the tail vein. Dynamic emission scans were acquired in list mode format over 60 minutes. Data were sorted into 0.5-mm sinogram bins and 19 time frames for image reconstruction by filtered back projection ( $4 \times 15$  seconds,  $4 \times 60$  seconds and  $11 \times 300$  seconds).

For [ $^{18}\text{F}$ ]D4-FCH studies in HCT116-shRNA tumour bearing mice, cohorts were imaged on a GENISYS4 small animal PET scanner (Sofie Biosciences), following a bolus i.v. injection of ca. 1.85 MBq of radiotracer. Dynamic PET images were acquired in list mode format and data were sorted into 19 time frames for image reconstruction by maximum-likelihood expectation maximisation ( $4 \times 15$  seconds,  $4 \times 60$  seconds and  $11 \times 300$  seconds).

To image proliferation using [ $^{18}\text{F}$ ]FLT, ca. 1.85 MBq radiotracer was injected i.v. and static scans were acquired on a GENISYS4 scanner for 10 minutes (50–60 minutes post injection) and images were reconstructed using maximum-likelihood expectation maximisation.

The Siemens Inveon Research Workplace software was used for visualisation of radiotracer uptake. To define 3-dimensional regions of interest (ROI), 30 to 60-minute cumulative images of the dynamic data and the 10-minute frame of static scans were employed. Arterial input function was estimated by drawing ROIs over the centre of the heart cavity using cumulative images from 0.25 to 2 minutes of the dynamic series, a method, previ-

ously validated for use in rodents [114]. The count densities were averaged for all ROIs at each time point to obtain time versus radioactivity curves (TAC). Tumour TACs were normalised to injected dose measured by a VDC-304 dose calibrator (Veenstra Instruments) and normalised uptake was expressed as percentage injected dose per mL tissue (NUV; %ID/mL).

## 2.26 Kinetic modelling of [ $^{18}\text{F}$ ]D4-FCH data

Kinetic analysis of PET data was performed by Dr. Giampaolo Tomasi applying a standard two-tissue irreversible compartmental model described in detail elsewhere [110].

## 2.27 Antitumour Activity

For efficacy studies HCT116 tumour bearing mice were employed. Dosing commenced when tumours reached ca.  $50\text{ mm}^3$  using described schedules and changes in tumour volume and body weight were monitored.

## 2.28 shRNA targeting CHKA

Doxycycline (DOX)-inducible lentiviral pTRIPZ vectors encoding for shRNAs targeting CHKA2 (ThermoScientific, clones: V2THS\_113013, V3THS\_335370 and V3THS\_335372) or non-targeting control (ThermoScientific) were purified from bacterial stocks using Plasmid Midi Kit (Qiagen) and size verified on a 1% agarose gel. Recombinant lentiviruses were generated using Trans-Lentiviral shRNA Packaging System (Open Biosystems). 6  $\mu\text{g}$  lentiviral transfer vector shRNA, 4.2  $\mu\text{L}$  trans-lentiviral packaging mix and 15  $\mu\text{L}$   $\text{CaCl}_2$  were diluted with water to a total volume of 150  $\mu\text{L}$ . While vortexing, 150  $\mu\text{L}$   $2 \times \text{HBSS}$  was added, precipitates allowed to form for 3 minutes. The suspension was added to  $1.2 \times 10^6$  HEK293T cells plated in 6-well plates. The following day, the medium was replaced with 2 mL reduced-serum medium (high glucose DMEM containing 5% FCS, 2 mM L-glutamine and  $1 \times$  penicillin-streptomycin). Cells were incubated for additional 48 hours. The viral particles-containing supernatants were centrifuged at  $2000 \times g$  at  $4^\circ\text{C}$  for 10 minutes to pellet cell debris and 200  $\mu\text{g}/\text{mL}$  polybrene (Sigma-Aldrich) was added to supernatants. The solution was added to  $3 \times 10^4$  HCT116 cells seeded in 24-well plates and incubated overnight. The medium was replaced with complete RPMI and cells incubated for ad-

ditional 48 hours. Transduced clones were selected by addition of 1  $\mu\text{g}/\text{mL}$  puromycin (Invitrogen). Clones were induced with 0.5  $\mu\text{g}/\text{mL}$  DOX for 48 hours and the 90<sup>th</sup> percentile of cells with highest fluorescent intensity collected by fluorescence-activated cell sorting (FACS). Knockdown of protein was determined by western blotting.

## 2.29 Drug combination experiments

HCT116 cells were seeded at a density of 2000 cells per well into 96-well plates. For each drug combination, 5 plates were used. The following day, cells were treated with 9 doses of ICL-CCIC-0019 alone or in combination with 0.1, 0.5, 1 and 5  $\mu\text{M}$  C1A or 0.01, 0.05, 0.1, 0.5  $\mu\text{M}$  vorinostat. Each plate therefore contained varying concentrations of ICL-CCIC-0019 and a fixed concentration of HDAC inhibitor. After 72 hours, proliferation was measured by SRB assay as described in section 2.6. Data was analysed using CalcuSyn software, based on the Chou-Talalay method [171]. The derived combination index (CI) indicates antagonism if  $\text{CI} > 1$ , additive effects if  $\text{CI} = 1$  and synergy if  $\text{CI} < 1$ . Data represent the mean of 3 independent experiments carried out in sextuplicate.

## 2.30 Surface Plasmon Resonance

This experiment was carried out by Syngene Inc. and data provided by GE Healthcare. Human, rhesus and rat HER2-ECD-Fc (SINO Biological, Cat. Nr: 10004-H02H, 90020-K02H, and 80079-R02H), as well as human HER2-ECD-Fc-6XHis (R&D Systems, Cat. Nr: 1129-ER) and p95HER2 ECD-Fc-6XHis (Syngene) were diluted with 50 mM sodium acetate pH 4.5 (Biacore coupling buffer; GE Healthcare) to a final concentration of 10  $\mu\text{g}/\text{mL}$ . Antigen coupling to sensor chip CM5 (GE Healthcare; Cat. Nr: BR-1005-30) was done according to manufacturer's amine coupling protocol. HBS-EP buffer (10 mM HEPES pH 7.4, 150 mM NaCl, 3 mM EDTA and 0.005% surfactant P20; GE Healthcare; Cat. Nr: BR-1006-69) was used as running buffer and as solvent for isotopically unmodified GE-226. The affinity studies were performed using a Biacore T100 (GE Healthcare). GE-226 was injected over the surface in concentration range of 0.05–50 nM followed by HBS-EP to monitor dissociation. The chip was regenerated with 50 mM sodium hydroxide followed by a 60 seconds run of HBS-EP to stabilise the surface. Kinetic calculations were performed using Langmuir 1:1 binding model and simultaneous calculation of association and dissociation phase.

### 2.31 Cells and treatments for evaluation of [ $^{18}\text{F}$ ]GE-226

For siRNA-mediated HER2 knockdown, SKOV-3 cells were transfected with 25 nM scramble control or HER2-targeting siRNA (Invitrogen ERBB2 Silencer Select Validated siRNA; Cat. Nr: 4457298) by reverse transfection with Lipofectamine RNAiMAX (Invitrogen) according to manufacturer's instructions.  $3 \times 10^5$  cells were seeded in 12-well plates 48 hours prior to uptake experiment. Target knockdown was verified by western blotting on cells that were transfected in parallel.

For all uptake studies in response to drug treatment,  $2.5 \times 10^5$  SKOV-3 cells were seeded in complete medium 48 hours prior to uptake experiments. Cells were incubated with indicated doses of NVP-AUY922 (LC Laboratories) for 24 hours and 10  $\mu\text{g}/\text{mL}$  trastuzumab (Roche) for 1 or 24 hours prior to addition of radiotracer.

### 2.32 *In vitro* [ $^{18}\text{F}$ ]GE-226 uptake assay

For baseline uptake,  $3 \times 10^5$  cells were seeded in complete media in 12-well plates and allowed to recover overnight. Cells were washed twice with serum-free medium and pulsed with 370 kBq in 500  $\mu\text{L}$  serum-free medium for 1 hour. For blocking studies, cells were co-incubated with tracer and 0.5 mg/mL cold, isotopically unmodified GE-226.

Cells were washed with PBS, trypsinised, neutralised with complete medium and centrifuged. The pellet was washed three times with PBS and lysed in 120  $\mu\text{L}$  RIPA buffer. The radioactivity of 100  $\mu\text{L}$  lysate was counted on a Packard Cobra II gamma counter (Perkin Elmer). Radioactivity was normalised to applied radioactivity and protein content, as determined by BCA assay.

### 2.33 Small animal experimental models and treatments for [ $^{18}\text{F}$ ]GE-226 PET studies

For all but SKOV-3 xenografts, mice were s.c. implanted with 0.72 mg/60 day release oestradiol pellets (Innovative Research of America) approximately 2 days before cell inoculation. Xenografts were established by s.c. injection of 100  $\mu\text{L}$  MCF7-vector, MCF7-p95HER2 and MCF7-HER2 cells ( $1.5 \times 10^7$  cells in PBS mixed 1:1 with Matrigel, BD Bioscience), MDA-MB-361 cells ( $5 \times 10^6$  cells in PBS mixed 1:1 with Matrigel) or SKOV-3 cells ( $5 \times 10^6$  cells in PBS) on the back of mice. Tumour dimensions were measured fre-

quently by calliper measurements, as described in section 2.23. When tumour volumes reached approximately 50–100 mm<sup>3</sup> (MCF7 models ca. 4 weeks post injection, MDA-MB-361 xenografts ca. 3 weeks post injection and SKOV-3 xenografts ca. 6 weeks post injection), mice were used for subsequent studies.

For blocking studies, SKOV-3 xenograft bearing mice were administered 500 µg (ca. 25 mg/kg) cold isotopically unmodified GE-226 i.v. through the tail vein 20 minutes before administration of radiotracer. To assess interaction of radiotracer with trastuzumab, SKOV-3 xenograft-bearing mice were treated with 50 mg/kg trastuzumab i.p. 2 hours prior to the scan. Animals were recovered, treated twice more with 25 mg/kg trastuzumab i.p. and re-scanned 7 days after initial dose. To investigate response to HSP90 inhibition, SKOV-3 xenograft-bearing mice were treated with 50 mg/kg NVP-AUY922 or equivalent volume of vehicle (ca. 5 µL/g body weight; 10% DMSO and 5% Tween-20 in PBS) once a day i.p. for three days. 24 hours after the last treatment, animals were used for PET imaging.

### **2.34 [18F]GE-226 PET-CT imaging**

Mice were anaesthetised through isoflurane inhalation and 60 minute dynamic emission scans acquired on a Siemens Multimodality Inveon small animal PET-CT scanner, as described in section 2.25. Where indicated, cumulative images of the dynamic data (30 to 60 minutes) were iteratively reconstructed (OSEM3D) for qualitative image visualisation.

### **2.35 ELISA**

Excised and snap frozen tumour tissue samples were homogenised in RIPA buffer with the PreCellys 24 homogenizer and CK14 beads-containing tubes (two cycles of 25 seconds at 6 500 rpm). HER2 expression was determined by ELISA (Calbiochem, c-ErbB2/c-Neu Rapid Format ELISA Kit, Cat. Nr: QIA10-1EA) according to manufacturer's instructions.

### **2.36 Metabolic stability of [18F]GE-226**

Metabolic stability of the radiotracer was assessed by GE Healthcare. Male Wistar rats were administered 20 MBq [18F]GE-226 i.v. through the tail vein. At 10, 30 and 60 minute post injection, rats were exsanguinated via cardiac puncture and plasma obtained by centrifugation. Radioactive plasma metabolites were trapped on a tC2 SPE cartridge



(Oasis), washed with water and eluted in a mixture of 50% of 100 mM ammonium acetate (mobile phase A) and 50% of acetonitrile (mobile phase B). The eluate was diluted 1:4 with mobile phase A and 1 mL analysed by radio-HPLC (Gilson) equipped with a BGO dual coincidence detector. Metabolites were separated using a Luna C5 5 $\mu$  4.6  $\times$  150 mm analytical column (Phenomenex) at 1 mL/min with a gradient of 95% A for 2 minutes, 95–5% A for 12 minutes, 5–0% A for 4 minutes, 0% A for 4 minutes, 0–95% A for 2 minutes, and 95% A for 8 minutes.

### 2.37 Biodistribution

Tumour-bearing BALB/c nude mice were administered ca. 3.7 MBq [ $^{18}\text{F}$ ]GE-226 i.v. through the tail vein. Mice were sacrificed at different time points by exsanguination. Tissues were excised, weighed and radioactivity counted using a Packard Cobra II gamma counter and decay corrected. Data were expressed as percent injected dose per gram of tissue (%ID/g).

### 2.38 Kinetic modelling of [ $^{18}\text{F}$ ]GE-226

Kinetic analysis of PET data was performed by Dr. Giampaolo Tomasi applying a standard two-tissue irreversible compartmental model to fit each tumour TAC with the corresponding image-derived plasma TAC as input function (IF) to estimate  $K_1$  (mL/cm $^3$ /min),  $k_2$  (1/min) and  $k_3$  (1/min) and the blood vascular component  $V_b$  (mL blood/mL tissue; unitless). The irreversible uptake rate  $K_i$  (mL/cm $^3$ /min) was computed as  $K_1 \times k_3 / (k_2 + k_3)$ . To estimate the kinetic parameters the measured tumour TAC (tTAC) was modelled as

$$tTAC(t) = (1 - V_b)h(t) \otimes pIF(t) + V_bIF(t) \quad (2.3)$$

with  $h(t)$  indicating the unknown tissue impulse function and  $\otimes$  the convolution operator. The parameter vector  $p = [K_1, k_2, k_3, V_b]$  was estimated with the standard Weighted Non-Linear Least Squares (WNLLS) by minimizing the Weighted Residual Sum of Squares (WRSS) function

$$WRSS(p) = \sum_{i=1}^N w_i [tTAC(t_i, p)^{MODEL} - tTAC(t_i)]^2 \quad (2.4)$$

with  $tTAC(t_i)$  and  $t_i$  indicating the measured concentration in the tumour and mid-time of  $i$ -th frame, respectively, and  $N$  denoting numbers of frames. Weights were set to

$$\frac{\Delta_i}{C(t_i) \exp(\lambda t_i)} \quad (2.5)$$

with  $\Delta_i$  and  $\lambda$  representing the duration of the  $i$ -th frame and decay-constant of  $^{18}\text{F}$  REF. [172]. The two-tissue irreversible model was chosen after visual assessment of the tumour TACs, which showed clear irreversible uptake in most cases. Furthermore, when a two-tissue reversible compartment model was used, non-physiological estimates of the parameters characterised by high variance were obtained.

### 2.39 Synthesis of fluorescein labelled GE-226

Synthesis of fluorescein labelled GE-226 was carried out by Dr. Susan Hoppmann, GE Healthcare. It was prepared by mixing 5 mg  $Z_{HER2:2891}$  with 1.5 mg fluorescein-5-maleimide (Pierce, Cat. Nr: 46130) in 1.5 mL 33% acetonitrile/water. The solution was adjusted to pH 6 by adding ammonium acetate and the reaction mixture shaken for 2 hours. Dimethylformamide (0.5 mL) and water (3 mL) were added and the mixture was shaken for another hour, diluted with 4 mL water/0.1% trifluoroacetic acid. The product was purified by semi-preparative HPLC (gradient: 20–35% acetonitrile over 50 minutes) and lyophilised.

### 2.40 Small animal model for fluorescent GE-226 experiment

This experiment was carried out by Dr. Susan Hoppmann, GE Healthcare. The bilateral A431/NCI-N87 model was established by s.c. injection of A431 ( $1 \times 10^7$  cells) and NCI-N87 cells ( $2 \times 10^6$  cells) in 100  $\mu\text{L}$  PBS mixed 1:1 with Matrigel in the lower flanks of 4–6 week old male CD-1 nude mice (Charles River Laboratories). Tumour volumes were monitored frequently as described in section 2.23 and when they reached 50–100  $\text{mm}^3$  (approximately 3–4 weeks), mice were administered a mixture of Hoechst (ca. 20 mg/kg) and fluorescein-conjugated GE226 (ca. 15 mg/kg) in 100  $\mu\text{L}$  PBS i.v. through the tail vein. Tumours were excised 120 minutes post injection, immediately fixed in formalin and embedded in paraffin. Sections were sliced and stored in the dark at  $-80^\circ\text{C}$ . Immunofluorescent images were acquired at  $400\times$  magnification using a Leica DMRB microscope with a Nikon DS-Ri1 camera and Nikon NIS-Elements D 3.2 software. Fluorescent images were

acquired by keeping exposure times constant across all slides. Adjacent tumour sections were immunohistochemically stained with HercepTest.

## 2.41 Immunohistochemistry

Analysis of HER2 protein expression in excised tumours was carried out by GE Healthcare using the HercepTest (Dako, Cat. Nr: K5204) according to manufacturer's instructions.

## 2.42 Sequencing

Genomic DNA of SKOV-3 cell line and indicated tumour samples were extracted using PureLink Genomic DNA extraction kit (Invitrogen). Exon 8 was PCR amplified, as previously described [173], using the following primers: forward, TCAGATCCTGGCT-GACTGTG; reverse, AACAGCCACATGAGCATCAG (synthesised by Invitrogen). PCR products were purified using ExoSAP-IT (Affymetix) and sent for bi-directional sequencing at the MRC CSC Genomics Laboratory. Sequences were analysed using Sequencher software version 5.2.3.

## 2.43 Statistical analysis

Data were expressed as mean  $\pm$  standard deviation (SD) or standard error of the mean (SEM). Unless otherwise specified, the significance of comparison between two data sets was determined using unpaired, two-tailed Student's t test (GraphPad Prism version 5.1) and  $P < 0.05$  defined as significant.



## Chapter 3

# Design and Evaluation of Choline Kinase Inhibitors

This work is associated with [1]:

Trousil S, Carroll L, Kalusa A, Aberg O, Kaliszczak M, Aboagye EO. Design of symmetrical and nonsymmetrical *N,N*-dimethylaminopyridine derivatives as highly potent choline kinase alpha inhibitors. *MedChemComm*. 2013;4:693–6.

Inhibition of CHKA is thought to be a promising intervention for tumours with deregulated choline metabolism. Most results have been achieved by posttranscriptional silencing or with inhibitors that are difficult to synthesise and not commercially available. In order to develop accessible inhibitors with drug-like properties and new scaffolds the CHKA crystal structure was examined.

### 3.1 Analysis of CHKA crystal structure

The CHKA crystal structures solved by Malito et al. [71] and Hong et al. [174] were taken as basis to analyse the binding sites of choline and ATP to rationally design novel inhibitors (Figure 3.1). The ATP binding site shares similarities with all CHK isoforms, eukaryotic protein kinases and aminoglycoside phosphotransferases [71]. It comprises of many highly conserved amino acids, including Asn122, Leu124, Leu144, Arg146 and Leu313, where induced mutations lead to a loss of function [71]. The choline-binding site contains a deep hydrophobic groove with negatively charged residues on its rim (Glu215, 217, 218, 309, 349,

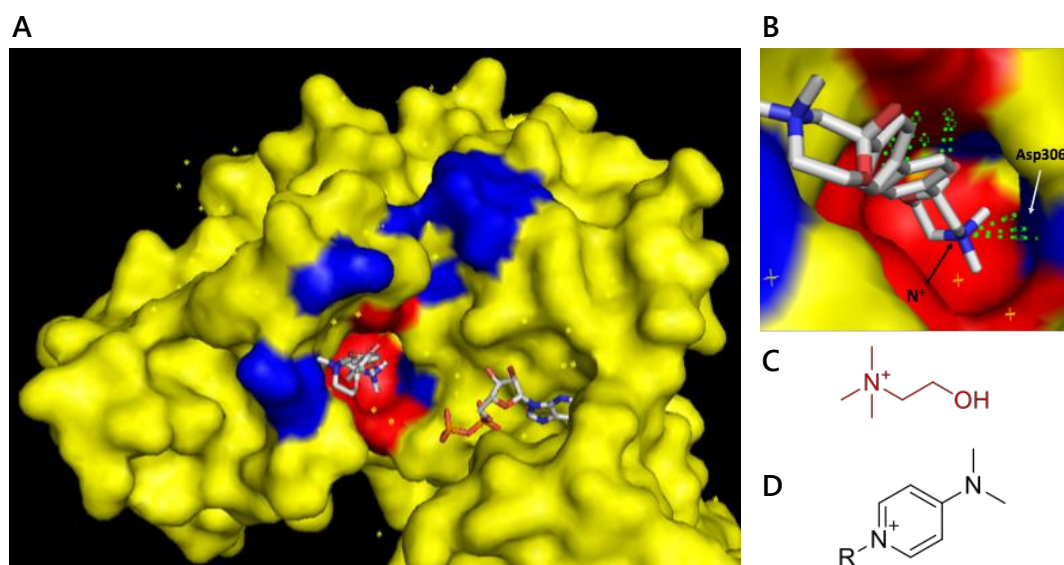


Figure 3.1: Crystal structure of CHKA. A, The structure was derived from RCSB Protein Data Bank (accession code 3F2S) and analysed in PyMOL. CHKA is in complex with HC-3 (left co-crystallised structure occupying the choline pocket) and ADP (right). Regions in blue indicate negatively charged amino acids and red represent lipophilic amino acids. B, Close-contact interactions of HC-3 with the deep end of the choline pocket. Green dashed lines refer to intermolecular interactions. C, Structure of choline. D, Structure of *N,N*-dimethylaminopyridine.

357, 434 and Asp353) and at the deep end of the groove (Asp306, Asp330 and Glu349; [71]; Figure 3.1A). It appears that the negatively charged residues on the outside attract the positively charged choline to guide it into the binding pocket, where it is fixed by Asp306, Asp330 and Glu349 (Figure 3.1B). The long hydrophobic groove contains aromatic amino acids (Tyr333, Tyr354, Tyr440 and Trp420, Trp423), which further stabilise the positively charged amine [71]. Choline phosphorylation occurs through a double displacement mechanism, whereby in two discrete steps the  $\gamma$ -phosphate of ATP is transferred to choline via a phospho-enzyme intermediate [147].

Due to the structure of CHKA it was concluded that small-molecule inhibitors should have the following features: (i) a positively charged quaternary amine group, which mimics choline and (ii) an aromatic moiety adjacent to the amine, which allows  $\pi$ - $\pi$  interaction with the hydrophobic groove, in particular with Tyr354 (Figure 3.1B). Therefore, *N,N*-dimethylaminopyridine (DMAP) was employed as cationic choline-mimicking moiety (Figure 3.1C–D), as this had been shown in previous work to be a highly effective pharmacophore [144]. Although the charge of DMAP is formally on the pyridine nitrogen, it is in fact delocalised and interacts with the aromatic ring and the nitrogen of the dimethylamino group. It therefore possesses good balance of charge, lipophilicity and aromaticity.

It was intended to create two different scaffolds (Figure 3.2). Symmetrical *bis*-DMAP

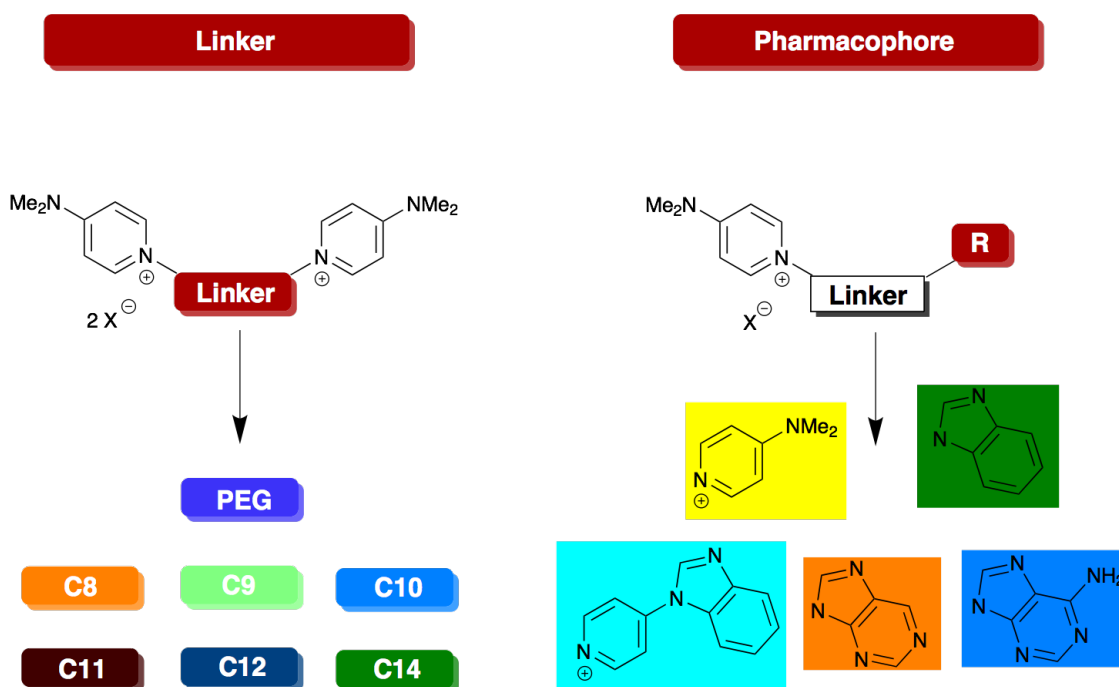


Figure 3.2: Overview of designed choline kinase inhibitor scaffolds. Symmetric inhibitors (left) with different linker lengths were designed to only interact with the choline pocket. Additionally, nonsymmetrical inhibitors (right) aimed to inhibit both choline and ATP pockets were designed.

compounds with different aliphatic linkers would be tested in anticipation to interact with the negatively charged amino acids and therefore solely inhibit the choline pocket. It was further attempted to exploit the proximity of the ATP and choline pockets by creating novel scaffolds that — for the first time — would permit simultaneous inhibition of both catalytic sites. These compounds would comprise of a DMAP and the introduction of an ATP-mimicking moiety in ca. 14 Å distance, which corresponds to a chain of ca. 12 carbons. Such molecules could potentially have high affinity towards CHKA, while avoiding the promiscuity of ATP-competitive kinase inhibitors. Furthermore, the decreased overall charge could potentially enhance its pharmacological properties. A focused chemical library comprising 13 compounds was designed and synthesised by Dr. Laurence Carroll and Dr. Andrew Kalusa, Imperial College London.

### 3.2 Development and validation of CHKA inhibition assay

In order to evaluate the potency of choline kinase inhibition, an assay was developed to facilitate (i) accurate  $IC_{50}$  determination, (ii) establishment of the mode of inhibition, thus revealing interactions with choline or ATP pockets, and ideally, (iii) rapid and simulta-

neous screening of multiple compounds. Several assays, based on various principles, were evaluated.

### 3.2.1 Radioactive assays using [ $^{18}\text{F}$ ]D4-FCH

Due to the initial unavailability of purified CHKA, two assays using the PET radiotracer [ $^{18}\text{F}$ ]D4-FCH were investigated. The conversion of tracer, mimicking choline, to its phosphorylated form, resembling PCho, was monitored by radio-HPLC. HCT116 cells, that are known to express CHKA [112], were used in assays involving whole cells (incorporating transport and phosphorylation) or cell lysates (incorporating only phosphorylation).

#### 3.2.1.1 Whole cell CHK activity assay

HCT116 cells, grown in 15 cm dishes, were pulsed with 5.5 MBq [ $^{18}\text{F}$ ]D4-FCH for 1 hour. Cells were scraped into PBS, washed, and lysed in methanol. Soluble metabolites, containing the radiotracer, were separated and analysed by radio-HPLC (Figure 3.3A).

In untreated cells, the tracer was almost completely converted to its phosphorylated analogue and the formation of betaine, the oxidation product of choline, was negligible (Figure 3.3B). It was then tested whether this method would be suitable to detect the modulation of CHKA. To this end, as the designed inhibitors were not available at that time, cells were pre-treated for 24 hours with 1 mM HC-3, a weak CHK inhibitor that also inhibits choline transporters, or 1  $\mu\text{M}$  MAPK/ERK (MEK) kinase inhibitor PD0325901, that was previously shown to downregulate CHKA protein expression [112]. Radioactivity was normalised to protein content and ratios of choline to PCho plotted (Figure 3.3C-E). Total tracer incorporation and PCho formation was significantly reduced by both treatments. Dual inhibition of CHKA and transporters abolished cell-associated radioactivity by more than 90%. In contrast, CHKA downregulation by MEK inhibition reduced PCho formation by 65% and increased the free choline fraction, indicating, that reduced CHKA expression inhibited PCho synthesis, resulting in an accumulation of free choline.

The assay proved to be of very slow throughput and, importantly, the results are a combination of choline transport and phosphorylation. Therefore, a cell lysate-based assay was developed, that would only measure choline phosphorylation.



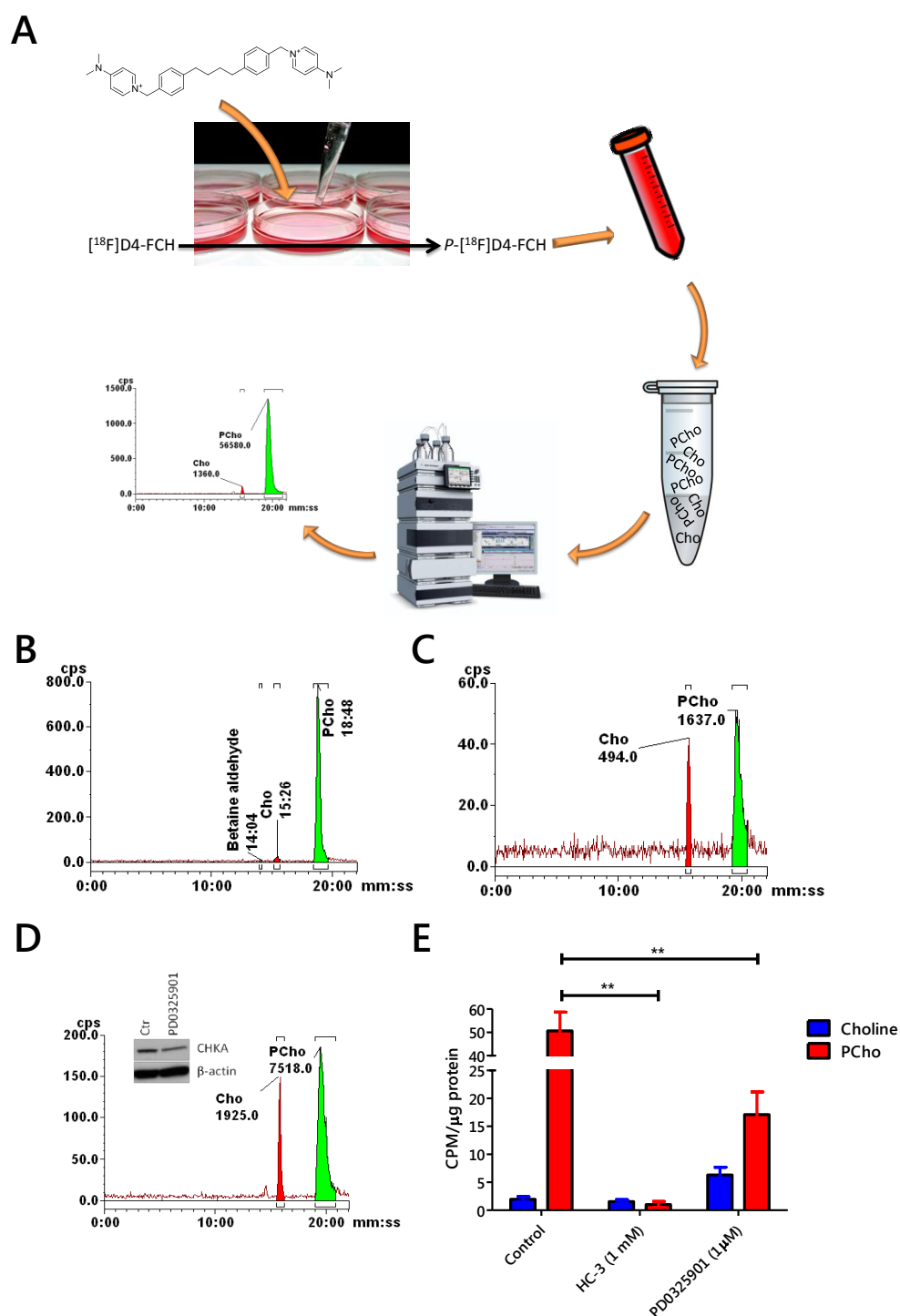


Figure 3.3: Cell-based inhibition assay using  $[^{18}\text{F}]\text{D4-FCH}$ . A, HCT116 cells were incubated with  $[^{18}\text{F}]\text{D4-FCH}$ , harvested and lysed in methanol and radioactive metabolites separated and analysed by radio-HPLC. Representative radio-HPLC chromatograms of untreated (B), HC-3 (1 mM for 24 hours; C), or PD0325901 (1  $\mu\text{M}$  for 24 hours; D) samples. Western blot in D shows CHKA expression after treatment with 1  $\mu\text{M}$  PD0325901 for 24 hours. E, Peak areas of indicated metabolites were normalised to total protein content and are expressed as radioactivity per  $\mu\text{g}$  protein. Mean of  $n = 3$  in triplicate  $\pm$  SD; \*\*  $P < 0.01$ .

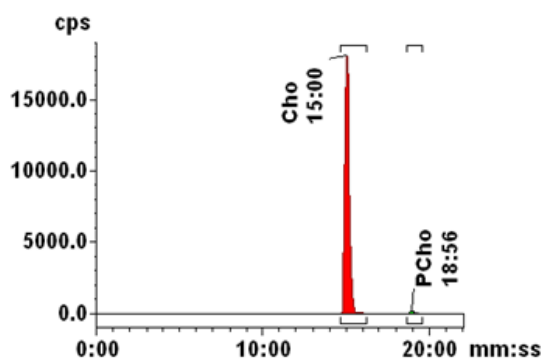


Figure 3.4: Representative radio-HPLC chromatogram of cell lysate-based assay, demonstrating <1% conversion of choline to PCho in cell lysates.

### 3.2.1.2 Cell lysate-based CHK activity assay

Cytosolic fractions of HCT116 cells were isolated in order to enrich for CHKA. In the first step, varying amounts of lysate were tested in order to determine the lowest concentration of CHKA-containing lysate required to catalyse the enzymatic reaction. Lysates with a total protein content of 10–1500  $\mu\text{g}$  were tested and supplemented with 10 mM ATP and 100 mM magnesium chloride ( $\text{MgCl}_2$ ), a co-factor required for catalytic activity. Samples were incubated with 740 kBq [ $^{18}\text{F}$ ]D4-FCH for 30 minutes at 37°C with occasional mixing and reactions were stopped by placing samples on ice and by addition of mobile phase containing acetonitrile. The mixture was filtered, separated and analysed by HPLC. Even at high total protein concentrations (> 500  $\mu\text{g}$ ), the cell lysates showed almost no CHK activity (Figure 3.4). While it is possible that the extraction process compromised enzymatic integrity, the assay bared additional disadvantages; extraction efficiencies might have varied across different batches and the ATP concentration could not be fully controlled, as the decomposition of endogenous ATP in the lysate was unknown. Therefore, this assay proved to be unsuitable and alternatives were investigated.

### 3.2.2 Assays using purified CHKA2

The initially tested assays were not able to fulfil the set criteria to accurately determine  $\text{IC}_{50}$  and mode of inhibition and in addition were expensive and time consuming. Therefore it was necessary to develop an assay using purified CHKA. The enzyme was kindly provided by Arnon Lavie, University of Illinois at Chicago, in form of  $\Delta 49\text{N}$  hCHKA2, an N-terminally truncated construct, as published elsewhere [71]. Different luminescent and UV-spectrophotometric assays were tested. In all assays, purified CHKA2 was incubated in

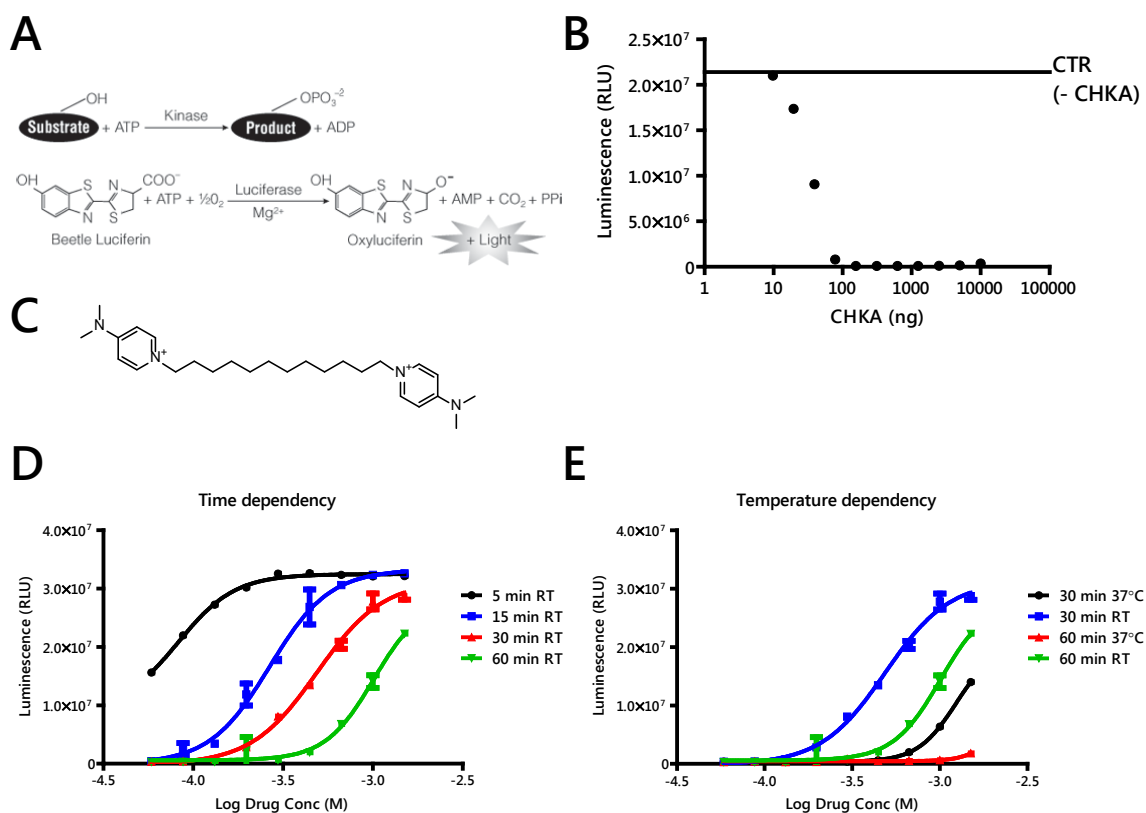


Figure 3.5: Kinase Glo assay. A, assay principle. A kinase reaction uses ATP to phosphorylate a substrate (i.e. choline). After completion of the enzymatic reaction, the Kinase Glo mix containing luciferase is added, which converts remaining ATP to light. Figure by Promega. B, Determination of the amount CHKA2 needed to alter luminescent signal (mean of  $n = 2$ ). C, Structure of compound **8**. D–E, The reaction was carried out in presence of inhibitor **8** and reaction progress curve monitored. A strong time-dependency (D) and temperature-dependency (E) was observed. Each data point represents mean of  $n = 3 \pm \text{SD}$ .

presence of choline, ATP and  $\text{Mg}^{2+}$ . The assay optimisation was conducted in accordance with NIH guidelines [175] and key literature [176].

### 3.2.2.1 Kinase Glo assay (Promega)

This assay is an endpoint measurement, where addition of a proprietary reaction mix terminates the enzymatic reaction. It measures ATP that has not been used up during a kinase reaction (Figure 3.5A). Remaining ATP gives a luminescent signal and high luminescence therefore corresponds to enzymatic inhibition.

In the first step, it was determined how much enzyme is required to sufficiently convert choline into PCho (Figure 3.5B). Different concentrations of enzyme were added and 80 ng per reaction found to be the smallest amount of enzyme capable of completely converting exogenous choline at room temperature within the 30-minute duration of the assay. Ambi-

ent temperature was chosen, as recommended by the manufacturer, to avoid experimental variations induced by varying substrate temperatures.

Next, one of the new inhibitors, which has already been synthesised at that point (compound **8**, Figure 3.5C) was added to the reaction. Different concentrations ranging from 58  $\mu\text{M}$  to 1.5 mM showed dose-dependent inhibition of the enzymatic reaction, however, the signal proved to be time- and temperature dependent (Figure 3.5D–E). It was unclear whether this effect was due to assay instability or rapid reaction kinetics. The main drawback, however, was that the maximal possible ATP concentration of 10  $\mu\text{M}$  for this assay was significantly below CHKA's reported  $K_M$  of 450  $\mu\text{M}$  [71]. Therefore, the ADP Glo assay was used instead.

### 3.2.2.2 ADP Glo assay (Promega)

In this assay, ADP, which is formed during the enzymatic reaction, generates the luminescent signal. This means, that high luminescence correlates with high enzyme activity (or low pharmacological inhibition) and vice versa. The assay permits ATP concentrations up to 1 mM. To validate the assay, the linearity of the signal was assessed against a standard curve of ADP and showed a large dynamic range up to 1 mM ADP (Figure 3.6A). Next, the smallest amount of kinase that generates an adequate signal-to-noise ratio and that produces luminescence within the linear range of the titration curve was determined. When 50 ng CHKA was used, a signal-to-noise ratio of ca. 130 was achieved (Figure 3.6B). Determination of  $\text{IC}_{50}$  has to be carried out in the initial linear phase of the reaction progress curve, which plots the amount of product generated over time. At 50 ng CHKA, the linearity was only maintained in the first minutes of the assay (Figure 3.6C). As this assay is an end-point measurement, it was difficult to retain accuracy at very short incubation times. Therefore, the amount of kinase was reduced, in hope that it would slow down the reaction time. This should result in delayed reaction progress curves, where the maximal luminescence remains the same. This is, because with less enzyme the same amount of substrate can be converted, just at a slower rate. However, less enzyme resulted in a flatter slope, indicating enzyme instability [175]. Therefore, the 50 ng reaction was further characterised and the reaction stopped at different time points (Figure 3.6D). Linearity was only given in the first 3 minutes and determination of  $K_M$  of both substrates (choline and ATP) were not accurately possible without real-time kinetic measurements (data not shown).

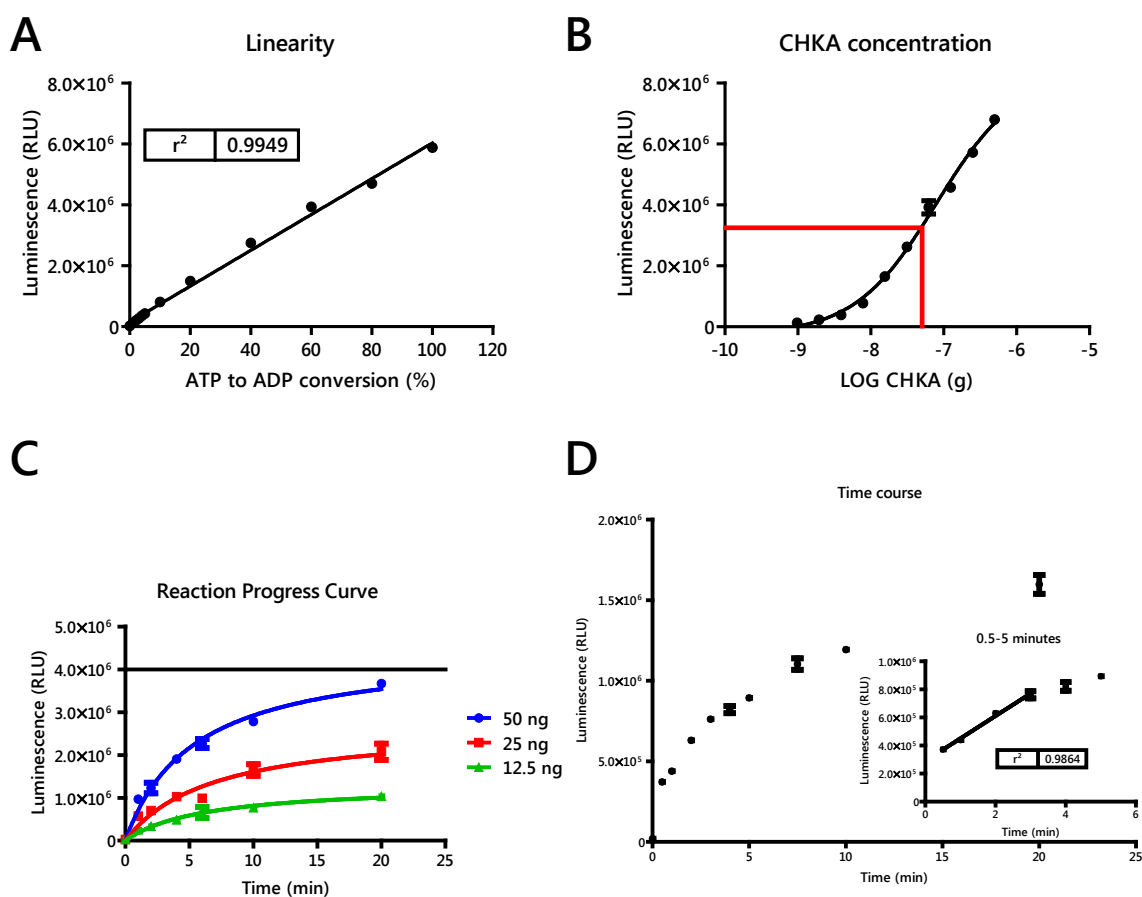


Figure 3.6: ADP Glo assay. A, The linearity of the signal was determined using an ADP standard curve in presence of ATP. E.g., 20% conversion corresponds to 20% ADP and 80% ATP. B, Different concentrations of CHKA2 were added to the reaction in order to optimise the amount enzyme needed for the reaction. The red line indicates 50 ng CHKA per reaction, which gave a signal-to-noise ratio of 130 and was in the linear range of the assay. C, Reaction progress curve, showing the amount of signal derived from different enzyme concentrations over time. The curves were fitted by GraphPad Prism version 5.01 using Michaelis-Menten kinetics. The line indicates the maximal velocity. D, The reaction was repeated with 50 ng CHKA and linearity in the first minutes of the reaction observed. Mean of  $n = 3 \pm \text{SD}$ .

Kinase and ADP Glo assays were employed, as they are non-radioactive, of high throughput and commonly used for screening [177]. However, both assays were unsuitable for CHKA, and therefore focus put on the development of an assay with robust readouts and that could determine reaction progress kinetics.

### 3.2.2.3 Phosphoenolpyruvate kinase / lactate dehydrogenase-coupled assay

A phosphoenolpyruvate kinase / lactate dehydrogenase (PK/LDH) coupled assay was adapted from one published by Maltio and colleagues [71] that indirectly measures the accumulation of ADP (Figure 3.7). The reaction can be carried out in a temperature-

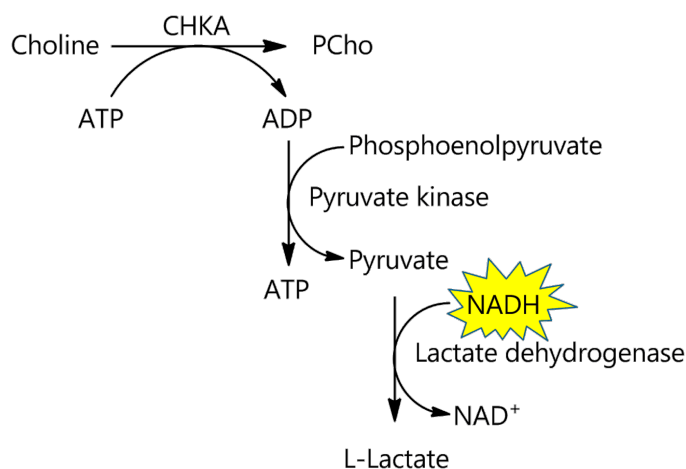


Figure 3.7: Assay principle of PK/LDH coupled kinase activity assays. The generated ADP during the CHKA reaction is used to form pyruvate from phosphoenolpyruvate (PEP) by pyruvate kinase (PK). Lactate dehydrogenase (LDH) then converts pyruvate to lactate under consumption of NADH. This decrease of NADH can be spectrophotometrically monitored, as NADH, but not NAD<sup>+</sup> is UV active at 340 nm.

controlled plate reader, where kinetic measurements are taken. Furthermore, half-area 96-well plates can be used allowing parallel processing of several compounds, while minimising sample volumes.

Most commonly used multiwell plates are not UV light translucent and therefore give low readings at this 340 nm, which is the maximal absorbance of NADH. Different 96-well plates were tested and Greiner Bio-One UVStar plates found to be most suitable (Figure 3.8). The detection limit for NADH was low (1  $\mu\text{M}$ ) and the signal linear over a broad concentration range (1–750  $\mu\text{M}$ ) and therefore the detection system proved suitable for NADH assay concentration of 250  $\mu\text{M}$ . The reported maximal absorption was confirmed to be at 340 nm.

Next, the stability of the NADH signal was investigated and the absorbance of 250  $\mu\text{M}$  NADH in 100 mM Tris monitored at 37°C over 30 minutes, which was anticipated to be the maximal assay duration. The loss of NADH signal over 30 minutes was only 1.6%, suggesting sufficient stability (Figure 3.9).

The assay components were chosen as recommended by Malito et al. [71] and scaled to a total volume of 50  $\mu\text{L}$ . The assay composition can be found in Table 3.1. Choline and ATP were used at their respective  $K_M$  of 72 and 450  $\mu\text{M}$ , as previously reported for this enzyme [71].

In order to determine the optimal CHKA concentration per reaction, several reactions were run using different quantities of enzyme and decrease of NADH monitored over 30

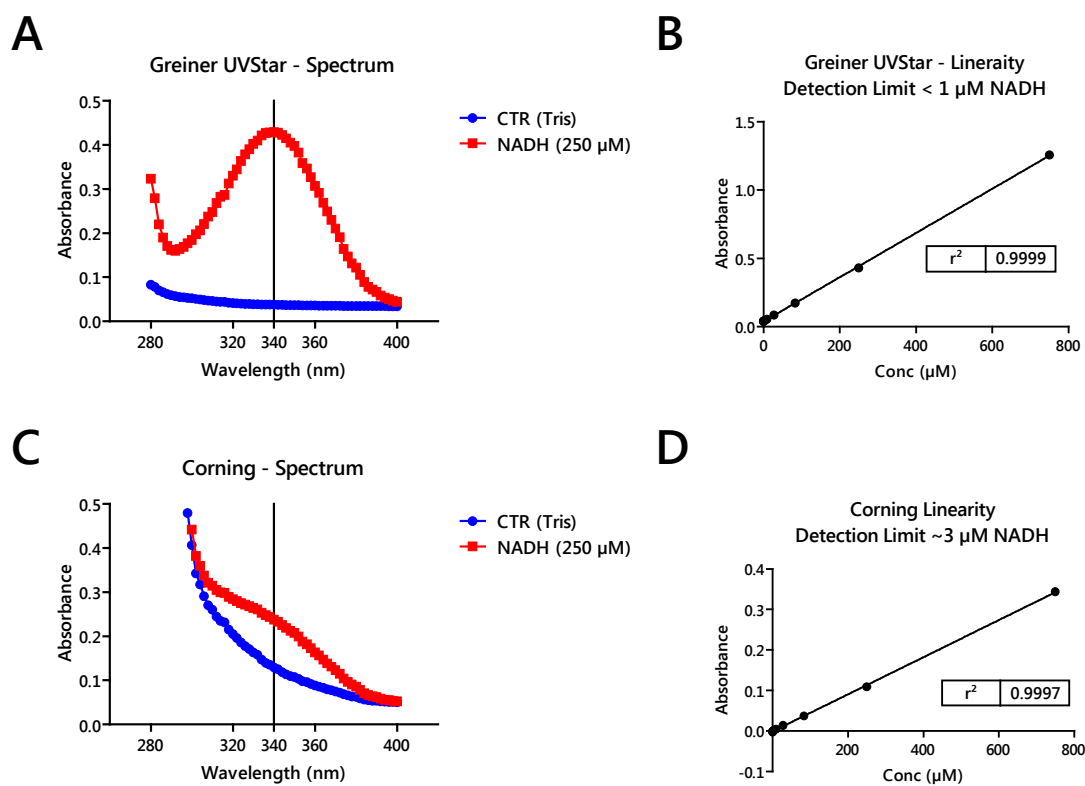


Figure 3.8: Identification of suitable microplates. UV-Vis spectra of 250  $\mu\text{M}$  NADH in 100 mM Tris buffer or buffer alone in different 96-well plates are shown. While commonly used lab ware was not sufficiently UV translucent (C, D), Greiner UVstar plates (A, B) showed a good signal-to-noise ratio and high linearity.

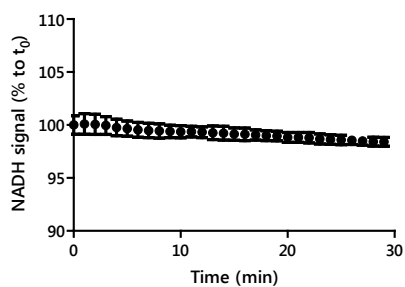


Figure 3.9: Stability of NADH in 100 mM Tris buffer was determined by monitoring the signal intensity at 340 nm over 30 minutes at 37°C. Time  $t_0$  refers to start of measurement.

Table 3.1: CHKA2 enzyme kinetics assay components at a total volume of 50  $\mu$ L.

	Stock Concentration	Volume per reaction ( $\mu$ L)	Final Concentration
Tris pH 7.5	1 M	5	100 mM
KCl	1 M	5	100 mM
MgCl <sub>2</sub>	100 mM	5	10 mM
PEP	5 mM	5	500 $\mu$ M
Pyruvate kinase	900-1400 U/mL	5	4 units
Lactate dehydrogenase	600-1000 U/mL	5	5 units
ATP	4.5 mM	5	450 $\mu$ M
Choline chloride	965.02 $\mu$ M*	5	96.5 $\mu$ M*
NADH	2.5 mM	5	250 $\mu$ M
$\Delta$ 49N CHKA	1 $\mu$ g/ $\mu$ L	5	Variable
Inhibitor	40 mM	5	Variable
<b>Total</b>		<b>50 <math>\mu</math>L</b>	

\* 96.5  $\mu$ M choline chloride for a final concentration of 72  $\mu$ M choline ( $=K_M$ ).

minutes (Figure 3.10). An enzyme concentration of 20 ng CHKA per reaction showed favourable velocity of enzymatic reaction and good linearity in the first 15 minutes.

The assay was then employed for screening. MN58B proved too difficult to synthesise as a reference compound and due to the lack of a literature compound, one of the first synthesised inhibitors, compound **8**) was used. The reaction was carried out in presence of 9 different concentrations of inhibitor (4.5 nM–300  $\mu$ M) and compared to untreated controls (Figure 3.11). The reaction was highly linear within the first 10 minutes of the reaction, during which, sufficient amounts of NADH were available. After 10 minutes, the raw data curves started shifting to the right (data not shown for clarity), indicating substrate depletion. The IC<sub>50</sub> was determined in the phase, where untreated controls show linearity of the NADH signal and where < 20% substrate are depleted [175].

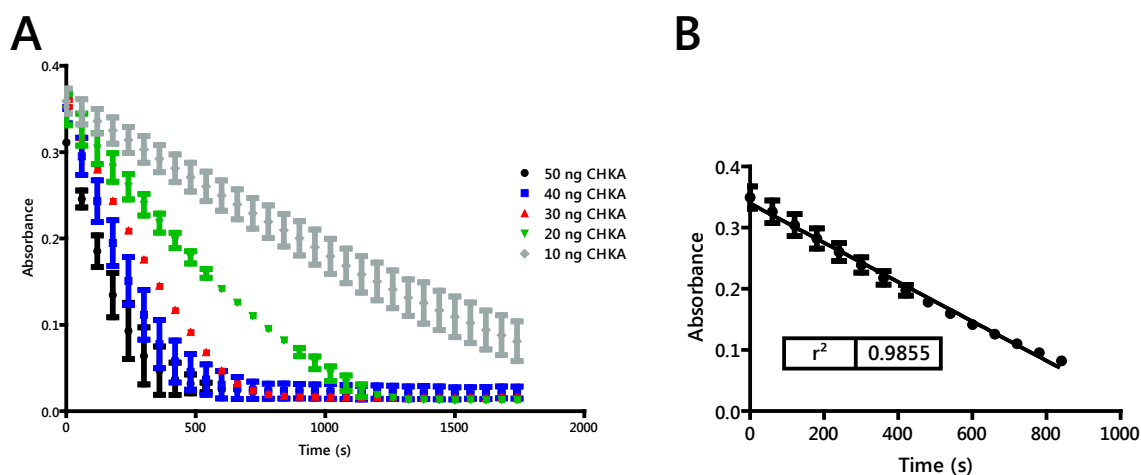


Figure 3.10: A, Reaction progress curves of different CHKA quantities. B, Linearity of NADH depletion in the first 15 minutes. Mean of  $n = 3 \pm$  SD.



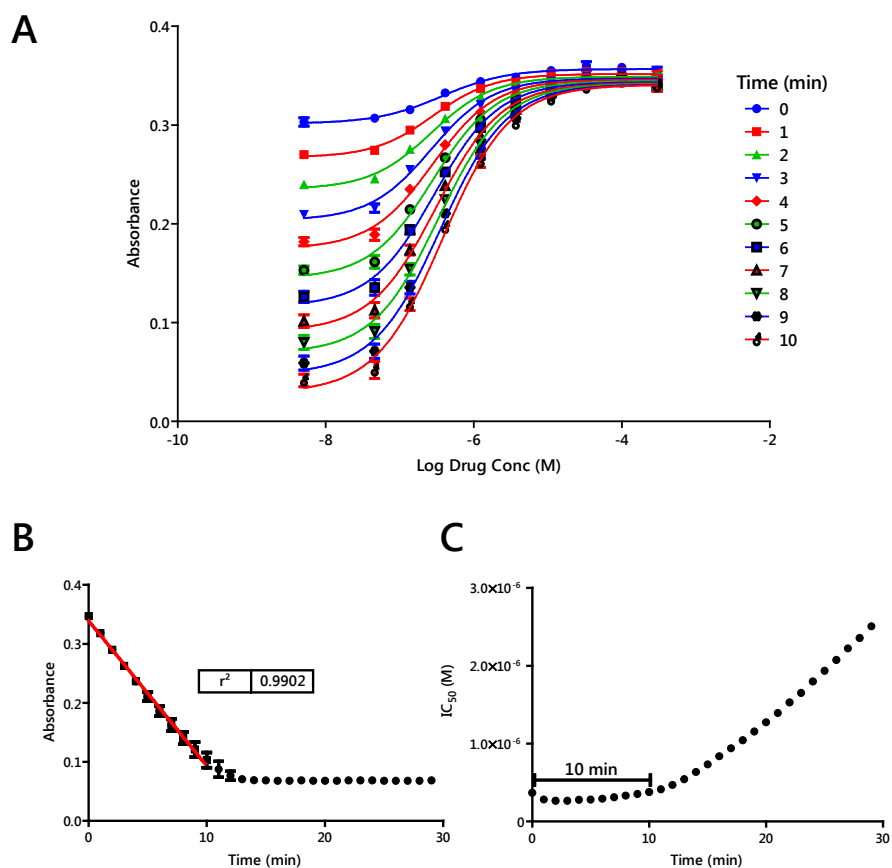


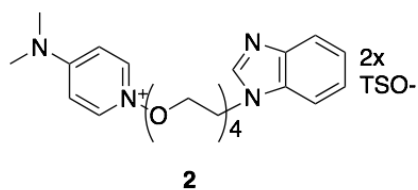
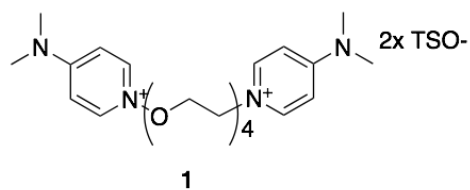
Figure 3.11: Determination of  $IC_{50}$ . A, Inhibition curves of compound **8** over time (in min) showing an increase of signal-to-noise ratio, as NADH is depleted during this phase. B, Absorbance of NADH in controls over time showed linearity in the first 10 minutes. This is the phase before all NADH has been used up in non-treated controls. C, Time-dependence of  $IC_{50}$  of **8**. In the first 10 minutes,  $IC_{50}$  was stable, which was followed by an increase (right shift of curves) due to substrate depletion. Mean of  $n = 3 \pm$  SD.

### 3.3 Evaluation of choline kinase inhibitors

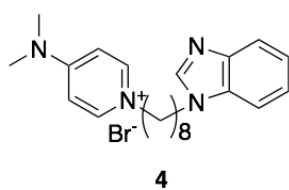
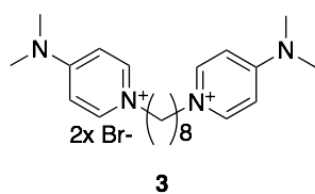
#### 3.3.1 CHKA enzymatic inhibition

A summary of all tested structures is shown in Figure 3.12. Elongation of the alkyl chain in the symmetrical *bis*-DMAP compounds successively increased potency against recombinant CHKA2 (Table 3.2 and Figure 3.13A–B). The C8 linker compound **3** had an  $IC_{50}$  of 2.7  $\mu$ M, which decreased to 150 nM when the two pharmacophores were separated by an additional 6 carbons. As expected, these compounds were found to be competitive with choline, but not with ATP, as exemplified by Lineweaver-Burk plots of **8** (Figure 3.14A and B), where the lines intersect at the ordinate when choline concentrations are varied and at the abscissa when ATP concentration are altered.

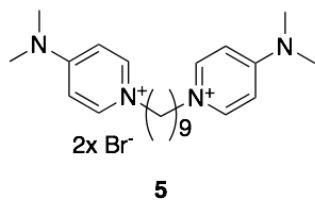
## 1. PEGylated Compounds



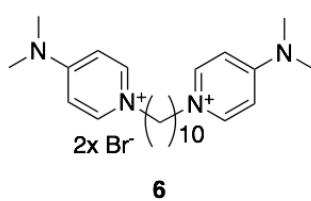
## 2. C8 Linker



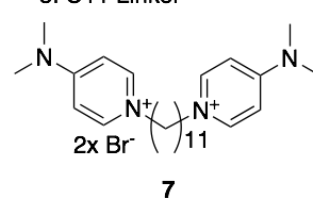
## 3. C9 Linker



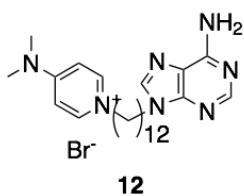
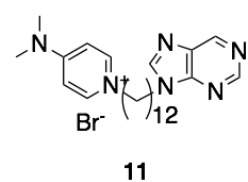
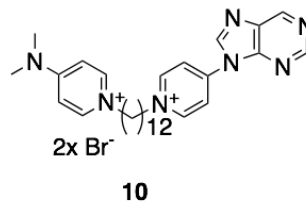
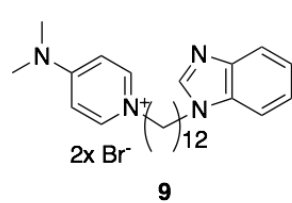
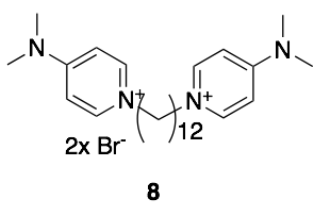
## 4. C10 Linker



## 5. C11 Linker



## 6. C12 Linker



## 7. C14 Linker

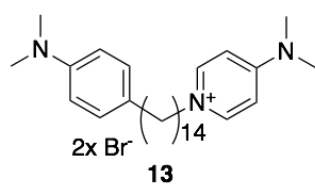


Figure 3.12: Structures of all tested compounds.

Table 3.2: Inhibitory activity against recombinant  $\Delta$ 49N CHKA2 ( $IC_{50}$ ) or human HCT116 and A549 cancer cell lines ( $GI_{50}$ ).

Compound	Linker	$\Delta$ 49N CHKA2		HCT116		A549	
		$IC_{50}$ ( $\mu$ M)	SD	$GI_{50}$ ( $\mu$ M)	SD	$GI_{50}$ ( $\mu$ M)	SD
1	PEG	n/d		> 1 mM		n/d	
2	PEG	n/d		> 1 mM		n/d	
3	C8	2.7	0.6	2.5	0.3	3.3	2
5	C9	1.3	0.1	2.6	0.5	4.0	0.3
6	C10	0.67	0.08	2.8	0.2	4.2	0.6
7	C11	0.29	0.02	2.0	0.05	1.6	0.3
8	C12	0.27	0.06	0.64	0.05	0.38	0.04
9	C12	5.1	1	0.69	0.03	1.3	0.5
10	C12	0.34	0.009	1.1	0.05	0.75	0.07
12	C12	0.80	0.08	4.1	1	5.3	3
13	C14	0.15	0.04	0.29	0.01	0.33	0.009

In the series of nonsymmetrical inhibitors (**9–12**), substitution of one DMAP resulted in loss of activity, although this was less severe when charges were retained on both pharmacophores, as exemplified by compound **10**. Compound **11** was found to be unstable and therefore not investigated. While the benzimidazole derivative **9** had low activity, introduction of an adenine (**12**) was associated with a significant increase in inhibitory activity ( $IC_{50} = 803$  nM). As expected, **12** displayed mixed inhibition, as shown by Lineweaver-Burk plots, where the lines intersect at the second quadrant above the x-axis (Figure 3.14C and D).

### 3.3.2 Molecular Modelling

Molecular modelling was employed to further characterise possible binding modes. The model was validated by docking HC-3 into the empty pocket, which superimposed with the co-crystallised structure (Figure 3.15A–B). In addition, the estimated free energy of binding (MM-GBSA) highly correlated with the experimental  $IC_{50}$  values of *bis*-DMAP compounds (Figure 3.15C).

When the *bis*-DMAP compounds **3**, **5–8** and **13** were docked, none of these interacted with the ATP cassette in their most stable poses and instead had a binding mode resembling the co-crystallised inhibitor HC-3. The inner cationic DMAP interacted with the positively charged Asp306 in the choline pocket while the carbon linker interacted with the hydrophobic side chains of Tyr333, Trp423, Trp420, Tyr354 and Tyr437 (Figure 3.16). The second DMAP was more solvent exposed and interacted predominately with the hydrophobic residues at the rim of the pocket. Altogether the biochemical and modelling data suggest that **8** and most likely also the other *bis*-DMAP compounds are choline-competitive inhibitors and solely interact with the choline active site.

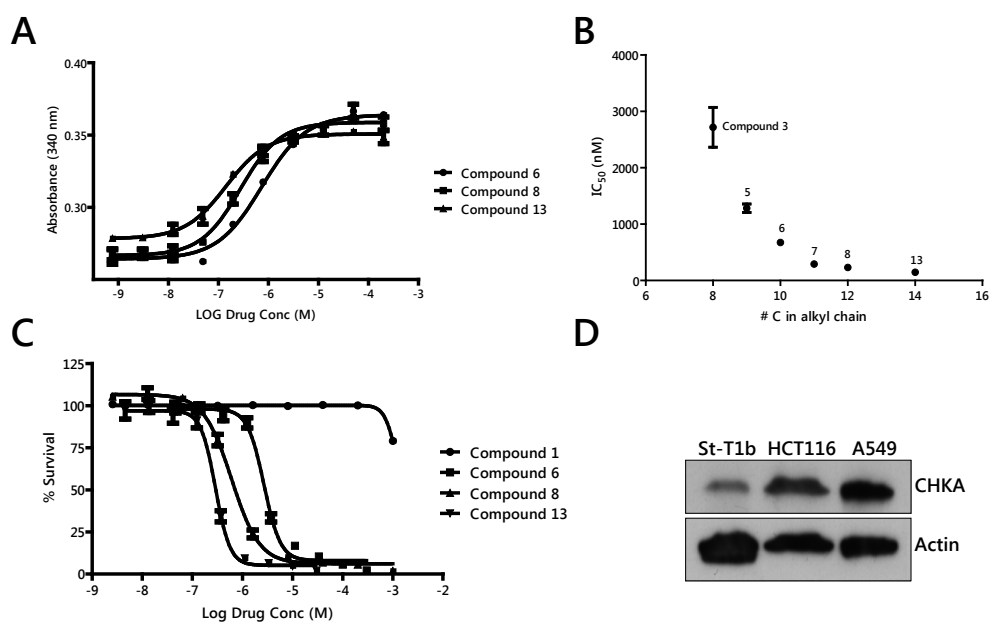


Figure 3.13: Inhibition of  $\Delta 49\text{N}$  CHKA2 and growth of human HCT116 cancer cell lines. A,  $\text{IC}_{50}$  was determined using a pyruvate kinase/lactate dehydrogenase-coupled assay that measures NADH depletion at 340 nm. High NADH levels reflect complete enzymatic inhibition. B, Structure activity relationship between linker length and  $\text{IC}_{50}$  of symmetrical compounds. C,  $\text{GI}_{50}$  in HCT116 cells was determined by sulforhodamine-B assay. For A and C, half-maximal inhibitory concentrations were determined by fitting of a sigmoidal curve with variable slope in GraphPad Prism version 5.01. D, confirmation of high CHKA protein expression by western blot in HCT116 and A549 cells in comparison with St-T1b cells.

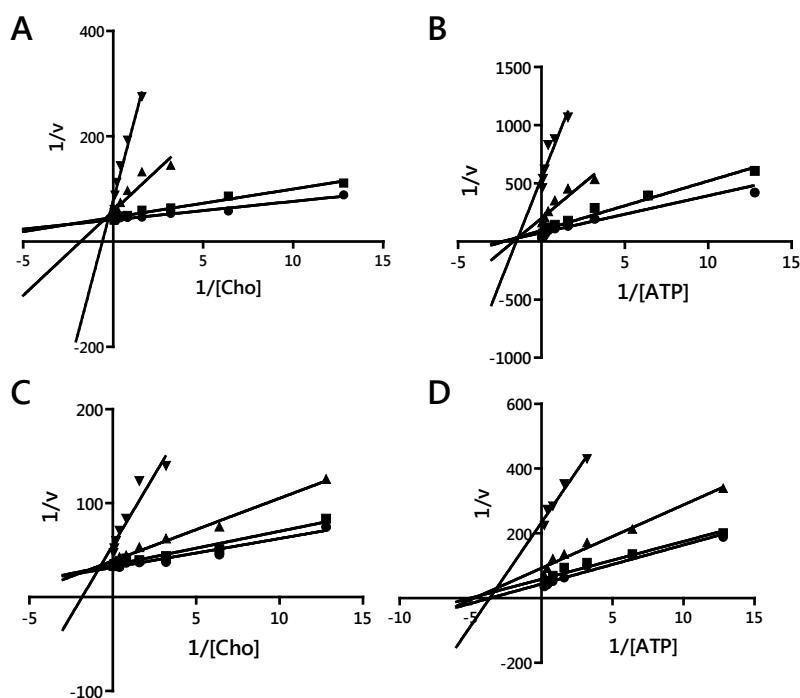


Figure 3.14: Lineweaver-Burk plots of compounds **8** (A and B) and **12** (C and D) against  $\Delta 49\text{N}$  CHKA2. Reaction kinetics were measured without inhibitor ( $\bullet$ ) or in presence of 0.1 ( $\blacksquare$ ), 1 ( $\blacktriangle$ ) or 10  $\mu\text{M}$  ( $\blacktriangledown$ ) **8** or **12**. In A and C, choline concentrations were varied and ATP kept constant at  $K_M$ , while in B and D choline was kept constant at  $K_M$  and ATP concentrations altered.

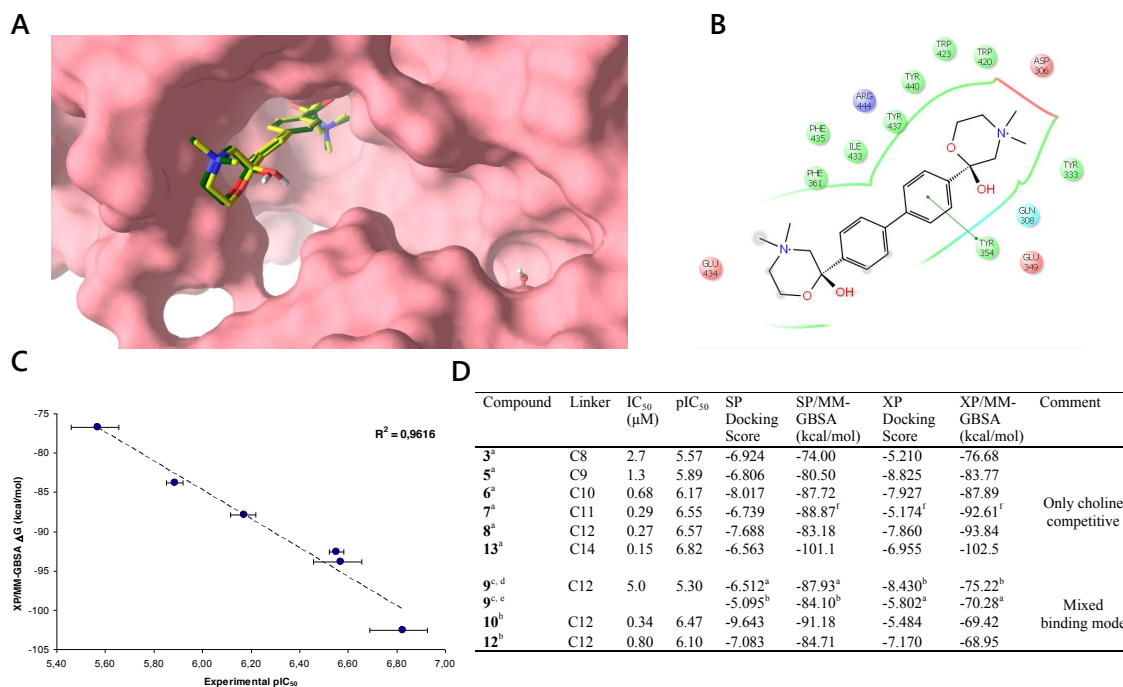


Figure 3.15: Validation of molecular model. A, The applied docking algorithm could successfully dock HC-3. The docked molecule (green) superimposes with the co-crystallised ligand (yellow). B, Close-contact interactions of HC-3 with CHKA2. C, Correlation for compound **3**, **5**, **6**, **7**, **8** and **13** between experimental pIC<sub>50</sub> against Δ49N CHKA2 and estimated free energies of binding (kcal/mol) obtained by Glide XP docking and MM-GBSA scoring. D, Different scoring functions applied to SP and XP docked poses. <sup>a</sup>Docks simultaneously in the choline site and the pocket rim in the highest ranked pose <sup>b</sup>Docks simultaneously in the choline site and in the ATP site in the highest ranked pose. <sup>c</sup>The calculated pK<sub>a</sub> of the benzimidazole moiety is 5.62. <sup>d</sup>Neutral. <sup>e</sup>Protonated. <sup>f</sup>XP docking resulted in an unrealistic pose, instead the XP refined SP docked pose was used. Molecular modelling was carried out by Dr. Ola Åberg.

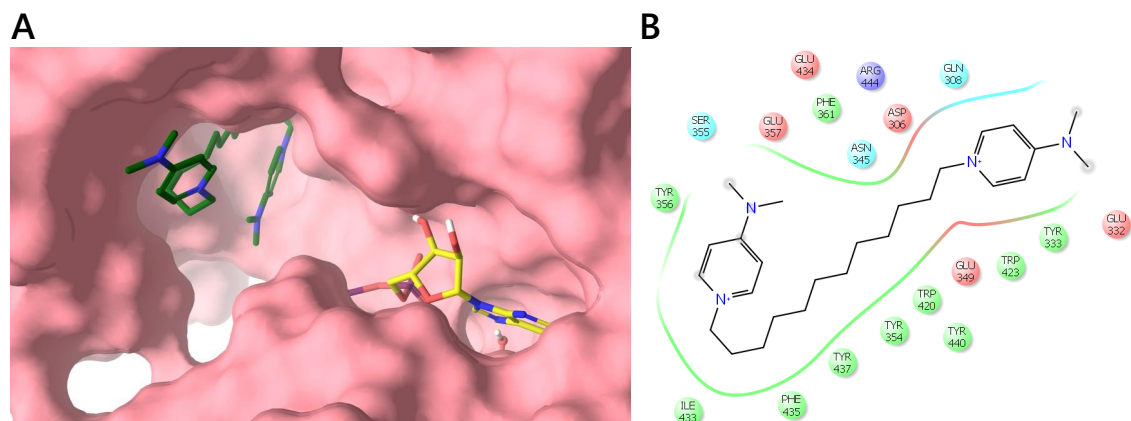


Figure 3.16: Proposed binding modes of *bis*-DMAP compounds. A, **8** (green) solely interacted with the choline pocket in its most stable pose. ADP (yellow) is shown as reference. B, Interactions of **8** in its most stable pose with the choline pocket and rim of CHKA2. Molecular modelling was carried out by Dr. Ola Åberg.

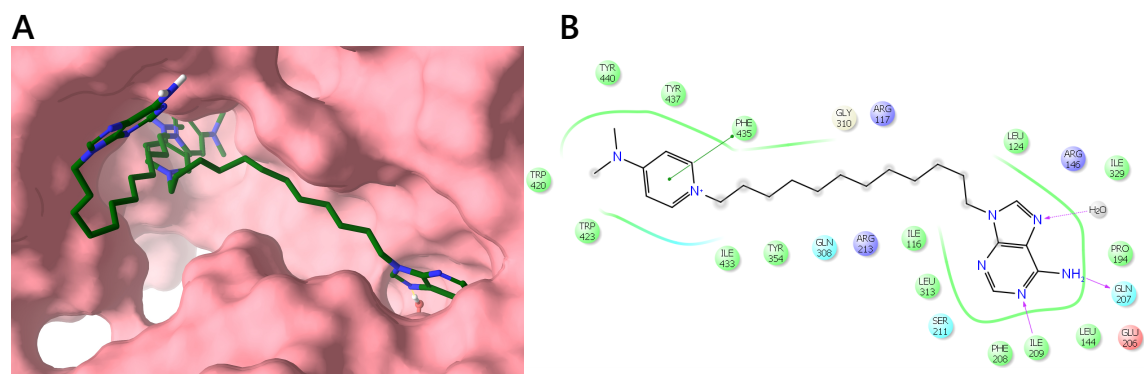


Figure 3.17: Proposed binding modes of nonsymmetrical inhibitors. A, **12** had two stable conformations, where DMAP was always interacting with the deep end of the choline pocket. The adenine moiety could either interact with the solvent exposed rim or the ATP cassette. B, Interactions of **12** in its most stable pose with the ATP cassette and the choline pocket. Molecular Modelling was carried out by Dr. Ola Åberg.

Compounds **9-12** on the other hand were designed with an adenine mimic to interact specifically with the ATP pocket. For example, when docked in the absence of ADP, **12** showed two predominant conformations (Figure 3.17). In its most stable pose, it simultaneously interacted with the ATP and choline binding sites. The adenine moiety of **12** almost completely superimposed with the co-crystallised adenine moiety of ADP and interacted with Glu206 via a water bridge in addition to hydrogen bonding to Ile209 and Gln207. Alternatively, in a lower ranked binding mode the adenine moiety of **12** pointed towards the solvent and hydrogen bonded to the backbone carbonyl of Ser355 at the rim of the enzyme without any interaction with the ATP cassette (Figure 3.17). Compound **12** can interact with both cavities, however, when docked in the presence of ATP, resembling physiological ATP concentrations, the adenine moiety is forced out of the ATP cassette and instead binds to the pocket rim in a fashion resembling HC-3 and compounds **3**, **5-8** and **13**. Therefore, docking studies together with the kinetic experimental data suggested a mixed type of binding.

### 3.3.3 Fragment-based screen of ATP mimics

It was then attempted to increase the potency of the ATP-mimicking component through a fragment-based approach. A small library of ATP mimics was designed by Dr. Andrew Kalusa, Imperial College London (Figure 3.18). Such an approach required probing of the fragments at relatively high concentrations, as only minor interaction with the enzyme could be anticipated. The CHKA activity assay was designed to test each fragment at

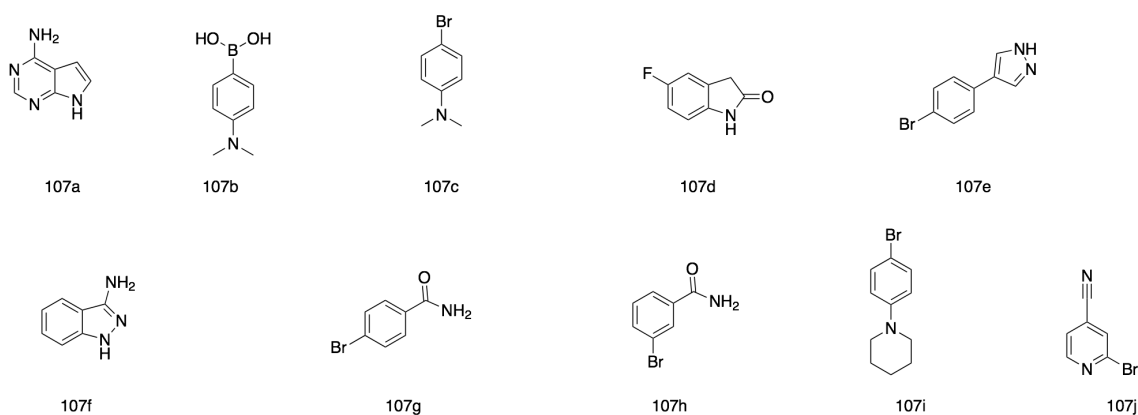


Figure 3.18: ATP mimicking fragments included in screen against CHKA2.

two concentrations (10 and 30  $\mu\text{M}$ ) in hope to detect dose-dependence and with two concentrations of ATP [450  $\mu\text{M}$  ( $=K_M$ ) and 1.3 mM ( $=3 \times K_M$ )], as decreased inhibitory properties at high ATP concentrations could indicate ATP competitiveness. None of the investigated compounds could efficiently inhibit CHKA at the tested concentrations (Table 3.3) and therefore this approach was not further pursued.

### 3.3.4 Antiproliferative activity

Anti CHKA activity of symmetrical and nonsymmetrical compounds translated well into antiproliferative activity against HCT116 colorectal adenocarcinoma and A549 lung cancer cell lines, which express CHKA at high levels (Table 3.2 and Figure 3.13C–D). In accordance with the cell-free assay, linker elongation in the symmetrical compounds strongly increased cellular efficacy and resulted in compounds with submicromolar growth inhibitory

Table 3.3: Inhibitory activity of ATP mimicking fragments against CHKA2. Mean of  $n = 3$ .

Compound	Fragment [10 $\mu\text{M}$ ]		Fragment [30 $\mu\text{M}$ ]		Fragment [10 $\mu\text{M}$ ]		Fragment [30 $\mu\text{M}$ ]	
	ATP [450 $\mu\text{M}$ ]		ATP [450 $\mu\text{M}$ ]		ATP [1.35 mM]		ATP [1.35 mM]	
	%inhibition		%inhibition		%inhibition		%inhibition	
	Mean	SD	Mean	SD	Mean	SD	Mean	SD
DMSO CTR	0.00	0.00	0.00	0.00	0.00	0.00	0.00	0.00
107A	6.94	11.72	3.29	7.28	5.36	4.04	4.67	0.91
107B	-2.68	14.30	1.19	10.93	6.28	6.20	2.21	7.35
107C	3.06	11.48	6.81	7.26	9.54	5.28	13.78	9.77
107D	-9.28	5.93	2.35	2.38	7.05	5.01	-2.44	4.36
107E	-4.68	8.67	5.52	9.43	3.91	1.37	3.38	3.90
107F	-13.16	11.58	-0.17	3.38	2.16	13.77	0.09	9.60
107G	-11.58	11.98	0.70	7.50	-0.63	1.95	2.70	5.62
107H	-8.31	14.38	1.71	5.25	5.93	4.91	1.93	2.60
107I	-7.34	9.78	4.02	10.71	0.46	6.99	1.20	5.94
107J	-13.73	11.86	3.63	13.14	1.88	12.39	3.89	3.63
107K	-5.23	9.98	6.32	5.66	3.14	3.95	-2.15	3.89

concentrations. The nonsymmetrical compound **9** showed higher cellular than enzymatic activity, suggesting that growth inhibition is mediated by effect on targets other than CHKA. The PEGylated compounds **1** and **2** showed no activity up to a concentration of 1 mM. The growth inhibitory properties were assessed in a larger panel of cancer cell lines (Table 3.4). Compounds **8** and **13** were most effective with a median GI<sub>50</sub> of 620 and 330 nM, respectively.

### 3.3.5 Inhibition of CHK in HCT116 cells

Next, the ability of the several compounds to inhibit the CHK reaction in whole cells was assessed. To this end, HCT116 cells were incubated with [<sup>3</sup>H]choline in the presence of varying concentrations of inhibitors and [<sup>3</sup>H]PCho formation was measured. [<sup>3</sup>H]PCho was efficiently separated from [<sup>3</sup>H]choline using a modified Bligh and Dyer extraction method (Figure 3.19), REF. [164]. The fundamental principle of this assay is, that choline with one positive charge can be scavenged by negatively charged tetraphenylborate (TPB, see Figure 3.19 for structure). The TPB-bound choline is lipophilic and can be isolated by phase separation. In contrast, the zwitterionic PCho has a net charge of zero and therefore

Table 3.4: Growth inhibition (GI<sub>50</sub> in μM) of indicated compounds in various cancer cell lines. Mean of  $n = 3$ ; n/d, not determined.

1. PEGylated			2. C8 Linker				4			
Compound	<b>1</b>	SD	<b>2</b>	SD	<b>3</b>	SD	GI <sub>50</sub> (μM)	SD	GI <sub>50</sub> (μM)	SD
cell line	GI <sub>50</sub> (μM)		GI <sub>50</sub> (μM)		GI <sub>50</sub> (μM)					
HCT116	> 1mM		> 1mM		2.5	0.28	40	12		
MCF7	n/d		n/d		4.6	1.3	25	6.9		
A431	n/d		n/d		2.9	0.76	48	14		
A549	n/d		n/d		3.3	2.3	38	6.1		
A2780	n/d		n/d		3.3	0.64	15	4.7		
Ishikawa	n/d		n/d		3.2	0.16	39	4.5		
median					3.2		38			

3. C9 Linker			4. C10 Linker		5. C11 Linker					
Compound	<b>5</b>	SD	<b>6</b>	SD	<b>7</b>	SD	GI <sub>50</sub> (μM)	SD	GI <sub>50</sub> (μM)	SD
cell line	GI <sub>50</sub> (μM)		GI <sub>50</sub> (μM)		GI <sub>50</sub> (μM)					
HCT116	2.6	0.5	2.8	0.2	2.0	0.1				
A2780	5.9	0.4	4.2	0.6	1.6	0.4				
A549	4.0	0.3	4.2	0.6	1.6	0.3				
median	4.0		4.2		1.6					

6. C12 Linker			9		10		12		7. C14 Linker	
Compound	<b>8</b>	SD	<b>9</b>	SD	<b>10</b>	SD	<b>12</b>	SD	<b>13</b>	SD
cell line	GI <sub>50</sub> (μM)		GI <sub>50</sub> (μM)		GI <sub>50</sub> (μM)		GI <sub>50</sub> (μM)		GI <sub>50</sub> (μM)	
HCT116	0.64	0.052	0.69	0.030	1.1	0.046	4.1	1.3	0.29	0.01
MCF7	1.6	0.60	0.71	0.20	2.4	1.1	3.7	2.5	n/d	
A431	2.7	0.46	1.1	0.40	2.1	0.54	7.5	2.7	n/d	
A549	0.38	0.035	1.3	0.47	0.75	0.074	5.3	2.8	0.33	0.01
A2780	0.54	0.11	0.60	0.030	0.86	0.54	1.6	0.11	0.33	0.05
Ishikawa	0.59	0.040	2.9	0.65	1.4	0.13	5.0	0.29	n/d	
median	0.62		0.88		1.3		4.6		0.33	



Table 3.5: Inhibition of [ $^3\text{H}$ ]PCho formation in HCT116 cells.

Compound	EC <sub>50</sub> ( $\mu\text{M}$ )	SD
8	0.67	0.28
9	5.2	1.9
10	0.93	0.34
12	2.5	1.5
13	0.52	0.15

does not interact with TPB. The efficiency of the [ $^3\text{H}$ ]choline and [ $^3\text{H}$ ]PCho extraction was tested and typically  $13.7 \pm 1.6\%$  [ $^3\text{H}$ ]choline detected in the PCho fraction, while  $1 \pm 0.6\%$  [ $^3\text{H}$ ]choline was present in the PCho fraction.

All compound efficiently inhibited the choline kinase reaction in whole cells (Table 3.5). Compounds **8** and **13** were highly effective and associated with an EC<sub>50</sub> of  $0.67 \pm 0.3 \mu\text{M}$  and  $0.52 \pm 0.2 \mu\text{M}$ , respectively, and inhibited [ $^3\text{H}$ ]PCho formation  $> 75\%$  at concentrations above  $6.5 \pm 4$  and  $2.4 \pm 1 \mu\text{M}$ , respectively.

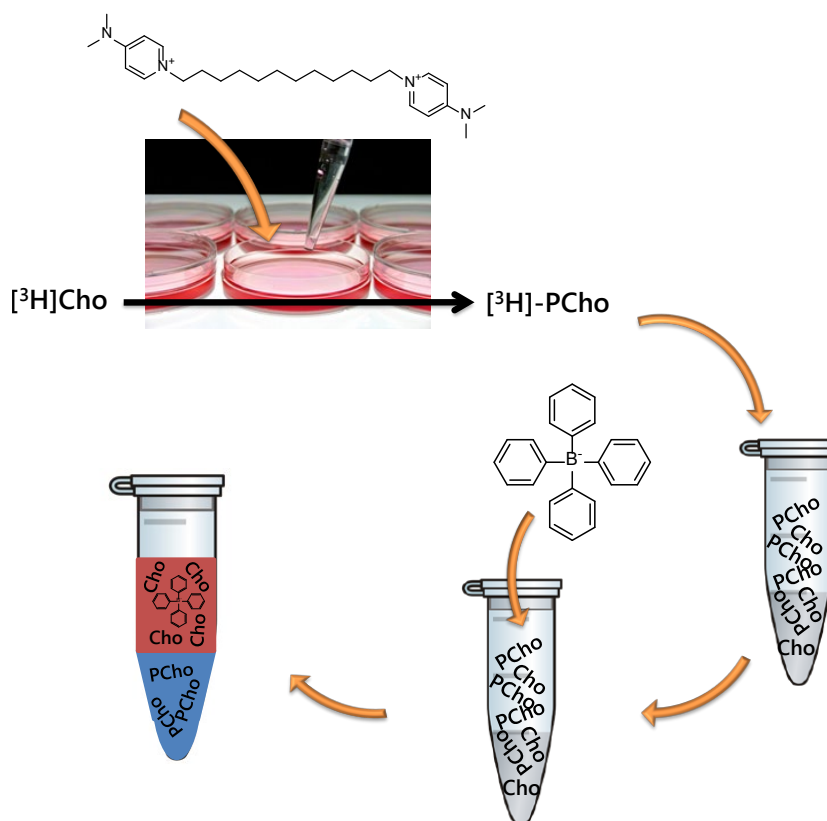


Figure 3.19: Assay principle of Bligh and Dyer extraction. The negatively charged tetrabutylborate (TPB) preferentially binds to choline (net positive charge) over PCho (net neutral) and the TPB-choline complex can be extracted by phase separation with organic solvents. PCho remains in the lower aqueous phase. Cho, choline; PCho, phosphocholine.

### 3.4 Discussion

The increased expression and activity of CHKA in many different solid tumours together with the growth-promoting role of choline metabolites make CHKA an attractive target for anticancer therapy. Previously designed inhibitors, such as MN58B, have the disadvantage of a challenging synthesis, which could be part of the reason why such inhibitors are not commercially available. The short ethyl chain between the benzyl moieties of MN58B, for example, is relatively difficult to functionalise, and therefore only gives poor yields.

Here, the evaluation of highly effective CHKA inhibitors, which are synthetically readily available is presented. The symmetrical inhibitors **8** and **13** potently inhibited CHKA, which translated well into high cellular efficacy in different cancer cell lines. Furthermore, these compounds were able to fully inhibit the CHK reaction in whole cells, which is a key requirement for further development, as CHKA inhibitors need to compete with high endogenous choline concentrations of 10–50  $\mu\text{M}$  [178]. By comparison to other compounds published in the literature and summarised in Table 1.2, the inhibitors presented here are — with the caveat of different assays used — among the most effective compounds described to date with respect to their  $\text{IC}_{50}$  and  $\text{GI}_{50}$ .

It was further aimed to develop novel scaffolds of CHKA inhibitors, which simultaneously inhibit the choline and ATP pockets. It was demonstrated through biochemical evaluation backed by computational modelling that this binding mode may exist but the inability of these compounds to elicit ATP-competitiveness at higher ATP concentrations suggests that symmetrical inhibitors may be more favourable candidates. A similar approach was since attempted by another group [150]. Although the structures of this report are related to the nonsymmetrical inhibitors presented here, these molecules were relatively inactive ( $\text{GI}_{50} > 50 \mu\text{M}$ ,  $\text{IC}_{50}$  6–10  $\mu\text{M}$ ).

With respect to the *bis*-DMAP compounds, the inhibitory activity against CHKA strongly depended on the linker length. Molecular modelling elucidated that both DMAPs interacted with negatively charged amino acids in the deep end of the pocket and the rim. Therefore sufficient space and flexibility is required to maximise the charge-charge interactions.

Different linker types were tested, however, the PEGylated compounds were unstable in solution and inactive in cell systems, which is why this approach was not further pursued. Given the time and resources of this project it was unfortunately not possible to

diversify the linkers. Based on these data, however, it appears that the charge interactions were essential for biological activity. Scaffold modifications would need to be done with careful consideration and ideally jointly with X-ray crystallography in order to maximise intermolecular interactions, while trying to minimise increases in lipophilicity. TCD-717, which is an evolution of MN58B and therefore likely to have higher affinity to CHKA, is characterised by a large molecular weight of 878 g/mol and a cLogP of 3.3, suggesting that the enhanced interaction is likely to be driven by size and lipophilicity, which therefore might not translate into potent inhibition in an *in vivo* context. Furthermore, the combination of high molecular weight and 6 aromatic ring systems make it more prone to be a substrate for drug resistance transporters.

To improve the pharmacologic properties of CHKA inhibitors, it would be desirable to reduce the overall charge of the compounds. CK37 is an uncharged CHK inhibitor and lack of charge-charge interactions at the deep end of the pocket make it relatively ineffective in cell-free assays ( $IC_{50}$  ca. 25  $\mu$ M), REF. [149]. The ATP-competitive inhibitor V-11-0711 possesses good inhibitory properties in cell-free assays ( $IC_{50}$  against CHKA 20 nM; CHKB 220 nM), which does not translate into effective growth inhibition or induction of apoptosis [148]. It remains unclear why V-11-0711 does not phenocopy the effect of CHKA knockdown, as demonstrated in the same study. It is possible that due to similarities between the ATP cassettes of CHKA with CHKB, eukaryotic protein kinases and aminoglycoside phosphotransferases [71], cross reactivity with other targets prevents biological activity. A recent report highlighted that simultaneous inhibition of CHKA and CHKB indeed prevents cells to undergo apoptosis [65].

Due to unavailability of purified CHKB, it was not possible to determine isoform selectivity for the inhibitors presented here. Although the overall differences between the CHKA and CHKB binding pockets are only subtle, it can be anticipated that the compounds presented have higher affinity towards CHKA than CHKB. The loop connecting helices  $\alpha 9$  and  $\alpha 10$  ( $L\alpha 9\alpha 10$ ) at the deep end of the hydrophobic groove is folded inwards in CHKA, allowing interaction of the quaternary amine with Glu434. In CHKB this loop is positioned away from the groove, potentially negatively affecting binding [174].

Synthesis of non-isoform selective ATP competitive inhibitors might not form the most suitable strategy to reduce the charge of these inhibitors. Alternative approaches could be to employ a pro-drug mechanism, where a charge-masking moiety is removed in the tumour, or to create compounds that imitate PCho instead of choline. Such phosphocholine-

mimetics would potentially have a neutral overall charge while retaining selectivity to the enzyme. These approaches, however, would be challenging from a chemistry perspective and have not been attempted to date.

## Chapter 4

# Use of ICL-CCIC-0019 to elucidate CHKA biology in cancer

Symmetrical *bis*-DMAP compounds emerged as most potent CHKA inhibitors from the focused library screen. Compounds **8** and **13** were most promising with IC<sub>50</sub> values of 270 and 150 nM, respectively, and GI<sub>50</sub> values of 640 and 290 nM, respectively, against HCT116 cells and 380 and 330 nM, respectively, against A549 cells. These results, paired with efficient inhibition of CHK in whole cells at physiological choline concentrations, demonstrated that these compounds were among the most potent and promising evaluated to date and warrant further characterisation. While **13** had slightly higher inhibitory properties than **8**, unforeseeable reasons led to limited availability of chemistry facilities, which prevented synthesis of larger amounts of **13**. Due to comparable qualities of both compounds, **8** was further evaluated, as sufficient quantities were already available at that point. Compound **8** was subsequently named ICL-CCIC-0019. Slight variations between data acquired in the initial screen compared to results in this chapter account to different batches used.

### 4.1 Selection of cancer cell lines

Prior to the pharmacologic evaluation of ICL-CCIC-0019, the expression of CHKA in different cancer cell lines was investigated to identify models, which are suitable to study the effects of CHKA inhibition.

#### 4.1.1 The Cancer Cell Line Encyclopaedia (CCLE)

The Cancer Cell Line Encyclopaedia comprising 1037 cell lines across a wide array of different cancer types was analysed for CHKA mRNA expression levels [179]. While cancers of the biliary tract, liver, pancreas, stomach and breast showed highest median expression, certain lung cancer samples were also characterised by elevated CHKA expression (Figure 4.1A). All 1037 analysed cell lines were then ranked from highest to lowest expression and CHKA mRNA levels of several lineages, which were commonly used in the literature to study choline metabolism, are indicated in Figure 4.1B.

DNA copy number variations were not responsible for mRNA expression profiles (Figure 4.1C), suggesting that intrinsic regulatory mechanisms drive CHKA expression rather than genetic alterations. Across all cancer cell lines derived from CCLE, no CHKA mutation could be identified, although common polymorphisms, allelic fraction less than 10% and putative neutral variants were excluded from the analysis. Data for CHKB does not exist, due to overall low expression in cancer.

For subsequent experiments, HUH-7, MDA-MB-468 and HCT116 cell lines were used. While HUH-7 and MDA-MB-468 cells represent highly CHKA expressing cell lines, HCT116 cells were employed in most assays, due to their sensitivity to ICL-CCIC-0019, as established in the initial screen, and the capacity to readily form xenografts, allowing rapid translation from *in vitro* to *in vivo*.

#### 4.1.2 Validation of HCT116 model by siRNA

The effects of transient siRNA-mediated knockdown of CHKA and CHKB were assessed in HCT116 cells. CHKA silencing resulted in reduced cell proliferation (−38%, Figure 4.2A) and increased caspase 3/7 activation (2.3-fold, Figure 4.2B) 72 hours post transfection. However, silencing of CHKB or double knockdown of CHKA and CHKB did not alter proliferation or induction of apoptosis compared to scramble transfected control. CHKA knockdown unexpectedly increased Akt phosphorylation in HCT116 cells (Figure 4.2 C), which is in contrast to reports of other cell lines [132]. Erk phosphorylation or the expression of the apoptosis-related proteins Bcl-2 and Bax were not altered. Furthermore, reduced CHKA expression increased the sub-G1 population, representing apoptotic cells (72 h post transfection; Figure 4.2D).

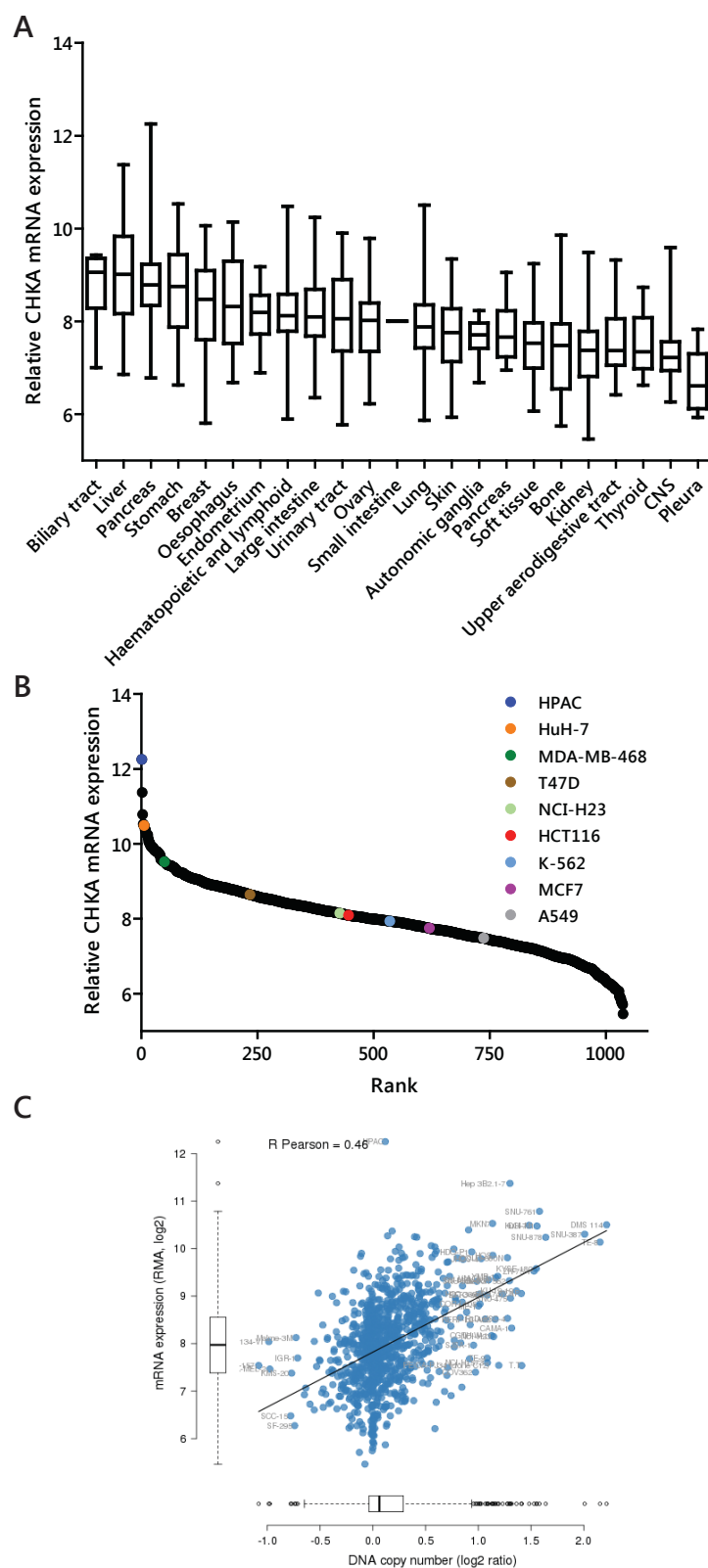


Figure 4.1: CHKA mRNA expression in different cancer cell lines. A, Box plot of quantile normalised mRNA expression in cell lines derived of indicated tumours. B, All 1037 cell lines were ranked from highest to lowest expression and selected cell lines are highlighted. C, CHKA mRNA expression was plotted against DNA copy number variation. Data derived from the Cancer Cell Line Encyclopaedia [179].

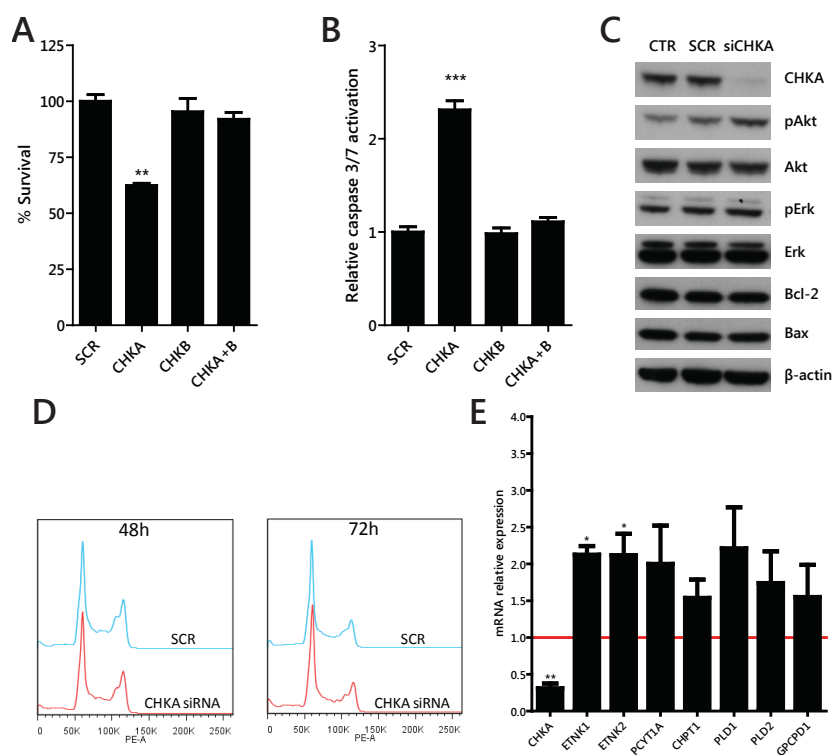


Figure 4.2: Effects of CHKA knockdown in HCT116 cells. Cells were exposed to non-targeting scramble control siRNA (SCR) or siRNAs targeting CHKA, B or both for 48 hours. A, Proliferation was measured by SRB assay and (B) apoptosis assessed by caspase 3/7 Glo assay. Mean of  $n = 3$  in quadruplicate  $\pm$  SD; \*\*  $P < 0.01$ ; \*\*\*  $P < 0.001$ . C, Lysates were analysed by western blot for expression and phosphorylation of indicated proteins. CTR, untreated control. D, After exposure to indicated siRNAs for 48 or 72 hours, cells were fixed and cell cycle analysed by flow cytometry using propidium iodide staining. E, Total mRNA was extracted from lysates collected after 48-hour incubation with CHKA siRNA and expression of indicated enzymes compared to SCR controls. ENTK, ethanolamine kinase; PCYT1A, cytidyltransferase alpha; CHPT1, choline phosphotransferase 1; PLD, phospholipase; GPCPD1, glycerophosphocholine phosphodiesterase. Mean of  $n = 3$  in duplicate  $\pm$  SD; \*  $P < 0.05$ .

Knockdown of CHKA caused compensatory elevated expression of genes involved in choline biochemistry. Ethanolamine kinase 1 and 2 expression was significantly upregulated, potentially to countervail reduced PtdCho formation by activation of the PEMT pathway. In addition, expression levels of members of the Kennedy pathway (PCYT1A and CHPT1) and the catabolic deacylation pathway (PLD1, PLD2 and GPCPD1) were also non-significantly higher compared to scramble controls.

#### 4.1.3 Establishment and evaluation of isogenic CHKA and CHKB over-expressing U2OS cells

Knockdown of CHKA evoked response of the apoptotic machinery and impaired proliferation. To cross validate these findings, a CHKA and CHKB overexpressing model



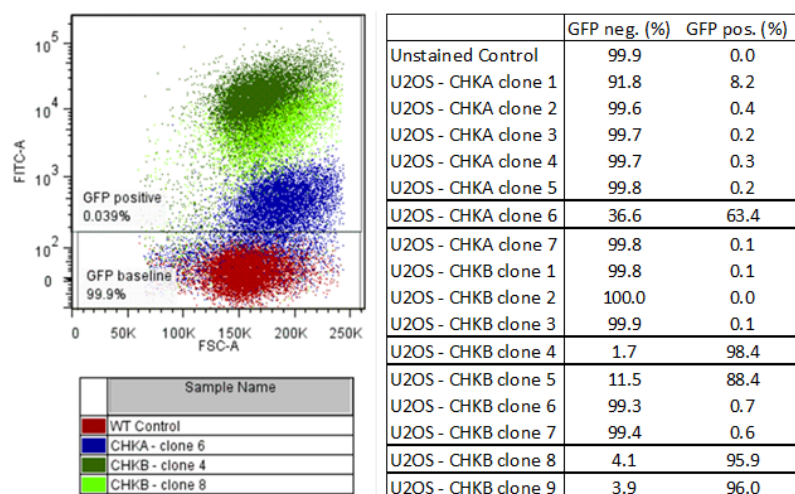


Figure 4.3: U2OS cells were transfected with GFP-tagged CHKA and CHKB and selected by G418. Individual clones were picked and green fluorescence was quantified by FACS. Data represent per cent GFP positive cells compared to wild-type.

was generated. U2OS osteosarcoma cell lines, which express CHKA at endogenously low levels, were stably transfected with GFP-tagged isoforms and individual clones selected. Clones with highest fluorescence were identified by FACS (Figure 4.3) and subsequently characterised by western blot and functional assays. While no clones with sufficient high expression of CHKA could be identified in the initial screen, further clones were evaluated, and clones CHKA16, CHKA18 and CHKB4 identified to have highest expression of the two isoforms (Figure 4.4A). CHKB expression could not be quantified due to poor quality of CHKB antibodies.

Increased CHKA expression, however, was only associated with a marginal increase in [ $^3\text{H}$ ]choline uptake (+22%) and no changes in proliferation (Figure 4.4 B, C). To explore why the vast expression of CHKA did not translate into functionally active enzyme complexes, it was tested whether the GFP tag potentially prohibited the formation of active dimers. Clone CHKA18 was analysed by native gel electrophoresis, which demonstrated that overexpressed CHKA dimerised (Figure 4.4D). However, the GFP tag possibly interfered with the enzymatic activity and therefore, this model was not further pursued.

## 4.2 ICL-CCIC-0019 has low off-target effects

The pharmacological properties of ICL-CCIC-0019 were then characterised. To assess kinase specificity, ICL-CCIC-0019 was tested against a panel of 131 human kinases (Figure 4.5, Dundee Kinase Screen, for full results table see Appendix B). The compound

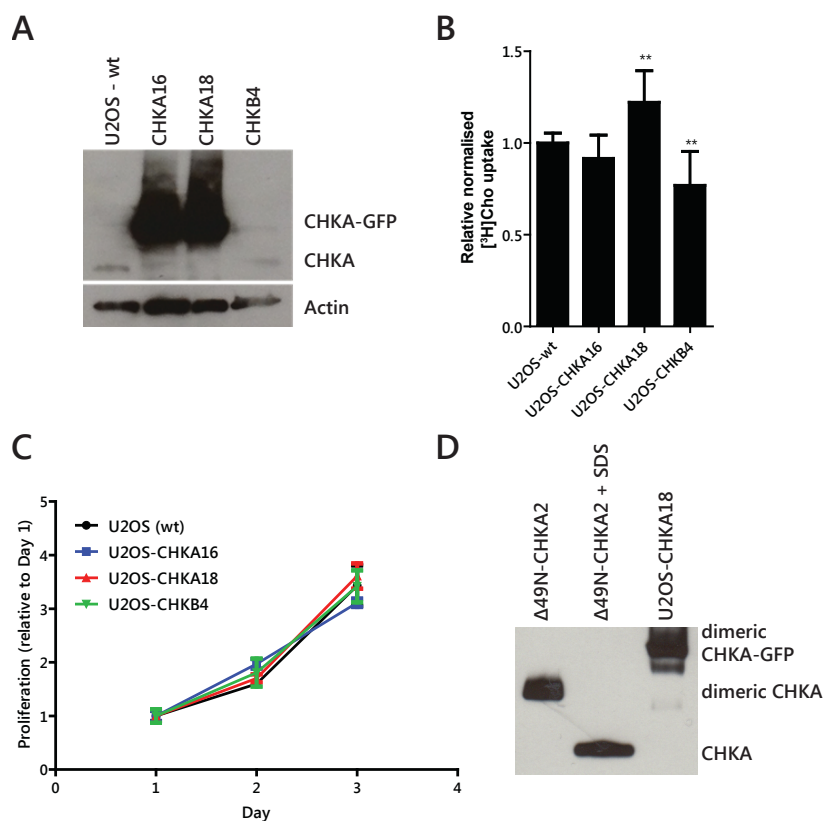


Figure 4.4: Characterisation of isogenic U2OS CHKA and CHKB model. A, Western blot against CHKA in wild-type, two CHKA-GFP overexpressing clones and one CHKB overexpressing clone. Molecular weight CHKA: 52 kDa; CHKA-GFP: 79 kDa. B,  $[^3\text{H}]$ choline uptake in U2OS model and (C) impact on proliferation as determined by SRB assay. Mean of  $n = 3$  in triplicate  $\pm$  SD; for statistical analysis all 9 data points were pooled; \*\*  $P < 0.01$ . D, Homogenates of U2OS-CHKA18 were obtained in passive lysis buffer to maintain integrity of protein complexes. Samples were analysed by native gel electrophoresis (BN-PAGE) and purified CHKA2 in its native condition or pre-treated with SDS to dissociate CHKA complexes used as controls.

showed low off-target effects as only 5 kinases were inhibited more than 20% at a concentration of 10  $\mu\text{M}$  ( $< 35\%$  in all 131 kinases). Inhibition greater than 20% was attained for insulin-like growth factor 1 (IGF-1R,  $35 \pm 7\%$  inhibition), mitogen-activated protein kinase-activated protein kinase 3 (MAPKAP-K3,  $33 \pm 6\%$ ), extracellular signal regulated kinase 8 (ERK8,  $31 \pm 4\%$ ), ribosomal S6 kinase 1 (RSK1,  $22 \pm 6\%$ ), v-erb-a erythroblastic leukemia viral oncogene homolog 4 (HER4,  $21 \pm 7\%$ ).

### 4.3 ICL-CCIC-0019 has potent antiproliferative activity

Determination of antiproliferative activity was incorporated in the screening and compound selection phase and was subsequently expanded for ICL-CCIC-0019 in the context

MKK1	MKK2	MKK6	ERK1	ERK2	JNK1	JNK2	JNK3	p38a MAPK	p38b MAPK	p38g MAPK	% Inhibition
p38d MAPK	ERK8	RSK1	RSK2	PDK1	PKBa	PKBb	SGK1	S6K1	PKA	ROCK 2	0
PRK2	PKCa	PKCy	PKCz	PKD1	STK33	MSK1	MNK1	MNK2	MAPKAP-K2	MAPKAP-K3	10
PRAK	CAMKKb	CAMK1	SmMLCK	PHK	DAPK1	CHK1	CHK2	GSK3b	CDK2	CDK9	20
PLK1	Aurora A	Aurora B	TLK1	LKB1	AMPK	MARK1	MARK2	MARK3	MARK4	BRSK1	30
BRSK2	MELK	NUAK1	SIK2	SIK3	TSSK1	CK1γ2	CK1δ	CK2	TTBK1	DYRK1A	40
DYRK2	DYRK3	NEK2a	NEK6	IKKb	IKKe	TBK1	PIM1	PIM2	PIM3	SRPK1	50
EF2K	EIF2AK3	HIPK1	HIPK2	HIPK3	CLK2	PAK2	PAK4	PAK5	PAK6	MST2	60
MST3	MST4	GCK	MINK1	MEK1	MLK1	MLK3	TESK1	TAO1	ASK1	TAK1	70
IRAK1	IRAK4	RIPK2	OSR1	TTK	MPSK1	WNK1	Src	Lck	CSK	YES1	80
ABL	BTK	JAK2	SYK	ZAP70	TIE2	BRK	EPH-A2	EPH-A4	EPH-B1	EPH-B2	90
EPH-B3	EPH-B4	FGF-R1	HER4	IGF-1R	IR	IRR	TrkA	DDR2	VEG-FR		100

Figure 4.5: Selectivity of ICL-CCIC-0019. The compound was screened against 131 kinases at a concentration of 10  $\mu$ M. Screen was carried out by MRC Kinase Screen, Dundee University.

of inhibition of cellular proliferation in normal cells. In an initial screen comprising 8 cancer and 3 normal cell lines, cancer-derived lineages were preferentially inhibited with a median  $GI_{50}$  of 1.09  $\mu$ M, while normal cells were not affected at these concentrations ( $GI_{50}$  30–120  $\mu$ M; Figure 4.6A–B).

The key role of CHKA is to ensure the availability of membrane lipid precursors, while its involvement in oncogenesis is less well understood. Intriguingly, the antiproliferative activity did not correlate with the population doubling time (Figure 4.6 C). The higher sensitivity of cancer cells to CHKA inhibition suggests that hyperactivation of CHKA could be indicative of a malignant phenotype. Due to its bolaamphiphilic character comparable to surfactants, ICL-CCIC-0019 was investigated for its potential to non-specifically lyse cells. Cell lysis, as caused by surfactants, would trigger formation of pores in the cell membrane and subsequent release of cytosolic proteins into the supernatant [187]. Activity of lactate dehydrogenase (LDH), an exclusively cytosolic protein with high stability [188], in the medium can be measured as a surrogate of cell membrane integrity. Incubation of HCT116 cells with 1–25  $\mu$ M ICL-CCIC-0019, did not elevate LDH release to the supernatant (Figure 4.6 D).

The compound was then screened against a larger panel of cancer cell lines of diverse histopathologic origin, the NCI-60 screen [189]. The median  $GI_{50}$  across all cell lines was 1.29  $\mu$ M (range 0.0389–16.2  $\mu$ M, Figure 4.7A–B). Breast and non-small lung cancer cell lines were most sensitive (median  $GI_{50}$  0.627 and 0.751  $\mu$ M, respectively, Figure 4.7C), which is line with evidence in the literature of particularly deregulated choline biochemistry in those cancers [30, 78]. Twelve cell lines were found to have a  $GI_{50}$  below 0.5  $\mu$ M, with MDA-MD-468 being most sensitive (38 nM). The least sensitive cell line, NCI/ADR-RES (16.2  $\mu$ M), an adriamycin-resistant OVCAR-8 variant, is characterised by high ex-

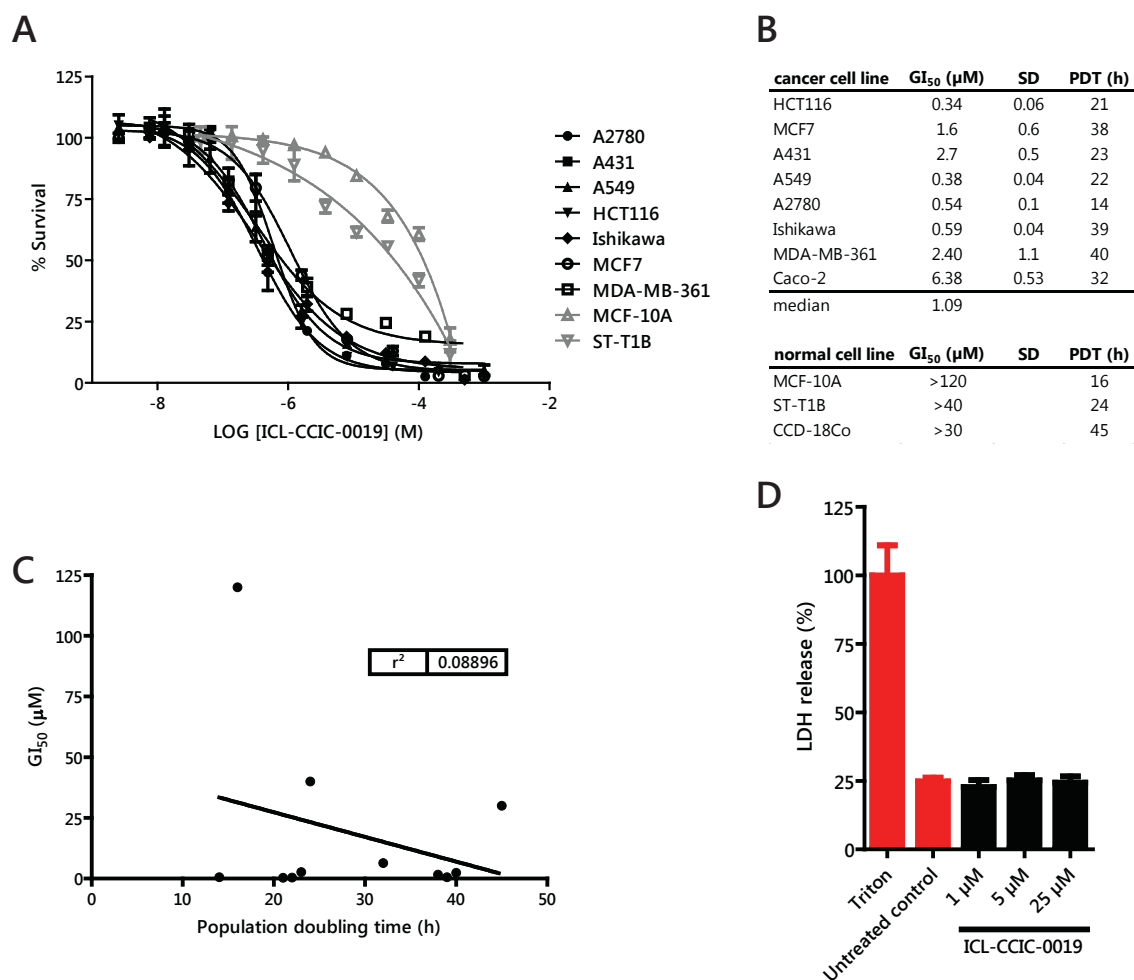


Figure 4.6: ICL-CCIC-0019 preferentially inhibits growth of cancer cells. A, Comparison of its antiproliferative activity in cancer (black) and normal cells (grey). B, GI<sub>50</sub> values in tested cell lines and population doubling times (PDT) of cell lines in hours. PDT were obtained from the literature [162, 180–186]. C, Relationship between PDT and antiproliferative activity. D, Lactate dehydrogenase (LDH) release to the supernatant was measured as a surrogate of cell membrane integrity. HCT116 cells were incubated with indicated concentrations of inhibitor for 4 hours and LDH activity measured in the supernatant. Triton X-100 was used as positive control. Mean of  $n = 3 \pm \text{SD}$ ;  $P < 0.001$  for untreated control and treated samples in comparison to triton X-100, as determined by one-way ANOVA.

pression of the multidrug resistance transporter MDR1 (also known as P-glycoprotein) [190–193], suggesting a potential role of ABC transporters in mediating resistance to bis-pyridinium CHK inhibitors. Surprisingly, antiproliferative activity did not correlate with CHKA mRNA expression (Figure 4.7D). The data of the NCI-60 screen correlated well with the GI<sub>50</sub> data generated in house and displayed in Figure 4.6B ( $r^2 = 0.87$ ; data not shown), although only three of the cell lines were part of both screens.

As previous literature indicates that CHKA could be regulated by activating mutations of kinases, such as Ras [120], the sensitivity of NCI60 cell lines was correlated to the

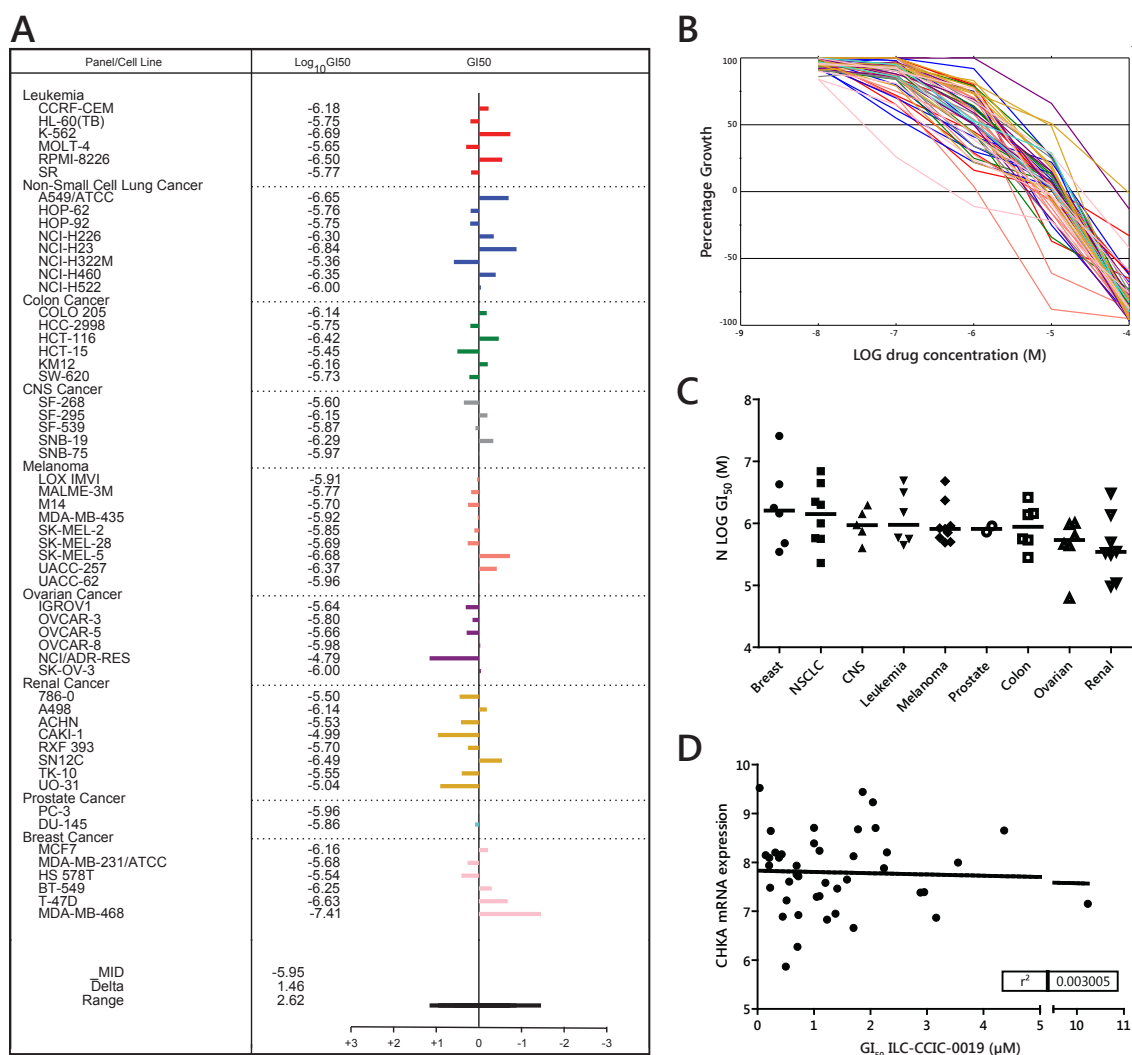


Figure 4.7: NCI-60 screen. A, Mean bar graph and GI<sub>50</sub> values of all tested cell lines. Bars depict the deviation of individual tumour cell lines from the overall mean value for all the cells tested. B, Summary graph of all growth inhibitory curves. C, Median GI<sub>50</sub> of cell lines grouped by tumour type. N LOG GI<sub>50</sub>, negative logarithmic GI<sub>50</sub> in mol/L. D, Relationship between GI<sub>50</sub> (µM) and CHKA mRNA expression, as derived from the Cancer Cell Line Encyclopaedia [179]. Growth inhibition data was obtained and analysed by NCI using ILC-CCIC-0019 at a concentration range between 10 nM and 100 µM.

presence of mutations commonly detected in cancer (Table 4.1). With the limitation that some mutations were either absent or only present in a small subset of lineages, no correlation existed between sensitivity against the inhibitor and investigated genetic alterations, when analysed by binary logistic regression ( $r^2 = 0.36$ ;  $P = 0.52$ ) using SPSS version 21.



#### 4.4 Effect of ICL-CCIC-0019 on CHKA dimerisation

As dimerisation is required to exert CHKA activity, it was tested whether as part of the mechanism of action, the inhibitor could destabilise CHKA complexes. Treated HCT116 cell lysates were analysed by native gel electrophoresis, which showed that dimer integrity was not compromised by treatment (Figure 4.8).

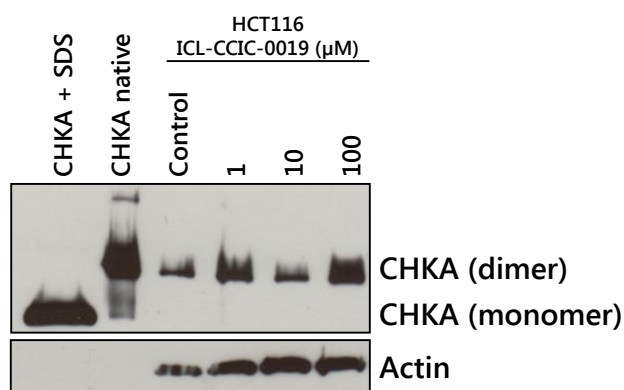


Figure 4.8: ICL-CCIC-0019 does not destabilise CHKA dimers. HCT116 cells were treated with indicated doses for 24 hours and proteins separated by BN-PAGE. Purified CHKA ( $\Delta 49\text{N}$  CHKA2; expected molecular weight: 48kDa) treated with or without SDS were used as controls. CHKA dimers were detected at ca. 100 kDa.

#### 4.5 ICL-CCIC-0019 reduces membrane lipid formation

It was then investigated, whether the inhibition of CHKA translated not only into reduced PCho (as demonstrated in Table 3.5), but also PtdCho formation. In a pulse-chase experiment, HCT116 cells were incubated with inhibitor for 1 hour and pulsed with 18.5 kBq [ $^3\text{H}$ ]choline for an additional hour in presence of drug. The media was replaced with fresh RPMI and cells incubated for additional six hours (chase period). Cells were washed and choline-containing metabolites separated.

Consistent with initial screening experiments, ICL-CCIC-0019 dose-dependently reduced the formation of PCho, while free [ $^3\text{H}$ ]choline concentrations were comparable to untreated controls (Figure 4.9). Importantly, the incorporation of [ $^3\text{H}$ ]choline into the lipid-containing fraction was reduced at similar levels to PCho, suggesting that the ICL-CCIC-0019 not only deplete the intracellular PCho pool, but also inhibits the synthesis of choline-containing lipids, like PtdCho.

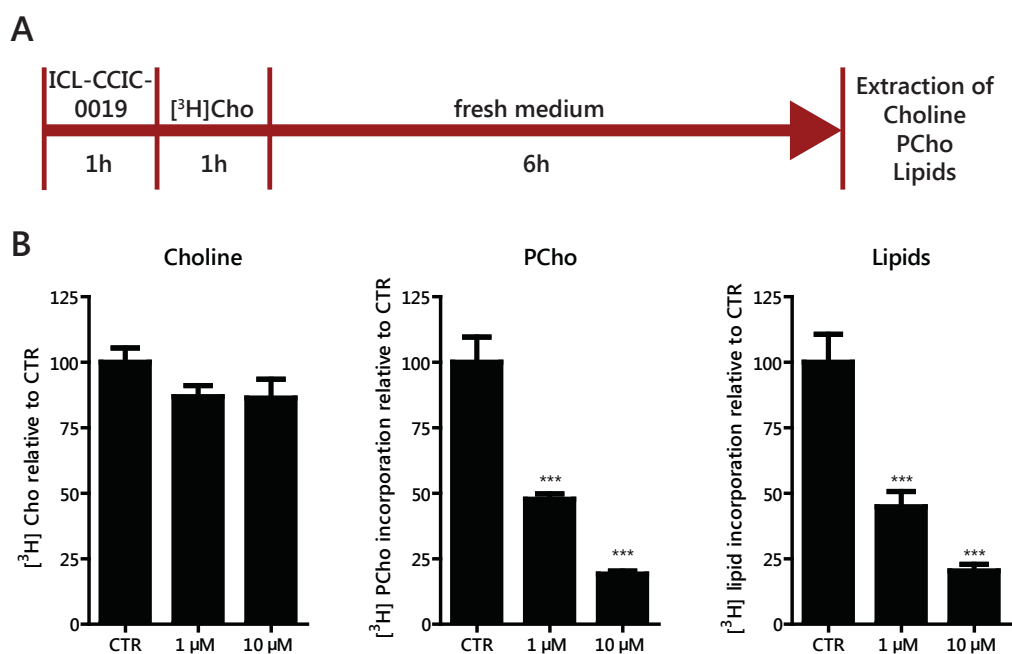


Figure 4.9: ICL-CCIC-0019 treatment decreases formation of choline-containing lipids. A, experimental outline of pulse-chase experiment. B, Quantification of choline metabolites. Cho, choline; PCho, phosphocholine. Mean of  $n = 3$  in triplicate  $\pm$  SD; \*\*\*  $P < 0.001$ .

#### 4.6 ICL-CCIC-0019 induces cell death via endoplasmic reticulum stress mechanism

Depletion of PtdCho has previously shown to induce ER stress [155]. Therefore, it was investigated whether ICL-CCIC-0019 causes expression of ER stress response markers in HCT116 cells. The compound dose- and time-dependently increased the expression of ATF4, a transcription factor for target proteins that resolve ER stress, and to lesser extent IRE1 $\alpha$  (Figure 4.10A). This increased the expression and nuclear localisation of the transcription factor CHOP (Figure 4.10B). This was independent of total protein ubiquitination and HSP70 expression. Moderate increases in HSP90 expression further contributed to the ER stress phenotype. Tunicamycin, an inhibitor of N-linked glycosylation and well-characterised inducer of ER stress, was used as positive control.

#### 4.7 ICL-CCIC-0019 arrests cells in G1 phase of cell cycle

The effects of ICL-CCIC-0019 on cell cycle progression were evaluated by flow cytometry. The inhibitor caused dose-dependent arrest of cell populations in the G1 phase of the cell cycle after 24 hours of treatment (2-fold increase at 10  $\mu$ M; Figure 4.11 A). After



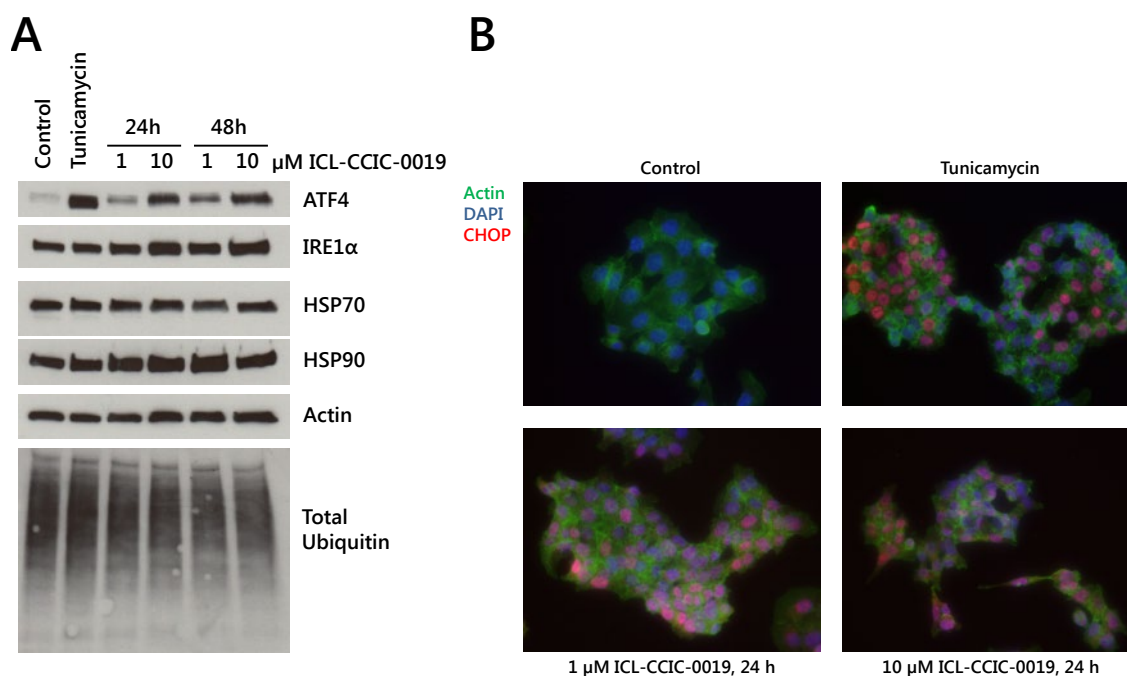


Figure 4.10: CHKA inhibition induces ER stress. A, HCT116 cells were treated with ICL-CCIC-0019 and expression of key regulators of ER stress assessed by western blot. B, HCT116 cells were treated with 1 or 10  $\mu\text{M}$  ICL-CCIC-0019 for 24 hours and stained for CHOP (red), actin (green) and nuclei with DAPI (blue). Immunofluorescent microscopy images were acquired at  $400\times$  magnification. For A and B, 2  $\mu\text{g}/\text{mL}$  tunicamycin was used for 4 hours as positive control.

48 hours, 1  $\mu\text{M}$  inhibitor also yielded in 2-fold increased G1 population, whereas 10  $\mu\text{M}$  resulted in a 3.7-fold increased sub-G1 population, representing apoptotic and dead cells (Figure 4.11B).

#### 4.8 ICL-CCIC-0019 prompts caspase 3/7 activation

Incubation with varying concentrations of ICL-CCIC-0019 for 48 hours induced activation of caspase 3/7 mediated apoptosis in HCT116, HUH-7 and MDA-MB-468 cells (Figure 4.12A). The effect was more prominent in MDA-MB-468 cells (5-fold increase at 10  $\mu\text{M}$ ) than HCT116 and HUH-7 cells (2.9 and 3.7-fold, respectively, at the same concentration). While cell viability decreased dose-dependently (Figure 4.12B), caspase 3/7 activation was not dose related.

#### 4.9 *In vitro* pharmacology

In addition to cellular potency, satisfactory pharmacological properties are crucial to achieve *in vivo* efficacy. Administration, distribution, metabolism and excretion (ADME)

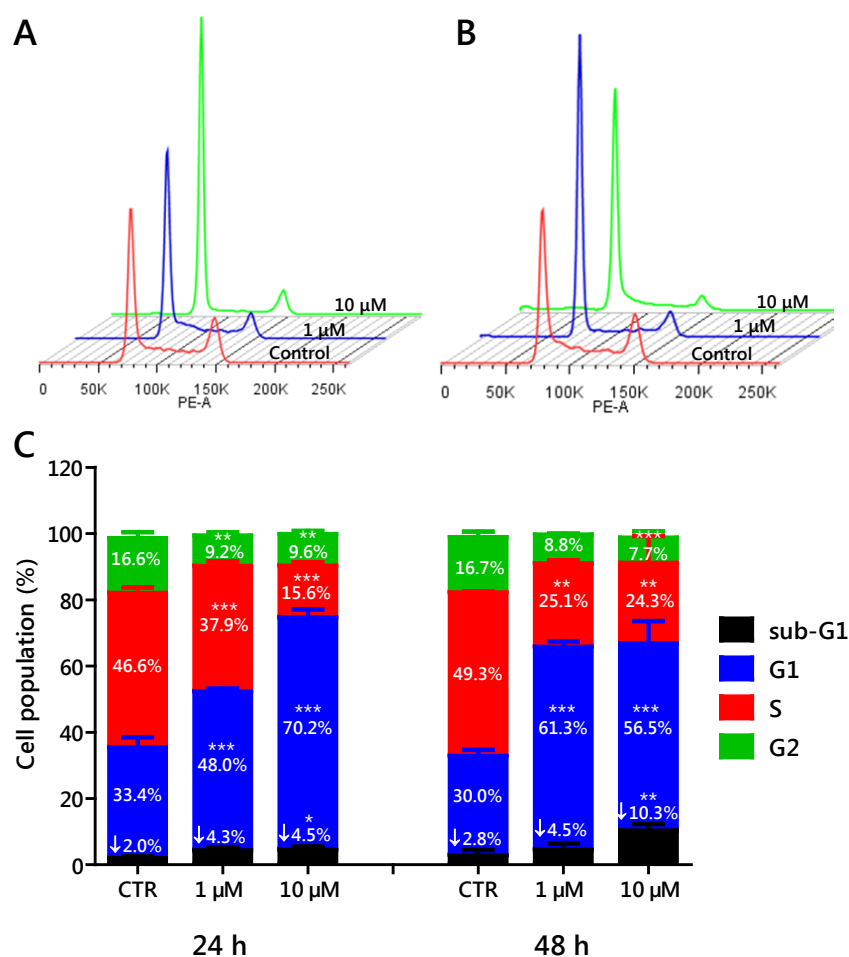


Figure 4.11: ICL-CCIC-0019 induces G1 arrest and increases sub-G1 population. HCT116 cells were incubated with inhibitor for 24 (A) or 48 (B) hours and cell cycle populations quantified by flow cytometry using propidium iodide staining. C, Quantification of populations in various states of the cell cycle, as evaluated in A and B. Mean of  $n = 3 \pm \text{SD}$ . Statistical significance compared to control: \*  $P < 0.05$ , \*\*  $P < 0.01$ , \*\*\*  $P < 0.001$ .

define the duration and extend to which a compound can be biologically active. While a compound's pharmacokinetic profile cannot be predicted *in vitro* or *in silico*, individual parameters can be estimated to avoid *in vivo* evaluation of compounds that are likely to have insufficient characteristics. Therefore, experiments to determine metabolic stability, cell permeability, multidrug resistance transporter substrate activity and plasma protein binding were conducted.

#### 4.9.1 Microsomal stability

The predominant organ of metabolism is the liver, where the majority of approved drugs are cleared. Metabolism usually occurs in at least two steps. In phase I, a compound is enzymatically modified by oxidation, reduction or hydrolysis. The cytochrome P-450

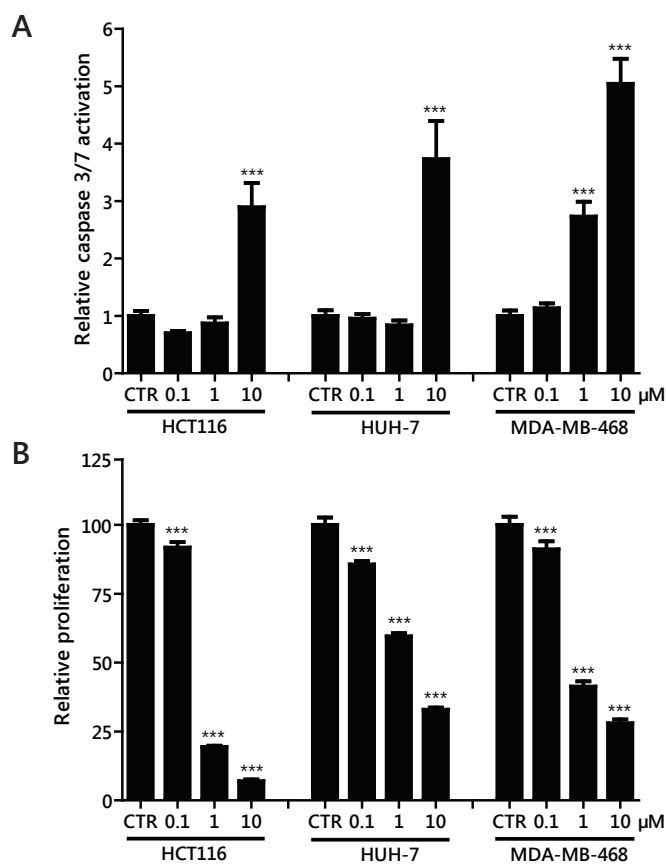


Figure 4.12: ICL-CCIC-0019 activates caspases 3 and 7 and reduces cell viability. HCT116 cells were incubated with indicated doses of ICL-CCIC-0019 for 48 hours. A, Caspase 3/7 activity was determined by caspase Glo assay and normalised to protein. B, Cell viability was measured by SRB assay. Mean of  $n=6 \pm$  SD. Statistical significance was analysed by one-way ANOVA with Bonferroni's multiple comparison test; \*\*\*  $P < 0.001$ .

system is the predominant catalyst for these reactions. In phase II, the compound is further modified by conjugation with endogenous substances, such as glucuronic acid, amino acids, glutathione, acetate or sulphate.

ICL-CCIC-0019 was highly stable in human microsomes and S9 fractions. In the respective mouse preparations, 40% and 70% parent compound were detected at the end of the experiment (Figure 4.13A). The metabolic stability of verapamil was comparable to values reported in the literature [195].

#### 4.9.2 Cell permeability and ABC transporter substrate specificity

The ability of a compound to permeate cell membranes is important for oral absorption and transport into tissues and cells. This was assessed in a transwell system, where Caco-2 colon adenocarcinoma cell lines form a tight monolayer that separates two compartments with media. Caco-2 cells resemble the orientation of the gut lining, with an apical (A) and

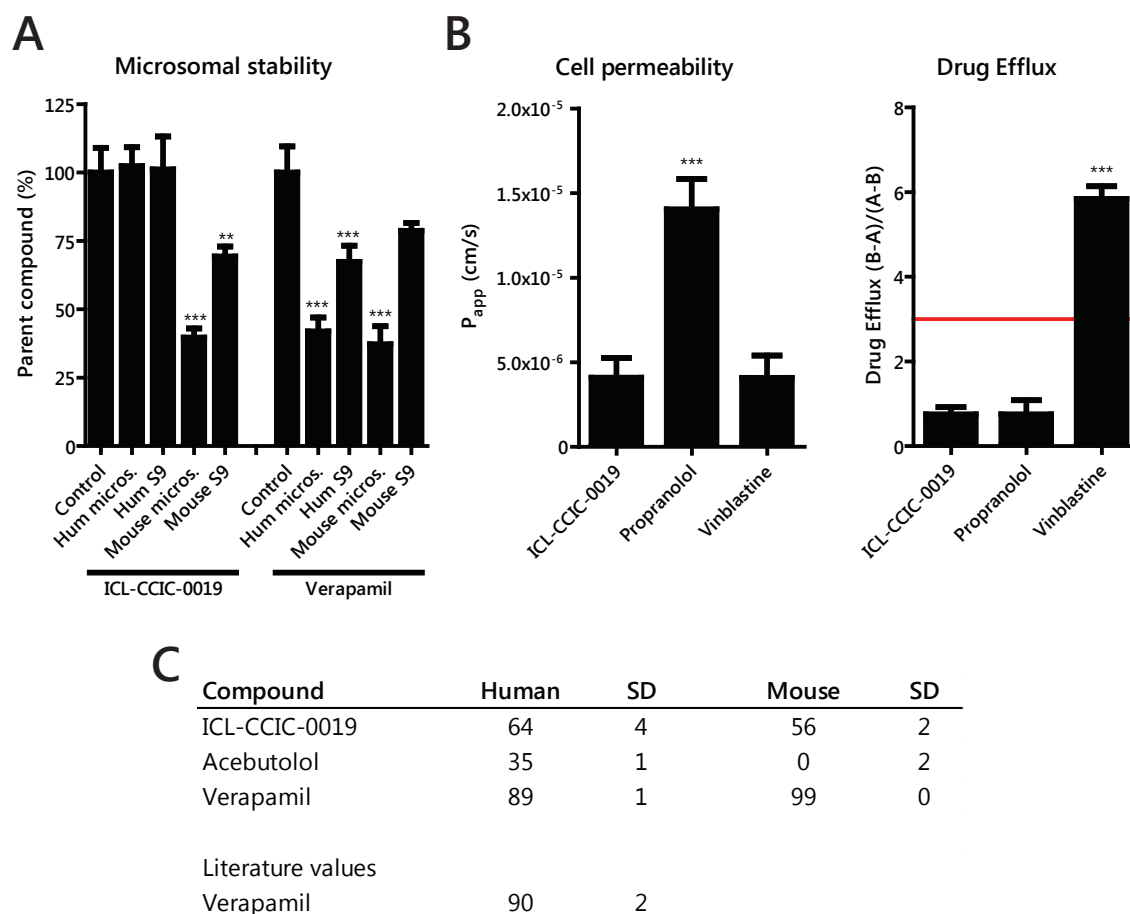


Figure 4.13: Microsomal stability, cell permeability and plasma protein binding of ICL-CCIC-0019. A, Metabolism of ICL-CCIC-0019 was predicted by incubating human and mouse microsomes and S9 fractions with 10  $\mu$ M ICL-CCIC-0019. Metabolites were quantified by HPLC and amount parent compound normalised to controls without microsomes. B, Cell permeability was determined using Caco-2 transwell system by determining the rate of migration of 10  $\mu$ M ICL-CCIC-0019 from the apical to the basal compartment (A–B). Propranolol and vinblastine were used as controls. Drug efflux was determined by the ratio of (B–A)/(A–B) transport. The red line indicates a ratio of 3, which is commonly used as an indicator of multidrug resistance transporter substrate activity. Vinblastine was used as positive and propranolol as negative control. C, Plasma protein binding was determined at a concentration of 10  $\mu$ M using Rapid Equilibrium Dialysis (RED) method (Pierce). For all assays: mean of  $n = 3 \pm$  SD; \*\*  $P < 0.01$ , \*\*\*  $P < 0.001$ .

basal side (B). ICL-CCIC-0019 was added to the apical media and the rate of transport to the basal compartment determined ( $P_{app\ A-B}$ ). Propranolol and vinblastine were used as controls, which are known to have high and low cell permeability, respectively. ICL-CCIC-0019 had a permeability of  $3.5 \pm 0.74 \times 10^{-6}$  cm/s, which was comparable to vinblastine (Figure 4.13B). Transport of propranolol was significantly higher and values for both control compounds were in line with values reported in the literature [196, 197].

In addition, multidrug resistance transporter substrate activity was measured in this assay. Many cancer drugs fail to demonstrate clinical efficacy, due to their efflux from can-

cer cells by ATP-binding cassette (ABC) transporters, preventing the drugs from reaching their intracellular targets [198]. In this Caco-2 transwell system, P-glycoprotein is located on the apical side. Therefore, if a compound is not substrate to P-glycoprotein, flux from A–B and B–A will be equal. However, if a compound possesses substrate specificity, there will be significantly stronger flux from B–A than A–B. A ratio of B–A/A–B greater than 3 is generally considered to be indicative of substrate specificity [198]. In separate wells, the rate of transport from A–B and B–A was determined and ICL-CCIC-0019 found to have similar permeability coefficients for both directions of transport. Vinblastine’s P-glycoprotein substrate specificity was confirmed by a B–A/A–B ratio of 6.3 (Figure 4.13B).

### 4.9.3 Plasma protein binding

While circulating in the blood, drug molecules can either be bound to proteins or lipids in the plasma or are free [199]. Only unbound drug can diffuse to its target and exert pharmacological activity. While the free drug concentration in the plasma does not necessarily correlate with *in vivo* efficacy, as this is dependent on the free drug concentration surrounding the target, it has profound influence on the pharmacokinetic properties and potential toxicity [199]. Plasma protein binding (PPB) was 64%, as determined by equilibrium dialysis method (Figure 4.13C), indicating a satisfactory balanced profile. Verapamil (high PPB) and acebutolol (low PPB) were used as positive and negative controls, respectively [200].

## 4.10 Pharmacokinetics of ICL-CCIC-0019

Encouraged by the cellular potency and the predicted pharmacologic parameters, ICL-CCIC-0019 was further examined *in vivo*. To this end, initial experiments were carried out to assess its tolerability.

### 4.10.1 Tolerability

Tolerability was assessed in BALB/c mice by monitoring body weight changes in response to different dosing regimens. Mice were randomised into groups of three and treated with vehicle (PBS) or subsequently escalating, i.p. administered doses of ICL-CCIC-0019. A starting dose of 1 mg/kg was chosen, as comparable *bis*-pyridinium compounds were shown to be tolerated at doses 5 mg/kg [146]. No alterations in body weight were detected after

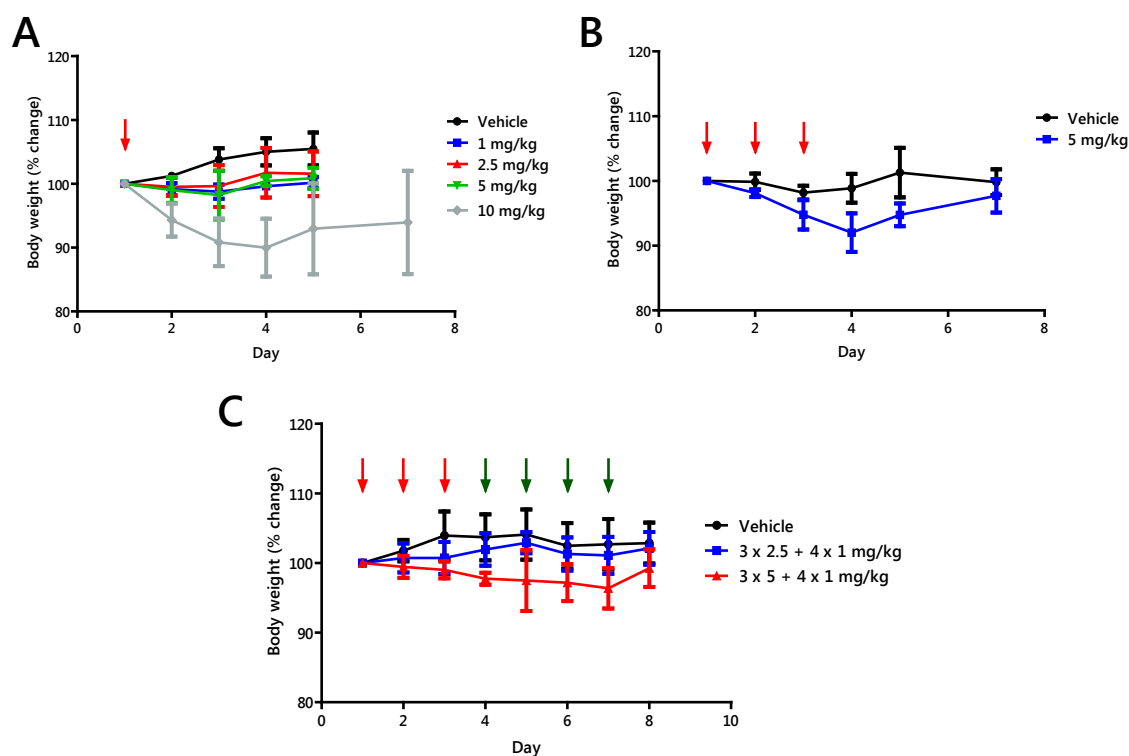


Figure 4.14: Body weight changes in response to ICL-CCIC-0019. A, BALB/c mice were administered a single dose of vehicle (PBS) or indicated doses of ICL-CCIC-0019 i.p. and body weight monitored for seven days ( $n = 3$  per group). B, As in A, however, with three subsequent doses of 5 mg/kg i.p. once a day. Dosing days are indicated by red arrows. C, As in A, however, three doses of 2.5 or 5 mg/kg i.p. once a day (red arrows) followed by four doses of 1 mg/kg i.p. once a day (green arrows) were administered. Mean of  $n = 3 \pm$  SD.

single doses up to 5 mg/kg (Figure 4.14A). 10 mg/kg ICL-CCIC-0019 caused a mean decrease of 4% body weight after 24 hours. The mean body weight further decreased up until 72 hours post injection, after which 2 out of 3 mice recovered and regained their initial body weight within a week of the initial dose. One mouse maintained a reduced body weight for the duration of the experiment (Figure 4.14A).

Subsequently, tolerability of multiple doses of 5 mg/kg was assessed. Three doses of 5 mg/kg i.p. once a day time-dependently decreased the mean body weight by 8% within 72 hours, but mice regained their initial weight within a week of treatment initiation (Figure 4.14B).

Finally, two continuous dosing schemes were tested. They comprised three doses of 2.5 or 5 mg/kg i.p., followed by four maintenance doses of 1 mg/kg i.p. No significant body weight changes were observed and therefore,  $3 \times 5$  mg/kg followed by  $4 \times 1$  mg/kg was identified as tolerated. For short-term experiments, a single dose of 10 mg could alternatively be used.

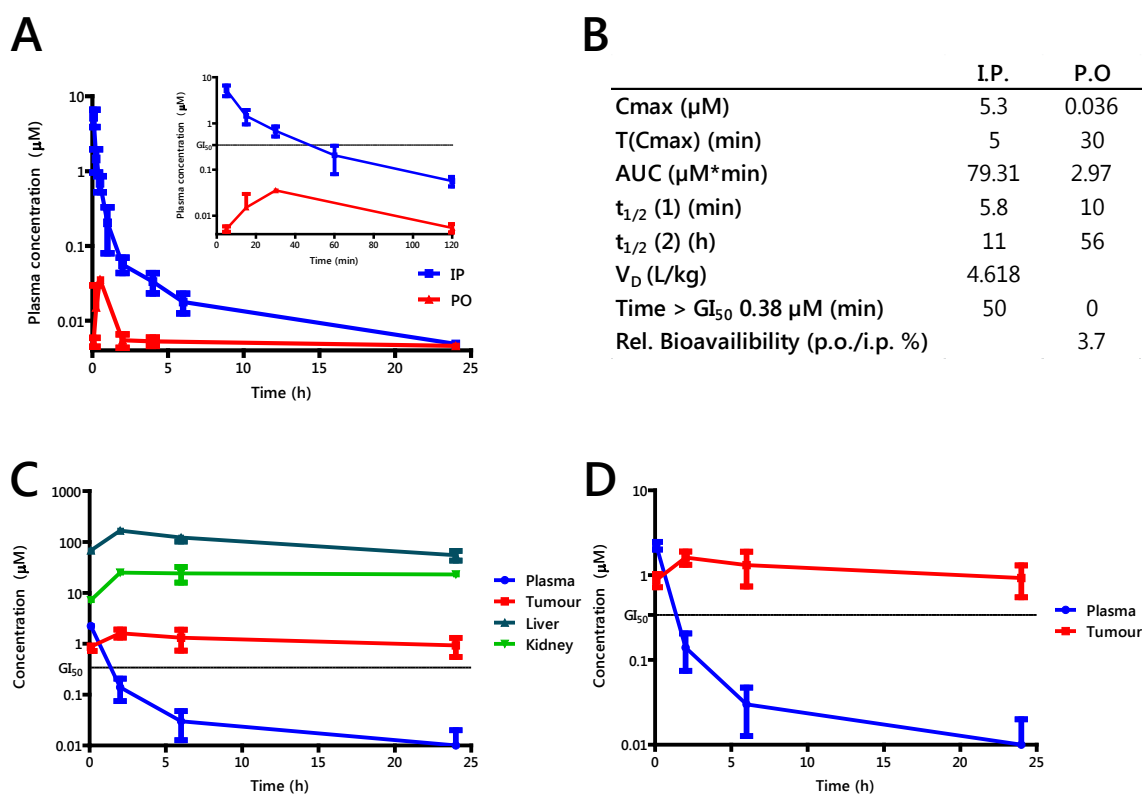


Figure 4.15: Plasma and tissue pharmacokinetics of ICL-CCIC-0019. A, BALB/c mice were administered 10 mg/kg ICL-CCIC-0019 p.o. or i.p. and plasma obtained 5, 15, 30, 60 minutes and 2, 4, 6 and 24 hours post injection. Figure insert displays first 120 minutes only. Compound plasma concentrations were determined by LC-MS. B, Plasma pharmacokinetic variables derived from A. C, Tissue distribution of ICL-CCIC-0019. HCT116 xenograft bearing BALB/c nude mice were treated with 10 mg/kg ICL-CCIC-0019 and plasma, tumour, liver and kidney harvested after 5 min, 2, 6 and 24 hours. D, Same data as C, but only displaying plasma and tumour for clarity. Tissue concentrations were determined by LC-MS. For all graphs, lines indicate  $GI_{50}$  in HCT116 cells; mean of  $n = 3$  per time point  $\pm$  SD.

#### 4.10.2 Pharmacokinetics

Plasma and tissue pharmacokinetic profiles were established following a single injection of 10 mg/kg ICL-CCIC-0019. Plasma variables were derived in BALB/c mice at 5, 15, 30, 60 minutes and 2, 4, 6 and 24 hours post administration. As tissue distribution was expected to be less erratic, compound concentrations were determined at 5 minutes, 2, 6 and 24 hours only. BALB/c nude mice bearing HCT116 xenografts were employed and tumour, liver, kidney and plasma analysed.

The compound was rapidly cleared from the plasma following i.p. administration (Figure 4.15A) and plasma concentrations above the  $GI_{50}$  of HCT116 cells were maintained for ca. 50 minutes. The compound was not orally bioavailable, as plasma concentrations did not reach concentrations of the  $GI_{50}$ , which would be necessitated to exert antitumour

Table 4.2: Plasma metabolites of ICL-CCIC-0019. Plasma samples of BALB/c mice treated with 10  $\mu$ M ICL-CCIC-0019 for 2 hours used for tissue PK experiments were pooled and analysed for parent peak and metabolites by LC-MS. Analysis was performed by Cyprotex Inc.

Mass	Metabolite		Mass difference		Ion	Retention time (min)	Metabolite reference	Abs area	Area percentage
	name	Formula	from parent	m/z found					
412	Parent	C <sub>26</sub> H <sub>44</sub> N <sub>4</sub>	-	206	[M] <sup>2+</sup>	7.38	-	7.17E+07	41.3
246	Loss of 166	-	-166	246	[M] <sup>+</sup>	2.58	M1	1.02E+07	5.88
246	Loss of 166	-	-166	246	[M] <sup>+</sup>	2.73	M2	1.22E+07	7.03
305	Loss of 107	-	-107	305	[M] <sup>+</sup>	2.78	M3	7.54E+06	4.35
305	Loss of 107	-	-107	305	[M] <sup>+</sup>	3.45	M4	1.31E+07	7.55
338	Loss of 74	-	-74	338	[M] <sup>+</sup>	3.54	M5	1.01E+07	5.82
538	Gain of 126	-	126	538	[M] <sup>+</sup>	10.46	M6	1.12E+07	6.46
563	Gain of 151	-	151	563	[M] <sup>+</sup>	7.47	M7*	3.74E+07	21.6

All remaining peaks in the sample were either in the control sample or not believed to be related to test compound. Percentages have been calculated assuming that each metabolite is equally as sensitive as parent.

activity. Plasma pharmacokinetic variables are shown in Figure 4.15B.

The compound was quickly extracted by the examined tissues and tumour concentrations above the GI<sub>50</sub> were maintained throughout the study (Figure 4.15C–D). Extensive accumulation in liver and kidneys were observed, although clearance from liver was more rapid than from tumour.

### 4.10.3 *In vivo* metabolism

In conjunction with the pharmacokinetic characterisation, the metabolites of ICL-CCIC-0019 in plasma were characterised. The 2-hour plasma samples of BALB/c nude mice were pooled and ICL-CCIC-0019-derived metabolites compared to untreated plasma samples. Seven metabolites could be identified (Table 4.2), of which five represented breakdown products and two conjugates to biomolecules. The metabolites were matched against a database of commonly detected drug metabolites (Table 4.3), but no similarities were obtained.



Table 4.3: List of expected metabolites. Data provided by Cyprotex, Inc.

Mass Difference	Formula	Description
0	-	Parent
+1.98	-CH <sub>2</sub> +O	Demethylation and Hydroxylation
+2	+-H	Hydrogenation
+14	+CH <sub>2</sub>	Methylation
+14	+O -H <sub>2</sub>	CH <sub>2</sub> to CO
+16	+O	Hydroxylation, N, S oxidation, epoxidation
+30	+O <sub>2</sub> -H <sub>2</sub>	CH <sub>3</sub> to CO <sub>2</sub> H
+32	+O <sub>2</sub>	Di-hydroxylation
+80	+SO <sub>3</sub>	Sulfate conjugation (Phase 2 only)
+96	+SO <sub>4</sub>	Hydroxylation and Sulfate conjugation (Phase 2 only)
+107	+C <sub>2</sub> H <sub>5</sub> NO <sub>2</sub> S	Taurine conjugation (Phase 2 only)
+176	+C <sub>6</sub> H <sub>8</sub> O <sub>6</sub>	Glucuronide conjugation (Phase 2 only)
+192	+C <sub>6</sub> H <sub>8</sub> O <sub>7</sub>	Hydroxylation and glucuronidation (Phase 2 only)
-2	-H <sub>2</sub>	Dehydrogenation
-14	-CH <sub>2</sub>	Demethylation
-17	-NH <sub>3</sub>	Loss of NH <sub>3</sub>
-18	-H <sub>2</sub> O	Alcohol dehydration
-28	-C <sub>2</sub> H <sub>4</sub>	De-ethylation or di-demethylation
-30	-NO	Loss of NO
-42	-C <sub>3</sub> H <sub>6</sub>	Depropylation (deacetylation also fits integer mass)

## 4.11 ICL-CCIC-0019 inhibits CHK activity *in vivo*

### 4.11.0.1 [<sup>18</sup>F]D4-FCH PET imaging

To determine whether ICL-CCIC-0019 could attenuate CHK activity *in vivo*, [<sup>18</sup>F]D4-FCH PET imaging was performed. Tracer and compound compete for the same target, thus permitting non-invasive assessment of competitive antagonism in the physiological and complex milieu of the tumour.

24 and 48 hours after a single dose of 10 mg/kg, a marked reduction in tracer uptake was observed in treated HCT116 xenografts compared to the vehicle-treated cohort [AUC<sub>0-60</sub> control: 191.9 (%ID/mL)\*min; AUC<sub>0-60</sub> 24 hours: 145.8 (%ID/mL)\*min; AUC<sub>0-60</sub> 48 hours: 139.4 (%ID/mL)\*min; Figure 4.16 and Figure 4.17]. Interestingly, despite the rapid tissue distribution, where ICL-CCIC-0019 concentrations in the tumours peaked at 2 hours post injection, PET imaging at 6 hours post administration did not result in significant reduction of [<sup>18</sup>F]D4-FCH uptake [AUC<sub>0-60</sub> 6 hours: 187.7 (%ID/mL)\*min]. Reductions of tumour tracer accumulation were most prominent within the first 20 minutes of dynamic scans, reflecting the early delivery and retention phase. While cardiac TACs were not influenced by treatment, liver and kidney tracer retentions were diminished, comparably to tissue pharmacokinetics data (Figure 4.17).

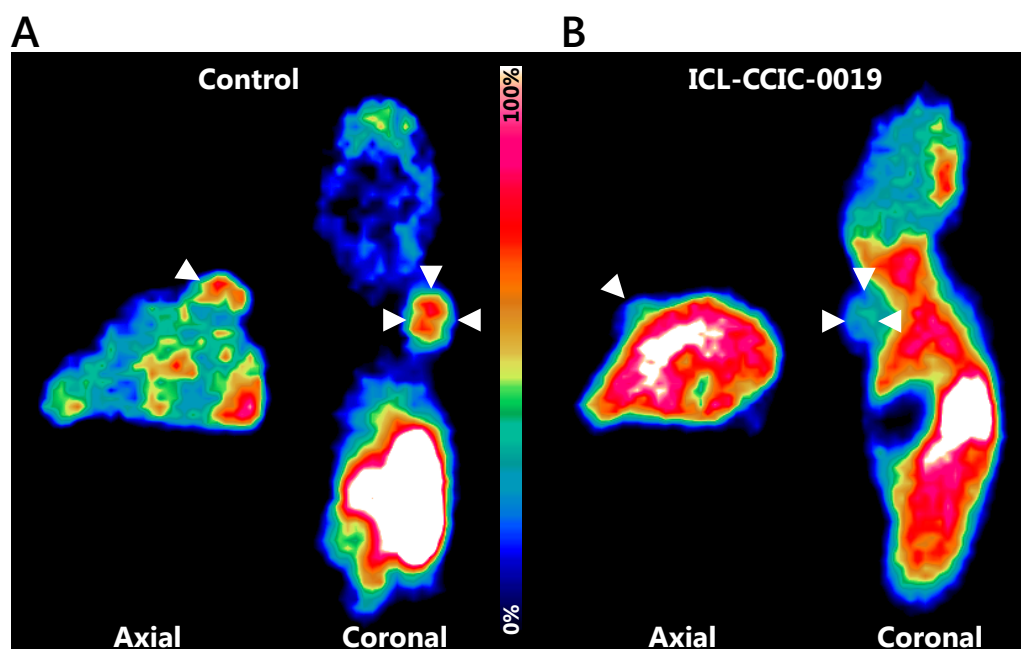


Figure 4.16: ICL-CCIC-0019 inhibits choline kinase activity *in vivo*. Representative [ $^{18}\text{F}$ ]D4-FCH PET images of HCT116 xenograft bearing BALB/c nude mice, treated with vehicle (PBS; A) or 10 mg/kg ICL-CCIC-0019 i.p. for 24 hours (B). Images show summed frames from 30–60 minutes and tumours are indicated by white arrowheads.

#### 4.11.0.2 Pharmacokinetic modelling of CHK inhibition

To further characterise ICL-CCIC-0019 mediated choline kinase inhibition *in vivo*, kinetic modelling was employed. Whereas normalised tissue uptake values reflect tracer concentration in a three-dimensional region of interest, kinetic modelling accounts for tissue uptake relative to plasma. A two-tissue irreversible compartmental model, as previously reported [110], was employed with the hypothesis that  $k_3$  would represent the rate by which the tracer is phosphorylated by choline kinase (see Introduction and Figure 1.6). Although this enzymatic reaction is in principle reversible, it was assumed that the high dependency of cancer cells to incorporate choline made it unlikely that catalytic hydrolysis of PCho prevails. Best fits and more physiological parameters were obtained with a 3k (excluding  $k_4$ ) instead of 4k model.

ICL-CCIC-0019 treatment significantly decreased  $K_1$ , denoting the flux from blood to tissue, at all investigated time points in the tumour (73% decrease compared to control after 24 hours, 75% decrease after 48 hours) and to a lesser extent in kidneys and liver (Figure 4.18A). The opposing flux from tissue into the blood stream,  $k_2$ , was not significantly influenced by treatment across all tissues (Figure 4.18B). Interestingly, the rate constant  $k_3$ , which represents intracellular tracer trapping, was also non-significantly

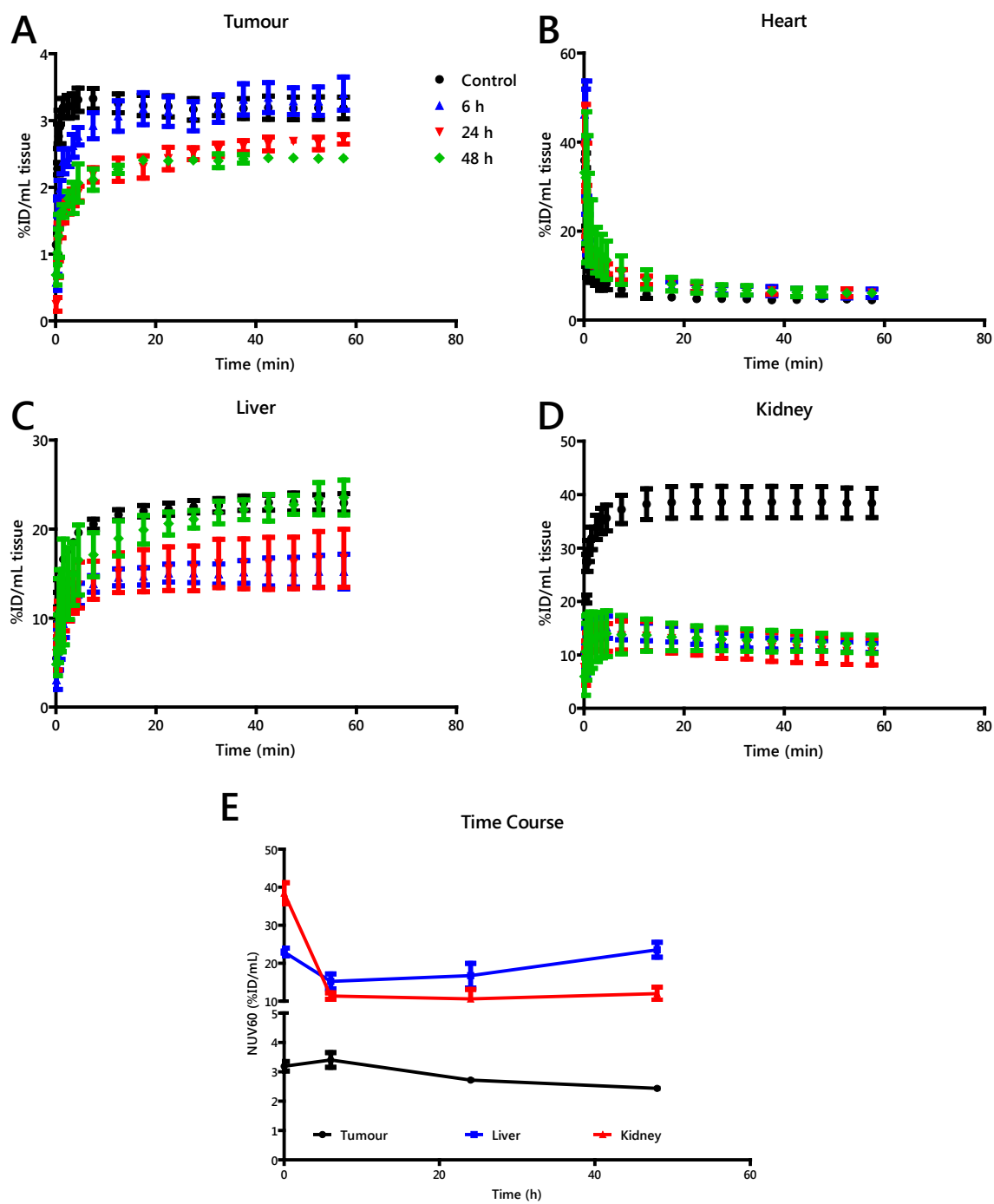


Figure 4.17: Tumour TACs of HCT116 xenograft-bearing mice in groups of four were treated with a single dose of 10 mg/kg ICL-CCIC-0019 i.p. and imaged at indicated times post injection in comparison to untreated control mice. A, Tumour; B, heart; C, liver; D, kidney TACs. E, time course of  $[^{18}\text{F}]$ D4-FCH uptake in tumour, liver and kidney; data represent NUV<sub>60</sub> as a function of time, where 0 represents the NUV<sub>60</sub> of control mice. Mean of  $n = 4 \pm \text{SEM}$ .

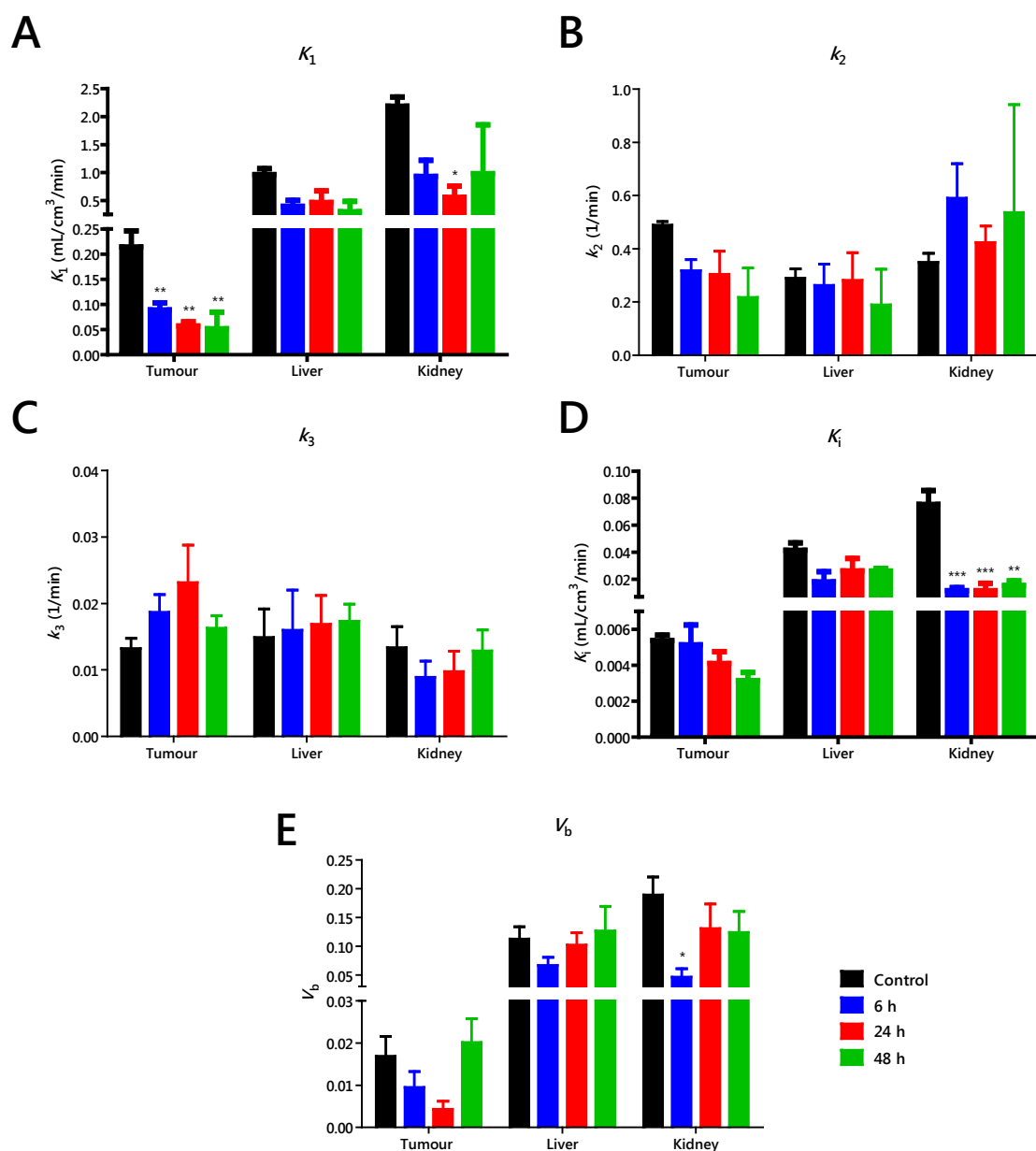


Figure 4.18: Pharmacokinetic modelling of competitive inhibition of CHKA by ICL-CCIC-0019 using  $[^{18}\text{F}]\text{D4-FCH}$  in HCT116 xenograft-bearing mice. Statistical significance was determined by one-way ANOVA and Bonferroni's Multiple Comparison Test; \*  $P < 0.05$ ; \*\*  $P < 0.01$ ; \*\*\*  $P < 0.001$ . Kinetic modelling was performed by Dr. Giampaolo Tomasi.

altered (Figure 4.18C). In consequence to these micro parameter changes, the macro parameter  $K_i$  denoting the irreversible uptake rate was decreased, however, not significantly (Figure 4.18D). Unexpectedly, changes in kinetic flux were predominantly driven by alterations in  $K_1$ . In all examined tissues, the blood volume  $V_b$  decreased initially after treatment (Figure 4.18E). These perfusion deficits were more pronounced and persistent in tumour compared to liver and kidney.

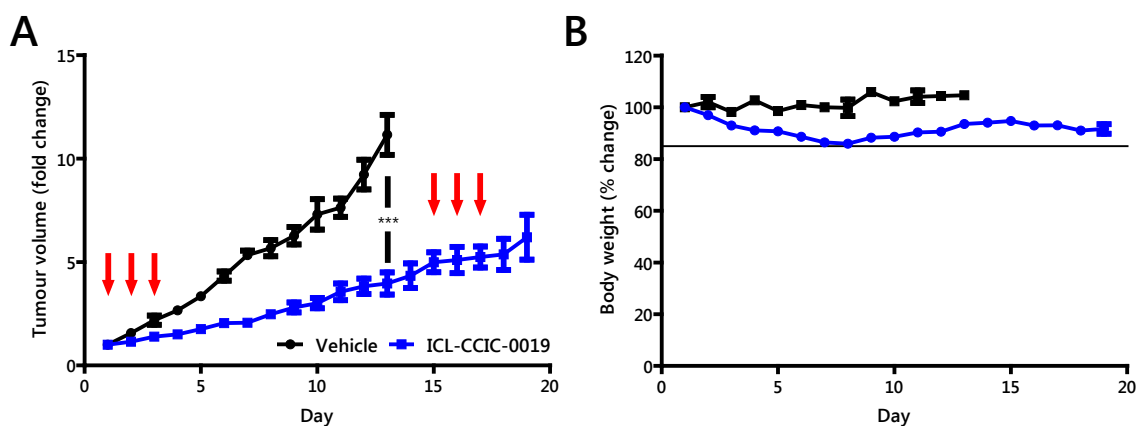


Figure 4.19: Antitumour activity of ICL-CCIC-0019. HCT116 xenograft-bearing mice were treated with vehicle (PBS) or 5 mg/kg i.p. once a day on indicated days (red arrows). A, Antitumour activity; B, body weight changes compared to day 1. Line indicates 85%. Mean of  $n = 6 \pm \text{SEM}$ ; \*\*\*  $P < 0.001$ .

## 4.12 Antitumour activity

Antitumour activity was assessed in HCT116 xenograft bearing mice (Figure 4.19). It was intended to apply the initially optimised dosing scheme, however, body weight loss was more profound in BALB/c nude compared to BALB/c mice (maximal decrease 15%) and the schedule had therefore be intermitted. Mice were treated on days 1–3 with 5 mg/kg i.p. once a day followed by a 11 day recovery period. ICL-CCIC-0019 resulted in potent antitumour activity.

## 4.13 [ $^{18}\text{F}$ ]FLT PET

To determine whether the antiproliferative response could be predicted non-invasively and at early time points, treatment response of [ $^{18}\text{F}$ ]FLT uptake was assessed. Thymidine is a vital metabolite for DNA synthesis and therefore in demand in proliferating tissues. Reduction of abnormally high proliferation was shown to frequently reduce FLT uptake [201]. Surprisingly, three doses of 5 mg/kg increased FLT uptake by 33% in HCT116 xenografts (Figure 4.20).

## 4.14 Inducible CHKA shRNA model

Given the multitude of effects observed with ICL-CCIC-0019 it was necessary to further verify the pharmacologic effect by alternative - genetic - means. Therefore, an inducible shRNA targeting CHKA was created in HCT116 cells. In contrast to transient siRNA

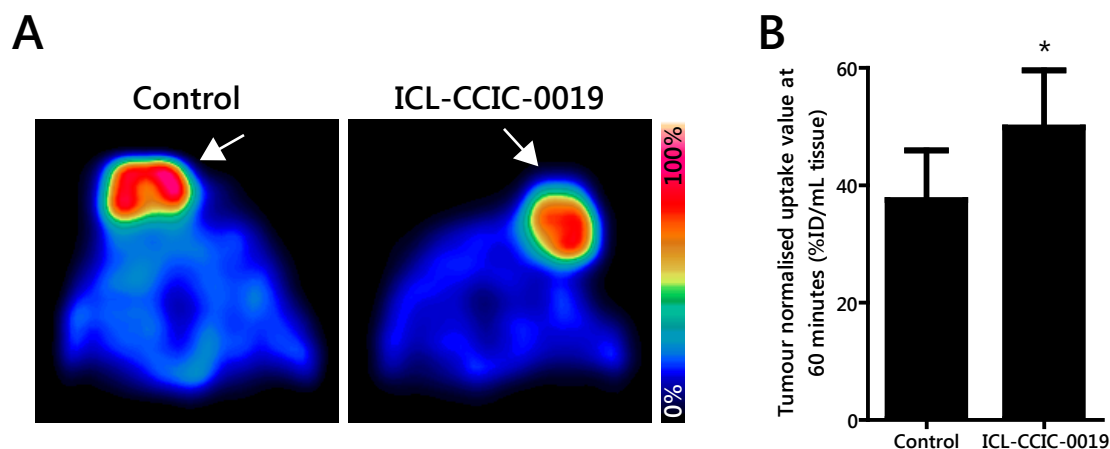


Figure 4.20: ICL-CCIC-0019 treatment increased [ $^{18}\text{F}$ ]FLT uptake *in vivo*. HCT116 tumour-bearing BALB/*c* nude mice were treated with 5 mg/kg once a day i.p. for 3 days and imaged 24 hours after the last dose. A, Representative PET images; white arrows indicate tumour. B, NUV<sub>60</sub> values of control and treatment groups. Mean of  $n = 6 \pm \text{SEM}$ ; \*  $P = 0.0403$ .

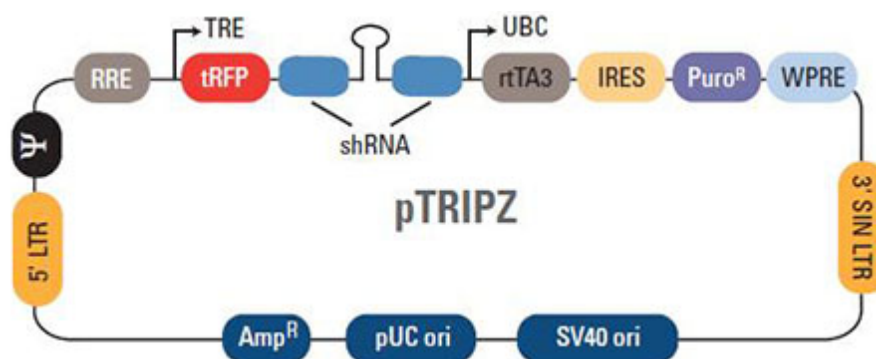
transfection, it bears the advantage of stable incorporation of the shRNA into the host DNA. The employed pTRIPZ vector contains a hairpin consisting of 22 nucleotides and a TurboRFP sequence under the control of a tetracycline-inducible promoter sequence (Figure 4.21). The Tet-On configuration provides expression of the shRNA and TurboRFP in the presence of doxycycline (DOX).

#### 4.14.1 Identification of shRNA sequence that sufficiently silences CHKA

Three different shRNA sequences were tested to identify one that produces the strongest knockdown. Induction was carried out by incubation with 0.5  $\mu\text{g}/\text{mL}$  DOX, which was found to be non-toxic in HCT116 cells (Figure 4.22A). Transduced cells under DOX induction were FACS sorted to isolate a pool that contains the 90<sup>th</sup> percentile with the highest TurboRFP expression. The resulting lines were further characterised. While all 3 sequences sufficiently knocked down CHKA by western blot, sequence 3 elicited lowest [ $^3\text{H}$ ]choline uptake and strongest antiproliferative activity as well as caspase 3/7 activation (Figure 4.22B–E). Therefore, this lineage was further characterised.

#### 4.14.2 Characterisation of HCT116-shCHKA3 cell line

HCT116-shCHKA3 was evaluated in greater detail. Onset of CHKA knockdown occurred two days post DOX induction and protein expression was almost completely diminished 4 days post induction (Figure 4.23A). Choline uptake decreased by 50% after 7 days of DOX



Vector Element	Utility
TRE	Tetracycline-inducible promoter
tRFP	TurboRFP reporter for visual tracking of transduction and shRNA expression
shRNA	microRNA-adapted shRNA (based on miR-30) for gene knockdown
UBC	Human ubiquitin C promoter for constitutive expression of rtTA3 and puromycin resistance genes
rtTA3	Reverse tetracycline-transactivator 3 for tetracycline-dependent induction of the TRE promoter
PuroR	Puromycin resistance permits antibiotic-selective pressure and propagation of stable integrants
IRES	Internal ribosomal entry site allows expression of rtTA3 and puromycin resistance genes in a single transcript
5' LTR	5' long terminal repeat
3' SIN LTR	3' self-inactivating long terminal repeat for increased lentivirus safety
Ψ	Psi packaging sequence allows viral genome packaging using lentiviral packaging systems
RRE	Rev response element enhances titer by increasing packaging efficiency of full-length viral genomes
WPRE	Woodchuck hepatitis posttranscriptional regulatory element enhances transgene expression in the target cells

Figure 4.21: Scheme of pTRIPZ vector. Figure from [202].

treatment, while control cells were not affected by DOX treatment (Figure 4.23B). The onset of shRNA expression could further be monitored by fluorescent microscopy detecting TurboRFP expression (data not shown).

#### 4.14.3 [<sup>18</sup>F]D4-FCH PET imaging of CHKA shRNA model

The model was then evaluated *in vivo*. BALB/c nude mice were inoculated with shCTR or shCHKA3 cells and xenografts of ca. 40 mm<sup>3</sup> allowed to form. Mice were then randomised into two groups per cell line and treated for seven days with or without DOX-supplemented diet. IVIS fluorescent imaging confirmed induction of the shRNA in the DOX-induced cohorts (Figure 4.24A–B). No changes in tumour volume were observed from the time of induction (data not shown). Mice were then imaged with [<sup>18</sup>F]D4-FCH, but no differences in tumour uptake observed among the groups (Figure 4.24C–E). Some degree of heterogeneity was observed and therefore tumours were further analysed by their highest voxel intensity. No differences were observed in the intensities of the 90<sup>th</sup> percentile of voxels across all cohorts (Figure 4.24F). Tumours were then analysed for CHKA expression and no significant reduction in the shCHKA group fed with DOX diet observed (Figure 4.24G).

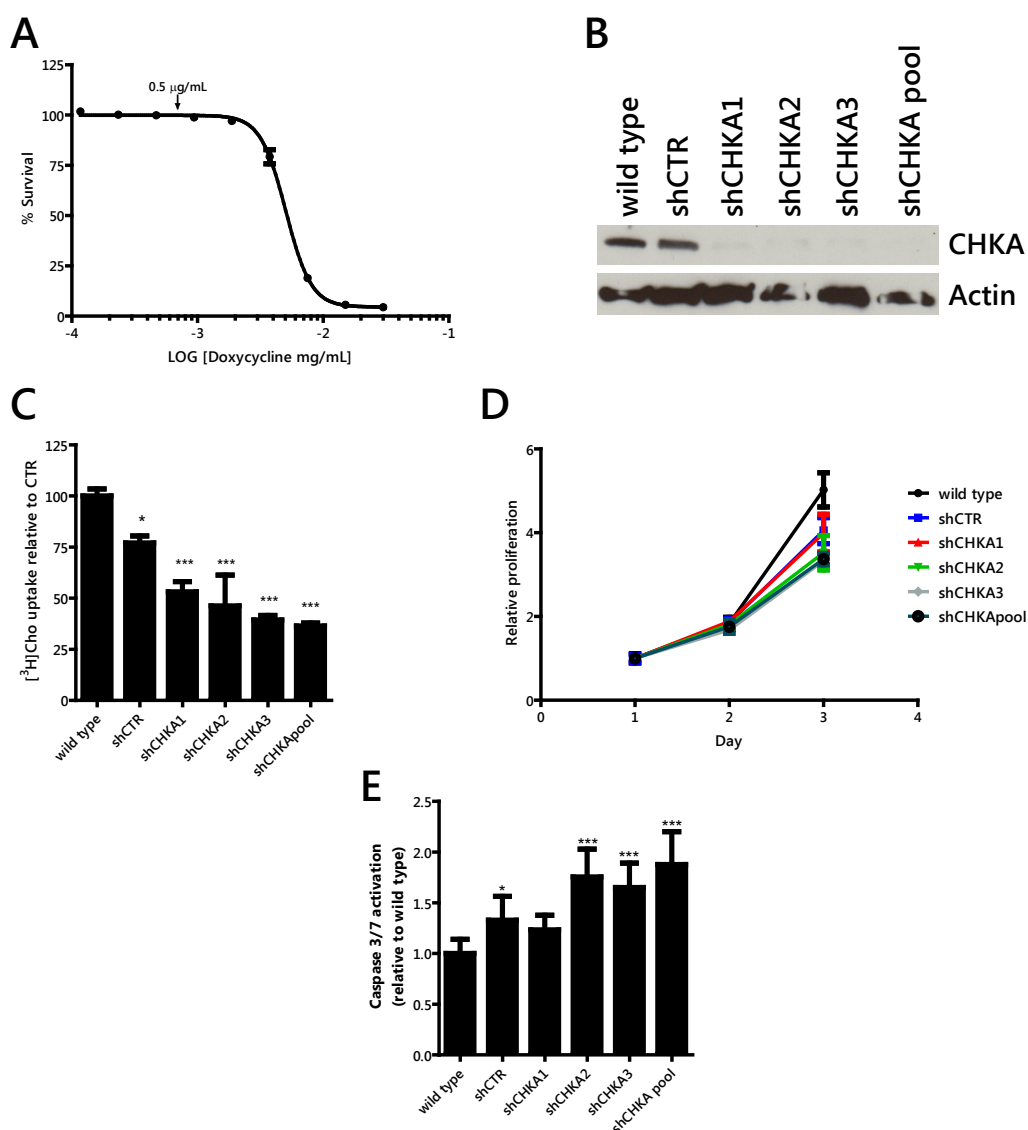


Figure 4.22: Selection of HCT116 cells transduced with CHKA targeting shRNA. A, HCT116 wild type cells were exposed to varying concentrations of DOX for 72 hours and 0.5  $\mu\text{g/mL}$  identified to be non-toxic. B–D, Cells transduced with indicated shRNAs were incubated with 0.5 mg/mL DOX for 7 days. The day before initiation of experiments, untreated wild type cells and shRNA-induced cells were seeded at equal cell numbers. B, western blot against CHKA. C, Uptake of  $[^3\text{H}]$ choline was determined for each DOX-induced cell line and compared to wild type cells. D, Relative proliferation was measured by SRB assay and absorbance normalised to cell density at day 1. E, Apoptosis was measured 24 hours post seeding by caspase 3/7 Glo assay. Mean of  $n = 3 \pm \text{SD}$ ; \*  $P < 0.1$ , \*\*  $P < 0.01$ , \*\*\*  $P < 0.001$ .

#### 4.15 Effects of combined CHK and HDAC inhibition

Effective inhibition of CHK by ICL-CCIC-0019 diminished the intracellular accumulation of PCho and PtdCho, which resulted in potent antiproliferative activity. Combination therapies with histone deacetylase (HDAC) inhibitors were examined, as these drugs increase choline kinase expression and intracellular PCho accumulation.



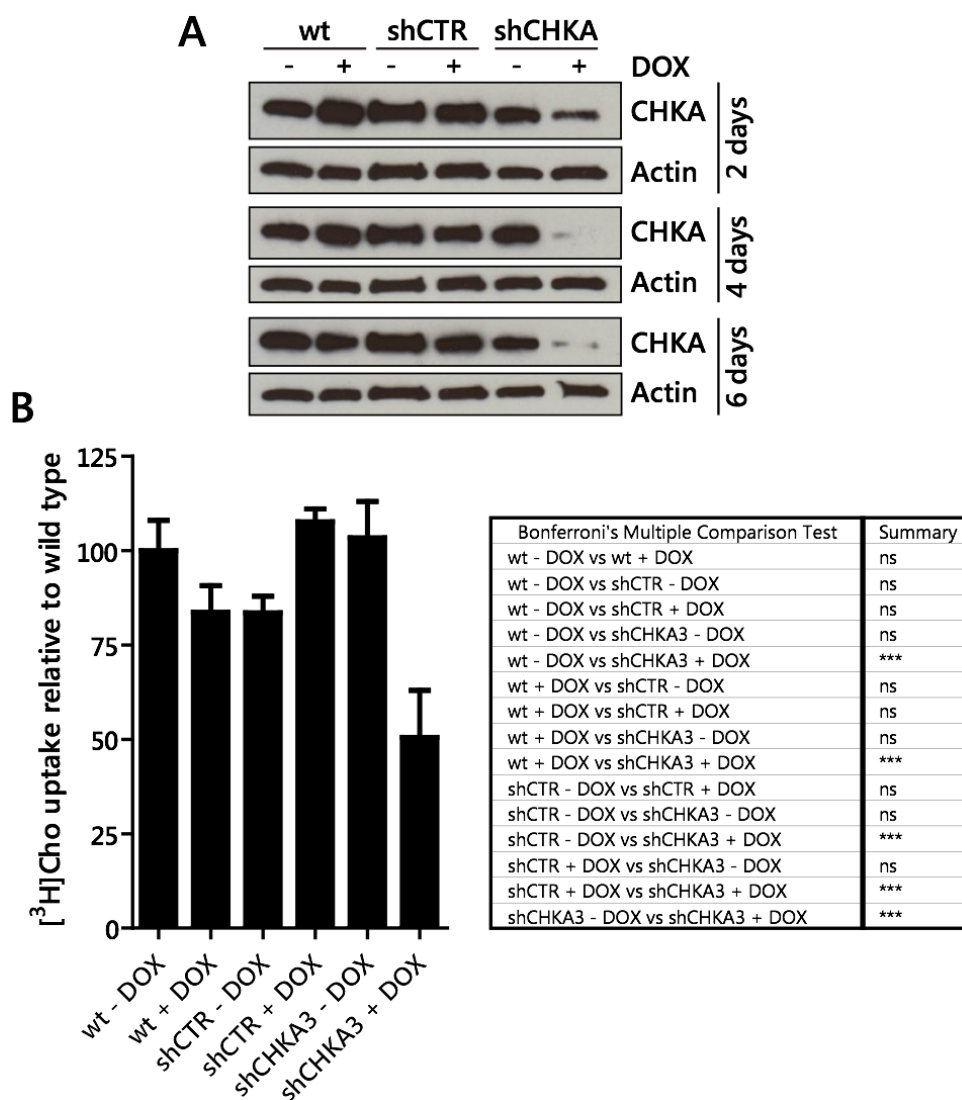


Figure 4.23: Characterisation of HCT116-shCHKA3 cell line. A, Indicated cell lines were treated with or without DOX and at after 2, 4 and 6 days, cells were harvested and knockdown confirmed by western blot. B, [<sup>3</sup>H]choline uptake was determined in cells treated with or without DOX for seven days. Mean of  $n = 3 \pm SD$ . Statistical significance was determined by one-way ANOVA with Bonferroni's multiple comparison test (see table).

Depending on the transcriptional requirements of a cell, DNA alternates between “open” and “closed” conformations. This process, called chromatin remodelling, modulates the accessibility and the sensitivity of regulatory proteins to DNA [203, 204]. Post-translational modifications of histones, most notably acetylation, orchestrate these changes [205, 206]. Acetylation occurs through histone acetyltransferases (HATs) to result in a transcriptionally repressed conformation. This process is reverted by HDACs leading to a transcriptional active state [207]. Therefore these enzymes have profound implications for development and diseases, such as cancer.

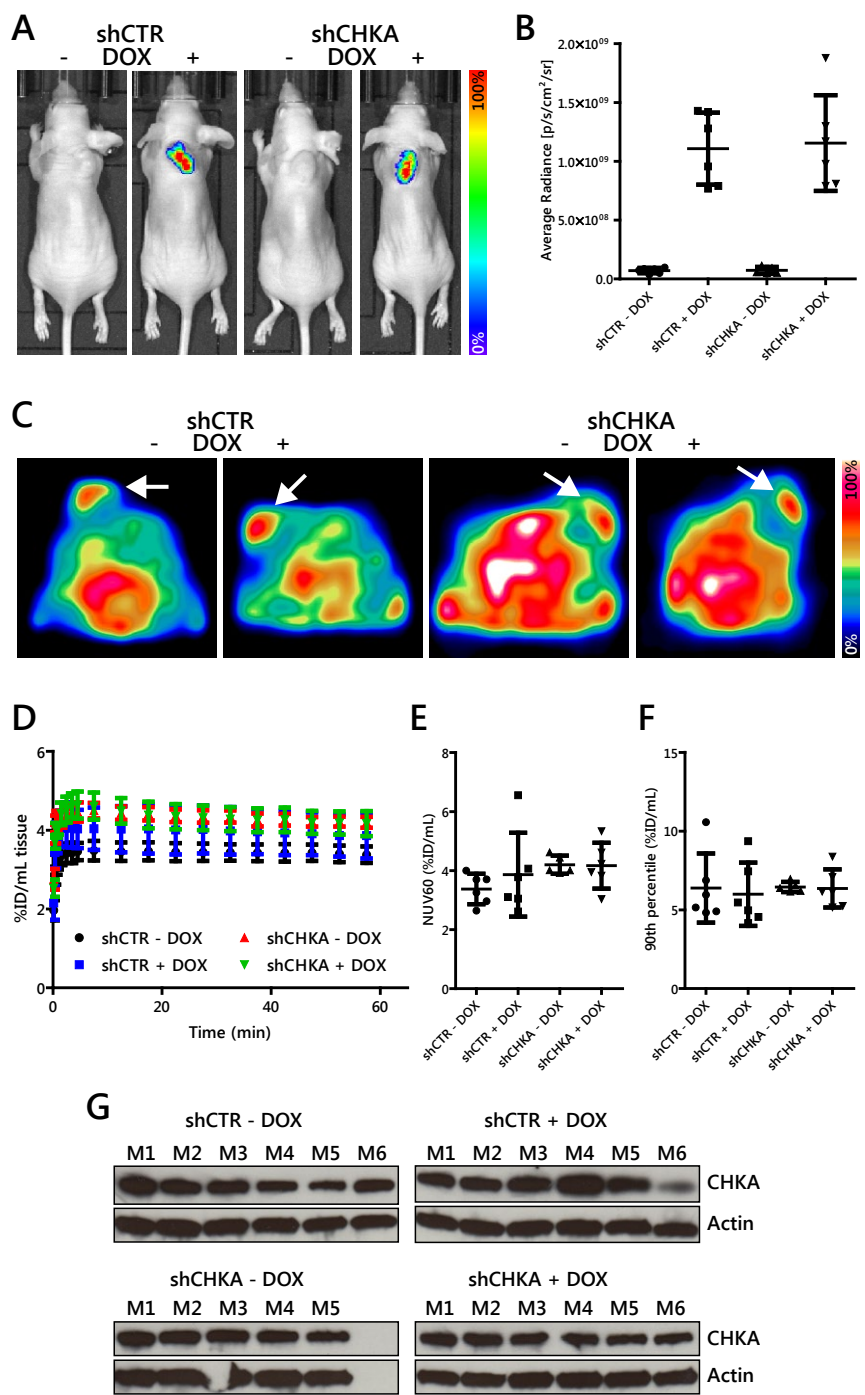


Figure 4.24: *In vivo* characterisation of HCT116-shCHKA model. BALB/c nude mice were inoculated with HCT116-shCTR and HCT116-shCHKA3 cells and randomised into two groups per xenograft model after tumour reached 40 mm<sup>3</sup>. Groups of each model were fed for seven days either normal diet or chow supplemented with DOX (*n* = 6 per group with the exception of shCHKA on normal diet: *n* = 5) A, Representative IVIS fluorescent images depicting TurboRFP, which is co-expressed with the shRNA upon DOX induction. B, Quantification of IVIS-derived average of radiance obtained from two-dimensional ROIs drawn over the tumours. C, Representative [<sup>18</sup>F]D4-FCH PET images of cumulative 30–60 minute frames of dynamic scans. Tumours are indicated by white arrows. D, Dynamic tumour TACs of indicated groups and their respective NUV<sub>60</sub> values (E) are shown. F, Summed 40–60 minute scans were histogrammed and highest intensity voxels analysed. The 90<sup>th</sup> percentile for each tumour is shown. Note that Y-axis scales vary in between panels E and F. G, Western blot analysis of CHKA expression in tumours excised directly after imaging.

Table 4.4: Effects of combined treatment of HCT116 cells with ICL-CCIC-0019 and HDAC inhibitors C1A or vorinostat, as determined by combination index (CI). CI > 1 indicates antagonism, CI = 1 additive effects and C < 1 synergy. Mean of  $n = 3$  in sextuplicate  $\pm$  SD.

<b>ICL-CCIC-0019 plus</b>	<b>Combination index at</b>
0.1 $\mu$ M C1A	1.75 $\pm$ 0.12
0.5 $\mu$ M C1A	0.91 $\pm$ 0.31
1 $\mu$ M C1A	0.4 $\pm$ 0.16
5 $\mu$ M C1A	3.36E-08 $\pm$ 3.71E-08
0.01 $\mu$ M vorinostat	1.11 $\pm$ 0.15
0.05 $\mu$ M vorinostat	1.24 $\pm$ 0.19
0.1 $\mu$ M vorinostat	1.17 $\pm$ 0.084
0.5 $\mu$ M vorinostat	0.18 $\pm$ 0.056

In recent years, HDACs have been intensively investigated for their potential as cancer therapeutics. 18 different HDACs, subdivided into four subclasses, have been identified and two pan-inhibitors (vorinostat or SAHA, and romidepsin) gained FDA approval [208]. In addition, specific HDAC6 inhibitors are currently in development [3, 209]. In contrast to other HDACs, this isoform exists in the cytoplasm and is also responsible for deacetylation of non-histone targets. Therefore HDAC6 inhibitors have limited involvement in epigenetic regulation, while controlling the activity of multiple client proteins.

Elevated PCho intracellular concentrations have been detected in response to pan-HDAC inhibitors vorinostat and LAQ824 and are driven by increased expression of CHKA and choline transporters [100, 101, 210, 211]. The relevance of this pharmacodynamic marker in the context of selective HDAC6 inhibition is unknown.

As elevated CHKA expression is linked to proliferation, it was hypothesised, that HDAC inhibitor-driven PCho changes could be part of a feedback mechanism to maintain cell survival. Therefore combined CHKA and HDAC inhibition was evaluated. Four doses (ranging between GI<sub>20</sub> and GI<sub>80</sub>) of a pan-HDAC (vorinostat) or HDAC6 specific inhibitor (C1A) were added, while assessing cell survival in response to 9 different doses of ICL-CCIC-0019 in HCT116 cells.

In combination with ICL-CCIC-0019, both HDAC inhibitors were antagonistic at low and synergistic at high concentrations (Table 4.4). Synergy was particularly strong in combination with the HDAC6 selective inhibitor C1A. Interestingly, both HDAC inhibitors did not elevate incorporation of [<sup>3</sup>H]choline after 24 hours drug treatment, as expected in response to the described elevated expression of CHKA. In contrast, both drugs and more profoundly C1A decreased its uptake (Figure 4.25).

## 4.16 Discussion

### CHKA is a valid drug target

By means of pharmacologic inhibition and posttranscriptional silencing, it was demonstrated that inhibition of CHKA is viable strategy for treatments of cancers with hyper-activated choline biochemistry.

Previous attempts to create drug-like CHKA inhibitors, either yielded compounds with a disconnect of cellular and enzymatic activity or lacked detailed pharmacologic data on metabolic stability, pharmacokinetics, pharmacodynamic response or off-target effects. It was a key objective of this project to develop new synthetically readily available CHKA inhibitors with detailed pharmacological characterisation, permitting investigations of choline metabolic handling in the complex milieu of the tumour. Interference with essential nutrient utilisation, such as of choline, glutamine or glucose, forms a new trend in cancer therapy to exploit the striking differences in metabolic handling of cancer cells versus normal tissues to accumulate biomass and satisfy the demand for energy equivalents [212]. CHKA indeed features several characteristics that make it a putative and druggable target. Analysis of the Cancer Cell Line Encyclopaedia revealed consistently high expression of CHKA, but not CHKB, in most human lineages, underpinning the global relevance of this gene in malignancy. Furthermore, it contains a distinct, hydrophobic pocket allowing intervention with small-molecule inhibitors. Lack of mutations and regulation by copy

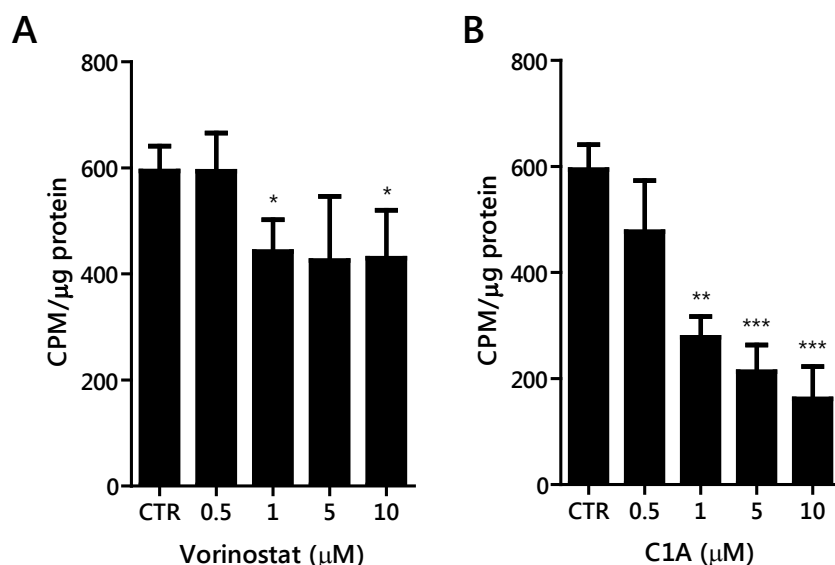


Figure 4.25: [<sup>3</sup>H]choline uptake normalised to protein content in HCT116 cells treated with HDAC inhibitors vorinostat (A) and C1A (B) for 24 hours. Mean of  $n = 3 \pm$  SD; \*  $P < 0.1$ , \*\*  $P < 0.01$ , \*\*\*  $P < 0.001$ .

number variations are ground for optimism that — in contrast to most other currently targeted kinases — genetic alterations might not impede response.

The validity of the target was confirmed by RNA interference, whereby transient knockdown induced apoptosis and reduced proliferation HCT116 cells. This is in line with previous reports, indicating comparable responses in a variety of cancer cell lines [136, 139]. Double knockdown of CHKA and CHKB did not induce apoptosis or decelerate proliferation. This has been previously reported by Gruber *et al.* [65] and highlights the importance of balanced CHKA and CHKB expression. Assuming equal transfection efficiencies for CHKA and CHKB, knockdown of CHKA decreased protein levels to or below those of CHKB, resulting in cell death due to the lack of CHKA. In case of double knockdown, however, both CHKA and CHKB expression equally decreased, and relatively higher CHKA than CHKB expression can still contribute to the oncogenic cell survival mechanism [65]. While this hypothesis requires further investigations, it highlights the importance of selective CHKA inhibitors.

The growth inhibitory effect of CHKA siRNA was not mediated by alteration of Akt or Erk phosphorylation, which has been previously shown to be a downstream marker of CHKA inhibition in MDA-MB-468 and HeLa cells [132, 136]. The mechanism of this interaction is unclear, but occurs downstream of PI3K. Furthermore, CHKA does not directly interact with Akt, as shown by co-immunoprecipitation experiments and indicated by a lag time of 8 hours between CHKA inhibition by MN58B and changes in Akt phosphorylation [132]. Different results regarding Akt dephosphorylation in this and previous studies might be due to genetic differences of cell lines, such as PTEN or Akt phosphatase PHLPP expression. The profound antiproliferative effect of ICL-CCIC-0019 in a great variety of lineages with heterogeneous genetic backgrounds (NCI-60 screen) might infer that Akt is — although affected in some cases — not essential to mediate the cytotoxic response.

The importance of CHKA in PtdCho metabolism was further substantiated by the compensatory expression of enzymes of the PEMT pathway, namely ethanolamine kinase 1 and 2 upon CHKA knockdown. Additionally, non-significant upregulation of enzymes of the Kennedy pathway underline the importance for HCT116 cells to have a functional choline-PtdCho axis, to provide enough lipids for proliferation and signalling. Elevated choline catabolic activity in response to CHKA downregulation might suggest a high turnover of lipid second messengers, as some of these enzymes would be involved in generation of DAG and phosphatidic acid.

It was attempted to relate the effects of gene knockdown to a CHKA overexpressing system, which could have also served as a model to test compound selectivity for CHKA over CHKB in a biological context. However, transfection of c-terminally GFP-tagged CHKA or CHKB did not result in functionally active enzymes. While in comparable studies, untagged CHKA was used, c-terminally His-tagged CHKA showed full activity in *Toxoplasma gondii* [213]. Due to the steric involvement of sequences close to the C and N terminal sites in formation of both catalytic cavities [71], it is possible that the GFP tag prevented accurate protein folding, as it was ruled out that the C-terminal tag prevented CHKA dimerisation. Considering the potential formation of complexes with c-Src or EGFR, future studies should explore overexpression without GFP tag.

### **ICL-CCIC-0019 effectively inhibits CHK**

Based on these findings, ICL-CCIC-0019 underwent further pharmacological evaluation to permit its use to elucidate choline biochemistry. Several lines of evidence suggest that the inhibitor is selective for CHK: (i) a kinase screen against 131 human kinases showed minimal inhibition of other kinases, (ii)  $IC_{50}$  in enzyme-based assays,  $EC_{50}$  measuring depletion of PCho formation in whole cells and  $GI_{50}$  determining antiproliferative activity are comparable, and (iii) CHKA is efficiently inhibited *in vivo*, as measured by CHK-specific tracer [ $^{18}F$ ]D4-FCH.

For the first time, a detailed kinase screen has been carried out for a choline-competitive inhibitor and ICL-CCIC-0019 showed low off-target effects against the panel of 131 human kinases. CHKA and CHKB were not available as part of the panel at the time of the screen, and therefore isoform selectivity could not be determined. As indicated above, it can be anticipated that ICL-CCIC-0019 has greater affinity towards CHKA than CHKB due to the conformational differences in the loop connecting helices  $\alpha 9$  and  $\alpha 10$  ( $L\alpha 9\alpha 10$ ) at the deep end of the hydrophobic groove. This loop is folded inwards in CHKA, allowing interaction of the quaternary amine with Glu434, whereas it is positioned away from the groove in CHKB, potentially negatively affecting binding [174].

There is a lack of compound selectivity data of previously published compounds, however, the disparity between  $IC_{50}$  in enzymatic assays,  $EC_{50}$  measuring PCho depletion in cell-based assays and  $GI_{50}$  data suggests off-target effects for these compounds. For example, the most-published inhibitor, MN58B, has an  $IC_{50}$  of 22  $\mu M$  against yeast CHK, an  $EC_{50}$  of 4.2  $\mu M$  to deplete [ $^3H$ ]PCho formation in HT-29 cells after 14 hours of incubation

with drug and a  $GI_{50}$  of 0.5  $\mu\text{M}$  against HT-29 cells [144, 146]. Similarly, CK37 was shown to have an  $IC_{50}$  of around 25  $\mu\text{M}$ ,  $EC_{50}$  of around 7  $\mu\text{M}$  and  $GI_{50}$  of 5–10  $\mu\text{M}$  [149]. While the kinase screen conducted here cannot rule out off-target effects apart from the selected proteins, the tight relation between  $IC_{50}$  (0.27  $\mu\text{M}$ ),  $EC_{50}$  (0.67  $\mu\text{M}$  after 1 hour incubation in HCT116 cells) and  $GI_{50}$  of 0.34  $\mu\text{M}$  against HCT116 cells, are indicative of on-target effects.

ICL-CCIC-0019 showed potent antiproliferative activity against the NCI-60 panel of cell lines, while three normal cell lines were not affected. The superior effect on malignant cells paired with the independence of doubling time and antiproliferative activity suggests that the inhibitor is specific to an oncogenic phenotype and that CHKA has greater roles in malignancy than simply to satisfy cell membrane synthesis requirements. Similar observations were previously made in breast cancer cells [33] and gives hope that this strategy could selectively target tumour cells.

The antiproliferative activity did not correlate with CHKA mRNA expression. While mRNA provides a robust and easily quantifiable parameter, it does not always translate into protein expression and cannot take activating or inhibitory posttranslational modifications in consideration.

### **CHK inhibition induces cell death via ER stress response**

ICL-CCIC-0019 did not rupture cell membranes, as could be expected by structurally related surfactants. This was demonstrated by absence of spillage of cytosolic LDH to the supernatant as a surrogate. A short incubation time of 4 hours and relatively high inhibitor concentrations were chosen, as extracellular pH of the medium or extended culture periods are known to compromise LDH stability [214]. Additionally, it could be shown that ICL-CCIC-0019 did not inhibit CHKA activity by destabilisation of the enzyme complex.

Antiproliferative activity subsequent to CHK inhibition by ICL-CCIC-0019 was triggered by decreased PtdCho synthesis that caused cells to arrest in the G1 phase of the cell cycle and induction of ER stress. The connection between PtdCho synthesis and cell cycle regulation is apparent, as increased availability of membrane lipids is necessary for cell division [215]. Small changes in PtdCho by uncontrolled synthesis would rapidly result in cells with either excess amounts of or deficient membrane surface [215]. In light of the regulation of PtdCho synthesis during the G1 phase of the cell cycle by cyclins A and

E in conjunction with CDK2, a checkpoint for G1/S transition [216–218], CHKA inhibition appears to prevent cells from correct transitioning through this cell cycle checkpoint. Microarray studies have confirmed deregulated expression of genes involved in cell cycle progression upon CHKA overexpression [137] or knockdown [32].

Furthermore, pharmacological CHK inhibition induced ER stress response mechanisms. ER stress is typically caused by accumulation of unfolded proteins or depletion of PtdCho synthesis [155, 156] and culminates in unfolded protein response (UPR). UPR is initiated by activation of at least one of the three effector proteins inositol-requiring protein-1 (IRE1), activating transcription factor-6 (ATF6) or protein kinase RNA (PKR)-like ER kinase (PERK) [156]. PERK promotes the phosphorylation of eukaryotic translation initiation factor-2 alpha ( $eIF2\alpha$ ) to suppress general protein synthesis, but induction of the transcription factors ATF4 and its downstream target CHOP. ICL-CCIC-0019 activated this branch of the UPR with marked dose- and time-dependent increases of ATF4. This enhanced transcriptional activity of CHOP, as confirmed by its nuclear localisation. The temporal evolution of different UPR triggers orchestrates the fate of the response. While concurrent activation of IRE1 $\alpha$  and PERK pathways promote cell survival with the aim of stress resolution, attenuation of the IRE1 $\alpha$  signal and persistent activation of the PERK–CHOP axis commits to cell death via apoptosis or autophagy [219–221]. IRE1 $\alpha$ -mediated UPR was only mildly activated at 24 and 48 hours continuous treatment of ICL-CCIC-0019, but it remains to be elucidated whether apoptosis or autophagy account for cell death response seen at these time points. A complex switch depending on timing and strengths of ATF4 and CHOP signals determines the commitment to either of these cell death pathways [221]. If apoptotic pathways are involved, it is unlikely to be mediated by caspases 3 and 7, as their modest activation was not in proportion to the profound antiproliferative activity. No changes in total protein ubiquitination were observed, but a more detailed characterisation of autophagic effectors are required to further understand possible implications of ICL-CCIC-0019 on this cell death mechanism.

As part of ER stress resolution, chaperon molecules such as HSP70 and HSP90 can be expressed to counteract misfolding of proteins [222]. HSP70 expression was not influenced by ICL-CCIC-0019, while a small increase in HSP90 expression was observed. It is possible, that this response could be profound enough to permit synergistic interaction of combined CHKA and HSP90 inhibition.



### CHK inhibition yields in potent antitumour activity

The compound was then tested for key pharmacological properties that could affect its behaviour *in vivo*. Using human and mouse liver microsomes predicted good compound metabolic stability. The positive charges of ICL-CCIC-0019 restrain its cell permeability, however it was found to have sufficient capabilities to cross membranes with a comparable range to other approved drugs [196]. Plasma protein binding of 64% indicated a balanced equilibrium of bound and free drug fractions [199]. Additionally, ICL-CCIC-0019 did not possess ABC drug resistance transporter substrate activity. Nonetheless, it seems likely that resistance could arise through upregulation of these transporters, as NCI/ADR-RES, an adriamycin-resistant OVCAR-8 variant with high MDR1 expression was least sensitive to the inhibitor. This is further supported by a ca. 10-fold higher sensitivity of HCT116 cells, that express low levels of ABC transporters, compared to HCT15 cells with high ABC transporter expression.

The results obtained to that point warranted further *in vivo* evaluation. Initial dose finding studies revealed that 5–10 mg/kg ICL-CCIC-0019 were tolerated. This is comparable to previously described *bis*-cationic CHK inhibitors, especially MN58B, for which 2–5 mg/kg 3 times a week were described as tolerated doses. [146]. The occurring toxicity was characterised by body weight loss followed by relatively quick recovery in BALB/c mice. BALB/c nude mice displayed greater body weight loss and therefore the initially optimised dosing scheme could not be completed and treatment had to be intermitted. Pharmacokinetic variables demonstrated rapid clearance from the plasma and accumulation in tissues, such as tumour, liver and kidneys. This was also detected by [<sup>18</sup>F]D4-FCH PET imaging and reflected by a relatively large volume of distribution. In spite of the low cellular permeability, the compound was selectively retained in tissues. Potentially, physicochemical properties of ICL-CCIC-0019, such as  $pK_a$ , favour cellular trapping by virtue of differences in ionisation that may not be obvious in the case of an *in vitro* assay with a relatively high extracellular pH of 7.4. Pharmacokinetic data support the notion that dosing schedules to lower  $C_{max}$  and increase exposure are required to achieve the optimal therapeutic index. Mechanisms to reduce liver and kidney retention, e.g. via appropriate formulation, would be helpful for future investigations, although recovery in liver appears to be rapid within 48 hours.

High accumulation in the liver and kidneys was observed in both pharmacokinetic and PET studies, which could account for the body weight changes. Liver accumulation

is unlikely to be related to the intrinsic, charged chemical structure of ICL-CCIC-0019. Neuromuscular blocking agents, which comprise a class of approved drugs that are denoted by *bis*-cationic moieties of quaternary amines, are both renally and hepatically cleared. Importantly, the route of excretion depends on their lipophilicity, with hydrophilic compounds favouring renal and lipophilic compounds hepatic clearance [223]. The structural similarity of ICL-CCIC-0019 to this drug class, suggests that the main route of excretion could be via kidneys and that the compound accumulation in liver may be attributed to specific interaction with choline metabolic pathways in this organ. Unlike neuromuscular blocking agents, ICL-CCIC-0019 is not expected to interact with nicotinic acetylcholine receptors, due to subtle but important structural differences. Neuromuscular blocking agents mimic acetylcholine and therefore usually contain a quaternary amine in proximity to an ester [224]. More specifically, depolarising neuromuscular blockers, like suxamethonium chloride, require a choline ester to be exposed to the receptor as part of their mechanism of action [225]. Non-depolarising neuromuscular blockers, like tubocurarin and atracurium, comprise of larger and more lipophilic quaternary moieties and encompass a more rigid often ester-containing linker [226]. However, if ICL-CCIC-0019 proceeds into clinical evaluation, it would be imperative to assess the interaction with acetylcholine receptors as part of experimental preclinical toxicology studies.

CHKA expression and activity is particularly high in the liver, as this organ is one of the key metabolic sites for lipid — including choline — metabolism and the formation of betaine [41]. As indicated above, strong retention of ICL-CCIC-0019 in liver could therefore be related to specific interactions with CHKA and arrest its physiological roles. If this was the case, this form of on-target toxicity could have profound implications for CHK inhibitors in general. To better understand the effect of CHKA inhibition in hepatic tissues, it will be necessary to monitor the changes in choline-containing metabolites (especially choline, PCho, PtdCho and betaine) and relate them to liver function perturbations. Testing the antiproliferative activity in cell normal liver cell lines could provide preliminary evidence of toxicity in cells with high endogenous choline turnover. It is plausible, however, that if a suitable therapeutic window for the liver can be identified, CHK inhibition could be a viable therapeutic strategy for hepatocellular carcinomas or liver metastasis. The former have been recently shown to have elevated CHKA expression that adversely affect overall survival [227].

PET imaging confirmed the target inhibition *in vivo* by a marked decrease of [<sup>18</sup>F]D4-

FCH uptake compared to controls. Interestingly, despite the rapid tissue distribution, inhibition was strongest after 24–48 hours post single treatment. Potentially, the *bis*-cationic structure required time to homogeneously penetrate areas of a tumour that are further away from vascularisation. Additionally, a lag time might be required to inhibit CHKA and reduce the relatively high intracellular PCho concentrations. The PET imaging-derived data reflected the tissue pharmacokinetic behaviour. In future drug development programs, [ $^{18}\text{F}$ ]D4-FCH PET could therefore serve as a valuable tool to rank compounds according to their affinity to the target *in vivo*, while predicting the tissue biodistribution of major organs. This has advantages over MRS, where only changes in total choline containing metabolites (choline, PCho, GPC) can be detected *in vivo*. Furthermore, PET permitted deeper analysis of the enzymatic modulation by fitting of a kinetic model. Changes in tumour-associated radioactivity were mostly driven by  $K_1$ , the perfusion-dependent rate constant describing flux from the plasma to the tissue. It was anticipated based on previous experiments [110], that  $k_3$  would reflect CHKA inhibition. It appears plausible that because of the very rapid tissue distribution of [ $^{18}\text{F}$ ]D4-FCH, where all tumour-associated tracer is delivered within the first two minutes of imaging, CHKA-mediated retention is indeed more reflected by the initial delivery phase. Potentially, however, the fairly rapid metabolisation of the tracer — albeit lower than [ $^{11}\text{C}$ ]choline — could adversely impact the input function of the kinetic model. The higher rate of metabolism in mice compared to humans may limit the accuracy of the model. Interaction of ICL-CCIC-0019 with choline transporters can also not be ruled out and further studies will be required to fully address choline transporter inhibition.

Target inhibition *in vivo* translated into potent antitumour activity, but not tumour regression. This is comparable to other inhibitors targeting metabolic handling, such as IDH1 inhibitor AGI-5198 [228], the AMP-activated protein kinase (AMPK) agonist phenformin [229], or FASN inhibitor orlistat [230]. As metabolic pathways are very interlinked, alternative routes are likely to compensate. During CHKA inhibition, for example, PEMT pathway via ENTK1 and 2 could take over the roles of PtdCho synthesis or potentially the membrane lipid composition could change with higher content of non-choline containing lipids. This stresses the importance of understanding the metabolic consequences caused by inhibition of a specific pathway to rationally develop combination therapy approaches.

The changes in proliferation could not be predicted at early time points by [ $^{18}\text{F}$ ]FLT. In contrast, treatment increased tracer retention, which is referred to as ‘flare effect’. This

temporal elevation is usually detected upon inhibition of *de novo* DNA synthesis as a consequence of redistribution of the human equilibrative nucleoside transporter type 1 (hENT1) to the cell membrane [231]. The causal link between CHKA and flare [<sup>18</sup>]FLT uptake remains to be elucidated.

These results of pharmacological CHK inhibition were aimed to be cross validated by an inducible shRNA model. While siRNA is a useful tool for *in vitro* research, its short duration of action of about one week makes it unsuitable for *in vivo* experiments. By comparison to constitutive shRNA expression, this approach has the advantage that tumours can be grown without interfering with oncogenic targets before treatment initiation, resembling a clinical scenario. Additionally, engraftment of the cells is not influenced by inhibition of potentially essential targets.

The model showed good knockdown *in vitro* after exposure to DOX, which yielded in about 50% reduction of PCho formation. Previous reports using gene silencing have provided similar results [138, 142, 232]. Residual amounts of kinase appear to be able to generate considerable quantities of PCho, which favours pharmacological inhibitors with high affinity and good pharmacokinetic properties over RNAi, as pharmacological intervention is more likely to result in complete target inhibition.

While shRNA expression was confirmed *in vivo*, it did not downregulate CHKA protein levels and therefore no differences in [<sup>18</sup>F]D4-FCH uptake were seen. While 1 week of DOX dietary supplementation was sufficient to activate RFP expression, it was probably too short to mediate CHKA knockdown. Longer exposures to DOX would be required, but the rapid growth of HCT116 xenografts (tumours reach 50–100 mm<sup>3</sup> ca. 10 days post inoculation) might prove this lineage to be unsuitable.

### **Effects on combined treatment with HDAC inhibitors**

Metabolic pathways are profoundly interlinked and understanding of their connections could permit the rational design of highly effective combination therapies. Combined inhibition of CHK and HDAC was tested due to the activation of CHKA upon pan-HDAC inhibition [100, 101, 210, 211] and found to be synergistic, particularly in the setting of HDAC6-selective inhibition by C1A. The HDAC inhibitors used in this study exert their antiproliferative activity through different mechanisms. In contrast to the pan-HDAC inhibitor vorinostat, which induces G1 arrest and subsequently apoptosis, C1A rapidly and potently triggers apoptosis [3]. The earlier onset of C1A-mediated effects could explain

why this combination was more favourable than with pan-HDAC inhibition.

Previously reported PCho increases in response to pan-HDAC inhibition could not be confirmed. Importantly, past studies were based on MRS, which represents the sum of catabolic and anabolic events, that could confound the effects of CHK activity. Future studies will be required to examine the molecular relationship between CHKA and HDACs.



## Chapter 5

# Affibody PET Imaging of HER2 Expression

This work is associated with [2]:

Trousil S, Hoppmann S, Nguyen Q-D, Kaliszczak M, Tomasi G, Iveson P, Hiscock, Duncan, Aboagye, Eric O. Positron Emission Tomography Imaging with  $^{18}\text{F}$ -Labeled  $Z_{HER2:2891}$  Affibody for Detection of HER2 Expression and Pharmacodynamic Response to HER2-Modulating Therapies. Clin Cancer Res. 2014;20:1632-43.

### 5.1 Introduction

Choline metabolism and the consequences of its inhibition have been mainly examined in breast and lung cancer. Both diseases are characterised by frequent overexpression of the epidermal growth factor receptor family members EGFR and HER2 (also referred to as HER2/neu or ErbB-2) [233]. EGFR and HER2 exert at least part of their transforming capabilities through interaction with the non-receptor tyrosine kinase c-Src, which is overexpressed in  $> 60\%$  of breast cancers [234–236]. As highlighted on page 44, c-Src is the only interaction partner that has been identified to date to directly phosphorylate and activate CHKA [122]. Consequently, human mammary epithelial cell lines that are engineered to express HER2 exhibit increased levels of PCho and total choline containing metabolites compared to their wild-type counterparts, without changes in their doubling times [33]. HER2 expression also dramatically increases the PCho:GPC ratio, a surrogate for ma-

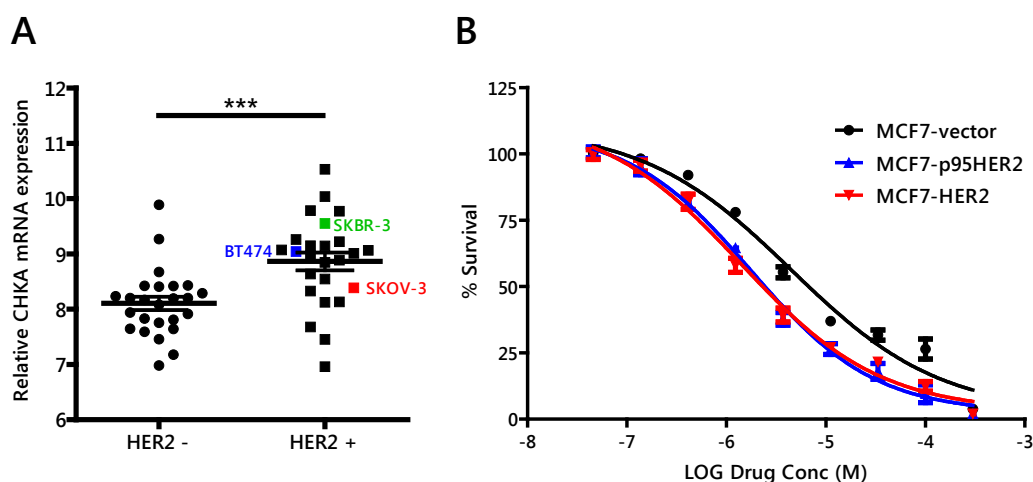


Figure 5.1: Functional interaction between HER2 and CHKA. A, Cell lines of the Cancer Cell Line Encyclopaedia were analysed and ranked by HER2 mRNA expression. The 25 lowest and 25 highest expressing cell lines were investigated for CHKA expression ( $P = 0.0005$ ). Data derived from Cancer Cell Line Encyclopaedia [179]. B, Antiproliferative activity of ICL-CCIC-0019 against MCF7-vector (HER2 negative) and MCF7-p95HER2 (transfected with the truncated but signalling remnant p95HER2) and MCF7-HER2 (transfected with full-length HER2) cells was measured.

ligand transformation [33]. Furthermore, HER2 positive cancer cell lines — including commonly studied BT474, SKBR-3 and SKOV-3 cells — exhibit higher CHKA expression than HER2 negative lineages (Figure 5.1A,  $P < 0.001$ ). As a result, HER2 positive cell lines are more sensitive to CHKA inhibition than HER2 negative lineages (Figure 5.1B). In an isogenic model comprising of HER2 negative MCF7 cells transfected with empty vector (MCF7-vector), truncated but signal remnant p95HER2 (MCF7-p95HER2) or full-length HER2 (MCF7-HER2), treatment with ICL-CCIC-0019 impaired proliferation more in cell lines with functional HER2 signal transduction ( $GI_{50}$  MCF7-p95HER2: 2.54  $\mu\text{M}$  and MCF7-HER2: 2.19  $\mu\text{M}$ ) than in the HER2-negative line ( $GI_{50}$ : 6.05  $\mu\text{M}$ ,  $P < 0.001$  compared to both positive lines). Conversely, patients responding to pharmacologic inhibition of HER2 display reduced [ $^{11}\text{C}$ ]choline uptake by PET imaging [237]. Therefore, patients with HER2 amplification are more likely respond to CHKA inhibition. To identify such patients more readily, and permit the hypothesis to be clinically tested, a novel, non-invasive, PET-imaging-based HER2-targeting diagnostic tool, [ $^{18}\text{F}$ ]GE-226, was developed.

HER2 is a 185 kDa transmembrane receptor and its gene amplification and protein overexpression play pivotal roles in the pathogenesis and progression of many types of cancer. HER2 is overexpressed in around 20% of breast, 15-35% of gastric and 9-32% of ovarian cancers and is correlated with poor survival [238–240]. The protein has conse-



quently emerged in recent years as an important predictive biomarker and target of cancer therapy [241]. Homo- or heterodimerisation with other members of its family prompts activation of the intracellular tyrosine kinase domain and triggers cell survival and proliferation mediated through MAPK and Akt signalling pathways [242, 243].

Available HER2-targeted therapies in the clinic include antibodies, such as trastuzumab (Herceptin, Genentech) and pertuzumab (Perjeta, Genentech), which prevents receptor dimerisation, antibody–drug conjugates, such as T-DM1 (Kadcyla, Genentech) or small molecule inhibitors targeting the tyrosine kinase domain (e.g., lapatinib, Tyverb, Glaxo-SmithKline; a dual HER2 and EGFR inhibitor). Proteolytic shedding of the extracellular domain or alternative splicing in limited cases can generate a truncated, signalling remnant p95HER2 domain, which presents one potential mechanism of resistance to anti-HER2 therapies [244]. Although trastuzumab forms the mainstay of anti-HER2 targeted therapies, it does not reverse HER2 protein expression in patients [245, 246]. Inhibitors of the molecular chaperone HSP90, which elicit HER2 proteasomal degradation, are therefore currently under investigation in this context. A phase II clinical trial of one such inhibitor, NVP-AUY922 (Novartis), has recently been completed in patients with HER2 or ER positive locally advanced or metastatic breast cancer (NCT00526045).

Accurate testing of HER2 status is crucial for patient stratification to identify individuals that may benefit most from such targeted therapies. However, this can be intricate as HER2 expression may vary through progression from primary to secondary disease with locoregional and distant recurrences often not being amenable to biopsy [247]. Furthermore, recent studies have highlighted spatial heterogeneity as a potential source of incorrect assessment [248]. The vast majority of FDA-approved diagnostics are based on immunohistochemistry (IHC) and fluorescence in situ hybridisation (FISH). IHC determines the HER2 protein expression in formalin-fixed paraffin embedded (FFPE) tumour biopsies, while FISH detects HER2 gene amplifications, which are considered a legitimate surrogate as HER2 overexpression is generally caused by copy number variations [249]. The utility of serum-based alternatives by detecting soluble extracellular domains is also under investigation [250].

Tumour marker-targeted molecular imaging using radiolabeled Affibodies, which are non-immunoglobulin-derived affinity proteins, might provide an accurate and non-invasive alternative to HER2 molecular diagnostics. Affibodies are engineered as three-helix bundle Z proteins derived from the staphylococcal protein A [251]. They are characterised by

nano- to picomolar binding affinities, small size of ca. 6.5 kDa compared to antibodies or antibody fragments (ca. 20–150 kDa), and short plasma residence time, thus permitting rapid and homogenous tissue distribution. Consequently, high contrast images can be obtained within the first hour or two of administration [252, 253]. Due to their favourable pharmacokinetic properties, these molecules are suitable for radiolabeling with short-lived radioisotopes by comparison with full IgG antibodies.

Here, it is demonstrated that the HER2-targeting Affibody [ $^{18}\text{F}$ ]GE-226 provides a viable strategy to determine differential HER2 expression irrespective of lineage or pre-treatment with trastuzumab within one hour after injection. Insights into the kinetic characteristics of the Affibody interaction with HER2 are provided using full length versus p95HER2 transfected cells and siRNA HER2 as controls, or HSP90 inhibitor treatment to degrade HER2.

## 5.2 Affibody-HER2 binding properties

To ensure the fluorinated prosthetic group does not adversely influence the Affibody binding kinetics, the receptor interaction of the isotopically unmodified Affibody analogue was measured using surface plasmon resonance and compared to binding of human full-length and truncated p95HER2, as well as rhesus and rat full-length HER2 (Figure 5.2). While the tracer showed very strong binding to human ( $K_D = 76$  pM) and rhesus HER2 ( $K_D = 67$  pM), it did not interact with p95HER2 or rat HER2 (Table 5.1).

Table 5.1: Summary of GE-226 binding kinetics to human and rhesus HER2.

Kinetic properties	Human HER2	Rhesus HER2
On-rate $k_{\text{on}}$	$1.73 \times 10^7 \text{ M}^{-1} \text{ s}^{-1}$	$6.37 \times 10^6 \text{ M}^{-1} \text{ s}^{-1}$
Off-rate $k_{\text{off}}$	$1.31 \times 10^{-3} \text{ s}^{-1}$	$4.25 \times 10^{-4} \text{ s}^{-1}$
Affinity $K_D$	$7.58 \times 10^{-11} \text{ M}$	$6.67 \times 10^{-11} \text{ M}$
Rmax	133.5	138.1
Chi-Square $\chi^2$	0.607	1.12
U-value	3	7

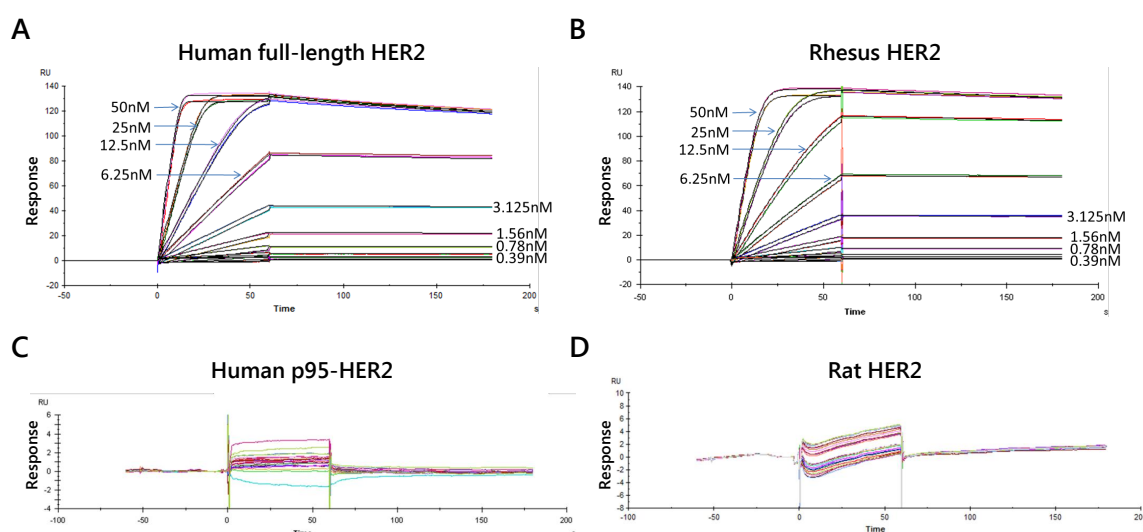


Figure 5.2: Interaction of GE-226 with HER2 as determined by surface plasmon resonance. GE-226 binds with high affinity to human (A) and rhesus (B) HER2, but not to human p95HER2 (C) or rat HER2 (D). Data were obtained from Syngene.

### 5.3 [ $^{18}\text{F}$ ]GE-226 exhibits specific and lineage-independent HER2 binding

The tracer retention was tested in 10 different cell lines derived from breast, upper gastrointestinal tract and ovarian cancer, of which half were HER2 negative and the other half HER2 positive. The panel included an isogenic model comprising of HER2 negative MCF7 cells, which were transfected with empty vector (MCF7-vector), p95HER2 (MCF7-p95HER2) or full-length HER2 (MCF7-HER2). While all HER2 negative and p95HER2 transfected cell lines had only marginal background uptake ( $1.2 \pm 0.5\%$  applied radioactivity per mg protein across all lines), all HER2 positive cell lines retained the tracer at high levels (between  $13.6 \pm 3.4$  and  $79.9 \pm 12.1\%$  applied radioactivity per mg protein) and in good agreement with endogenous HER2 expression. Tracer binding was, however, independent of expression of another epidermal growth factor receptor family member, EGFR. Figure 5.3A shows one representative uptake experiment, as initial experiments revealed that the uptake was dependent on the specific activity. In comparison to freshly prepared [ $^{18}\text{F}$ ]GE-226, the same radiotracer preparation yielded only  $39.5 \pm 8.5$  and  $24.9 \pm 3.8\%$  tracer uptake if incubation was initiated 70 and 140 minutes later (Figure 5.3B). Transient siRNA-mediated knockdown of HER2 decreased tracer uptake compared to non-targeting scramble control (Figure 5.3C,  $100 \pm 12\%$  versus  $18 \pm 9\%$ ,  $P < 0.0001$ ). Target knockdown was confirmed by western blot. To further investigate

the specificity of the signal, SKOV-3 cells were co-incubated with tracer and large excess (ca. 2000 fold) of its non-radioactive  $^{19}\text{F}$ -labelled analogue (Figure 5.3D). This reduced uptake to  $3.1 \pm 2.6\%$  compared to control cells ( $100 \pm 12\%$ ;  $P < 0.0001$ ).

#### **5.4 $[^{18}\text{F}]\text{GE-226}$ exhibits a different binding site than trastuzumab and predicts detection of HER2 degradation by NVP-AUY922**

An important question when developing a HER2-targeting imaging probe is whether the tracer can correctly determine the HER2 status of a patient independently of potential trastuzumab treatment. Pre-treatment of SKOV-3 cells with  $10 \mu\text{M}/\text{mL}$  trastuzumab for 1 hour did not alter tracer binding, however, incubation for 24 hours prior to uptake experiment reduced tracer binding by  $32 \pm 11\%$  compared to drug-naïve controls (Figure 5.4A;  $P < 0.0001$ ).

It was investigated, whether HER2 degradation consequent to HSP90 inhibition (HER2 is a client protein of HSP90 [254]) would result in detectable changes in tracer uptake. The HSP90 inhibitor NVP-AUY922 caused a dose-dependent decrease of HER2 protein expression compared to untreated controls, which consequently translated into reduced tracer uptake, further supporting its specificity (Figure 5.4B;  $P < 0.0001$  for all tested concentrations compared to control).

#### **5.5 $[^{18}\text{F}]\text{GE-226}$ discriminates differential HER2 expression *in vivo***

Based on the *in vitro* data, the ability of the tracer to distinguish varying degrees of HER2 expression in the complex tumour milieu *in vivo* was investigated. Figure 5.5A shows representative small-animal  $[^{18}\text{F}]\text{GE-226}$  PET images of SKOV-3 and MCF7-vector xenograft-bearing mice. High tumour uptake contrasts the low non-specific retention in the body. Across different tumour models, the tracer discriminated well between HER2 positive and negative xenografts. Both tumour-specific distribution and retention kinetics accounted for these differences. While HER2 negative MCF7-vector and MCF7-p95HER2 xenografts exhibited low tumour retention and a steady-state tissue radioactivity after initial delivery, HER2 positive xenografts had increased uptake and followed a pattern

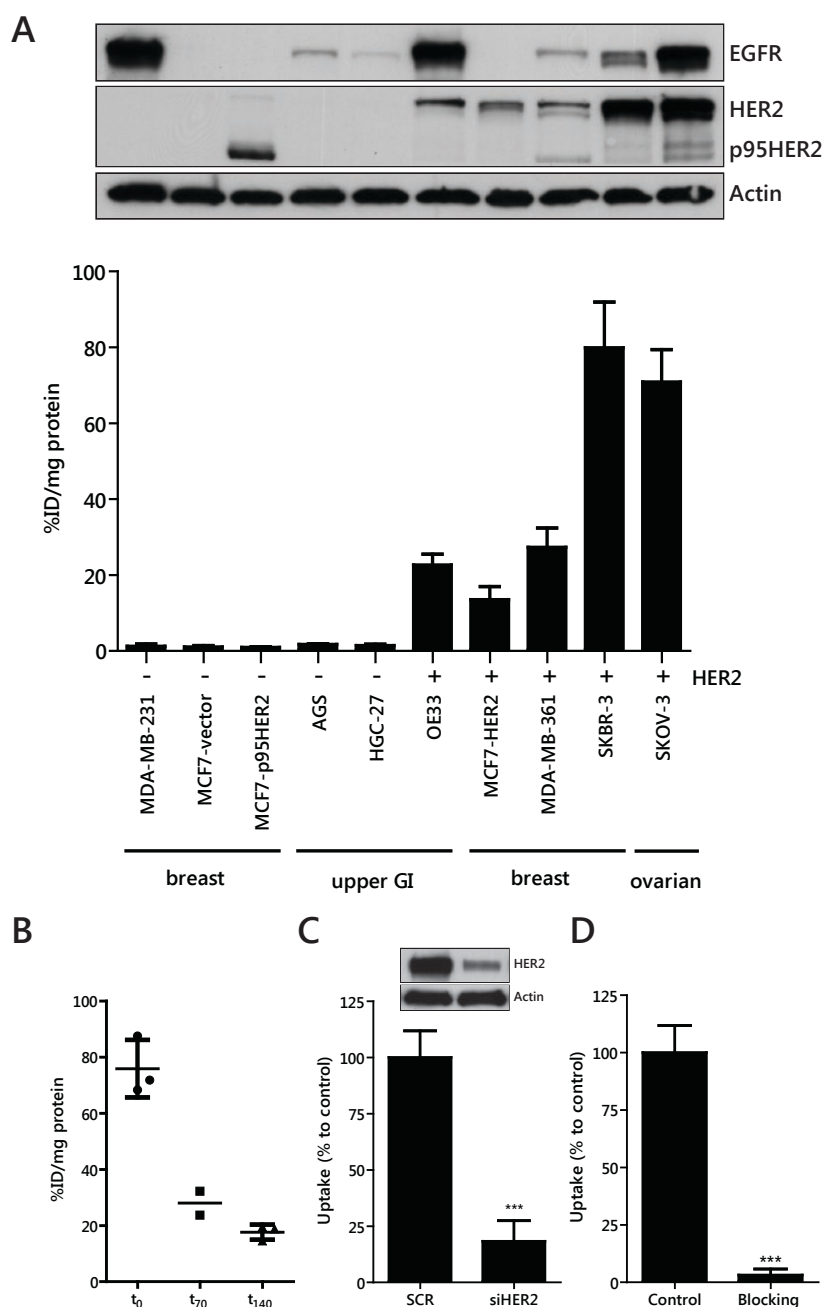


Figure 5.3: [ $^{18}\text{F}$ ]GE-226 binds with high selectivity and sensitivity to HER2. A, Cell lines of diverse lineages and differential HER2 status were exposed to [ $^{18}\text{F}$ ]GE-226 for 60 minutes and retained radioactivity measured as percent applied radioactivity normalised to total protein (mean of  $n = 1$  with 5–6 replicates  $\pm$  SD). Full-length and truncated p95 HER2 protein expression as determined by western blot is shown for the same cell lines in the panel above. B, SKOV-3 cells were pulsed with 740 kBq/mL [ $^{18}\text{F}$ ]GE-226 either immediately upon receipt of tracer ( $t_0$ ; typically 2–3 h after synthesis), 70 min ( $t_{70}$ ) or 140 min ( $t_{140}$ ) after first incubation and cell-bound radioactivity measured. The amount of cold GE-226 Affibody per well was ca. 50 ng at the start of the experiment and ca. 80 and ca. 130 ng at 70 and 140 min, respectively. Mean of  $n = 1$  in at least duplicate. Error bars: SD. C, HER2 expression was transiently abrogated by siRNA and tracer retention after 60 minutes compared to non-targeting scramble control (mean of  $n = 3$  in triplicate on three different days  $\pm$  SD,  $P < 0.0001$ ); knock-down confirmed by western blot. D, SKOV-3 cells were incubated with [ $^{18}\text{F}$ ]GE-226 in the presence or absence of 0.5 mg/mL blocking dose of isotopically unmodified GE-226 for 60 minutes and cell-bound activity measured (mean of  $n = 3$  in triplicate on three different days  $\pm$  SD,  $P < 0.0001$ ).

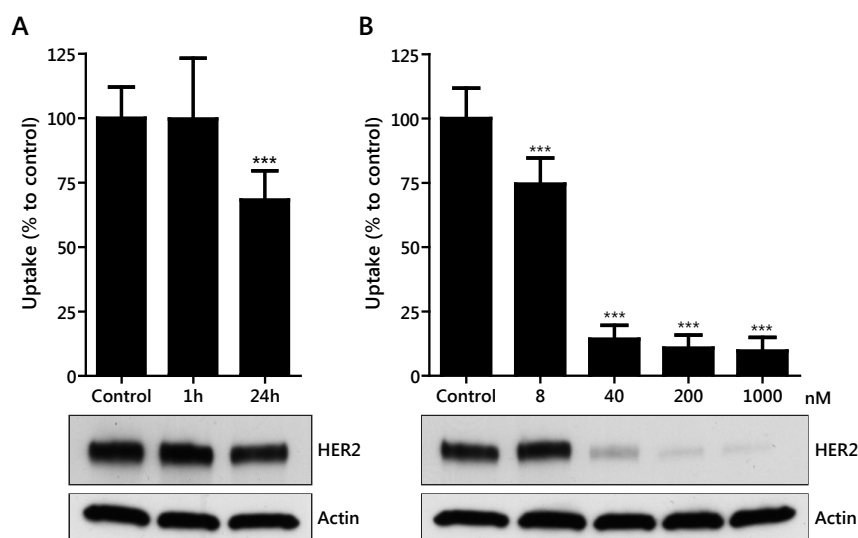


Figure 5.4: [ $^{18}\text{F}$ ]GE-226 possesses a different binding site than trastuzumab and detects HER2 degradation upon HSP90 inhibition. A, SKOV-3 cells were treated with 10  $\mu\text{M}/\text{mL}$  trastuzumab for 1 or 24 hours and incubated for an additional hour with [ $^{18}\text{F}$ ]GE-226 and retained activity compared to untreated controls ( $^{***} P < 0.0001$ ; mean of  $n + 5$  in triplicate on five different days  $\pm$  SD). Effect on HER2 protein expression is shown in the panel below. B, Effect of HSP90 inhibitor NVP-AUY922 on HER2 expression and consequent impact on tracer uptake ( $P < 0.0001$  for all concentrations compared to control; mean of  $n + 3$  in triplicate on three different days  $\pm$  SD).

of net irreversible binding (Figure 5.5B–C). Thus [ $^{18}\text{F}$ ]GE-226 PET was able to distinguish HER2-negative (MCF7-vector and MCF7-p95HER2) from low (MCF7-HER2) and moderately (MDA-MB-361) HER2-expressing xenografts. However, tissue radioactivity was comparable in tumours with moderate and highly (SKOV-3) HER2-expression when simple measures of uptake were employed for PET analysis (Figure 5.5B–C). Nonetheless, radiotracer uptake correlated well with HER2 protein expression as determined by ELISA ( $r^2 = 0.78$ ; Figure 5.5D–E).

The tracer was metabolically stable and predominately and rapidly excreted via the renal route (Figures 5.6 and 5.7).

It was hypothesised that kinetic modelling, which accounts for tissue uptake relative to plasma as opposed to tissue uptake alone, could further help discern the various HER2 groups. A two-tissue irreversible compartmental model was employed to derive the net irreversible uptake rate constant,  $K_i$  (Figure 5.8A). No metabolite correction was necessary as the tracer was stable *in vivo* (Figure 5.6A). With this model, all groups could be distinguished, even MDA-MB-361 from SKOV-3 xenografts (Figure 5.8A). As expected,  $K_i$  highly correlated with  $\text{NUV}_{60}$  among all groups ( $r^2 = 0.82$ ;  $P = 0.008$ ; Figure 5.8B). Figure 5.8C–F shows other pharmacokinetic parameters.

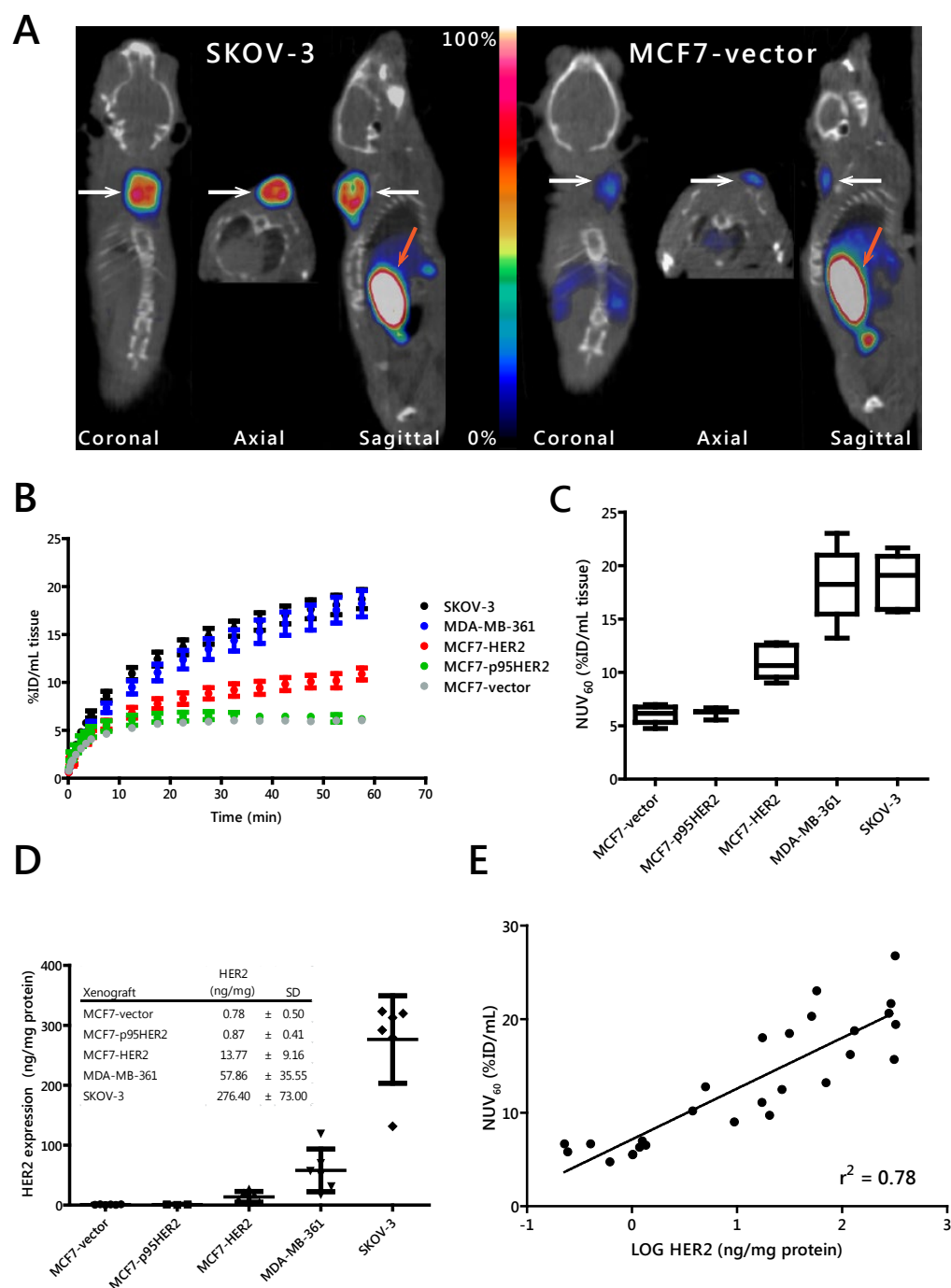


Figure 5.5: Tumour profiles of [ $^{18}\text{F}$ ]GE-226 in differentially HER2 expressing xenograft models. A, Representative OSEM3D reconstructed PET-CT images of SKOV-3 and MCF7-vector xenograft-bearing mice. White arrow indicates tumour, orange arrow kidney. B, Comparison of tumour time versus radioactivity curves in indicated xenograft models (mean of  $n = 6 \pm \text{SEM}$  with exception of MCF7-p95HER2  $n = 3 \pm \text{SEM}$ ). C, Box plot representing  $\text{NUV}_{60}$  values of [ $^{18}\text{F}$ ]GE-226 in various xenograft models.  $\text{NUV}_{60}$  is a measure of retained radioactivity in a defined region of interest (tumour) 60 minutes after tracer administration. The box extends from the 25<sup>th</sup> to 75<sup>th</sup> percentile, with the line in the middle representing the median. The whiskers indicate the highest and the lowest value. D, HER2 expression in various xenograft models as determined by ELISA on tumour samples that were excised post imaging. E, Correlation between  $\text{NUV}_{60}$  and HER2 expression as determined by ELISA on tumour samples.

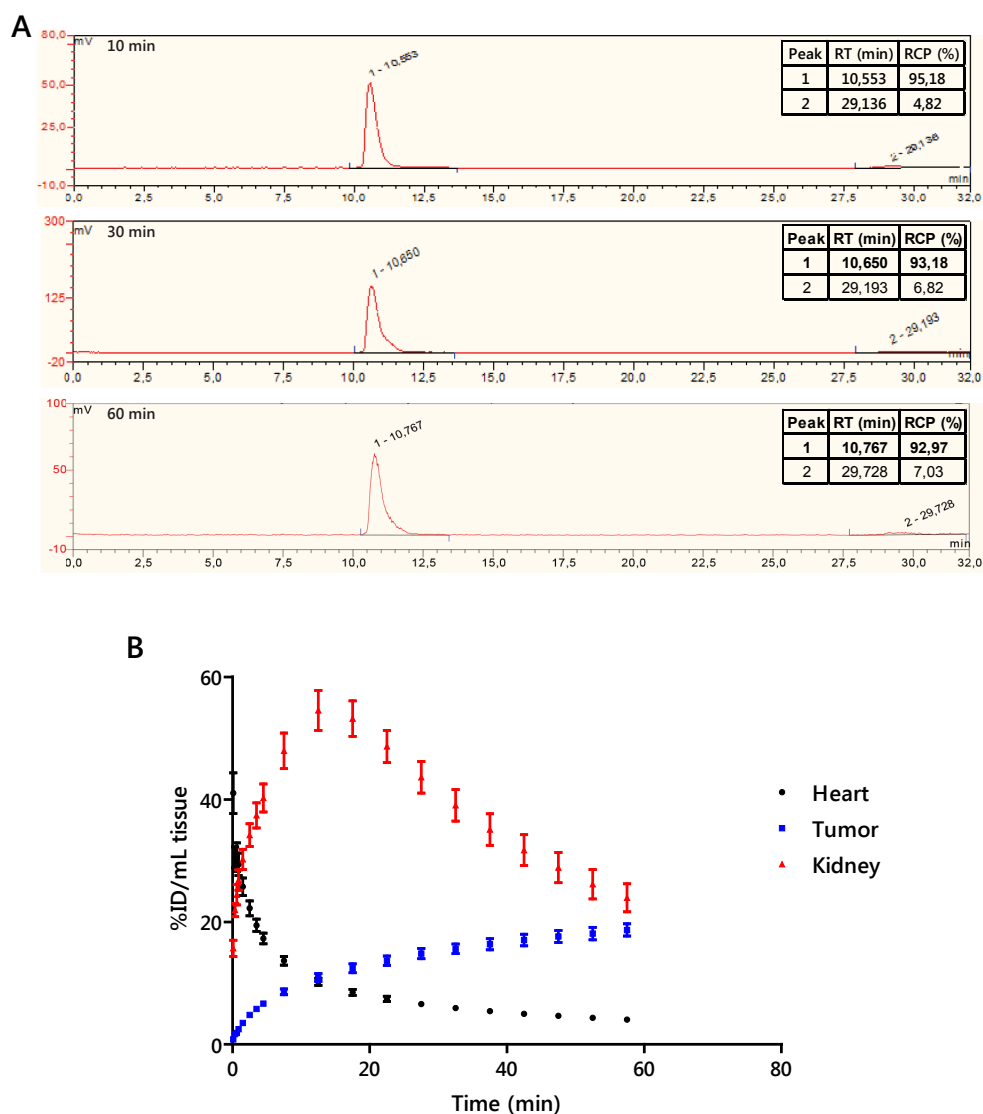


Figure 5.6: Plasma metabolite profile and tissue pharmacokinetics of [ $^{18}\text{F}$ ]GE-226. A, Rats were administered 20 MBq [ $^{18}\text{F}$ ]GE-226 i.v. and metabolites quantified by radio-HPCL 10, 30 and 60 minutes post injection. Metabolic stability was assessed by comparison of parent peak (retention time (RT) ca. 10.6 minutes) with metabolites (RT ca. 29 minutes) and is represented as percent radiochemical purity (RCP). Data provided by GE Healthcare. B, Time versus radioactivity curves derived from PET data for uptake in heart, tumour and kidneys in SKOV-3 xenograft bearing mice (mean of  $n = 6 \pm \text{SEM}$ ).

To lend further support to the specificity of the Affibody, blocking studies were carried out by injecting 30 mg/kg isotopically unmodified GE-226 i.v. 20 minutes prior to PET scan (ca. 100-fold mass equivalent of hot tracer). The cold ligand, by blocking specific binding sites, resulted in significantly reduced tracer uptake (NUV<sub>60</sub>  $18.7 \pm 2.4$  versus  $7.1 \pm 1.6$  in controls and blocked tumours,  $P = 0.0003$ ) and  $K_i$  (Figure 5.9). It is noteworthy that the kinetics of tracer uptake were distinctly different between controls and blocked samples, in that the latter share characteristics of HER2 negative tumours.



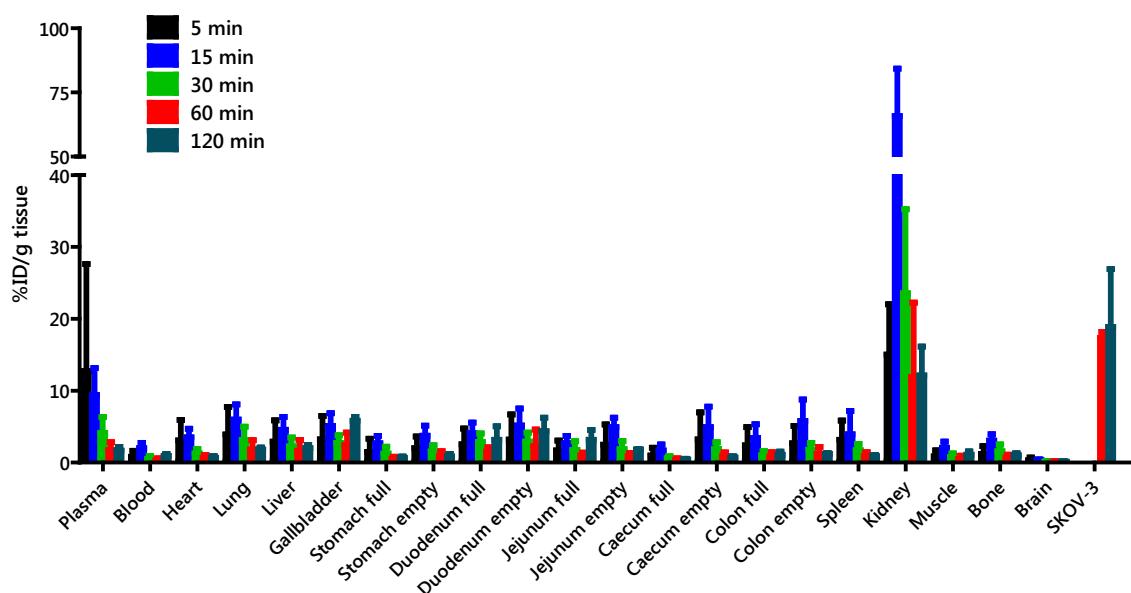


Figure 5.7: Biodistribution of  $[^{18}\text{F}]$ GE-226 in tumour-bearing BALB/c nude mice. Tissues were excised at indicated time points and associated radioactivity measured on a gamma counter. Uptake is expressed as %ID/g tissue  $\pm$  SD ( $n = 3$  per time point).

## 5.6 Localisation and intensity of fluorescein-labelled GE-226 correlates with DAKO HercepTest

To examine tissue localisation, GE-226 was labelled with fluorescein and its localisation and fluorescent intensity in tumour sections compared with FDA approved DAKO HercepTest. In contrast to PET experiments, normalisation to injected dose is not possible with fluorescent compounds. To eliminate inter-subject variability, experiments were performed in bilateral tumour-bearing mice. Because HER2 positive and negative xenografts described in Figure 5.5 have greatly varying growth rates and require differential hormonal treatments, A431 (HER2 negative) and NCI-N87 (HER2 positive) xenografts were employed as previously described [160]. A mixture of 20 mg/kg Hoechst and 15 mg/kg fluorescein-conjugated GE-226 in PBS were injected i.v. and two hours post injection, tumours were excised, formalin fixed and paraffin embedded and adjacent tumour sections prepared for HercepTest staining or fluorescent microscopy. Tissue processing for immunofluorescence microscopy removed any unbound tracer and signal therefore accounts only for specific HER2-Affibody interaction. Figure 5.10 shows that fluorescent staining co-localised with regions that are HER2 positive in NCI-N87 tumours and that both HercepTest and fluorescent staining in A431 tumours were negligible.

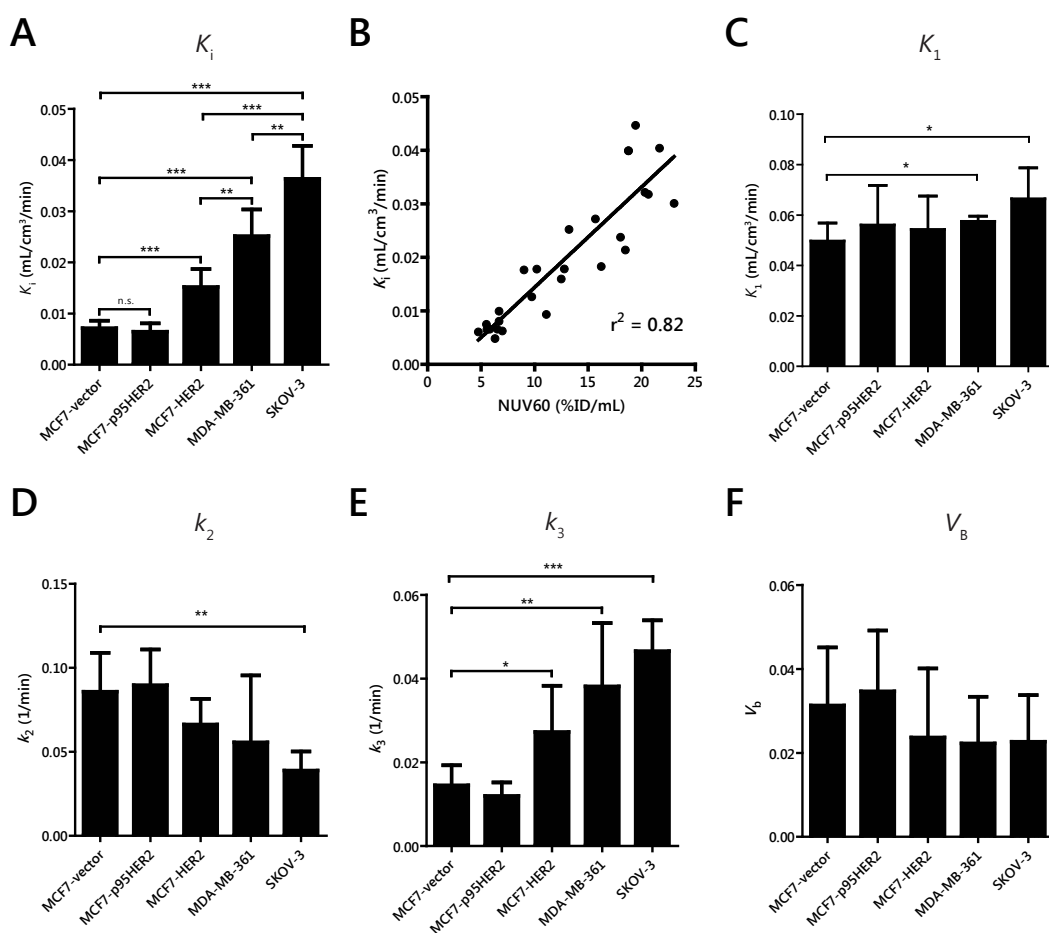


Figure 5.8: Tissue pharmacokinetic analysis using a single input 2-tissue 3k model. A,  $K_i$ , the rate constant for the net irreversible retention of the tracer in the tumour. B, Correlation between NUV<sub>60</sub> and  $K_i$  to support validity of the kinetic model. C–F, Kinetic parameters of [<sup>18</sup>F]GE-226 binding in these xenografts. Graph shows mean of  $n = 6$  per group with exception of MCF-P95HER2  $n = 3 \pm$  SD. Statistical significance was determined by one-way ANOVA with Bonferroni's Multiple Comparison test. \*  $P < 0.05$ ; \*\*  $P < 0.01$ ; \*\*\*  $P < 0.001$ . Mathematical modelling was carried out with help of Dr. Giampaolo Tomasi.

## 5.7 [<sup>18</sup>F]GE-226 can correctly assess HER2 status independently of prior trastuzumab treatment and predicts for response to NVP-AUY922 *in vivo*

SKOV-3 tumour bearing mice were treated with three doses of trastuzumab and imaged 2 hours post initial dose and re-imaged 48 hours after last treatment (i.e. 7 days after initial scan). Neither treatment adversely affected tumour tracer retention (Figure 5.11A), albeit 7 days of continuous treatment reduced  $K_i$  by 24% ( $P = 0.025$ ) as a consequence of elevated arterial input function and altered renal excretion (Figure 5.11B–F). This confirmed by comparison to trastuzumab, that the Affibody possesses different HER2 binding sites.

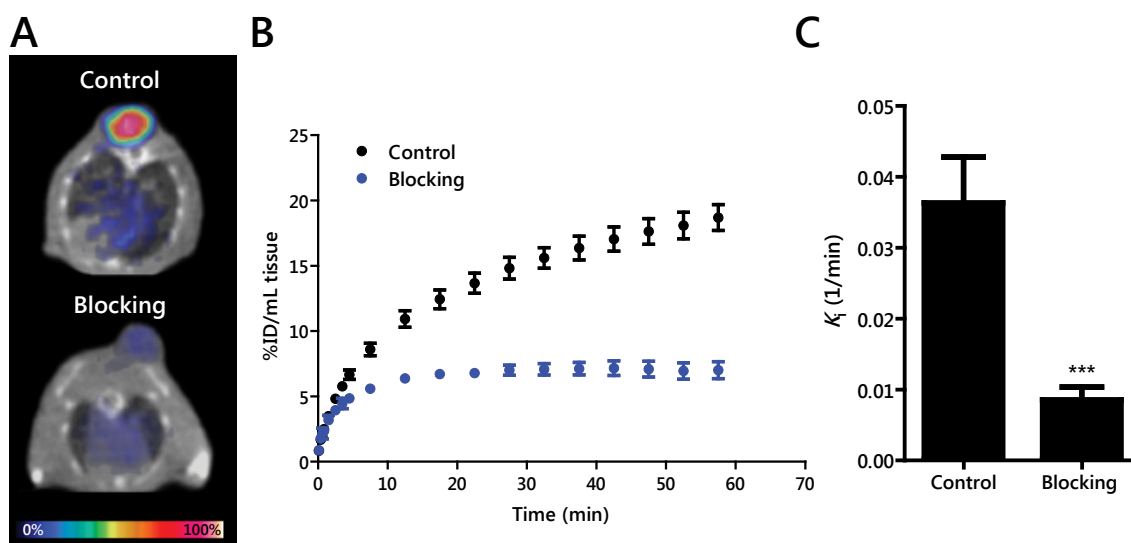


Figure 5.9: Specificity of  $[^{18}\text{F}]$ GE-226 receptor interaction was determined by blocking studies. SKOV-3 xenograft bearing mice were treated with 30 mg/kg cold isotopically unmodified GE-226 in PBS i.v. 20 minutes before PET scan and compared to untreated controls. A, Representative axial PET-CT images of mice treated with or without blocking dose. B, Graph shows mean tumour time versus radioactivity curves of  $n = 6$  per group  $\pm$  SEM. C, Kinetic analysis of blocking experiment.  $P < 0.0001$ . Mathematical modelling was carried out with help of Dr. Giampaolo Tomasi.

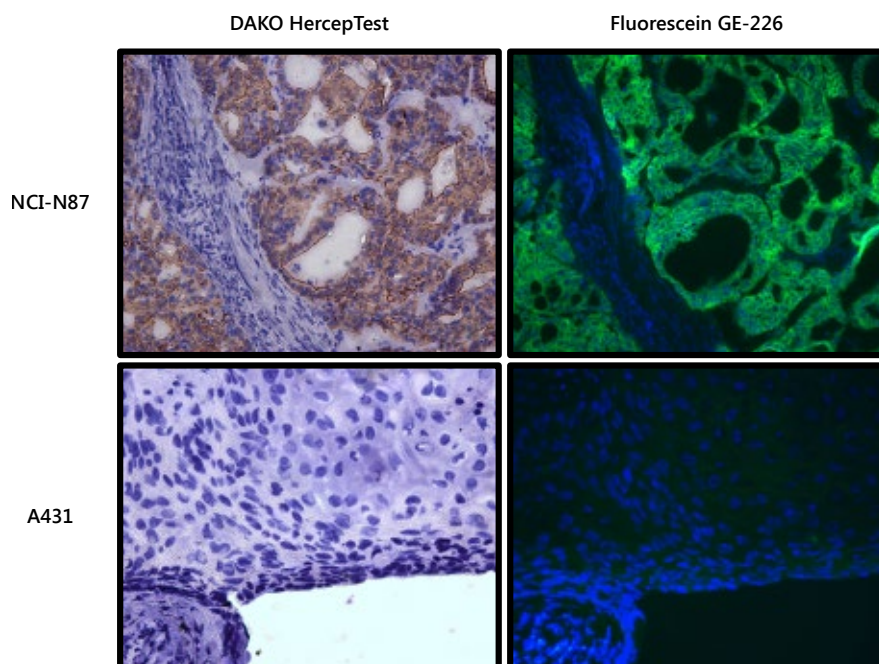


Figure 5.10: GE-226 co-localises with HER2 protein expression in tumours with spatial heterogeneity. GE-226 was labelled with fluorescein and injected in mice bearing both NCI-N87 and A431 tumours, which express high and low levels of HER2, respectively. Tumours were sectioned and adjacent slides either stained with DAKO HercepTest or used for immunofluorescent microscopy. Staining was conducted at GE Healthcare.

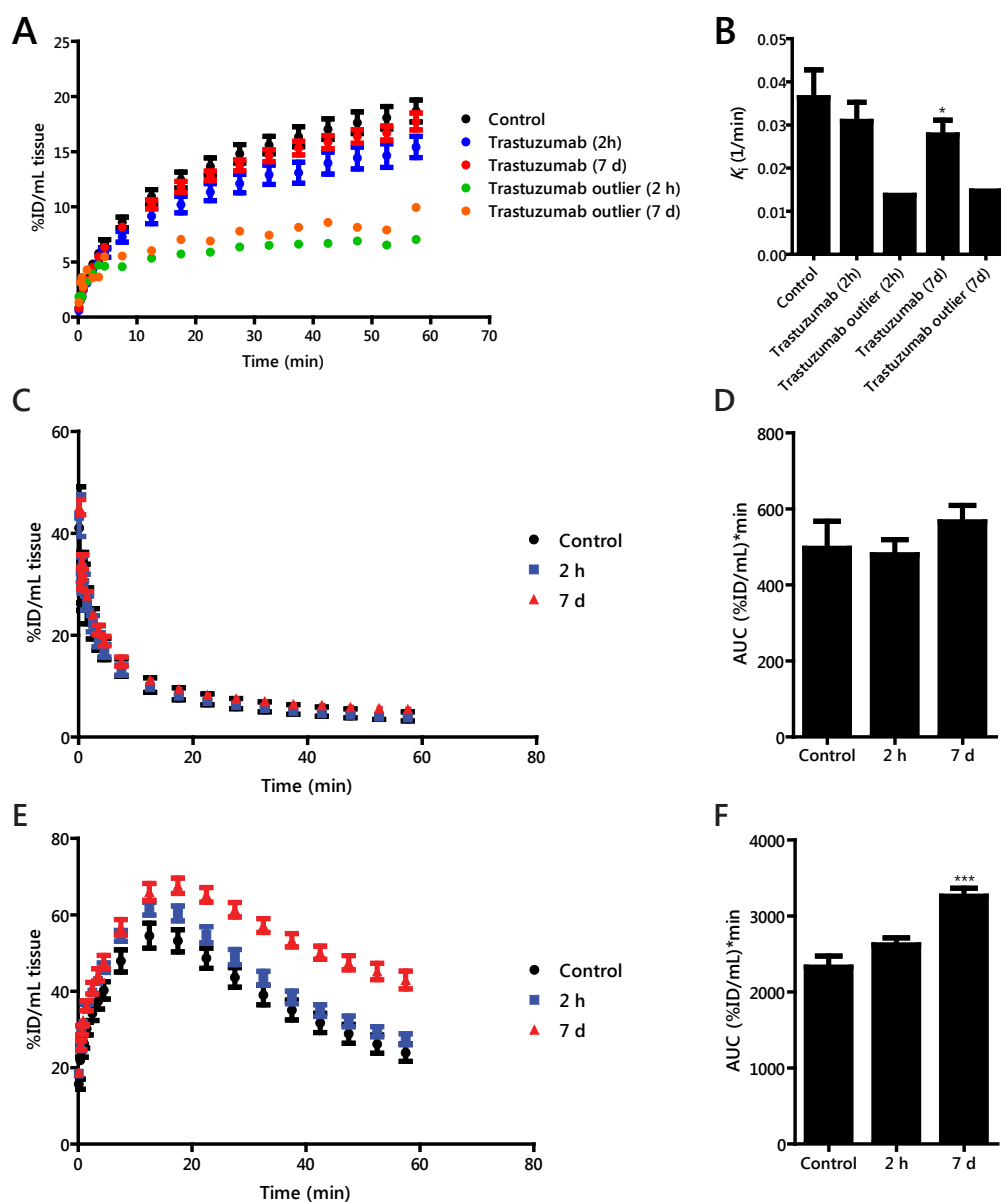


Figure 5.11:  $[^{18}\text{F}]\text{GE-226}$  binding does not interfere with trastuzumab treatment. A, Mice bearing SKOV-3 xenografts were treated with 50 mg/kg trastuzumab i.v. 2 hours prior to scan. Animals were recovered, treated twice more with 25 mg/kg trastuzumab and re-imaged 7 days after initial scan (mean of  $n=6 \pm \text{SEM}$ ). One mouse, which was an outlier with low tracer uptake both on early and late scan, is displayed separately. B, Pharmacokinetic analysis of A ( $P=0.025$ ). TACs and  $\text{AUC}_{0-60}$  for uptake in heart (C, D) and kidney (E, F) of drug-naïve or trastuzumab-treated SKOV-3 xenograft bearing mice ( $***P=0.0004$ ). Mathematical modelling was carried out with help of Dr. Giampaolo Tomasi.

Interestingly, one mouse had significantly reduced uptake on both scans and was viewed separately for analysis. Tracer uptake could not be correlated with ELISA-derived HER2 expression values, as one of the ELISA antibodies interfered with bound trastuzumab. Therefore, western blot confirmed that trastuzumab treatment did not substantially alter

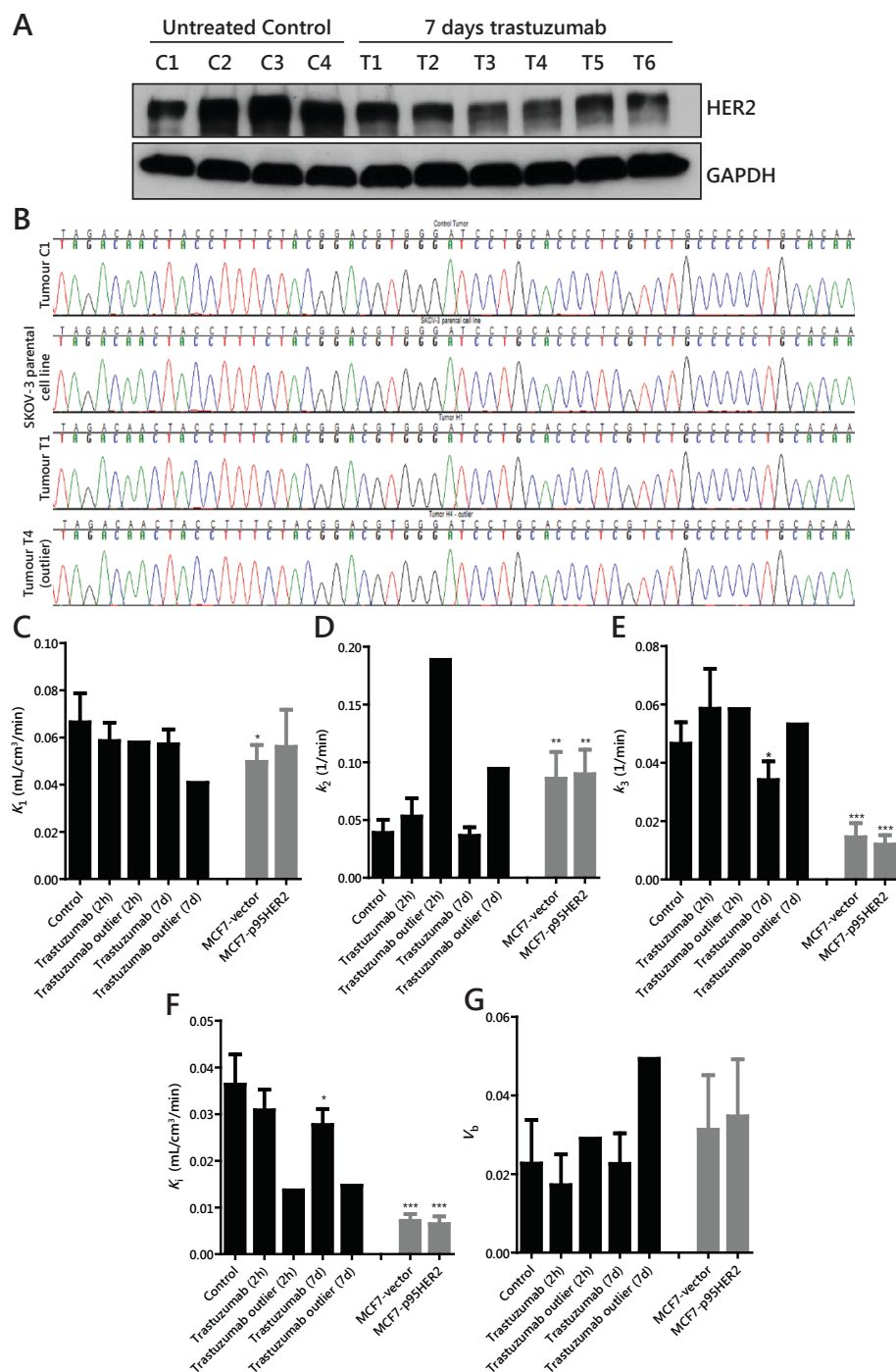


Figure 5.12: HER2 expression analysis and genomic DNA sequencing in relation to uptake rate constants in trastuzumab-treated or control xenografts. A, HER2 protein expression in SKOV-3 tumors after 7 days of treatment with trastuzumab. C1–4, representative controls, T1–6, trastuzumab treated samples, T4, outlier PET imaging. B, Aligned sequences of exon 8 of HER2 surrounding the region coding for amino acids 309 and 310. Samples include untreated control SKOV-3 xenograft (C1), parental SKOV-3 cell line, trastuzumab-treated xenograft with normal [<sup>18</sup>F]GE-226 uptake (T1) and outlier sample (T4, outlier). C–G, Kinetic parameters  $K_1$ ,  $k_2$ ,  $k_3$ ,  $K_i$  and  $V_b$  of controls and trastuzumab-treated SKOV-3 tumors in comparison to HER2-negative, drug-naïve xenografts (grey bars). Statistical significance was determined by comparison of each group to untreated SKOV-3 controls; \*  $P < 0.05$ , \*\*  $P < 0.01$ , \*\*\*  $P < 0.001$ . Mathematical modelling was carried out with help of Dr. Giampaolo Tomasi.

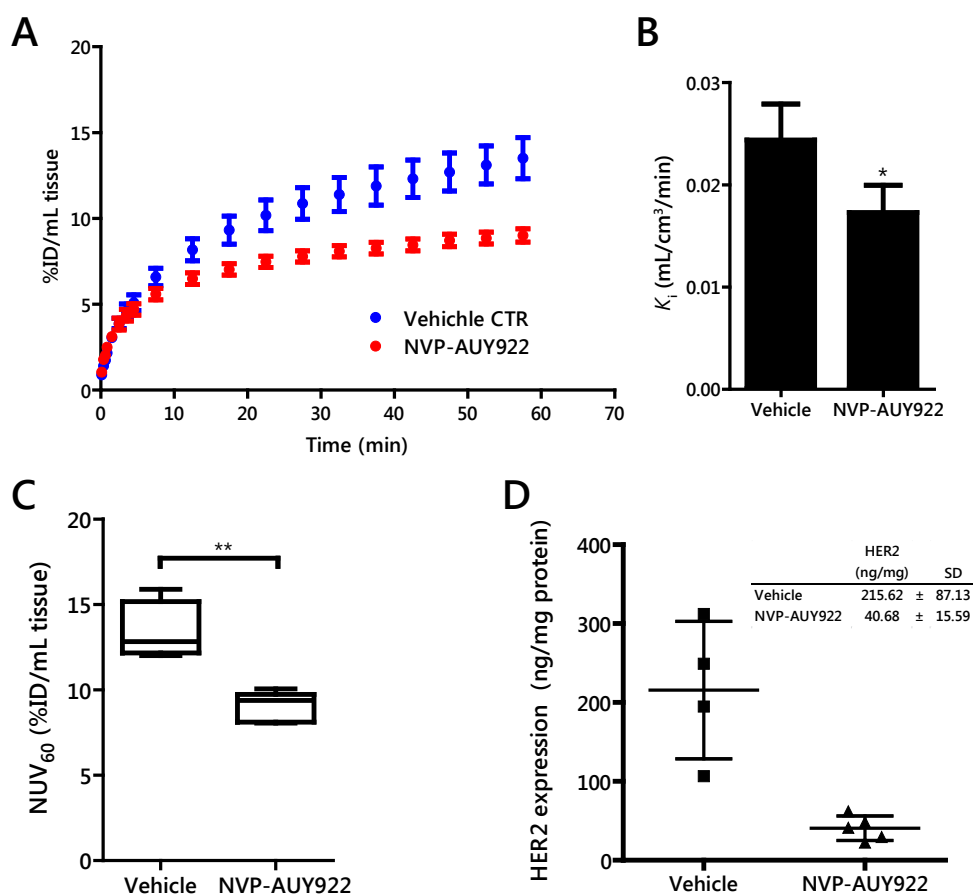


Figure 5.13: [<sup>18</sup>F]GE-226 can predict response to HSP90 inhibition. A, Comparison of NVP-AUY922 treatment (mean of  $n = 5 \pm \text{SEM}$ ) to vehicle treated controls (mean of  $n = 4 \pm \text{SEM}$ ) in the SKOV-3 xenograft model and B, kinetic analysis of inhibition constants ( $P = 0.011$ ). C, Box plot representing  $\text{NUV}_{60}$  values. The box extends from the 25<sup>th</sup> to 75<sup>th</sup> percentile, with the line in the middle representing the median. The whiskers indicate the highest and the lowest value. D, HER2 expression in SKOV-3 tumours after treatment with 3 doses of 50 mg/kg NVP-AUY922 in comparison to vehicle (10% DMSO and 5% Tween-20 in PBS). Mathematical modelling was carried out with help of Dr. Giampaolo Tomasi.

HER2 expression nor resulted in expression of truncated P95HER2 in the outlier sample (Figure 5.12A). Sequencing exon 8 of HER2, which has been previously described as a site for mutations on the extracellular domain of HER2 [255], indicated no sequence alterations in the outlier sample compared to controls (Figure 5.12B). Furthermore, kinetic modelling revealed increased tissue efflux ( $k_2$ ) of the outlier with similarities to HER2 negative tumours, suggesting a loss of interaction of the Affibody with its target (Figure 5.12C-G).

Finally, it was assess whether [<sup>18</sup>F]GE-226 is responsive to HSP90 inhibitor treatment *in vivo*. SKOV-3 xenograft bearing mice were treated with 3 doses of 50 mg/kg NVP-AUY922 or vehicle. This led to reduced HER2 expression with consequently decreased tracer uptake (Figure 5.13).

## 5.8 Discussion

With aid of kinetic modelling, it was demonstrated that the  $Z_{HER2:2891}$  Affibody, [ $^{18}\text{F}$ ]GE-226, quantitatively discriminates between HER2 negative and positive tumours within 1 hour, independent of lineage and prior treatment with trastuzumab. Affibody radiotracers have been developed to overcome the shortcomings of large (150 kDa) antibodies. To date most of the reported studies of radiolabeled Affibodies in the literature have employed analogues of  $Z_{HER2:342}$  labelled with radiometals or radiohalogens [252, 256–262]. Recently, re-engineering of this Affibody by Feldwisch and co-workers [263] led to an optimised scaffold containing 11 amino acid substitutions in the nonbinding surface of the Affibody removing similarity to the original protein A domain —  $Z_{HER2:2891}$ . Further to potential for automated site-specific good manufacturing practice-grade (GMP [264]) manufacture on FASTlab to allow broad clinical access to a HER2 imaging agent,  $Z_{HER2:2891}$  has improved thermal and chemical stability by avoiding deamidation, as well as increased hydrophilicity of the non-binding surface; positive attributes for ease of peptide synthesis and *in vivo* pharmacokinetics. The latter property is desirable to permit conduct of imaging studies within 1 or 2 hours post-radiotracer injection. However, within this early period non-specific uptake could contribute to tissue signal. Therefore the specificity of  $^{18}\text{F}$ -radiolabeled  $Z_{HER2:2891}$  Affibody, [ $^{18}\text{F}$ ]GE-226, was assessed for early imaging (1 hour) using both intrinsic cellular uptake and *in vivo* dynamic imaging to quantitatively discriminate between HER2 negative and positive tumours.

Optimisation of contrast is pivotal to successful development of imaging agents. High contrast results largely from high affinity of radiotracers and rapid pharmacokinetics. By comparison with other molecular imaging probes, Affibodies benefit from a short blood circulation time and high target affinity resulting in high contrast images within a relatively short time after injection, and slower internalisation rates [259, 265, 266]. This permits utilisation of more widely available short-lived radioisotopes, such as  $^{18}\text{F}$  and  $^{68}\text{Ga}$ , minimizing the patient’s dosimetry. In comparison with nanobodies, Affibodies excel through lower  $K_D$ , higher  $k_{\text{on}}$  and slower  $k_{\text{off}}$  rates [267]. Regarding affinity, Surface Plasmon Resonance experiments with isotopically unmodified GE-226 revealed high affinity binding to human and rhesus HER2-ECD-Fc comparable to the binding of parent  $Z_{HER2:2891}$  Affibody to human HER2-ECD-Fc (76 pM, REF. [263]). In contrast, GE-226 did not interact with rat HER2-ECD-Fc or human p95HER2, demonstrating specificity

to the ECD-containing human protein. Radiofluoridation to produce [ $^{18}\text{F}$ ]GE-226 did not affect radiotracer affinity either, as demonstrated by high specific cell intrinsic uptake in HER2 positive versus negative human breast, upper-gastrointestinal and ovarian cancer cell lines. Notably the lineage independence observed also lends support to the specificity of the radiotracer for HER2 versus other targets like EGFR and potential utility in cancers other than breast.

While preclinical imaging with  $Z_{\text{HER2}:2891}$  radiolabeled with  $^{111}\text{In}$  for single photon computed emission tomography (SPECT) displays good tumour targeting in SKOV-3 xenografts [265], it is expected that [ $^{18}\text{F}$ ]GE-226 with the superior sensitivity, resolution, and quantification of PET will provide improved contrast at the early time points.

This suggests that [ $^{18}\text{F}$ ]GE-226 could be used for detection of HER2 expression in primary tumours and distant metastasis, including liver, lung and bone. In this study, [ $^{18}\text{F}$ ]GE-226 did not cross the blood-brain-barrier so its utility for imaging of brain metastases remain to be seen.

Regarding systemic tracer disposition, high renal accumulation is characteristic of radiometal tracers due to loss of the radioactive ion and reabsorption in the proximal tubules [268]. In this context previous Affibodies labelled with  $^{68}\text{Ga}$  or  $^{111}\text{In}$  showed approximately 10-fold higher renal localisation than that seen in tumour [265, 266, 269], precluding imaging of tumours in the region around the kidney, as well as having an impact on dosimetry. Bioconjugation of the Affibody molecule with albumin, histidine containing tags or  $^{18}\text{F}$  radiolabels have been proposed as alternative approaches to avoid tubular reabsorption and permitting rapid glomerular filtration [159, 259, 270, 271]. The radiohalogen strategy with  $^{18}\text{F}$  used in this study demonstrated rapid renal clearance of [ $^{18}\text{F}$ ]GE-226, without substantial tracer accumulation in the kidneys; kidney radioactivity levels were comparable to levels in tumours at 60 minutes. Uptake in other organs, including the liver, was negligible and it remains elusive whether previously detected hepatic uptake of other Affibodies in the clinical setting is attributed to Affibody disposition or the labelling strategy [272].

Several lines of evidence indicated that the binding of [ $^{18}\text{F}$ ]GE-226 to HER2 is highly specific: (i) the tracer discriminated between HER2 positive and negative cells and tumours, (ii) siRNA knockdown of HER2 protein in cells reduced tracer uptake, (iii) pre-treatment of cells or mice with isotopically unmodified GE-226 resulted in significant reduction in uptake and (iv) tumour distribution of fluorescein-labelled GE-226 co-localised with



HER2 protein as determined by DAKO HercepTest. The latter also demonstrated that tumour distribution of the Affibody was non-limiting in the heterogeneous tumour models studied. The desirable affinity, specificity and pharmacokinetics properties of [ $^{18}\text{F}$ ]GE-226 led to very high contrast PET images, with the limitation that the high contrast is perhaps due also in part to the lack of tracer binding to rodent HER2. Nonetheless, it further substantiates the low non-specific binding of [ $^{18}\text{F}$ ]GE-226 as rodent data for Affibodies have been shown to translate well into human imaging profile.

An influence of specific radioactivity on Affibody uptake was observed *in vitro* where receptor numbers are limited in part due the 2D properties of *in vitro* culture, compared to a 3D system *in vivo*. It was hypothesised that with the higher amount of cold compound associated with the same level of radioactivity over time, the limited specific binding sites of an *in vitro* culture system are more readily blocked and result in a time-dependent decrease of tracer uptake. As this effect was not observed *in vivo* — potentially due to a much greater overall availability of receptors — this finding is not anticipated to hamper clinical development.

PET imaging demonstrated rapid tracer uptake in HER2 positive xenografts with net irreversible binding kinetics over time. The irreversible uptake (over the time of imaging) made it possible to distinguish between HER2 negative and HER2 positive tumours within 1 hour. Time versus radioactivity curves revealed steady-state (limited-washout) background uptake in HER2 negative xenografts, which was in keeping with the normal distribution kinetics of these types of peptides within the literature [259, 269, 273]. In HER2 negative xenografts (e.g., MCF7 and MCF7 p95HER2), uptake was rapid and remained stable over the 60-minute scan period. As wash-out mechanisms are primarily determined by size, tissue retention of Affibodies is longer than of small-molecules nonetheless more favourable than full immunoglobulins. Thus, the uptake observed in HER2 negative tumours can be attributed to non-specific background tissue distribution. In contrast, all HER2 positive models showed a continuous increased uptake throughout image acquisition timeframe. It was confirmed that the net irreversible trapping of the tracer in tumour was not due to differences in tracer delivery ( $K_1$ ) or blood volume ( $V_b$ ) but rather to specific uptake. Tumour uptake correlated with HER2 expression, suggesting specific Affibody-HER2 interactions and possibly some receptor internalisation [259, 265, 266]. Receptor internalisation was not assessed in this study but localisation of the fluorescein-labelled Affibody *in vivo* did not suggest substantial internalisation within the timeframe of the

study. Importantly, kinetic modelling permits definition of a threshold for HER2 positivity by determining the irreversible uptake in HER2 positive tumours. This concept requires clinical evaluation, but preliminary data indicate reliable detection of HER2 positive and negative lesions. Notably, a negative scan will be a clinically determined quantitative or semi-quantitative uptake cut-off value at a defined post-injection time, e.g. 1 hour, due to Affibody tracer distribution kinetics, and not, an absolute negative signal as seen by immunohistochemistry.

In view of trastuzumab being the most important HER2-targeting therapy, it was confirmed that tracer and antibody did not compete for the same extracellular epitope. X-ray crystallography revealed that  $Z_{HER2}$  Affibodies bind the extracellular domain of HER2 at the interface of domains III and IV, distinct from the trastuzumab binding site on domain IV [274]. Both *in vitro* and *in vivo* experiments confirmed that uptake of [ $^{18}\text{F}$ ]GE-226 was not obscured by the presence of trastuzumab. Minor, but significant, decreases in uptake after 24 hours pre-treatment with trastuzumab *in vitro* are more likely related to altered receptor internalisation or other dynamics due to the high concentration used [275, 276]. Continuous exposure of SKOV-3 xenografts to trastuzumab resulted in a slight downregulation of HER2 protein expression, as detected by western blot. This contrast to clinical data has been previously reported for pre-clinical models [261], but further validation would be required to investigate which of the complex dynamic changes upon trastuzumab treatment — including receptor internalisation, changes in vascularisation, immune response, cell death and selection of HER2 negative sub-populations — account for these discrepancies. In the *in vivo* studies, one HER2 tumour bearing mouse was characterised by low tumour tracer uptake. As HER2 was found not to be truncated in this sample (western blot analysis), mutations in the extracellular domain of HER2 were examined. Recent reports indicate that amino acids 309 and 310 on exon 8 are prone to mutations (G309A/E, S310F [173, 255], a site that has previously not been identified to contribute to the HER2-Affibody interaction [274]. No point mutations occurred in the outlier samples. Higher tissue efflux kinetics ( $k_2$ ) paired with a lowered  $K_1$  are indicative of lack of retention or potential perfusion deficits, causing reduced tracer delivery. If perfusion deficits are responsible for this unexpected finding, then an adverse implication on correct assessment of HER2 positivity by this technology is envisaged; the comparable clinical scenario is, however, unlikely to affect treatment stratification, as poor perfusion would potentially also reduce efficacy of trastuzumab. Finally it was confirmed that [ $^{18}\text{F}$ ]GE-

226 is suitable as pharmacodynamic marker of HSP90 inhibition and perhaps as patient enrichment tool for those likely to benefit from such therapies. The most promising of these drugs, NVP-AUY922 [277] is currently in Phase II clinical trials and has previously shown to downregulate HER2 expression [278], which was correctly confirmed *in vitro* and *in vivo* by [ $^{18}\text{F}$ ]GE-226 PET. This is in accordance with the report by Smith-Jones and co-workers who similarly demonstrated that the HSP90 inhibitor, 17-allylaminogeldanamycin, degrades HER2 leading to reduction in the uptake of [ $^{68}\text{Ga}$ ]-labelled F(ab')<sub>2</sub> fragment of trastuzumab [273, 279].

In conclusion, [ $^{18}\text{F}$ ]GE-226 PET imaging permits accurate discrimination of HER2 receptor expression, irrespective of tumour heterogeneity, cell lineage, or prior trastuzumab treatment. The tracer is expected to have good safety and dosimetry profiles due to its low nonspecific binding, the use of short-lived radiolabel and its favourable pharmacokinetic properties. These data support the clinical development of this tracer in cancer patients, which is planned. Furthermore, the strong specificity will allow use of this radiotracer for selecting patients for treatment with choline kinase inhibitors to test the hypothesis that patients with high HER2 will benefit from choline kinase inhibitor therapy.



## Chapter 6

# Summary and concluding remarks

### 6.1 Summary of work

In this thesis, novel CHK inhibitors with potent antitumour activity were developed and used to characterise choline biochemistry in cancer. The lead compound, ICL-CCIC-0019, emerged from a focused library screen, that investigated strategies to create inhibitors that solely interact with the choline pocket or simultaneously block the choline and ATP active sites. Biochemical assays and molecular modelling proved the latter approach feasible, however, with the caveat that the potency of these “hybrid” compounds was significantly lower than of choline-competitive inhibitors. In particular, the high antiproliferative activity and the ability to reduce CHK activity at endogenously high choline concentrations in whole cells, favoured the further characterisation and development of choline-competitive inhibitors, like ICL-CCIC-0019.

One characteristic challenge in the development of kinase inhibitors is the putative interaction with other kinases, attributed to the high evolutionary conservation of this target class. By avoiding interaction with the ATP pocket, ICL-CCIC-0019 demonstrated very low off-target effects against a large panel of human kinases. The compound had high antiproliferative activity against the NCI-60 panel of cell lines, while normal cell lines were insensitive to treatment. Pharmacological intervention phenocopied the effect of posttranscriptional silencing of CHKA in cancer cells. It was further demonstrated that the mechanism of action is executed entirely by inhibition of the catalytic activity of CHKA and not by destabilisation of dimer complexes. CHK inhibition decreased PCho accumulation and subsequently formation of PtdCho, triggering cell death via ER stress pathways. Detailed pharmacological profiling of ICL-CCIC-0019 was carried out, which considerably extended

beyond previously published reports of comparable compounds. This permitted for the first time the establishment of the connection between cellular potency, pharmacokinetics and pharmacodynamics. The compound was stable in plasma, had a balanced plasma protein binding, was a non-substrate for drug resistance transporters, but the intrinsic cationic nature limited the capacity to rapidly cross cellular membranes. Nonetheless, the latter feature was still within range of other currently approved anticancer drugs. PET imaging using a target-competitive radiotracer, [ $^{18}\text{F}$ ]D4-FCH, demonstrated modulation of the enzymatic reaction *in vivo*, which translated into potent antitumour activity. This response, however, could not be predicted at early time points using the proliferation tracer [ $^{18}\text{F}$ ]FLT. It was further aimed to validate the effects of pharmacological inhibition by genetic means. Therefore, an inducible shRNA model was created, that yielded sufficient CHKA knockdown *in vitro*, but failed to do so *in vivo*. The visualisation of co-expressed TurboRFP using fluorescent *in vivo* imaging confirmed transcription of shRNA, but potentially the relatively short study duration of one week prevented attenuation of protein expression. Lastly, it was identified that combined CHKA and HDAC6 inhibition is highly synergistic.

Figure 6.1 highlights the key findings, which were obtained by CHKA-selective inhibition and contrasts them to effects observed by combined CHKA and CHKB inhibition. CHKA selective inhibition with ICL-CCIC-0019 deactivated the Kennedy pathway and reduced PtdCho. Consequently, ER stress was induced via ATF4 and CHOP, which decreased via intermediate mechanisms cell viability. Additionally, pro-survival signal transduction was reduced, leading to G1 arrest and apoptosis, which ultimately resulted in cell death. In contrast, combined CHKA and CHKB inhibition, as shown by double siRNA knockdown and exemplified by non-isoform selective ATP-competitive inhibitors [148], has no effect on cell viability, which could tentatively be mediated through mitophagy or autophagy [280, 281].

In order to rapidly stratify patients that might benefit from CHK inhibitors, a HER2-targeted PET tracer, [ $^{18}\text{F}$ ]GE-226, was developed, as HER2 expression is linked to hyperactivated choline metabolism. An Affibody-based approach was chosen, as this non-immunoglobuline-derived affinity protein is characterised by very strong binding to HER2, while its small molecular weight enables rapid and homogenous tissue distribution. Surface plasmon resonance experiments confirmed that the radiolabel did not interfere with the binding properties of the Affibody. High specificity was confirmed by differential tracer

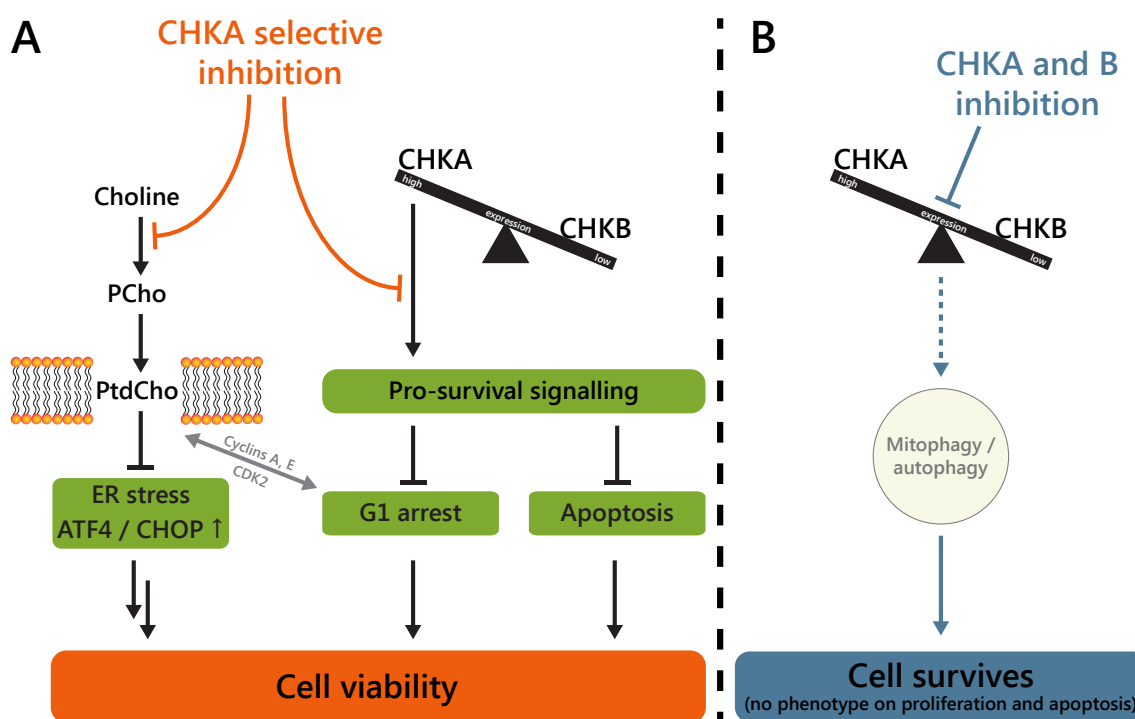


Figure 6.1: Consequences of (A) selective CHKA or (B) combined CHKA and CHKB inhibition. Black arrows indicate effects of choline biochemistry in cancer cells, that are perturbed by CHKA selective inhibitor (orange). Blue arrows represent impact of combined CHKA/CHKB inhibition, as observed with siRNA double knockdown or current ATP-competitive inhibitors. Grey arrow and circle indicate tentative mechanisms. Double arrows indicate that intermediate mechanisms are involved to impact cell viability. ATF4, activating transcription factor-6; CHKA/B, choline kinase alpha and beta; CHOP, CCAAT-enhancer-binding protein homologous protein; ER, endoplasmic reticulum; PCho, phosphocholine; PtdCho, phosphatidylcholine.

retention in cell lines and xenografts with varying HER2 expression, decreased uptake after blocking of the target with isotopically unmodified GE-226 and knockdown of HER2 by siRNA. A fluorophore-labelled GE-226 analogue co-localised with HER2 protein in tissues with heterogeneous HER2 expression. Furthermore, tracer binding was not sterically hindered by trastuzumab, demonstrating the applicability of this imaging modality for patients who already received this HER2-targeting therapy. Finally, the pharmacodynamic response to HSP90 inhibitor-mediated degradation of HER2 could be confirmed. High-contrast images were obtained with [ $^{18}\text{F}$ ]GE-226 and for the first time, the Affibody-HER2 interaction could be characterised by kinetic modelling.

## 6.2 Advances to previous studies and future directions

One central aim of this thesis was to provide a detailed pharmacological characterisation of ICL-CCIC-0019, as previous studies of CHK inhibitors failed to report data on selectivity,

pharmacokinetics, pharmacodynamics or toxicity. The use of PET imaging formed the centrepiece of this evaluation, as it quantitated the CHK inhibition *in vivo* and predicted the compound tissue pharmacokinetics in major organs. The obtained results were the sum of pharmacokinetic properties, cell permeability, target affinity and potential influences of the tumour microenvironment. It therefore well described the overall behaviour of CHK inhibitors *in vivo* and could easily be implemented in future drug discovery efforts. A kinetic model was employed to further discern the physiological processes, but limitations became apparent, as CHK inhibition was not predicted by changes in the irreversible binding constant  $k_3$ . Future studies will be required to validate this model. Genetically engineered xenografts with knockdown of CHKA, CHKB or choline transporters could assist to fully comprehend each pharmacokinetic parameter.

ICL-CCIC-0019 was associated with dose-limiting toxicity, depicted by dose-dependent decrease of body weight in mice. Pharmacokinetic and PET data indicated high liver and kidney accumulation, which is therefore a potential cause for body weight changes. For the first time, consequences of CHK inhibitor-mediated choline metabolism on other tissues than tumour were described. It remains to be understood, whether the effects were related to the compound or the high choline metabolic activity in liver and potentially also kidney. Subsequent experiments will be required to study the implications of CHK inhibition in malignant and benign settings of these organs. Diversification of inhibitor scaffolds will further contribute in understanding compound accumulation in various tissues. Recently investigated uncharged, ATP-competitive inhibitors were ineffective in cell-based assays, which is potentially due to the simultaneous inhibition of CHKA and CHKB. Further studies will be required to understand why the associated decrease in PCho with ATP-competitive inhibitors did not impact proliferation. Potentially, CHKA and CHKB have scaffolding properties that extend beyond their catalytic activity to generate PCho and PtdCho and which give them additional roles for pro-survival signalling. Dependent on which pocket is targeted, distinct conformational changes could influence the scaffolding properties for multi-protein complex formation. Additionally, the observed changes in PCho could occur via PLC and PLD, which will require additional direct effects on these proteins to be verified. As the ATP cavities of both isoforms share great similarities, it will require considerable effort to design CHKA-specific, ATP-competitive inhibitors. Therefore, development of novel — preferably uncharged — choline-competitive scaffolds are more likely to advance this class of compounds into an experimental clinical setting.



The complexity of the required medicinal chemistry efforts is perhaps the biggest challenge in future years.

In this study, an inducible shRNA models was created, but failed to repress CHKA expression *in vivo*. HCT116 cells, which were used as a target cell line, were perhaps too rapidly proliferating to allow sufficient time to induce target knockdown. Subsequent experiments should be aimed to identify suitable host cell lines, as inducible knockdown models are highly valuable tools to mimic a clinical scenario where treatment commences on already established lesions. Such models will be required to fully validate CHKA as a target, provide a comparison to pharmacologic inhibition with respect to antitumour activity verify kinetic models for PET imaging.

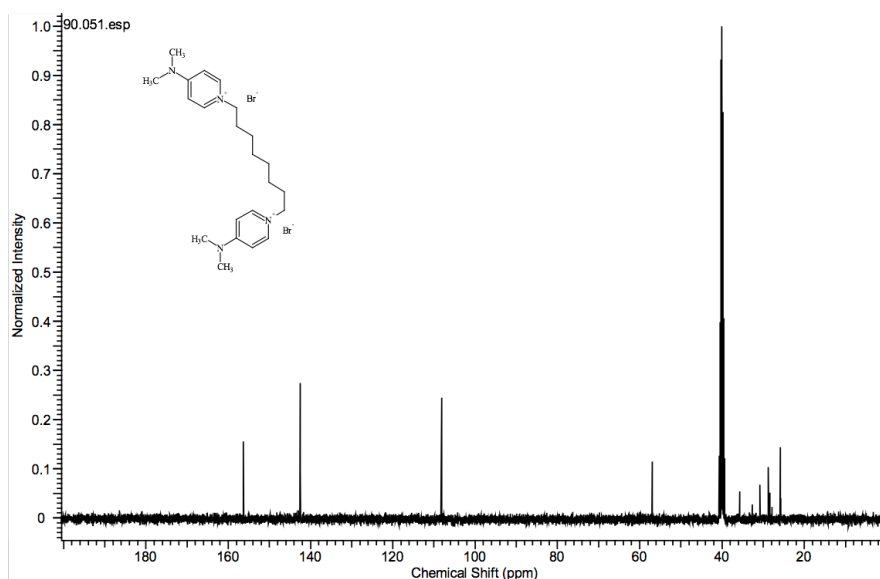
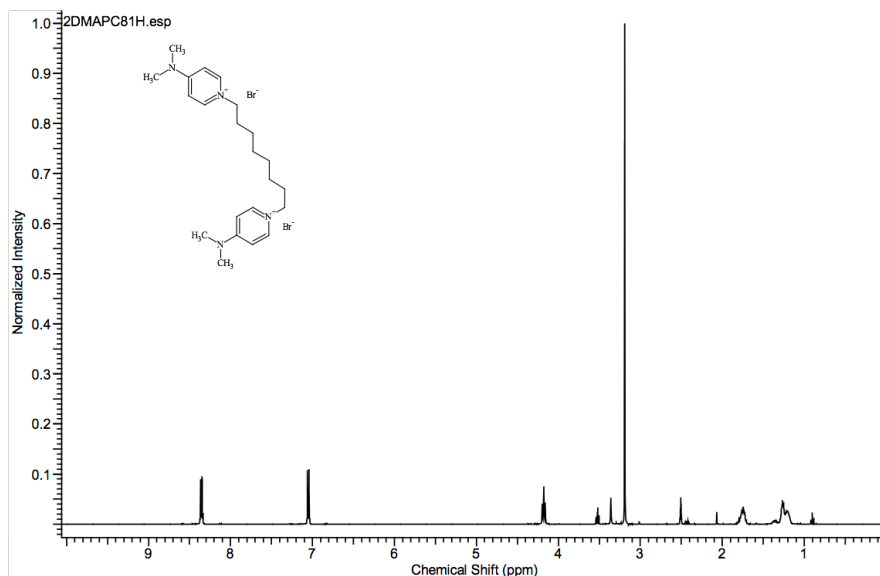
Future studies should aim to identify CHKA inhibition-related metabolic alterations and the elucidation of their regulatory mechanisms. Potential pathways could include glucose, amino acid and lipid biochemistry. This will highlight potential feedback loops and resistance mechanisms but might equally open opportunities for targeted combination therapies.

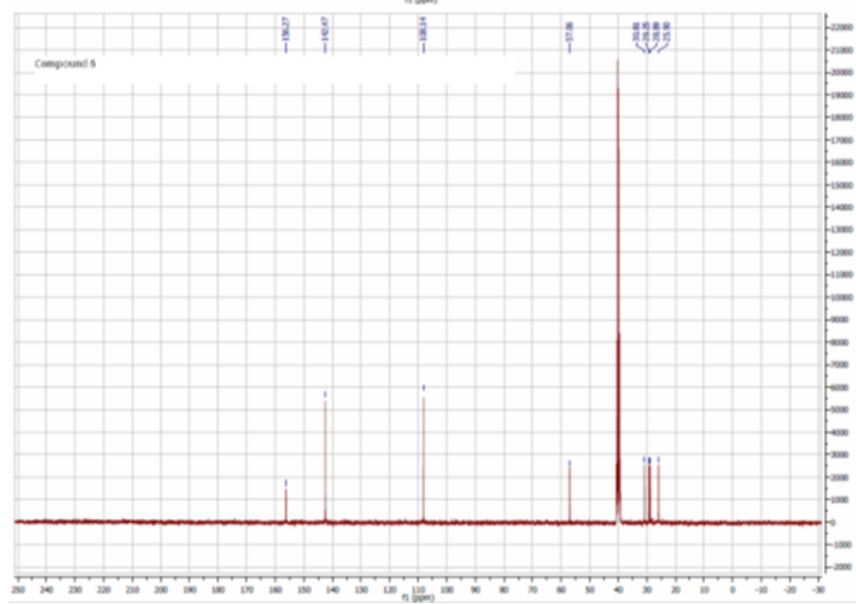
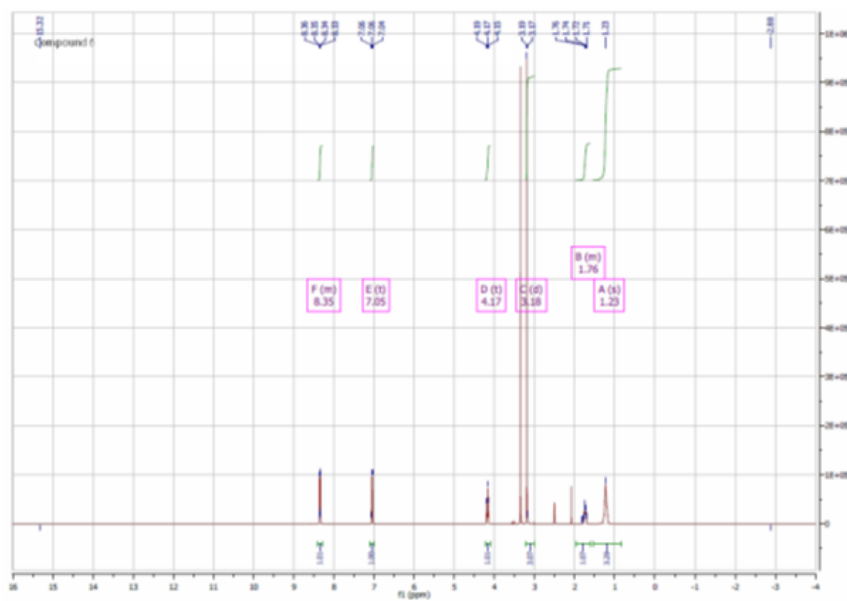
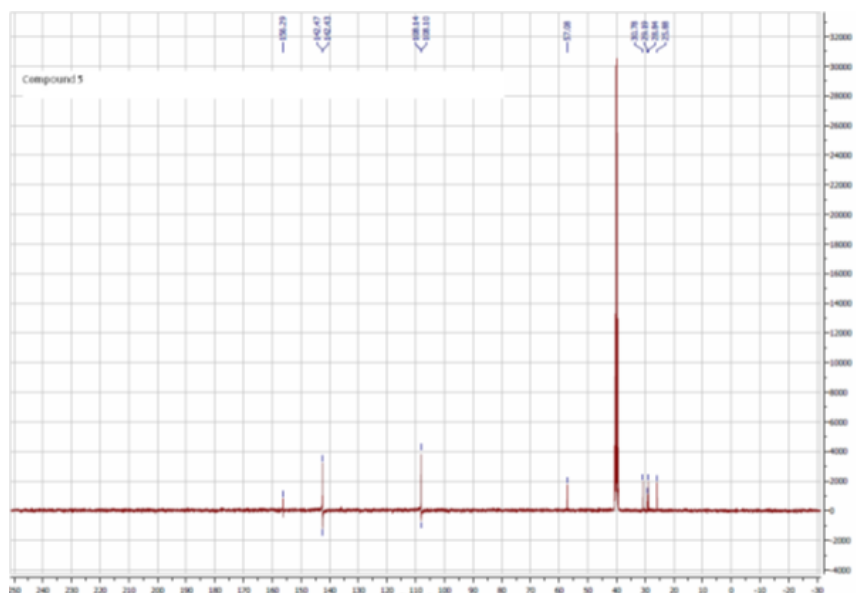
Lastly, an alternative approach to determine HER2 expression was proposed. Accurate assessment of a cancer patient's HER2 status remains a clinical challenge with up to 20% of patients being potentially withdrawn from therapy or exposed to unnecessary toxicity. Noninvasive imaging is widely seen as a viable alternative to current methods, in particular within the setting of locoregional and distant recurrences not amenable to biopsy, but clinical success by positron emission tomography has so far been hampered by prolonged tracer retention in liver and kidneys obstructing detection on proximate metastases. [<sup>18</sup>F]GE-226, overcame these limitations and demonstrated improved properties for large-scale and good manufacturing practice-grade synthesis and enhanced pharmacokinetic characteristics. Lineage independence of these results extends application beyond breast cancer. Future clinical studies will be required to determine patient dosimetry and assess the feasibility to image multiple lesions simultaneously. Potential patient benefits could arise by avoiding invasive procedures involving multiple biopsies. The kinetic model proposed in this thesis could further increase the accuracy of the image interpretation. Because of the specific annotation to HER2 and enhanced pharmacokinetic properties, [<sup>18</sup>F]GE-226 is now transitioning into clinical development. A method has therefore been developed that will permit the hypothesis that, patients with high HER2 will benefit from treatment with CHK inhibitors, to be tested.



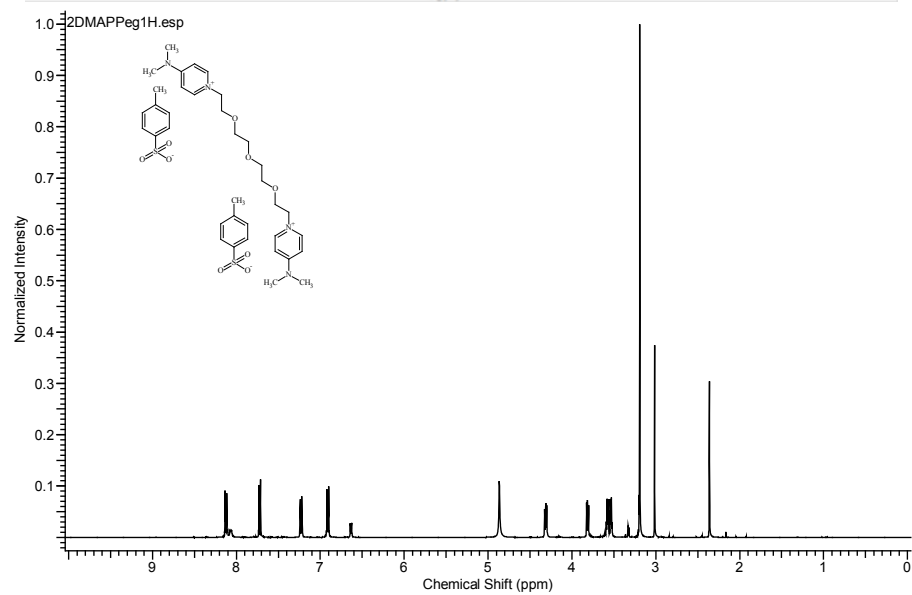
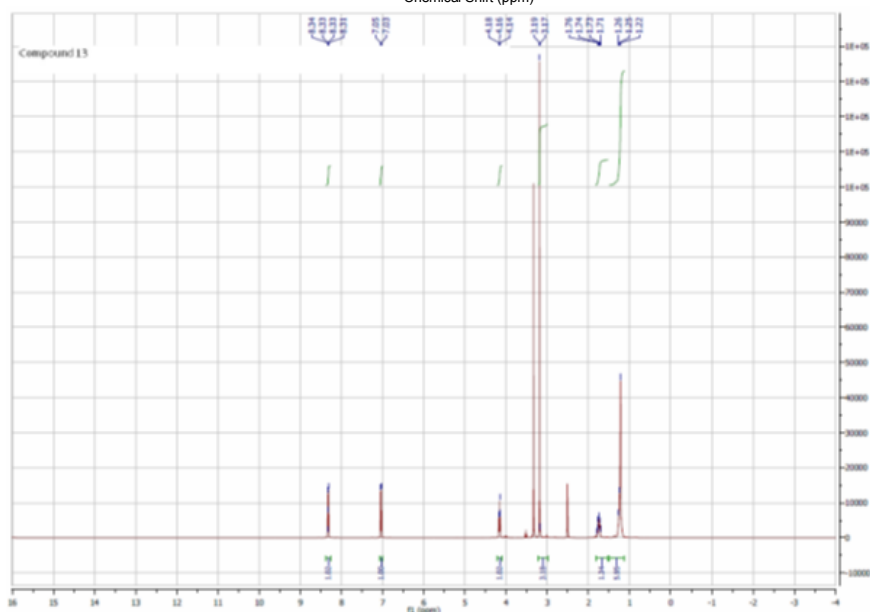
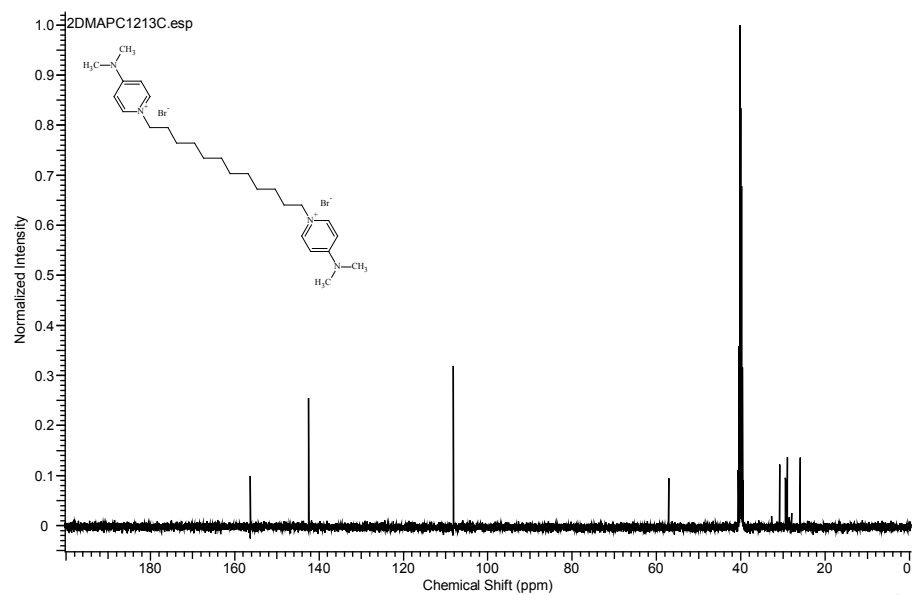
# Appendix A

## Spectra of relevant compounds

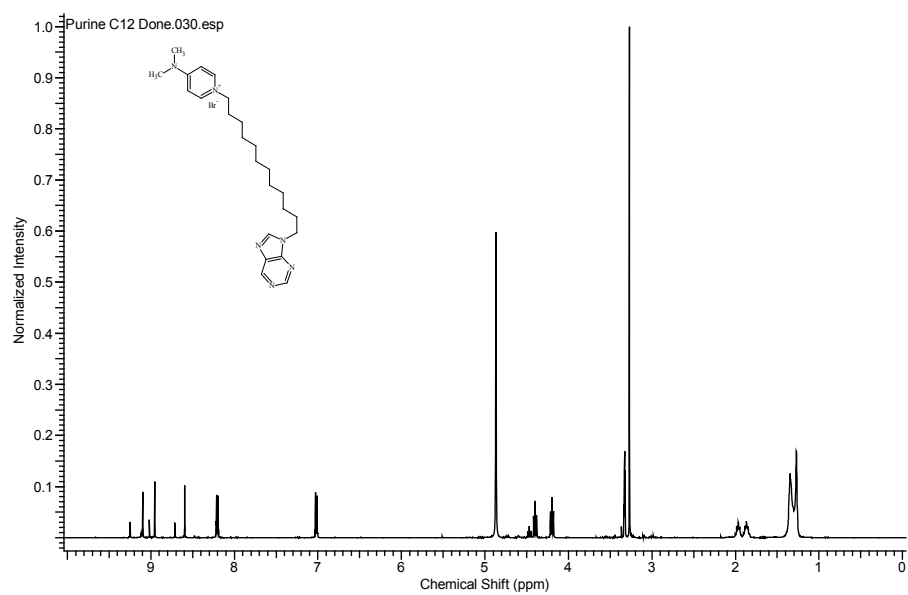
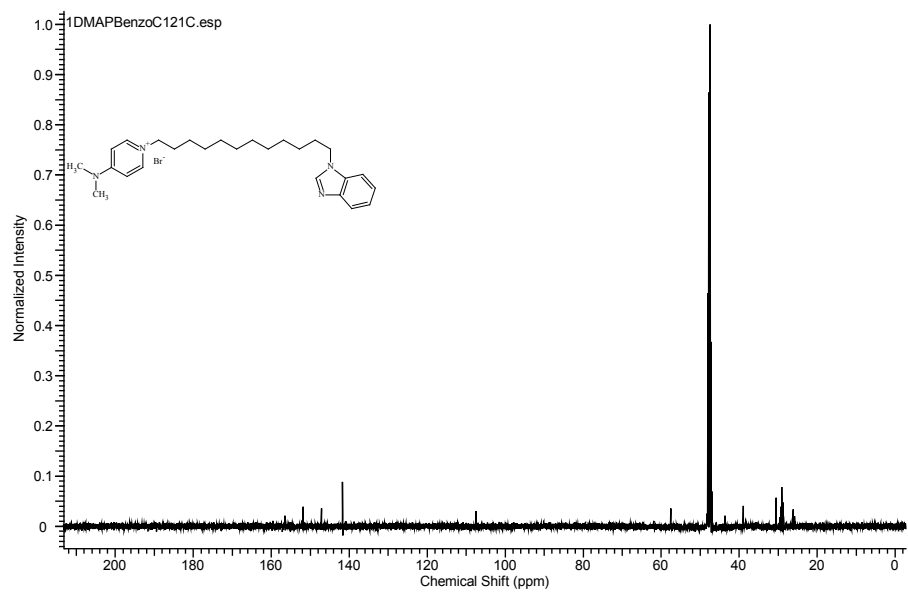
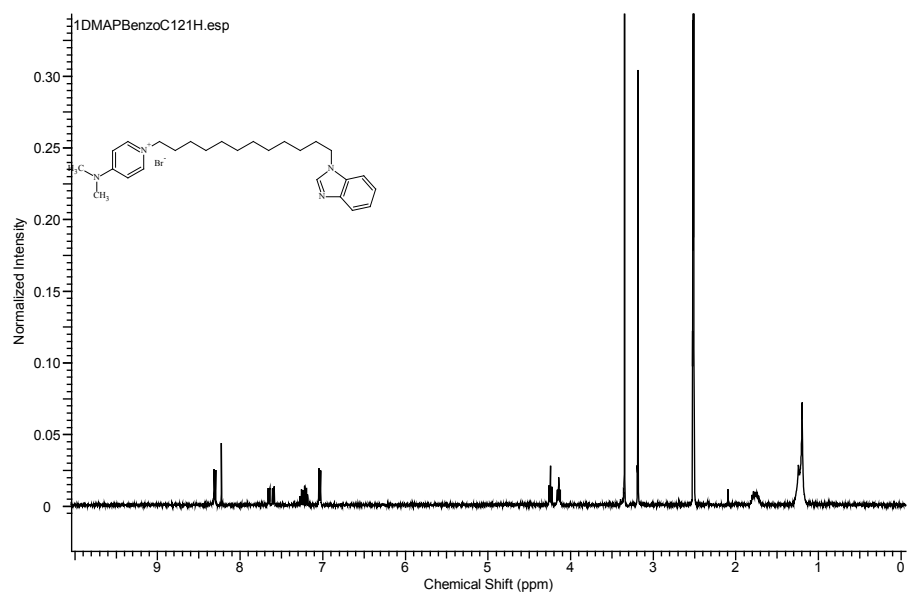




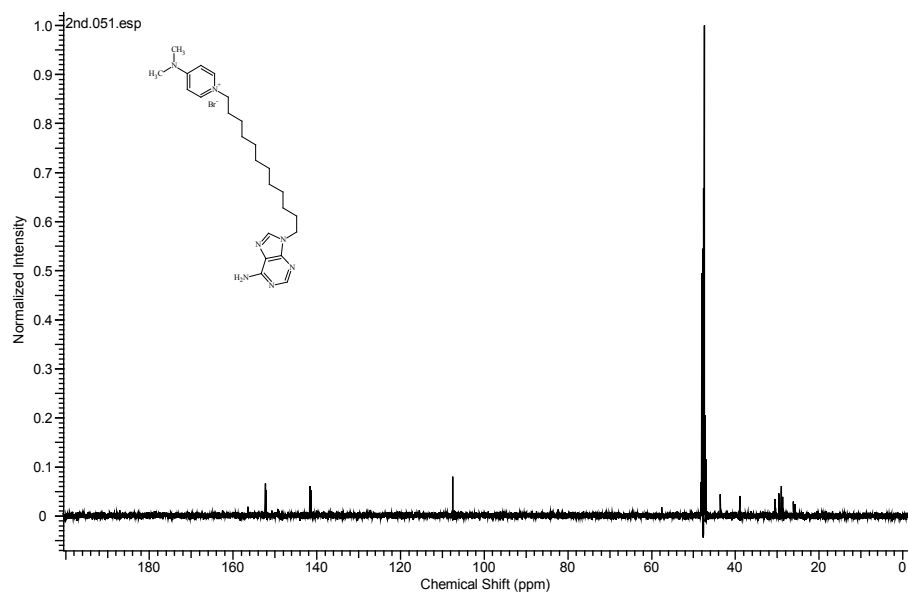
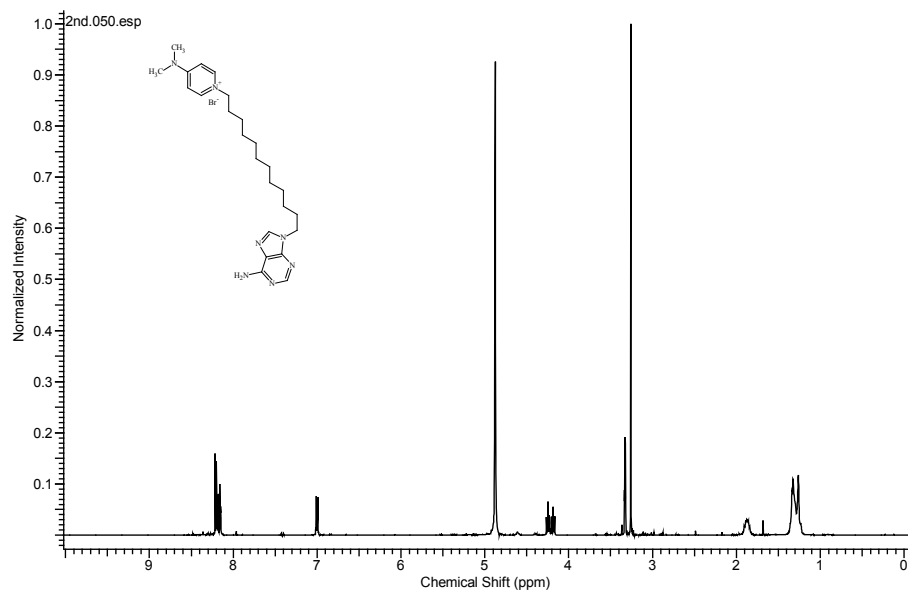
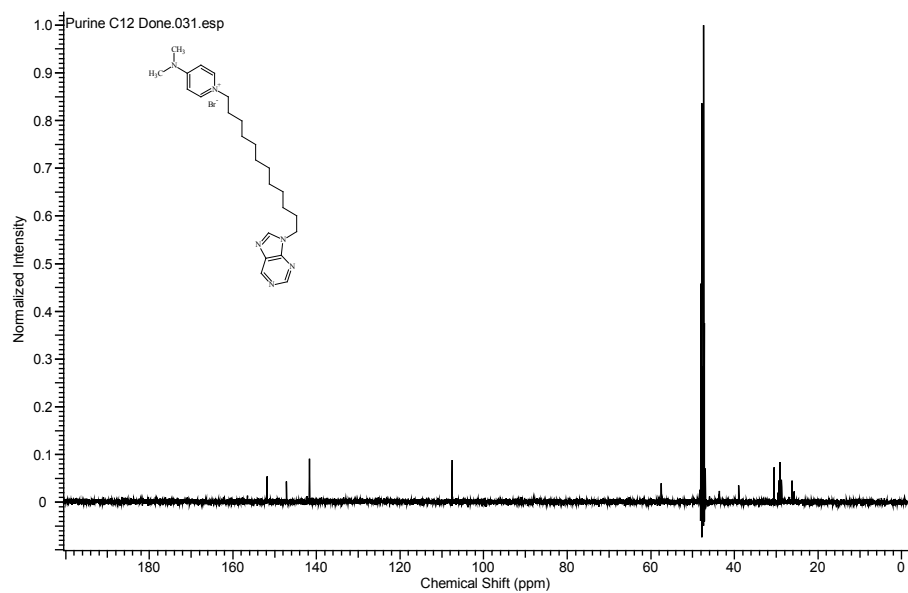


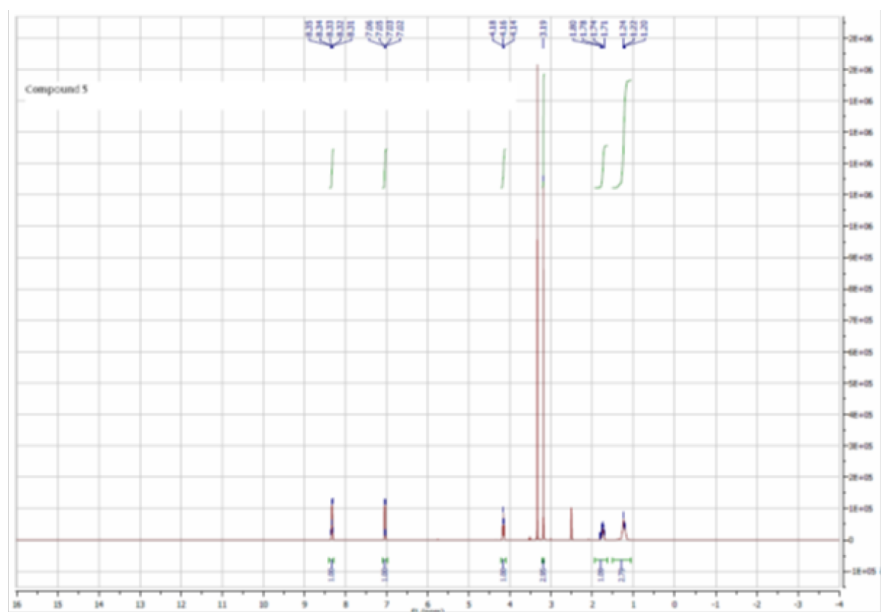












## Appendix B

### Kinase screen

<b>Kinase</b>	<b>Species</b>	<b>Accession no.</b>	<b>% activity remaining</b>	<b>SD</b>
ABL	human	NM_005157	112	5
AMPK	rat	Tissue purified	109	11
ASK1	human	NM_005923	119	5
Aurora A	human	BC027464	98	1
Aurora B	human	NM_004217	102	9
BRK	human	NM_005975	117	10
BRSK1	human	NM_032430	110	2
BRSK2	human	AF533878	94	3
BTK	human	NP_00052.1	131	1
CAMK1	human	NM_003656	110	11
CAMKKb	human	NM_153499	91	3
CDK2-Cyclin A	human	NM_001798/NM_001231	112	30
CDK9-Cyclin T	human	NM_001261/NM_001240	95	7
CHK1	human	AF016582	97	4
CHK2	human	NM_007194	90	2
CK1 $\gamma$ 2	human	BC018693.2	92	5
CK1 $\delta$	human	NM_001893	100	5
CK2	human	NM_001895	86	1
CLK2	human	NM_003993.2	101	1
CSK	human	NM_004383	96	1
DAPK1	human	NM_004938.2	96	13
DDR2	human	NM_006182	85	13
DYRK1A	human	NM_130437.2	114	1
DYRK2	human	NM_003583	96	2
DYRK3	human	AY590695	106	1
EF2K	human	AAH32665	99	11
EIF2AK3	human	NM_004836.5	97	1
EPH-A2	human	NM_004431	93	12
EPH-A4	human	NM_004438	124	10
EPH-B1	human	NM_004441	112	6

EPH-B2	human	NM_004442	90	1
EPH-B3	human	NM_004443	107	11
EPH-B4	human	NP_004435.3	110	5
ERK1	human	BC013992	91	1
ERK2	human	NM_002745	103	6
<b>ERK8</b>	<b>human</b>	<b>AY065978</b>	<b>69</b>	<b>4</b>
FGF-R1	human	M34641	92	11
GCK	human	BC047865	89	12
GSK3b	human	L33801	94	13
<b>HER4</b>	<b>human</b>	<b>NM_005235</b>	<b>79</b>	<b>7</b>
HIPK1	human	NM_198268	106	6
HIPK2	human	AF326592	104	3
HIPK3	human	NM_005734	112	35
<b>IGF-1R</b>	<b>human</b>	<b>NM_000875</b>	<b>65</b>	<b>7</b>
IKKb	human	XM_032491	101	8
IKKe	human	NM_014002	123	36
IR	human	NM_000208.2	103	16
IRAK1	human	NM_001569.3	89	12
IRAK4	human	BC013316.1	83	11
IRR	human	NM_014215	92	6
JAK2	human	NP_004963.1	90	4
JNK1	human	L26318	98	21
JNK2	human	L31951	100	15
JNK3	human	NM_002753	92	2
Lck	mouse	X03533	118	29
LKB1	human	NP_000446	100	7
MAPKAP-K2	human	NM_032960	89	4
<b>MAPKAP-K3</b>	<b>human</b>	<b>NM_004635</b>	<b>67</b>	<b>6</b>
MARK1	human	AF154845	103	8
MARK2	human	NM_004954	86	3
MARK3	human	U64205	106	5
MARK4	human	AK075272	95	4
MEKK1	human	XM_042066	92	1
MELK	human	NM_014791	106	14
MINK1	human	NM_015716	100	7
MKK1	human	L05624	82	0
MKK2	human	NM_030662	95	9
MKK6	human	NM_002758	102	2
MLK1	human	NM_005965	91	2
MLK3	human	NM_033141	110	4
MNK1	human	NM_002419	101	2
MNK2	human	AB000409	96	25
MPSK1	human	AF237775	105	5
MSK1	human	AF074393	96	2
MST2	human	CR407675	89	20
MST3	human	U60206	117	9
MST4	human	AAH65378	113	4
NEK2a	human	NM_016542	101	7
NEK6	human	NM_002497	86	6
NUAK1	human	NM_014397	103	20
OSR1	human	NM_014840	99	3
p38a MAPK	human	NM_005109.2	108	9
p38b MAPK	human	L35264	107	3
p38d MAPK	human	Y14440	100	2

p38g MAPK	human	Y10487	99	25
PAK2	human	Y10488	107	6
PAK4	human	NM_002577	114	5
PAK5	human	O96013	90	9
PAK6	human	Q9P286	107	7
PDK1	human	Q9NQU5	133	1
PHK	human	X80590	94	6
PIM1	human	NM_002613	102	8
PIM2	human	NM_002648	103	20
PIM3	human	U77735	113	2
PKA	human	Q86V86	106	2
PKBa	human	NM_002730	101	12
PKBb	human	BC000479	93	1
PKCa	human	NM_001626	98	3
PKCz	human	NM_002742	106	10
PKCy	human	NM_002737	93	4
PKD1	human	NM_002739	105	5
PLK1	human	NM_002744	112	20
PRAK	human	NM_005030	101	11
PRK2	human	AF032437	94	13
RIPK2	human	S75548	102	0
ROCK 2	human	NM_003821	97	1
<b>RSK1</b>	<b>rat</b>	<b>U38481</b>	<b>78</b>	<b>6</b>
RSK2	human	NM_002953.3	105	10
S6K1	human	NM_004586	88	1
SGK1	human	NM_003161	94	14
SIK2	human	NM_005627	109	3
SIK3	human	NM_015191.1	102	16
SmMLCK	human	Sugen Kinase Database 1	104	18
Src	human	NM_005417.3	105	1
SRPK1	human	NM_003137	106	3
STK33	human	BC031231.1	99	3
SYK	human	AAH01645.1	92	9
TAK1-TAB1	human	NM_003188 and NM_006	97	2
TAO1	human	NM_020791	100	13
TBK1	human	NM_013254	108	20
TESK1	human	NM_006285.2	101	17
TIE2	human	BC035514.1	89	4
TLK1	human	NM_012290.4	110	20
TrkA	human	NM_001007792.1	84	15
TSSK1	human	AY028964	107	5
TTBK1	human	NM_032538.1	97	4
TTK	human	NM_003318	101	5
VEG-FR	human	NM_002019.3	80	6
WNK1	human	NM_018979.3	102	2
YES1	human	NM_005433	110	4
ZAP70	human	NM_001079	102	5



# References

- [1] S. Trousil, L. Carroll, A. Kalusa, O. Aberg, M. Kaliszczak, and E. O. Aboagye. Design of symmetrical and nonsymmetrical N,N-dimethylaminopyridine derivatives as highly potent choline kinase alpha inhibitors. *MedChemComm*, 4(4):693–96, 2013.
- [2] S. Trousil, S. Hoppmann, Q.-D. Nguyen, M. Kaliszczak, G. Tomasi, P. Iveson, D. Hiscock, and E. O. Aboagye. Positron Emission Tomography Imaging with 18F-Labeled ZHER2:2891 Affibody for Detection of HER2 Expression and Pharmacodynamic Response to HER2-Modulating Therapies. *Clinical Cancer Research*, 20(6):1632–43, 2014.
- [3] M. Kaliszczak, S. Trousil, O. Aberg, M. Perumal, Q. D. Nguyen, and E. O. Aboagye. A novel small molecule hydroxamate preferentially inhibits HDAC6 activity and tumour growth. *Br J Cancer*, 108(2):342–50, 2013.
- [4] T. H. Witney, F. Pisaneschi, I. S. Alam, S. Trousil, M. Kaliszczak, F. Twyman, D. Brickute, Q. D. Nguyen, Z. Schug, E. Gottlieb, and E. O. Aboagye. Preclinical Evaluation of 18F-Fluoro-Pivalic Acid as a Novel Imaging Agent for Tumor Detection. *J Nucl Med*, Forthcoming 2014.
- [5] D. Hanahan and R. A. Weinberg. Hallmarks of cancer: the next generation. *Cell*, 144(5):646–74, 2011.
- [6] O. Warburg, K. Posener, and E. Negelein. Ueber den stoffwechsel der tumoren. *Biochemische Zeitschrift*, 152(1):319–44, 1924.
- [7] O. Warburg. On the origin of cancer cells. *Science*, 123(3191):309–14, 1956.
- [8] O. Warburg. On respiratory impairment in cancer cells. *Science*, 124(3215):269–70, 1956.

- [9] E. M. Rohren, T. G. Turkington, and R. E. Coleman. Clinical Applications of PET in Oncology. *Radiology*, 231(2):305–32, 2004.
- [10] M. G. Vander Heiden, L. C. Cantley, and C. B. Thompson. Understanding the Warburg Effect: The Metabolic Requirements of Cell Proliferation. *Science*, 324(5930):1029–33, 2009.
- [11] J. R. Cantor and D. M. Sabatini. Cancer Cell Metabolism: One Hallmark, Many Faces. *Cancer Discovery*, 2(10):881–98, 2012.
- [12] C. R. Santos and A. Schulze. Lipid metabolism in cancer. *FEBS J*, 279(15):2610–23, 2012.
- [13] L. L. Cheng, I. W. Chang, B. L. Smith, and R. G. Gonzalez. Evaluating human breast ductal carcinomas with high-resolution magic-angle spinning proton magnetic resonance spectroscopy. *J Magn Reson*, 135(1):194–202, 1998.
- [14] E. Ackerstaff, B. R. Pflug, J. B. Nelson, and Z. M. Bhujwalla. Detection of increased choline compounds with proton nuclear magnetic resonance spectroscopy subsequent to malignant transformation of human prostatic epithelial cells. *Cancer Res*, 61(9):3599–603, 2001.
- [15] R. Katz-Brull, D. Seger, D. Rivenson-Segal, E. Rushkin, and H. Degani. Metabolic markers of breast cancer: enhanced choline metabolism and reduced choline-ether-phospholipid synthesis. *Cancer Res*, 62(7):1966–70, 2002.
- [16] C. K. Wang, C. W. Li, T. J. Hsieh, S. H. Chien, G. C. Liu, and K. B. Tsai. Characterization of bone and soft-tissue tumors with in vivo  $^1\text{H}$  MR spectroscopy: initial results. *Radiology*, 232(2):599–605, 2004.
- [17] O. Celik, S. Hascalik, K. Sarac, M. M. Meydanli, A. Alkan, and B. Mizrak. Magnetic resonance spectroscopy of premalignant and malignant endometrial disorders: a feasibility of in vivo study. *Eur J Obstet Gynecol Reprod Biol*, 118(2):241–5, 2005.
- [18] L. L. Cheng, M. A. Burns, J. L. Taylor, W. He, E. F. Halpern, W. S. McDougal, and C.-L. Wu. Metabolic characterization of human prostate cancer with tissue magnetic resonance spectroscopy. *Cancer Res*, 65(8):3030–34, 2005.



- [19] E. Iorio, D. Mezzanzanica, P. Alberti, F. Spadaro, C. Ramoni, S. D'Ascenzo, D. Milimaggi, A. Pavan, V. Dolo, S. Canevari, and F. Podo. Alterations of choline phospholipid metabolism in ovarian tumor progression. *Cancer Res*, 65(20):9369–76, 2005.
- [20] A. Stadlbauer, S. Gruber, C. Nimsy, R. Fahlbusch, T. Hammen, R. Buslei, B. Tomandl, E. Moser, and O. Ganslandt. Preoperative grading of gliomas by using metabolite quantification with high-spatial-resolution proton MR spectroscopic imaging. *Radiology*, 238(3):958–69, 2006.
- [21] U. G. Mueller-Lisse and M. K. Scherr. Proton MR spectroscopy of the prostate. *Eur J Radiol*, 63(3):351–60, 2007.
- [22] R. E. Lenkinski, B. N. Bloch, F. Liu, J. V. Frangioni, S. Perner, M. A. Rubin, E. M. Genega, N. M. Rofsky, and S. M. Gaston. An illustration of the potential for mapping MRI/MRS parameters with genetic over-expression profiles in human prostate cancer. *MAGMA*, 21(6):411–21, 2008.
- [23] S. J. Booth, M. D. Pickles, and L. W. Turnbull. In vivo magnetic resonance spectroscopy of gynaecological tumours at 3.0 Tesla. *BJOG*, 116(2):300–3, 2009.
- [24] M. A. McLean, A. N. Priest, I. Joubert, D. J. Lomas, M. Y. Kataoka, H. Earl, R. Crawford, J. D. Brenton, J. R. Griffiths, and E. Sala. Metabolic characterization of primary and metastatic ovarian cancer by <sup>1</sup>H-MRS in vivo at 3T. *Magn Reson Med*, 62(4):855–61, 2009.
- [25] E. Iorio, A. Ricci, M. Bagnoli, M. E. Pisanu, G. Castellano, M. Di Vito, E. Venturini, K. Glunde, Z. M. Bhujwalla, D. Mezzanzanica, S. Canevari, and F. Podo. Activation of phosphatidylcholine cycle enzymes in human epithelial ovarian cancer cells. *Cancer Res*, 70(5):2126–35, 2010.
- [26] D. Yakoub, H. C. Keun, R. Goldin, and G. B. Hanna. Metabolic profiling detects field effects in nondysplastic tissue from esophageal cancer patients. *Cancer Res*, 70(22):9129–36, 2010.
- [27] K. Glunde and Z. M. Bhujwalla. Metabolic Tumor Imaging Using Magnetic Resonance Spectroscopy. *Seminars in Oncology*, 38(1):26–41, 2011.

- [28] K. Glunde, Z. M. Bhujwalla, and S. M. Ronen. Choline metabolism in malignant transformation. *Nat Rev Cancer*, 11(12):835–48, 2011.
- [29] A. Ramirez de Molina, R. Gutierrez, M. A. Ramos, J. M. Silva, J. Silva, F. Bonilla, J. J. Sanchez, and J. C. Lacal. Increased choline kinase activity in human breast carcinomas: clinical evidence for a potential novel antitumor strategy. *Oncogene*, 21(27):4317–22, 2002.
- [30] A. Ramirez de Molina, J. Sarmentero-Estrada, C. Belda-Iniesta, M. Taron, V. Ramirez de Molina, P. Cejas, M. Skrzypski, D. Gallego-Ortega, J. de Castro, and E. et al. Casado. Expression of choline kinase alpha to predict outcome in patients with early-stage non-small-cell lung cancer: a retrospective study. *Lancet Oncol*, 8(10):889–97, 2007.
- [31] T. Shah, F. Wildes, M. F. Penet, Jr. Winnard, P. T., K. Glunde, D. Artemov, E. Ackerstaff, B. Gimi, S. Kakkad, V. Raman, and Z. M. Bhujwalla. Choline kinase overexpression increases invasiveness and drug resistance of human breast cancer cells. *NMR Biomed*, 23(6):633–42, 2010.
- [32] A. Granata, R. Nicoletti, V. Tinaglia, L. De Cecco, M. E. Pisanu, A. Ricci, F. Podo, S. Canevari, E. Iorio, M. Bagnoli, and D. Mezzanzanica. Choline kinase-alpha by regulating cell aggressiveness and drug sensitivity is a potential druggable target for ovarian cancer. *Br J Cancer*, 110(2):330–40, 2014.
- [33] E. O. Aboagye and Z. M. Bhujwalla. Malignant transformation alters membrane choline phospholipid metabolism of human mammary epithelial cells. *Cancer Res*, 59(1):80–84, 1999.
- [34] J.-P. Galons, C. Job, and R. J. Gillies. Increase of GPC Levels in Cultured Mammalian Cells during Acidosis. A  $^{31}\text{P}$  MR Spectroscopy Study Using a Continuous Bioreactor System. *Magnetic Resonance in Medicine*, 33(3):422–26, 1995.
- [35] K. Glunde, T. Shah, Jr. Winnard, P. T., V. Raman, T. Takagi, F. Vesuna, D. Artemov, and Z. M. Bhujwalla. Hypoxia regulates choline kinase expression through hypoxia-inducible factor-1 alpha signaling in a human prostate cancer model. *Cancer Res*, 68(1):172–80, 2008.

- [36] G. P. Elvidge, L. Glenny, R. J. Appelhoff, P. J. Ratcliffe, J. Ragoussis, and J. M. Gleadle. Concordant regulation of gene expression by hypoxia and 2-oxoglutarate-dependent dioxygenase inhibition: the role of HIF-1alpha, HIF-2alpha, and other pathways. *J Biol Chem*, 281(22):15215–26, 2006.
- [37] T. Hara, A. Bansal, and T. R. DeGrado. Effect of hypoxia on the uptake of [methyl-3H]choline, [1-14C] acetate and [18F]FDG in cultured prostate cancer cells. *Nucl Med Biol*, 33(8):977–84, 2006.
- [38] A. Bansal, R. A. Harris, and T. R. Degrado. Choline phosphorylation and regulation of transcription of choline kinase alpha in hypoxia. *J Lipid Res*, 2011.
- [39] J. K. Blusztajn. Choline, a vital amine. *Science*, 281(5378):794–5, 1998.
- [40] L. M. Fischer, J. A. Scearce, M. H. Mar, J. R. Patel, R. T. Blanchard, B. A. Macintosh, M. G. Busby, and S. H. Zeisel. Ad libitum choline intake in healthy individuals meets or exceeds the proposed adequate intake level. *J Nutr*, 135(4):826–9, 2005.
- [41] S. H. Zeisel. Choline: critical role during fetal development and dietary requirements in adults. *Annu Rev Nutr*, 26:229–50, 2006.
- [42] Vance J E Vance, D. E. *Biochemistry of Lipids, Lipoproteins and Membranes*. Elsevier, 5 edition, 2008.
- [43] A. L. Buchman. The Addition of Choline to Parenteral Nutrition. *Gastroenterology*, 137(5):S119–S28, 2009.
- [44] K. A. da Costa, C. E. Gaffney, L. M. Fischer, and S. H. Zeisel. Choline deficiency in mice and humans is associated with increased plasma homocysteine concentration after a methionine load. *Am J Clin Nutr*, 81(2):440–4, 2005.
- [45] R. Clarke, L. Daly, K. Robinson, E. Naughten, S. Cahalane, B. Fowler, and I. Graham. Hyperhomocysteinemia: an independent risk factor for vascular disease. *New England Journal of Medicine*, 324(17):1149–55, 1991.
- [46] S. Seshadri, A. Beiser, J. Selhub, P. F. Jacques, I. H. Rosenberg, R. B. D’Agostino, P. W. F. Wilson, and P. A. Wolf. Plasma homocysteine as a risk factor for dementia and Alzheimer’s disease. *New England Journal of Medicine*, 346(7):476–83, 2002.

- [47] D. H. Sweet, D. S. Miller, and J. B. Pritchard. Ventricular choline transport: a role for organic cation transporter 2 expressed in choroid plexus. *J Biol Chem*, 276(45):41611–9, 2001.
- [48] G. van Meer, D. R. Voelker, and G. W. Feigenson. Membrane lipids: where they are and how they behave. *Nat Rev Mol Cell Biol*, 9(2):112–24, 2008.
- [49] J. T. Coyle, D. L. Price, and R. D. Mahlon. Alzheimer’s Disease: A Disorder of Cortical Cholinergic Innervation. *Science*, 219(4589):1184–90, 1983.
- [50] M. E. Hasselmo. The role of acetylcholine in learning and memory. *Current Opinion in Neurobiology*, 16(6):710–15, 2006.
- [51] D. M. Stafforini, T. M. McIntyre, G. A. Zimmerman, and S. M. Prescott. Platelet-activating factor, a pleiotropic mediator of physiological and pathological processes. *Crit Rev Clin Lab Sci*, 40(6):643–72, 2003.
- [52] V. Melnikova and M. Bar-Eli. Inflammation and melanoma growth and metastasis: the role of platelet-activating factor (PAF) and its receptor. *Cancer Metastasis Rev*, 26(3-4):359–71, 2007.
- [53] V. O. Melnikova, A. A. Mourad-Zeidan, D. C. Lev, and M. Bar-Eli. Platelet-activating factor mediates MMP-2 expression and activation via phosphorylation of cAMP-response element-binding protein and contributes to melanoma metastasis. *J Biol Chem*, 281(5):2911–22, 2006.
- [54] N. N. Desai, R. O. Carlson, M. E. Mattie, A. Olivera, N. E. Buckley, T. Seki, G. Brooker, and S. Spiegel. Signaling pathways for sphingosylphosphorylcholine-mediated mitogenesis in Swiss 3T3 fibroblasts. *J Cell Biol*, 121(6):1385–95, 1993.
- [55] T. Seufferlein and E. Rozengurt. Sphingosylphosphorylcholine rapidly induces tyrosine phosphorylation of p125FAK and paxillin, rearrangement of the actin cytoskeleton and focal contact assembly. Requirement of p21rho in the signaling pathway. *J Biol Chem*, 270(41):24343–51, 1995.
- [56] D. Meyer zu Heringdorf, H. M. Himmel, and K. H. Jakobs. Sphingosylphosphorylcholine-biological functions and mechanisms of action. *Biochim Biophys Acta*, 1582(1-3):178–89, 2002.

- [57] M. D. Niculescu and S. H. Zeisel. Diet, methyl donors and DNA methylation: interactions between dietary folate, methionine and choline. *J Nutr*, 132(8 Suppl): 2333S–35S, 2002.
- [58] H. Koepsell and H. Endou. The SLC22 drug transporter family. *Pflugers Arch*, 447 (5):666–76, 2004.
- [59] V. Michel, Z. Yuan, S. Ramsubir, and M. Bakovic. Choline transport for phospholipid synthesis. *Exp Biol Med (Maywood)*, 231(5):490–504, 2006.
- [60] T. Wang, J. Li, F. Chen, Y. Zhao, X. He, D. Wan, and J. Gu. Choline Transporters in Human Lung Adenocarcinoma: Expression and Functional Implications. *Acta Biochimica et Biophysica Sinica*, 39(9):668–74, 2007.
- [61] Z. Yuan, A. Tie, M. Tarnopolsky, and M. Bakovic. Genomic organization, promoter activity, and expression of the human choline transporter-like protein 1. *Physiological Genomics*, 26(1):76–90, 2006.
- [62] J. Klein, A. Koppen, K. Loffelholz, and J. Schmitthenner. Uptake and metabolism of choline by rat brain after acute choline administration. *J Neurochem*, 58(3):870–6, 1992.
- [63] S. M. Ferguson and R. D. Blakely. The choline transporter resurfaces: new roles for synaptic vesicles? *Mol Interv*, 4(1):22–37, 2004.
- [64] E. Yavin. Regulation of phospholipid metabolism in differentiating cells from rat brain cerebral hemispheres in culture. Patterns of acetylcholine phosphocholine, and choline phosphoglycerides labeling from (methyl-14C)choline. *Journal of Biological Chemistry*, 251(5):1392–97, 1976.
- [65] J. Gruber, W. C. See Too, M. T. Wong, A. Lavie, T. McSorley, and M. Konrad. Balance of human choline kinase isoforms is critical for cell cycle regulation: implications for the development of choline kinase-targeted cancer therapy. *FEBS J*, 279 (11):1915–28, 2012.
- [66] T. Uchida and S. Yamashita. Molecular cloning, characterization, and expression in *Escherichia coli* of a cDNA encoding mammalian choline kinase. *J Biol Chem*, 267 (14):10156–62, 1992.

- [67] T. Uchida. Regulation of choline kinase R: analyses of alternatively spliced choline kinases and the promoter region. *J Biochem*, 116(3):508–18, 1994.
- [68] C. Aoyama, K. Nakashima, M. Matsui, and K. Ishidate. Complementary DNA sequence for a 42 kDa rat kidney choline/ethanolamine kinase. *Biochim Biophys Acta*, 1390(1):1–7, 1998.
- [69] C. Aoyama, H. Liao, and K. Ishidate. Structure and function of choline kinase isoforms in mammalian cells. *Prog Lipid Res*, 43(3):266–81, 2004.
- [70] K. Contractor, A. Challapalli, T. Barwick, M. Winkler, G. Hellowell, S. Hazell, G. Tomasi, A. Al-Nahas, P. Mapelli, L. M. Kenny, P. Tadrous, R. C. Coombes, E. O. Aboagye, and S. Mangar. Use of [11C]choline PET-CT as a noninvasive method for detecting pelvic lymph node status from prostate cancer and relationship with choline kinase expression. *Clin Cancer Res*, 17(24):7673–83, 2011.
- [71] E. Malito, N. Sekulic, W. C. Too, M. Konrad, and A. Lavie. Elucidation of human choline kinase crystal structures in complex with the products ADP or phosphocholine. *J Mol Biol*, 364(2):136–51, 2006.
- [72] G. Wu, C. Aoyama, S. G. Young, and D. E. Vance. Early embryonic lethality caused by disruption of the gene for choline kinase alpha, the first enzyme in phosphatidylcholine biosynthesis. *J Biol Chem*, 283(3):1456–62, 2008.
- [73] R. B. Sher, C. Aoyama, K. A. Huebsch, S. Ji, J. Kerner, Y. Yang, W. N. Frankel, C. L. Hoppel, P. A. Wood, D. E. Vance, and G. A. Cox. A rostrocaudal muscular dystrophy caused by a defect in choline kinase beta, the first enzyme in phosphatidylcholine biosynthesis. *J Biol Chem*, 281(8):4938–48, 2006.
- [74] G. Wu, R. B. Sher, G. A. Cox, and D. E. Vance. Understanding the muscular dystrophy caused by deletion of choline kinase beta in mice. *Biochim Biophys Acta*, 1791(5):347–56, 2009.
- [75] G. Wu and D. E. Vance. Choline kinase and its function. *Biochem Cell Biol*, 88(4):559–64, 2010.
- [76] C. Kent. Regulation of phosphatidylcholine biosynthesis. *Prog Lipid Res*, 29(2):87–105, 1990.

- [77] A. Lykidis and S. Jackowski. Regulation of mammalian cell membrane biosynthesis. *Prog Nucleic Acid Res Mol Biol*, 65:361–93, 2001.
- [78] K. Glunde, C. Jie, and Z. M. Bhujwala. Molecular causes of the aberrant choline phospholipid metabolism in breast cancer. *Cancer Res*, 64(12):4270–6, 2004.
- [79] R. B. Cornell and I. C. Northwood. Regulation of CTP:phosphocholine cytidylyltransferase by amphitropism and relocalization. *Trends in biochemical sciences*, 25(9):441–47, 2000.
- [80] H. Sugimoto, C. Banchio, and D. E. Vance. Transcriptional regulation of phosphatidylcholine biosynthesis. *Prog Lipid Res*, 47(3):204–20, 2008.
- [81] S. Jackowski, J. E. Rehg, Y.-M. Zhang, J. Wang, K. Miller, P. Jackson, and M. A. Karim. Disruption of CCT beta 2 Expression Leads to Gonadal Dysfunction. *Molecular and Cellular Biology*, 24(11):4720–33, 2004.
- [82] L. Wang, S. Magdaleno, I. Tabas, and S. Jackowski. Early Embryonic Lethality in Mice with Targeted Deletion of the CTP:Phosphocholine Cytidylyltransferase Alpha Gene (Pcyl1a). *Molecular and Cellular Biology*, 25(8):3357–63, 2005.
- [83] T. A. Lagace, J. R. Miller, and N. D. Ridgway. Caspase Processing and Nuclear Export of CTP:Phosphocholine Cytidylyltransferase Alpha during Farnesol-Induced Apoptosis. *Molecular and Cellular Biology*, 22(13):4851–62, 2002.
- [84] Z. Li and D. E. Vance. Phosphatidylcholine and choline homeostasis. *J Lipid Res*, 49(6):1187–94, 2008.
- [85] A. L. Henneberry and C. R. McMaster. Cloning and expression of a human choline/ethanolaminephosphotransferase: synthesis of phosphatidylcholine and phosphatidylethanolamine. *Biochem. J.*, 339(2):291–98, 1999.
- [86] A. L. Henneberry, G. Wistow, and C. R. McMaster. Cloning, Genomic Organization, and Characterization of a Human Cholinephosphotransferase. *Journal of Biological Chemistry*, 275(38):29808–15, 2000.
- [87] D. J. Shields, J. Y. Altarejos, X. Wang, L. B. Agellon, and D. E. Vance. Molecular Dissection of the S-Adenosylmethionine-binding Site of Phosphatidylethanolamine N-Methyltransferase. *Journal of Biological Chemistry*, 278(37):35826–36, 2003.

- [88] Z. Cui, J. E. Vance, M. H. Chen, D. R. Voelker, and D. E. Vance. Cloning and expression of a novel phosphatidylethanolamine N-methyltransferase. A specific biochemical and cytological marker for a unique membrane fraction in rat liver. *Journal of Biological Chemistry*, 268(22):16655–63, 1993.
- [89] C. J. Walkey, L. R. Donohue, R. Bronson, L. B. Agellon, and D. E. Vance. Disruption of the murine gene encoding phosphatidylethanolamine N-methyltransferase. *Proceedings of the National Academy of Sciences*, 94(24):12880–85, 1997.
- [90] C. J. Walkey, L. Yu, L. B. Agellon, and D. E. Vance. Biochemical and Evolutionary Significance of Phospholipid Methylation. *Journal of Biological Chemistry*, 273(42):27043–46, 1998.
- [91] M. Liscovitch, M. Czarny, G. Fiucci, and X. Tang. Phospholipase D: molecular and cell biology of a novel gene family. *Biochem. J.*, 345(3):401–15, 2000.
- [92] D. S. Min, T. K. Kwon, W.-S. Park, J.-S. Chang, S.-K. Park, B.-H. Ahn, Z.-Y. Ryoo, Y. H. Lee, Y. S. Lee, D.-J. Rhie, S.-H. Yoon, S. J. Hahn, M.-S. Kim, and Y.-H. Jo. Neoplastic transformation and tumorigenesis associated with overexpression of phospholipase D isozymes in cultured murine fibroblasts. *Carcinogenesis*, 22(10):1641–47, 2001.
- [93] Y. Nishizuka. Protein kinase C and lipid signaling for sustained cellular responses. *The FASEB Journal*, 9(7):484–96, 1995.
- [94] E. M. Griner and M. G. Kazanietz. Protein kinase C and other diacylglycerol effectors in cancer. *Nat Rev Cancer*, 7(4):281–94, 2007.
- [95] J. D. Stewart, R. Marchan, M. S. Lesjak, J. Lambert, R. Hergenroeder, J. K. Ellis, C.-H. Lau, H. C. Keun, G. Schmitz, and J. et al. Schiller. Choline-releasing glycerophosphodiesterase EDI3 drives tumor cell migration and metastasis. *Proceedings of the National Academy of Sciences*, 109(21):8155–60, 2012.
- [96] N. M. Al-Saffar, H. Troy, A. Ramirez de Molina, L. E. Jackson, B. Madhu, J. R. Griffiths, M. O. Leach, P. Workman, J. C. Lacal, I. R. Judson, and Y. L. Chung. Non-invasive magnetic resonance spectroscopic pharmacodynamic markers of the choline kinase inhibitor MN58b in human carcinoma models. *Cancer Res*, 66(1):427–34, 2006.



- [97] C. Gabellieri, M. Belouèche-Babari, Y. Jamin, G. S. Payne, M. O. Leach, and T. R. Eykyn. Modulation of choline kinase activity in human cancer cells observed by dynamic  $^{31}\text{P}$  NMR. *NMR Biomed*, 22(4):456–61, 2009.
- [98] N. M. Al-Saffar, L. E. Jackson, F. I. Raynaud, P. A. Clarke, A. Ramirez de Molina, J. C. Lacal, P. Workman, and M. O. Leach. The Phosphoinositide 3-Kinase Inhibitor PI-103 Downregulates Choline Kinase  $\alpha$  Leading to Phosphocholine and Total Choline Decrease Detected by Magnetic Resonance Spectroscopy. *Cancer Res*, 2010.
- [99] M. Sankaranarayanapillai, N. Zhang, K. A. Baggerly, and J. G. Gelovani. Metabolic shifts induced by fatty acid synthase inhibitor orlistat in non-small cell lung carcinoma cells provide novel pharmacodynamic biomarkers for positron emission tomography and magnetic resonance spectroscopy. *Mol Imaging Biol*, 15(2):136–47, 2013.
- [100] Y. L. Chung, H. Troy, R. Kristeleit, W. Aherne, L. E. Jackson, P. Atadja, J. R. Griffiths, I. R. Judson, P. Workman, M. O. Leach, and M. Belouèche-Babari. Non-invasive magnetic resonance spectroscopic pharmacodynamic markers of a novel histone deacetylase inhibitor, LAQ824, in human colon carcinoma cells and xenografts. *Neoplasia*, 10(4):303–13, 2008.
- [101] M. Belouèche-Babari, V. Arunan, H. Troy, R. H. te Poele, A. C. te Fong, L. E. Jackson, G. S. Payne, J. R. Griffiths, I. R. Judson, P. Workman, M. O. Leach, and Y. L. Chung. Histone deacetylase inhibition increases levels of choline kinase  $\alpha$  and phosphocholine facilitating noninvasive imaging in human cancers. *Cancer Res*, 72(4):990–1000, 2012.
- [102] T. Hara, N. Kosaka, N. Shinoura, and T. Kondo. PET imaging of brain tumor with [methyl- $^{11}\text{C}$ ]choline. *J Nucl Med*, 38(6):842–7, 1997.
- [103] T. Hara, N. Kosaka, and H. Kishi. PET imaging of prostate cancer using carbon- $^{11}$ -choline. *J Nucl Med*, 39(6):990–5, 1998.
- [104] O. Kobori, Y. Kirihara, N. Kosaka, and T. Hara. Positron emission tomography of esophageal carcinoma using  $(^{11}\text{C})$ -choline and  $(^{18}\text{F})$ -fluorodeoxyglucose: a novel method of preoperative lymph node staging. *Cancer*, 86(9):1638–48, 1999.

- [105] T. Hara, K. Inagaki, N. Kosaka, and T. Morita. Sensitive detection of mediastinal lymph node metastasis of lung cancer with  $^{11}\text{C}$ -choline PET. *J Nucl Med*, 41(9):1507–13, 2000.
- [106] R. M. Pieterman, T. H. Que, P. H. Elsinga, J. Pruim, J. W. van Putten, A. T. Willemsen, W. Vaalburg, and H. J. Groen. Comparison of  $(^{11}\text{C})$ -choline and  $(^{18}\text{F})$ -FDG PET in primary diagnosis and staging of patients with thoracic cancer. *J Nucl Med*, 43(2):167–72, 2002.
- [107] G. Giovacchini, M. Picchio, E. Coradeschi, V. Scattoni, V. Bettinardi, C. Cozzarini, M. Freschi, F. Fazio, and C. Messa.  $[(^{11}\text{C})]$ choline uptake with PET/CT for the initial diagnosis of prostate cancer: relation to PSA levels, tumour stage and anti-androgenic therapy. *Eur J Nucl Med Mol Imaging*, 35(6):1065–73, 2008.
- [108] K. B. Contractor, L. M. Kenny, J. Stebbing, A. Al-Nahhas, C. Palmieri, D. Sinnett, J. S. Lewis, K. Hogben, S. Osman, S. Shousha, C. Lowdell, R. C. Coombes, and E. O. Aboagye.  $^{11}\text{C}$ choline positron emission tomography in estrogen receptor-positive breast cancer. *Clin Cancer Res*, 15(17):5503–10, 2009.
- [109] K. B. Contractor, L. M. Kenny, J. Stebbing, A. Challapalli, A. Al-Nahhas, C. Palmieri, S. Shousha, J. S. Lewis, K. Hogben, Q. De Nguyen, R. C. Coombes, and E. O. Aboagye. Biological basis of  $[(^{11}\text{C})]$ choline-positron emission tomography in patients with breast cancer: comparison with  $[(^{18}\text{F})]$ fluorothymidine positron emission tomography. *Nucl Med Commun*, 32(11):997–1004, 2011.
- [110] T. H. Witney, I. S. Alam, D. R. Turton, G. Smith, L. Carroll, D. Brickute, F. J. Twyman, Q. D. Nguyen, G. Tomasi, R. O. Awais, and E. O. Aboagye. Evaluation of Deuterated  $^{18}\text{F}$ - and  $^{11}\text{C}$ -Labeled Choline Analogs for Cancer Detection by Positron Emission Tomography. *Clin Cancer Res*, 18(4):1063–72, 2012.
- [111] E. O. Aboagye. The future of imaging: developing the tools for monitoring response to therapy in oncology: the 2009 Sir James MacKenzie Davidson Memorial lecture. *Br J Radiol*, 83(994):814–22, 2010.
- [112] J. Leyton, G. Smith, Y. Zhao, M. Perumal, Q.-D. Nguyen, E. Robins, E. Arstad, and E. O. Aboagye.  $^{18}\text{F}$ Fluoromethyl- $[1,2\text{-}^2\text{H}_4]$ -Choline: A Novel Radiotracer for

- Imaging Choline Metabolism in Tumors by Positron Emission Tomography. *Cancer Research*, 69(19):7721–28, 2009.
- [113] A. Challapalli, R. Sharma, W. A. Hallett, K. Kozlowski, L. Carroll, D. Brickute, F. Twyman, A. Al-Nahas, and E. O. Aboagye. Biodistribution and Radiation Dosimetry of Deuterium-Substituted  $^{18}\text{F}$ -Fluoromethyl-[1, 2- $^2\text{H}_4$ ]Choline in Healthy Volunteers. *Journal of Nuclear Medicine*, 55(2):256–63, 2014.
- [114] L. Zhao, A. Ashek, L. Wang, W. Fang, S. Dabral, O. Dubois, J. Cupitt, S. S. Pulamsetti, E. Cotroneo, and H. et al. Jones. Heterogeneity in Lung  $^{18}\text{F}$ FDG Uptake in Pulmonary Arterial Hypertension: Potential of Dynamic  $^{18}\text{F}$ FDG Positron Emission Tomography With Kinetic Analysis as a Bridging Biomarker for Pulmonary Vascular Remodeling Targeted Treatments. *Circulation*, 128(11):1214–24, 2013.
- [115] C. Vigo and D. E. Vance. Effect of diethylstilboestrol on phosphatidylcholine biosynthesis and choline metabolism in the liver of roosters. *Biochem J*, 200(2):321–6, 1981.
- [116] C. H. Warden and M. Friedkin. Regulation of choline kinase activity and phosphatidylcholine biosynthesis by mitogenic growth factors in 3T3 fibroblasts. *J Biol Chem*, 260(10):6006–11, 1985.
- [117] A. Cuadrado, A. Carnero, F. Dolfi, B. Jimenez, and J. C. Lacal. Phosphorylcholine: a novel second messenger essential for mitogenic activity of growth factors. *Oncogene*, 8(11):2959–68, 1993.
- [118] B. Jimenez, L. del Peso, S. Montaner, P. Esteve, and J. C. Lacal. Generation of phosphorylcholine as an essential event in the activation of Raf-1 and MAP-kinases in growth factors-induced mitogenic stimulation. *J Cell Biochem*, 57(1):141–9, 1995.
- [119] T. Uchida. Stimulation of phospholipid synthesis in HeLa cells by epidermal growth factor and insulin: activation of choline kinase and glycerophosphate acyltransferase. *Biochim Biophys Acta*, 1304(2):89–104, 1996.
- [120] A. Ramirez de Molina, V. Penalva, L. Lucas, and J. C. Lacal. Regulation of choline kinase activity by Ras proteins involves Ral-GDS and PI3K. *Oncogene*, 21(6):937–46, 2002.
- [121] A. Ramirez de Molina, M. Banez-Coronel, R. Gutierrez, A. Rodriguez-Gonzalez, D. Olmeda, D. Megias, and J. C. Lacal. Choline kinase activation is a critical

- requirement for the proliferation of primary human mammary epithelial cells and breast tumor progression. *Cancer Res*, 64(18):6732–39, 2004.
- [122] T. Miyake and S. J. Parsons. Functional interactions between Choline kinase alpha, epidermal growth factor receptor and c-Src in breast cancer cell proliferation. *Oncogene*, 31(11):1431–41, 2012.
- [123] K. H. Kim and G. M. Carman. Phosphorylation and regulation of choline kinase from *Saccharomyces cerevisiae* by protein kinase A. *J Biol Chem*, 274(14):9531–8, 1999.
- [124] Y. Yu, A. Sreenivas, D. B. Ostrander, and G. M. Carman. Phosphorylation of *Saccharomyces cerevisiae* choline kinase on Ser30 and Ser85 by protein kinase A regulates phosphatidylcholine synthesis by the CDP-choline pathway. *J Biol Chem*, 277(38):34978–86, 2002.
- [125] G. M. Carman and M. C. Kersting. Phospholipid synthesis in yeast: regulation by phosphorylation. *Biochem Cell Biol*, 82(1):62–70, 2004.
- [126] M. G. Choi, V. Kurnov, M. C. Kersting, A. Sreenivas, and G. M. Carman. Phosphorylation of the yeast choline kinase by protein kinase C. Identification of Ser25 and Ser30 as major sites of phosphorylation. *J Biol Chem*, 280(28):26105–12, 2005.
- [127] M. Wieprecht, T. Wieder, and C. C. Geilen. N-[2-bromocinnamyl(amino)ethyl]-5-isoquinolinesulphonamide (H-89) inhibits incorporation of choline into phosphatidylcholine via inhibition of choline kinase and has no effect on the phosphorylation of CTP:phosphocholine cytidyltransferase. *Biochem J*, 297 ( Pt 1):241–7, 1994.
- [128] Z. Dong, C. Huang, W. Y. Ma, B. Malewicz, W. J. Baumann, and Z. Kiss. Increased synthesis of phosphocholine is required for UV-induced AP-1 activation. *Oncogene*, 17(14):1845–53, 1998.
- [129] C. Aoyama, K. Ishidate, H. Sugimoto, and D. E. Vance. Induction of choline kinase alpha by carbon tetrachloride (CCl<sub>4</sub>) occurs via increased binding of c-jun to an AP-1 element. *Biochim Biophys Acta*, 1771(9):1148–55, 2007.
- [130] F. Morrish, N. Isern, M. Sadilek, M. Jeffrey, and D. M. Hockenbery. c-Myc activates multiple metabolic networks to generate substrates for cell-cycle entry. *Oncogene*, 28(27):2485–91, 2009.

- [131] A. Ramirez de Molina, A. Rodriguez-Gonzalez, V. Penalva, L. Lucas, and J. C. Lacal. Inhibition of ChoK is an efficient antitumor strategy for Harvey-, Kirsten-, and N-ras-transformed cells. *Biochem Biophys Res Commun*, 285(4):873–9, 2001.
- [132] B. T. Chua, D. Gallego-Ortega, A. Ramirez de Molina, A. Ullrich, J. C. Lacal, and J. Downward. Regulation of Akt(ser473) phosphorylation by Choline kinase in breast carcinoma cells. *Mol Cancer*, 8:131, 2009.
- [133] A. Ramirez de Molina, D. Gallego-Ortega, J. Sarmentero, M. Banez-Coronel, Y. Martin-Cantalejo, and J. C. Lacal. Choline kinase is a novel oncogene that potentiates RhoA-induced carcinogenesis. *Cancer Res*, 65(13):5647–53, 2005.
- [134] J. M. Besterman, V. Duronio, and P. Cuatrecasas. Rapid formation of diacylglycerol from phosphatidylcholine: a pathway for generation of a second messenger. *Proc Natl Acad Sci U S A*, 83(18):6785–9, 1986.
- [135] B. D. Price, J. D. Morris, C. J. Marshall, and A. Hall. Stimulation of phosphatidylcholine hydrolysis, diacylglycerol release, and arachidonic acid production by oncogenic ras is a consequence of protein kinase C activation. *J Biol Chem*, 264(28):16638–43, 1989.
- [136] A. Yalcin, B. Clem, S. Makoni, A. Clem, K. Nelson, J. Thornburg, D. Siow, A. N. Lane, S. E. Brock, U. Goswami, J. W. Eaton, S. Telang, and J. Chesney. Selective inhibition of choline kinase simultaneously attenuates MAPK and PI3K/AKT signaling. *Oncogene*, 29(1):139–49, 2010.
- [137] A. Ramirez de Molina, D. Gallego-Ortega, J. Sarmentero-Estrada, D. Lagares, T. Gomez Del Pulgar, E. Bandres, J. Garcia-Foncillas, and J. C. Lacal. Choline kinase as a link connecting phospholipid metabolism and cell cycle regulation: implications in cancer therapy. *Int J Biochem Cell Biol*, 40(9):1753–63, 2008.
- [138] N. Mori, M. Gadiya, F. Wildes, B. Krishnamachary, K. Glunde, and Z. M. Bhujwalla. Characterization of choline kinase in human endothelial cells. *NMR Biomed*, 2013.
- [139] K. Glunde, V. Raman, N. Mori, and Z. M. Bhujwalla. RNA interference-mediated choline kinase suppression in breast cancer cells induces differentiation and reduces proliferation. *Cancer Res*, 65(23):11034–43, 2005.

- [140] M. Gadiya, N. Mori, M. D. Cao, Y. Mironchik, S. Kakkad, I. S. Gribbestad, K. Glunde, B. Krishnamachary, and Z. M. Bhujwalla. Phospholipase D1 and choline kinase-alpha are interactive targets in breast cancer. *Cancer Biol Ther*, 15(5), 2014.
- [141] N. Mori, K. Glunde, T. Takagi, V. Raman, and Z. M. Bhujwalla. Choline kinase down-regulation increases the effect of 5-fluorouracil in breast cancer cells. *Cancer Res*, 67(23):11284–90, 2007.
- [142] B. Krishnamachary, K. Glunde, F. Wildes, N. Mori, T. Takagi, V. Raman, and Z. M. Bhujwalla. Noninvasive detection of lentiviral-mediated choline kinase targeting in a human breast cancer xenograft. *Cancer Res*, 69(8):3464–71, 2009.
- [143] V. Gomez-Perez, T. McSorley, W. C. See Too, M. Konrad, and J. M. Campos. Novel 4-Amino Bis-pyridinium and Bis-quinolinium Derivatives as Choline Kinase Inhibitors with Antiproliferative Activity against the Human Breast Cancer SKBR-3 Cell Line. *ChemMedChem*, 7(4):663–9, 2012.
- [144] J. Campos, M. C. Nunez, A. Conejo-Garcia, R. M. Sanchez-Martin, R. Hernandez-Alcoceba, A. Rodriguez-Gonzalez, J. C. Lacal, M. A. Gallo, and A. Espinosa. QSAR-derived choline kinase inhibitors: how rational can antiproliferative drug design be? *Curr Med Chem*, 10(13):1095–112, 2003.
- [145] R. Hernandez-Alcoceba, L. Saniger, J. Campos, M. C. Nunez, F. Khaless, M. A. Gallo, A. Espinosa, and J. C. Lacal. Choline kinase inhibitors as a novel approach for antiproliferative drug design. *Oncogene*, 15(19):2289–301, 1997.
- [146] R. Hernandez-Alcoceba, F. Fernandez, and J. C. Lacal. In vivo antitumor activity of choline kinase inhibitors: a novel target for anticancer drug discovery. *Cancer Res*, 59(13):3112–8, 1999.
- [147] C. S. Hudson, R. M. Knegt, K. Brown, P. A. Charlton, and J. R. Pollard. Kinetic and mechanistic characterisation of Choline Kinase-alpha. *Biochim Biophys Acta*, 2013.
- [148] S. C. Falcon, C. S. Hudson, Y. Huang, M. Mortimore, J. M. Golec, P. A. Charlton, P. Weber, and H. Sundaram. A non-catalytic role of choline kinase alpha is important in promoting cancer cell survival. *Oncogenesis*, 2:e38, 2013.

- [149] B. F. Clem, A. L. Clem, A. Yalcin, U. Goswami, S. Arumugam, S. Telang, J. O. Trent, and J. Chesney. A novel small molecule antagonist of choline kinase-alpha that simultaneously suppresses MAPK and PI3K/AKT signaling. *Oncogene*, 2011.
- [150] B. Rubio-Ruiz, A. Conejo-Garcia, P. Rios-Marco, M. P. Carrasco-Jimenez, J. Segovia, C. Marco, M. A. Gallo, A. Espinosa, and A. Entrena. Design, synthesis, theoretical calculations and biological evaluation of new non-symmetrical choline kinase inhibitors. *Eur J Med Chem*, 50:154–62, 2012.
- [151] L. A. Smart. Synthesis and biological activity of a 2-bromoethylamine (mustard) derivative of hemicholinium-3 and hemicholinium-15. *J Med Chem*, 26(1):104–7, 1983.
- [152] B. Palacios Izquierdo, P. Van Hoogevest, and M. L.S. Leigh. Pharmaceutical compositions of pyridinium and quinolinium derivatives, 28.06.2012 2012.
- [153] Y. A. Hannun and L. M. Obeid. Principles of bioactive lipid signalling: lessons from sphingolipids. *Nat Rev Mol Cell Biol*, 9(2):139–50, 2008.
- [154] A. Rodriguez-Gonzalez, A. Ramirez de Molina, F. Fernandez, and J. C. Lacal. Choline kinase inhibition induces the increase in ceramides resulting in a highly specific and selective cytotoxic antitumoral strategy as a potential mechanism of action. *Oncogene*, 23(50):8247–59, 2004.
- [155] M. H. van der Sanden, M. Houweling, L. M. van Golde, and A. B. Vaandrager. Inhibition of phosphatidylcholine synthesis induces expression of the endoplasmic reticulum stress and apoptosis-related protein CCAAT/enhancer-binding protein-homologous protein (CHOP/GADD153). *Biochem J*, 369(Pt 3):643–50, 2003.
- [156] D. Ron and P. Walter. Signal integration in the endoplasmic reticulum unfolded protein response. *Nat Rev Mol Cell Biol*, 8(7):519–29, 2007.
- [157] E. Sanchez-Lopez, T. Zimmerman, T. Gomez del Pulgar, M. P. Moyer, J. C. Lacal Sanjuan, and A. Cebrian. Choline kinase inhibition induces exacerbated endoplasmic reticulum stress and triggers apoptosis via CHOP in cancer cells. *Cell Death Dis*, 4:e933, 2013.

- [158] G. Smith, Y. Zhao, J. Leyton, B. Shan, Q.-d. Nguyen, M. Perumal, D. Turton, E. Arstad, S. K. Luthra, E. G. Robins, and E. O. Aboagye. Radiosynthesis and pre-clinical evaluation of [18F]fluoro-[1,2-2H4]choline. *Nuclear Medicine and Biology*, 38(1):39–51, 2011.
- [159] A. Orlova, A. Jonsson, D. Rosik, H. Lundqvist, M. Lindborg, L. Abrahmsen, C. Ekblad, F. Y. Frejd, and V. Tolmachev. Site-specific radiometal labeling and improved biodistribution using ABY-027, a novel HER2-targeting affibody molecule-albumin-binding domain fusion protein. *J Nucl Med*, 54(6):961–8, 2013.
- [160] M. Glaser, P. Iveson, S. Hoppmann, B. Indrevoll, A. Wilson, J. Arukwe, A. Danikas, R. Bhalla, and D. Hiscock. Three Methods for 18F Labeling of the HER2-Binding Affibody Molecule ZHER2:2891 Including Preclinical Assessment. *J Nucl Med*, 54(11):1981–8, 2013.
- [161] M. Scaltriti, F. Rojo, A. Ocana, J. Anido, M. Guzman, J. Cortes, S. Di Cosimo, X. Matias-Guiu, S. Ramon y Cajal, J. Arribas, and J. Baselga. Expression of p95HER2, a truncated form of the HER2 receptor, and response to anti-HER2 therapies in breast cancer. *J Natl Cancer Inst*, 99(8):628–38, 2007.
- [162] A. Samalecos, K. Reimann, S. Wittmann, H. M. Schulte, J. J. Brosens, A. M. Bamberger, and B. Gellersen. Characterization of a novel telomerase-immortalized human endometrial stromal cell line, St-T1b. *Reprod Biol Endocrinol*, 7:76, 2009.
- [163] V. Vichai and K. Kirtikara. Sulforhodamine B colorimetric assay for cytotoxicity screening. *Nat Protoc*, 1(3):1112–6, 2006.
- [164] J. J. Murray, T. T. Dinh, 3rd Truett, A. P., and D. A. Kennerly. Isolation and enzymic assay of choline and phosphocholine present in cell extracts with picomole sensitivity. *Biochem J*, 270(1):63–8, 1990.
- [165] T. D. Schmittgen and K. J. Livak. Analyzing real-time PCR data by the comparative C(T) method. *Nat Protoc*, 3(6):1101–8, 2008.
- [166] I. Wittig, H.-P. Braun, and H. Schagger. Blue native PAGE. *Nat. Protocols*, 1(1):418–28, 2006.



- [167] M. Markowska, R. Oberle, S. Juzwin, C. P. Hsu, M. Gryszkiewicz, and A. J. Streeter. Optimizing Caco-2 cell monolayers to increase throughput in drug intestinal absorption analysis. *J Pharmacol Toxicol Methods*, 46(1):51–5, 2001.
- [168] P. P. Tirumalasetty and J. G. Eley. Permeability enhancing effects of the alkylglycoside, octylglucoside, on insulin permeation across epithelial membrane in vitro. *J Pharm Pharm Sci*, 9(1):32–9, 2006.
- [169] J. Rautio, J. E. Humphreys, L. O. Webster, A. Balakrishnan, J. P. Keogh, J. R. Kunta, C. J. Serabjit-Singh, and J. W. Polli. In vitro p-glycoprotein inhibition assays for assessment of clinical drug interaction potential of new drug candidates: a recommendation for probe substrates. *Drug Metabolism and Disposition*, 34(5):786–92, 2006.
- [170] P. Workman, E. O. Aboagye, F. Balkwill, A. Balmain, G. Bruder, D. J. Chaplin, J. A. Double, J. Everitt, D. A. Farningham, and M. J. et al. Glennie. Guidelines for the welfare and use of animals in cancer research. *Br J Cancer*, 102(11):1555–77, 2010.
- [171] T.-C. Chou. Theoretical Basis, Experimental Design, and Computerized Simulation of Synergism and Antagonism in Drug Combination Studies. *Pharmacological Reviews*, 58(3):621–81, 2006.
- [172] G. Tomasi, A. Bertoldo, S. Bishu, A. Unterman, C. B. Smith, and K. C. Schmidt. Voxel-based estimation of kinetic model parameters of the L-[1-(11)C]leucine PET method for determination of regional rates of cerebral protein synthesis: validation and comparison with region-of-interest-based methods. *J Cereb Blood Flow Metab*, 29(7):1317–31, 2009.
- [173] H. Greulich, B. Kaplan, P. Mertins, T. H. Chen, K. E. Tanaka, C. H. Yun, X. Zhang, S. H. Lee, J. Cho, and L. et al. Ambrogio. Functional analysis of receptor tyrosine kinase mutations in lung cancer identifies oncogenic extracellular domain mutations of ERBB2. *Proc Natl Acad Sci U S A*, 109(36):14476–81, 2012.
- [174] B. S. Hong, A. Allali-Hassani, W. Tempel, Jr. Finerty, P. J., F. Mackenzie, S. Dimov, M. Vedadi, and H. W. Park. Crystal structures of human choline kinase isoforms

- in complex with hemicholinium-3: single amino acid near the active site influences inhibitor sensitivity. *J Biol Chem*, 285(21):16330–40, 2010.
- [175] G. S. Sittampalam, N. Gal-Edd, M. Arkin, et al., and editors. *Assay Guidance Manual [Internet]*. Bethesda (MD): Eli Lilly and Company and the National Center for Advancing Translational Sciences., 2004.
- [176] R. A. Copeland. *Evaluation of Enzyme Inhibitors in Drug Discovery: A Guide for Medicinal Chemists and Pharmacologists*. Wiley-Interscience, 1 edition, 2005.
- [177] Y. Jia, X.-j. Gu, A. Brinker, and M. Warmuth. Measuring the tyrosine kinase activity: a review of biochemical and cellular assay technologies. *Expert Opinion on Drug Discovery*, 3(8):959–78, 2008.
- [178] S. H. Zeisel. Choline: an essential nutrient for humans. *Nutrition*, 16(7-8):669–71, 2000.
- [179] J. Barretina, G. Caponigro, N. Stransky, K. Venkatesan, A. A. Margolin, S. Kim, C. J. Wilson, J. Lehar, G. V. Kryukov, and D. et al. Sonkin. The Cancer Cell Line Encyclopedia enables predictive modelling of anticancer drug sensitivity. *Nature*, 483(7391):603–307, 2012.
- [180] Y. Gong, Y. Anzai, L. C. Murphy, G. Ballejo, C. F. Holinka, E. Gurpide, and L. J. Murphy. Transforming growth factor gene expression in human endometrial adenocarcinoma cells: regulation by progestins. *Cancer Res*, 51(20):5476–81, 1991.
- [181] J. Yoshida, T. Ishibashi, and M. Nishio. Growth-inhibitory Effect of a Streptococcal Antitumor Glycoprotein on Human Epidermoid Carcinoma A431 Cells: Involvement of Dephosphorylation of Epidermal Growth Factor Receptor. *Cancer Research*, 61(16):6151–57, 2001.
- [182] D. Roberts, J. Schick, S. Conway, S. Biade, P. B. Laub, J. P. Stevenson, T. C. Hamilton, P. J. O’Dwyer, and S. W. Johnson. Identification of genes associated with platinum drug sensitivity and resistance in human ovarian cancer cells. *Br J Cancer*, 92(6):1149–58, 2005.
- [183] American Type Culture Collection. Thawing, propagation, and cryopreserving protocol. nci-pbcf-ccl247 (hct 116) colorectal carcinoma (atcc ccl-247)., 2012.

- [184] American Type Culture Collection. Thawing, propagation, and cryopreserving protocol. mcf-7 breast adenocarcinoma. nci-pbcf-htb22 (atcc htb-22)., 2012.
- [185] American Type Culture Collection. Thawing, propagation, and cryopreserving protocol. mcf10a-jsb breast adenocarcinoma. nci-pbcf-1000., 2012.
- [186] American Type Culture Collection. A549 (atcc ccl-185) homo sapiens lung carcinoma., 2014.
- [187] C. Korzeniewski and D. M. Callewaert. An enzyme-release assay for natural cytotoxicity. *J Immunol Methods*, 64(3):313–20, 1983.
- [188] A. Wagner, A. Marc, J. M. Engasser, and A. Einsele. The use of lactate dehydrogenase (LDH) release kinetics for the evaluation of death and growth of mammalian cells in perfusion reactors. *Biotechnology and Bioengineering*, 39(3):320–26, 1992.
- [189] R. H. Shoemaker. The NCI60 human tumour cell line anticancer drug screen. *Nat Rev Cancer*, 6(10):813–23, 2006.
- [190] G. Batist, A. Tulpule, B. K. Sinha, A. G. Katki, C. E. Myers, and K. H. Cowan. Overexpression of a novel anionic glutathione transferase in multidrug-resistant human breast cancer cells. *J Biol Chem*, 261(33):15544–9, 1986.
- [191] J. S. Lee, K. Paull, M. Alvarez, C. Hose, A. Monks, M. Grever, A. T. Fojo, and S. E. Bates. Rhodamine efflux patterns predict P-glycoprotein substrates in the National Cancer Institute drug screen. *Mol Pharmacol*, 46(4):627–38, 1994.
- [192] M. Alvarez, K. Paull, A. Monks, C. Hose, J. S. Lee, J. Weinstein, M. Grever, S. Bates, and T. Fojo. Generation of a drug resistance profile by quantitation of mdr-1/P-glycoprotein in the cell lines of the National Cancer Institute Anticancer Drug Screen. *J Clin Invest*, 95(5):2205–14, 1995.
- [193] L. A. Garraway, H. R. Widlund, M. A. Rubin, G. Getz, A. J. Berger, S. Ramaswamy, R. Beroukhi, D. A. Milner, S. R. Granter, and J. et al. Du. Integrative genomic analyses identify MITF as a lineage survival oncogene amplified in malignant melanoma. *Nature*, 436(7047):117–22, 2005.
- [194] O. N. Ikediobi, H. Davies, G. Bignell, S. Edkins, C. Stevens, S. O’Meara, T. Santarius, T. Avis, S. Barthorpe, and L. et al. Brackenbury. Mutation analysis of 24

- known cancer genes in the NCI-60 cell line set. *Mol Cancer Ther*, 5(11):2606–12, 2006.
- [195] R. S. Obach. Prediction of human clearance of twenty-nine drugs from hepatic microsomal intrinsic clearance data: An examination of in vitro half-life approach and nonspecific binding to microsomes. *Drug Metab Dispos*, 27(11):1350–9, 1999.
- [196] E. Hellinger, M. L. Bakk, P. Pocza, K. Tihanyi, and M. Vastag. Drug penetration model of vinblastine-treated Caco-2 cultures. *Eur J Pharm Sci*, 41(1):96–106, 2010.
- [197] Z. S. Teksin, P. R. Seo, and J. E. Polli. Comparison of drug permeabilities and BCS classification: three lipid-component PAMPA system method versus Caco-2 monolayers. *AAPS J*, 12(2):238–41, 2010.
- [198] G. Szakacs, J. K. Paterson, J. A. Ludwig, C. Booth-Genthe, and M. M. Gottesman. Targeting multidrug resistance in cancer. *Nat Rev Drug Discov*, 5(3):219–34, 2006.
- [199] D. A. Smith, L. Di, and E. H. Kerns. The effect of plasma protein binding on in vivo efficacy: misconceptions in drug discovery. *Nat Rev Drug Discov*, 9(12):929–39, 2010.
- [200] D. L. Keefe, Y.-G. Yee, and R. E. Kates. Verapamil protein binding in patients and in normal subjects. *Clin. Pharm. Ther.*, 29(1):21–26, 1981.
- [201] A. F. Shields, J. R. Grierson, B. M. Dohmen, H. J. Machulla, J. C. Stayanoff, J. M. Lawhorn-Crews, J. E. Obradovich, O. Muzik, and T. J. Mangner. Imaging proliferation in vivo with [F-18]FLT and positron emission tomography. *Nat Med*, 4(11):1334–6, 1998.
- [202] Thermo Scientific. *TRIPZ Inducible Lentiviral shRNA*. 2014. <http://dharmacon.gelifesciences.com/shrna/tripz-lentiviral-shrna/>.
- [203] J. E. Bolden, M. J. Peart, and R. W. Johnstone. Anticancer activities of histone deacetylase inhibitors. *Nat Rev Drug Discov*, 5(9):769–84, 2006.
- [204] M. Haberland, R. L. Montgomery, and E. N. Olson. The many roles of histone deacetylases in development and physiology: implications for disease and therapy. *Nat Rev Genet*, 10(1):32–42, 2009.

- [205] T. Jenuwein and C. D. Allis. Translating the histone code. *Science*, 293(5532):1074–80, 2001.
- [206] T. Kouzarides. Chromatin modifications and their function. *Cell*, 128(4):693–705, 2007.
- [207] P. A. Marks, R. A. Rifkind, V. M. Richon, R. Breslow, T. Miller, and W. K. Kelly. Histone deacetylases and cancer: Causes and therapies. *Nature Reviews Cancer*, 1(3):194–202, 2001.
- [208] M. A. Dawson and T. Kouzarides. Cancer Epigenetics: From Mechanism to Therapy. *Cell*, 150(1):12–27, 2012.
- [209] L. Santo, T. Hideshima, A. L. Kung, J. C. Tseng, D. Tamang, M. Yang, M. Jarpe, J. H. van Duzer, R. Mazitschek, and W. C. et al. Ogier. Preclinical activity, pharmacodynamic, and pharmacokinetic properties of a selective HDAC6 inhibitor, ACY-1215, in combination with bortezomib in multiple myeloma. *Blood*, 119(11):2579–89, 2012.
- [210] M. Sankaranarayananpillai, W. P. Tong, D. S. Maxwell, A. Pal, J. Pang, W. G. Bornmann, J. G. Gelovani, and S. M. Ronen. Detection of histone deacetylase inhibition by noninvasive magnetic resonance spectroscopy. *Molecular Cancer Therapeutics*, 5(5):1325–34, 2006.
- [211] C. S. Ward, P. Eriksson, J. L. Izquierdo-Garcia, A. H. Brandes, and S. M. Ronen. HDAC inhibition induces increased choline uptake and elevated phosphocholine levels in MCF7 breast cancer cells. *PLoS One*, 8(4):e62610, 2013.
- [212] M. G. Vander Heiden. Targeting cancer metabolism: a therapeutic window opens. *Nat Rev Drug Discov*, 10(9):671–84, 2011.
- [213] V. Sampels, A. Hartmann, I. Dietrich, I. Coppens, L. Sheiner, B. Striepen, A. Herrmann, R. Lucius, and N. Gupta. Conditional Mutagenesis of a Novel Choline Kinase Demonstrates Plasticity of Phosphatidylcholine Biogenesis and Gene Expression in *Toxoplasma gondii*. *Journal of Biological Chemistry*, 287(20):16289–99, 2012.
- [214] O. Kepp, L. Galluzzi, M. Lipinski, J. Yuan, and G. Kroemer. Cell death assays for drug discovery. *Nat Rev Drug Discov*, 10(3):221–37, 2011.

- [215] S. Jackowski. Cell Cycle Regulation of Membrane Phospholipid Metabolism. *Journal of Biological Chemistry*, 271(34):20219–22, 1996.
- [216] F. Terce, H. Brun, and D. E. Vance. Requirement of phosphatidylcholine for normal progression through the cell cycle in C3H/10T1/2 fibroblasts. *J Lipid Res*, 35(12):2130–42, 1994.
- [217] C. Banchio, L. M. Schang, and D. E. Vance. Phosphorylation of Sp1 by Cyclin-dependent Kinase 2 Modulates the Role of Sp1 in CTP:Phosphocholine Cytidylyltransferase alpha Regulation during the S Phase of the Cell Cycle. *Journal of Biological Chemistry*, 279(38):40220–26, 2004.
- [218] X. H. Zhang, C. Zhao, K. Seleznev, K. Song, J. J. Manfredi, and Z. A. Ma. Disruption of G1-phase phospholipid turnover by inhibition of Ca<sup>2+</sup>-independent phospholipase A2 induces a p53-dependent cell-cycle arrest in G1 phase. *Journal of Cell Science*, 119(6):1005–15, 2006.
- [219] J. H. Lin, H. Li, D. Yasumura, H. R. Cohen, C. Zhang, B. Panning, K. M. Shokat, M. M. LaVail, and P. Walter. IRE1 Signaling Affects Cell Fate During the Unfolded Protein Response. *Science*, 318(5852):944–49, 2007.
- [220] E. Thorp, G. Li, T. A. Seimon, G. Kuriakose, D. Ron, and I. Tabas. Reduced Apoptosis and Plaque Necrosis in Advanced Atherosclerotic Lesions of Apoe<sup>-/-</sup> and Ldlr<sup>-/-</sup> Mice Lacking CHOP. *Cell Metabolism*, 9(5):474–81, 2009.
- [221] H. Matsumoto, S. Miyazaki, S. Matsuyama, M. Takeda, M. Kawano, H. Nakagawa, K. Nishimura, and S. Matsuo. Selection of autophagy or apoptosis in cells exposed to ER-stress depends on ATF4 expression pattern with or without CHOP expression. *Biol Open*, 2(10):1084–90, 2013.
- [222] M. Schroder and R. J. Kaufman. The mammalian unfolded protein response. *Annu Rev Biochem*, 74:739–89, 2005.
- [223] W. E. Mol, F. Rombout, J. E. Paanakker, R. Oosting, A. H. Scaf, and D. K. Meijer. Pharmacokinetics of steroidal muscle relaxants in isolated perfused rat liver. *Biochem Pharmacol*, 44(7):1453–9, 1992.
- [224] J. Appiah-Ankam and J. M. Hunter. Pharmacology of neuromuscular blocking drugs. *Continuing Education in Anaesthesia, Critical Care and Pain*, 4(1):2–7, 2004.

- [225] C. Lee. Goodbye Suxamethonium! *Anaesthesia*, 64:73–81, 2009.
- [226] C. Lee. Structure, conformation, and action of neuromuscular blocking drugs. *British Journal of Anaesthesia*, 87(5):755–69, 2001.
- [227] S. A. Kwee, B. Hernandez, O. Chan, and L. Wong. Choline kinase alpha and hexokinase-2 protein expression in hepatocellular carcinoma: association with survival. *PLoS One*, 7(10):e46591, 2012.
- [228] D. Rohle, J. Popovici-Muller, N. Palaskas, S. Turcan, C. Grommes, C. Campos, J. Tsoi, O. Clark, B. Oldrini, and E. et al. Komisopoulou. An Inhibitor of Mutant IDH1 Delays Growth and Promotes Differentiation of Glioma Cells. *Science*, 340(6132):626–30, 2013.
- [229] P. Yuan, K. Ito, R. Perez-Lorenzo, C. Del Guzzo, J. H. Lee, C. H. Shen, M. W. Bosenberg, M. McMahon, L. C. Cantley, and B. Zheng. Phenformin enhances the therapeutic benefit of BRAFV600E inhibition in melanoma. *Proc Natl Acad Sci U S A*, 110(45):18226–31, 2013.
- [230] S. J. Kridel, F. Axelrod, N. Rozenkrantz, and J. W. Smith. Orlistat Is a Novel Inhibitor of Fatty Acid Synthase with Antitumor Activity. *Cancer Research*, 64(6):2070–75, 2004.
- [231] D. Soloviev, D. Lewis, D. Honess, and E. Aboagye. [18F]FLT: An imaging biomarker of tumour proliferation for assessment of tumour response to treatment. *European Journal of Cancer*, 48(4):416–24, 2012.
- [232] M. Banez-Coronel, A. Ramirez de Molina, A. Rodriguez-Gonzalez, J. Sarmentero, M. A. Ramos, M. A. Garcia-Cabezas, L. Garcia-Oroz, and J. C. Lacal. Choline kinase alpha depletion selectively kills tumoral cells. *Curr Cancer Drug Targets*, 8(8):709–19, 2008.
- [233] N. E. Hynes and H. A. Lane. ERBB receptors and cancer: the complexity of targeted inhibitors. *Nat Rev Cancer*, 5(5):341–54, 2005.
- [234] A. P. Belsches-Jablonski, J. S. Biscardi, D. R. Peavy, D. A. Tice, D. A. Romney, and S. J. Parsons. Src family kinases and HER2 interactions in human breast cancer cell growth and survival. *Oncogene*, 20(12):1465–75, 2001.

- [235] D. L. Wheeler, M. Iida, and E. F. Dunn. The Role of Src in Solid Tumors. *The Oncologist*, 14(7):667–78, 2009.
- [236] N. Kanomata, J. Kurebayashi, Y. Kozuka, H. Sonoo, and T. Moriya. Clinicopathological significance of Y416Src and Y527Src expression in breast cancer. *J Clin Pathol*, 64(7):578–86, 2011.
- [237] L. M. Kenny, K. B. Contractor, R. Hinz, J. Stebbing, C. Palmieri, J. Jiang, S. Shousha, A. Al-Nahhas, R. C. Coombes, and E. O. Aboagye. Reproducibility of [11C]choline-positron emission tomography and effect of trastuzumab. *Clin Cancer Res*, 16(16):4236–45, 2010.
- [238] J. Carlsson, H. Nordgren, J. Sjostrom, K. Wester, K. Villman, N. O. Bengtsson, B. Ostenstad, H. Lundqvist, and C. Blomqvist. HER2 expression in breast cancer primary tumours and corresponding metastases. Original data and literature review. *Br J Cancer*, 90(12):2344–8, 2004.
- [239] C. Gravalos and A. Jimeno. HER2 in gastric cancer: a new prognostic factor and a novel therapeutic target. *Annals of Oncology*, 19(9):1523–29, 2008.
- [240] W. Tai, R. Mahato, and K. Cheng. The role of HER2 in cancer therapy and targeted drug delivery. *Journal of Controlled Release*, 146(3):264–75, 2010.
- [241] J. S. Ross and J. A. Fletcher. The HER-2/neu oncogene in breast cancer: Prognostic factor, predictive factor, and target for therapy. *Stem Cells*, 16(6):413–28, 1998.
- [242] M. A. Olayioye, R. M. Neve, H. A. Lane, and N. E. Hynes. The ErbB signaling network: receptor heterodimerization in development and cancer. *EMBO J*, 19(13):3159–67, 2000.
- [243] C. A. Hudis. Trastuzumab - Mechanism of Action and Use in Clinical Practice. *New England Journal of Medicine*, 357(1):39–51, 2007.
- [244] R. Zagozdzon, W. M. Gallagher, and J. Crown. Truncated HER2: implications for HER2-targeted therapeutics. *Drug Discovery Today*, 16(17-18):810–16, 2011.
- [245] S. K. Mohsin, H. L. Weiss, M. C. Gutierrez, G. C. Chamness, R. Schiff, M. P. DiGiovanna, C.-X. Wang, S. G. Hilsenbeck, C. K. Osborne, D. C. Allred, R. Elledge,



- and J. C. Chang. Neoadjuvant Trastuzumab Induces Apoptosis in Primary Breast Cancers. *Journal of Clinical Oncology*, 23(11):2460–68, 2005.
- [246] L. N. Harris, F. You, S. J. Schnitt, A. Witkiewicz, X. Lu, D. Sgroi, P. D. Ryan, S. E. Come, H. J. Burstein, and B.-A. et al. Lesnikoski. Predictors of Resistance to Preoperative Trastuzumab and Vinorelbine for HER2-Positive Early Breast Cancer. *Clinical Cancer Research*, 13(4):1198–207, 2007.
- [247] A. Fabi, A. Di Benedetto, G. Metro, L. Perracchio, C. Nistico, F. Di Filippo, C. Ercolani, G. Ferretti, E. Melucci, S. Buglioni, I. Sperduti, P. Papaldo, F. Cognetti, and M. Mottolese. HER2 Protein and Gene Variation between Primary and Metastatic Breast Cancer: Significance and Impact on Patient Care. *Clinical Cancer Research*, 17(7):2055–64, 2011.
- [248] H. Shafi, K. Astvatsaturyan, F. Chung, J. Mirocha, M. Schmidt, and S. Bose. Clinicopathological significance of HER2/neu genetic heterogeneity in HER2/neu non-amplified invasive breast carcinomas and its concurrent axillary metastasis. *J Clin Pathol*, 66(8):649–54, 2013.
- [249] G. Pauletti, W. Godolphin, M. F. Press, and D. J. Slamon. Detection and quantitation of HER-2/neu gene amplification in human breast cancer archival material using fluorescence in situ hybridization. *Oncogene*, 13(1):63–72, 1996.
- [250] B. Leyland-Jones and B. R. Smith. Serum HER2 testing in patients with HER2-positive breast cancer: the death knell tolls. *Lancet Oncology*, 12(3):286–95, 2011.
- [251] P.-A. Nygren. Alternative binding proteins: Affibody binding proteins developed from a small three-helix bundle scaffold. *FEBS Journal*, 275(11):2668–76, 2008.
- [252] V. Tolmachev, A. Orlova, F. Y. Nilsson, J. Feldwisch, A. Wennborg, and L. Abrahamson. Affibody molecules: potential for in vivo imaging of molecular targets for cancer therapy. *Expert Opin Biol Ther*, 7(4):555–68, 2007.
- [253] J. Lofblom, J. Feldwisch, V. Tolmachev, J. Carlsson, S. Stahl, and F. Y. Frejd. Affibody molecules: Engineered proteins for therapeutic, diagnostic and biotechnological applications. *FEBS Letters*, 584(12):2670–80, 2010.

- [254] S. K. Calderwood, M. A. Khaleque, D. B. Sawyer, and D. R. Ciocca. Heat shock proteins in cancer: chaperones of tumorigenesis. *Trends in Biochemical Sciences*, 31(3):164–72, 2006.
- [255] R. Bose, S. M. Kavuri, A. C. Searleman, W. Shen, D. Shen, D. C. Koboldt, J. Monsey, N. Goel, A. B. Aronson, S. Li, C. X. Ma, L. Ding, E. R. Mardis, and M. J. Ellis. Activating HER2 mutations in HER2 gene amplification negative breast cancer. *Cancer Discov*, 3(2):224–37, 2013.
- [256] A. Orlova, M. Magnusson, T. L. Eriksson, M. Nilsson, B. Larsson, I. Hoiden-Guthenberg, C. Widstrom, J. Carlsson, V. Tolmachev, S. Stahl, and F. Y. Nilsson. Tumor imaging using a picomolar affinity HER2 binding affibody molecule. *Cancer Res*, 66(8):4339–48, 2006.
- [257] V. Tolmachev, F. Y. Nilsson, C. Widstrom, K. Andersson, D. Rosik, L. Gedda, A. Wennborg, and A. Orlova. In-111-benzyl-DTPA-Z(HER2 : 342), an affibody-based conjugate for in vivo imaging of HER2 expression in malignant tumors. *Journal of Nuclear Medicine*, 47(5):846–53, 2006.
- [258] G. Kramer-Marek, D. O. Kiesewetter, L. Martiniova, E. Jagoda, S. B. Lee, and J. Capala. [18F]FBEM-Z(HER2:342)-Affibody molecule-a new molecular tracer for in vivo monitoring of HER2 expression by positron emission tomography. *Eur J Nucl Med Mol Imaging*, 35(5):1008–18, 2008.
- [259] G. Kramer-Marek, D. O. Kiesewetter, and J. Capala. Changes in HER2 expression in breast cancer xenografts after therapy can be quantified using PET and 18F-labeled affibody molecules. *J Nucl Med*, 50(7):1131–9, 2009.
- [260] J. Malmberg, M. Sandstrom, K. Wester, V. Tolmachev, and A. Orlova. Comparative biodistribution of imaging agents for in vivo molecular profiling of disseminated prostate cancer in mice bearing prostate cancer xenografts: focus on 111In- and 125I-labeled anti-HER2 humanized monoclonal trastuzumab and ABY-025 affibody. *Nucl Med Biol*, 38(8):1093–102, 2011.
- [261] G. Kramer-Marek, M. Gijzen, D. O. Kiesewetter, R. Bennett, I. Roxanis, R. Zielinski, A. Kong, and J. Capala. Potential of PET to predict the response to trastuzumab

- treatment in an ErbB2-positive human xenograft tumor model. *J Nucl Med*, 53(4): 629–37, 2012.
- [262] G. Kramer-Marek, M. Bernardo, D. O. Kiesewetter, U. Bagci, M. Kuban, O. Aras, R. Zielinski, J. Seidel, P. Choyke, and J. Capala. PET of HER2-positive pulmonary metastases with <sup>18</sup>F-ZHER2:342 affibody in a murine model of breast cancer: comparison with <sup>18</sup>F-FDG. *J Nucl Med*, 53(6):939–46, 2012.
- [263] J. Feldwisch, V. Tolmachev, C. Lendel, N. Herne, A. Sjoberg, B. Larsson, D. Rosik, E. Lindqvist, G. Fant, I. Hoiden-Guthenberg, J. Galli, P. Jonasson, and L. Abrahmsen. Design of an optimized scaffold for affibody molecules. *J Mol Biol*, 398(2): 232–47, 2010.
- [264] EudraLex. *Volume 4 Good manufacturing practice (GMP) Guidelines*. European Commission, Brussels, 2013.
- [265] S. Ahlgren, A. Orlova, H. Wallberg, M. Hansson, M. Sandstrom, R. Lewsley, A. Wennborg, L. Abrahmsen, V. Tolmachev, and J. Feldwisch. Targeting of HER2-expressing tumors using <sup>111</sup>In-ABY-025, a second-generation affibody molecule with a fundamentally reengineered scaffold. *J Nucl Med*, 51(7):1131–8, 2010.
- [266] J. Malmberg, A. Perols, Z. Varasteh, M. Altai, A. Braun, M. Sandstrom, U. Garske, V. Tolmachev, A. Orlova, and A. E. Karlstrom. Comparative evaluation of synthetic anti-HER2 Affibody molecules site-specifically labelled with <sup>111</sup>In using N-terminal DOTA, NOTA and NODAGA chelators in mice bearing prostate cancer xenografts. *Eur J Nucl Med Mol Imaging*, 39(3):481–92, 2012.
- [267] C. Xavier, I. Vaneycken, M. D’Huyvetter, J. Heemskerk, M. Keyaerts, C. Vincke, N. Devoogdt, S. Muyldermans, T. Lahoutte, and V. Caveliers. Synthesis, preclinical validation, dosimetry, and toxicity of <sup>68</sup>Ga-NOTA-anti-HER2 Nanobodies for iPET imaging of HER2 receptor expression in cancer. *J Nucl Med*, 54(5):776–84, 2013.
- [268] T. M. Behr, D. M. Goldenberg, and W. Becker. Reducing the renal uptake of radiolabeled antibody fragments and peptides for diagnosis and therapy: present status, future prospects and limitations. *Eur J Nucl Med*, 25(2):201–12, 1998.
- [269] A. Orlova, V. Tolmachev, R. Pehrson, M. Lindborg, T. Tran, M. Sandstrom, F. Y. Nilsson, A. Wennborg, L. Abrahmsen, and J. Feldwisch. Synthetic Affi-

- body Molecules: A Novel Class of Affinity Ligands for Molecular Imaging of HER2-Expressing Malignant Tumors. *Cancer Research*, 67(5):2178–86, 2007.
- [270] S. Hoppmann, Z. Miao, S. Liu, H. Liu, G. Ren, A. Bao, and Z. Cheng. Radiolabeled Affibody-Albumin Bioconjugates for HER2-Positive Cancer Targeting. *Bioconjugate Chemistry*, 22(3):413–21, 2011.
- [271] C. Hofstrom, M. Altai, H. Honarvar, J. Strand, J. Malmberg, S. J. Hosseinimehr, A. Orlova, T. Graslund, and V. Tolmachev. HAHAAA, HEHEHE, HIIIII, or HKHKHK: Influence of Position and Composition of Histidine Containing Tags on Biodistribution of  $[^{99m}\text{Tc}(\text{CO})_3]^+$ -Labeled Affibody Molecules. *Journal of Medicinal Chemistry*, 56(12):4966–74, 2013.
- [272] R. P. Baum, V. Prasad, D. Muller, C. Schuchardt, A. Orlova, A. Wennborg, V. Tolmachev, and J. Feldwisch. Molecular Imaging of HER2-Expressing Malignant Tumors in Breast Cancer Patients Using Synthetic  $^{111}\text{In}$ - or  $^{68}\text{Ga}$ -Labeled Affibody Molecules. *Journal of Nuclear Medicine*, 51(6):892–97, 2010.
- [273] P. M. Smith-Jones, D. B. Solit, T. Akhurst, F. Afroze, N. Rosen, and S. M. Larson. Imaging the pharmacodynamics of HER2 degradation in response to Hsp90 inhibitors. *Nat Biotech*, 22(6):701–06, 2004.
- [274] C. Eigenbrot, M. Ultsch, A. Dubnovitsky, L. Abrahmsen, and T. Hard. Structural basis for high-affinity HER2 receptor binding by an engineered protein. *Proceedings of the National Academy of Sciences*, 107(34):15039–44, 2010.
- [275] R. Shukla, T. P. Thomas, J. L. Peters, A. M. Desai, J. Kukowska-Latallo, A. K. Patri, A. Kotlyar, and J. R. Baker. HER2 Specific Tumor Targeting with Dendrimer Conjugated Anti-HER2 mAb. *Bioconjugate Chemistry*, 17(5):1109–15, 2006.
- [276] G. Valabrega, F. Montemurro, and M. Aglietta. Trastuzumab: mechanism of action, resistance and future perspectives in HER2-overexpressing breast cancer. *Ann Oncol*, 18(6):977–84, 2007.
- [277] S. A. Eccles, A. Massey, F. I. Raynaud, S. Y. Sharp, G. Box, M. Valenti, L. Patterson, A. de Haven Brandon, S. Gowan, and F. et al. Boxall. NVP-AUY922: A Novel Heat Shock Protein 90 Inhibitor Active against Xenograft Tumor Growth, Angiogenesis, and Metastasis. *Cancer Research*, 68(8):2850–60, 2008.

- [278] T. H. Oude Munnink, M. A. d. Korte, W. B. Nagengast, H. Timmer-Bosscha, C. P. Schroder, J. R. d. Jong, G. A. M. S. v. Dongen, M. R. Jensen, C. Quadt, M. N. L.-d. Hooge, and E. G. E. d. Vries.  $^{89}\text{Zr}$ -trastuzumab PET visualises HER2 downregulation by the HSP90 inhibitor NVP-AUY922 in a human tumour xenograft. *European Journal of Cancer*, 46(3):678–84, 2010.
- [279] P. M. Smith-Jones, D. Solit, F. Afroze, N. Rosen, and S. M. Larson. Early tumor response to Hsp90 therapy using HER2 PET: comparison with  $^{18}\text{F}$ -FDG PET. *J Nucl Med*, 47(5):793–6, 2006.
- [280] S. Mitsuhashi, H. Hatakeyama, M. Karahashi, T. Koumura, I. Nonaka, Y. K. Hayashi, S. Noguchi, R. B. Sher, Y. Nakagawa, G. Manfredi, Y. Goto, G. A. Cox, and I. Nishino. Muscle choline kinase beta defect causes mitochondrial dysfunction and increased mitophagy. *Hum Mol Genet*, 20(19):3841–51, 2011.
- [281] B. A. Neel, Y. Lin, and J. E. Pessin. Skeletal muscle autophagy: a new metabolic regulator. *Trends Endocrinol Metab*, 24(12):635–43, 2013.